THE USE OF PNEUMATIC ACTUATION TO ADDRESS SHORTCOMINGS CONCERNING NORMALIZED OUTPUT POWER IN STATE OF THE ART MOBILE ROBOTICS

By

Keith W. Wait

Dissertation

Submitted to the Faculty of the

Graduate School of Vanderbilt University

in partial fulfillment of the requirements

for the degree of

DOCTOR OF PHILOSOPHY

in

Mechanical Engineering

August, 2010

Nashville, Tennessee

Approved:

Professor Michael Goldfarb

Professor Eric Barth

Professor Robert Roselli

Professor Nilanjan Sarkar

Professor Robert Webster

To Amber... finally.

ACKNOWLEDGMENTS

I very much appreciate the encouragement, support, and guidance of my advisor, Dr. Michael Goldfarb. I will never forget his first words to me after I took the tremendous leap of quitting my previous job as an engineer in the aerospace industry and relocating most of the way across the country to begin my graduate studies at Vanderbilt: “Who are you?” Despite this, he has been a great mentor and teacher and I have learned a great deal from my time spent in his tutelage.

I would also like to thank the members of my dissertation committee, Drs. Eric Barth, Robert Roselli, Nilanjan Sarkar, and Robert Webster for their time, effort, and guidance in helping me to complete this ordeal.

I am indebted to Scott Wojtulewicz and Rod Powell of Orbital Sciences Corporation for their (perhaps unintentional) encouragement by reminding me that the grass is not always greener outside of the ivory tower and that, in fact, it's dead and charred everywhere. Also, thanks to Lanny Smoot and Joe Marks of Disney Research for the fascinating experiences afforded to me during my time with them as well as for allowing me to make progress on this work while in their employ.

I am also grateful to the Vanderbilt University Graduate School and to the National Science Foundation's Engineering Research Center for Compact and Efficient Fluid Power for their financial support of my education and this research.

Also, thank you to my colleagues on the fifth floor for their occasionally good suggestions and especially to Kevin Fite for designing an amazing miniature proportional valve that works flawlessly every time and made my engineering life so wonderful for the last several years. I can only hope that you experience the same kinds of success in your endeavors that your valve has allowed me to achieve in mine.

The staff engineers of the Center for Intelligent Mechatronics, Don Truex and Jason Mitchell, have been an invaluable source of expertise for me to draw upon. Without their help, I would likely have floundered for even more months in trying to solve some of the more difficult problems that somehow crept into the process of designing and building the infernal machine described below.

Finally, the most sincere thanks to my wife Amber for putting up with all this nonsense. You have truly been the only bright spot in my life during the desolation that has been my graduate school career.

TABLE OF CONTENTS

Page

Appendix

LIST OF FIGURES

Figure Page

LIST OF TABLES

Table Page

CHAPTER I

INTRODUCTION

I.A The State of the Art

An extremely large number of polypedal walking robots (e.g. [1-9] and others [10]) have been designed and realized over the last forty years. These robots vary in many facets of their design, such as number of legs, whether they are dynamically or quasistatically stable, the type of control used (e.g. joint space or task space; force, position, impedance, or some other type of control), level of autonomy, mechanism design, power and actuator choice. However, the most important variation between these robots is their level of success.

Advancements in the field of walking and climbing robots have ranged from the development of novel mechanisms and materials [11] to highly stable dynamic walking [12] and beyond. However, one limitation that is common to almost all walking robot ventures undertaken to date is the lack of a combination of actuator and power supply with sufficient energetic, power, and force densities to be useful in non-tethered operation.

Electromagnetic actuation and power are very common in the field of robotics because of the ubiquity and ease of development and deployment of electromagnetic actuators such as DC motors and solenoids as well as portable electric power sources, i.e.

batteries. Fluid powered robots, while not as common due to the complexity of pneumatic and hydraulic systems relative to their electromagnetic counterparts, have nonetheless been fielded [13-15] in some past efforts.

Specifically, Hirose et al have devised and built a hybrid legged/wheeled robot that is pneumatically actuated for walking and hopping locomotion [16,17]. This effort is currently active and while there have been published demonstrations of wheeled motion and hopping, there have not yet been published data showing pneumatically actuated walking. Quinn et al developed a highly biomimetic pneumatic walker based on detailed studies of the *Blaberus discoidalis* cockroach [18,19]. While this robot is impressive in its design and potential, there does not appear to be any published evidence of its performance in self-locomotion. A group from the University of Portsmouth has developed a series of pneumatic climbing and walking robots [20-22] to be teleoperated in hazardous environments. Lastly, Binnard [23] developed a hexapedal walking robot with 16 pneumatic actuators that demonstrated a payload capacity of 40% of the robot's weight while walking at a speed of approximately .22 body length per second.

Advances in battery technology over the last several years have yielded quite high energy densities, but electromagnetic actuators will, for the foreseeable future, have low power and force densities, especially compared with commonplace pneumatic actuators [24]. Common pneumatic power sources, however, have energy densities which do not begin to approach those of batteries.

Motivated by the disparity between electromagnetic actuation that typically has high energy density but low power and force density and pneumatic actuation that typically has low energy density but high power and force density, it has been undertaken

to design and construct a robot that is driven by pneumatic actuators. However, the robot is agnostic with respect to the source of the working fluid of the actuators. Under this type of actuation, the robot has been shown to self locomote while carrying a payload in excess of 100% of its own body weight and to propel itself forward at a rate of approximately one body length per second.

I.B Benefits of Fluid Power in Mobile Systems

As noted above, a vast array of walking robots spanning a wide variety of sizes and types have been fielded by researchers over the last several decades. A sampling of both older and more recent noteworthy robots was surveyed and the salient performance characteristics compiled and tabulated in Table 1. In this table, the documented output metrics of the robot are given as the normalized maximum walking speed in robot body lengths per second and the normalized payload carried by the robot in robot body masses. The product of these two values (normalized speed and normalized payload) can be used as a metric for comparing many robots and will be referred to as the normalized output power.

Table 1
Normalized Power Characterizations of Selected Mobile Robots

Project	Body Length (m)	Body Mass (kg)	Max. Speed (BL/s)	Max Walking Payload (BM)	Notes
BigDog	1.1	109	1.82	1.41	On board power, Ascends 35 deg incline
Sprawl	0.16	.27	15	None Reported	On board power, 5 minutes of run time
RHex	.53	7	1.04	None Reported	On board power, 15 minutes of run time
Boadicea	.5	4.76	.22	.46	Tethered pneumatic power
Robot II	0.5	1	0.28	None Reported	
Robot III	.76	13.6	None Reported	None Reported	Lifted 1 BM while not walking
Puppy	0.6	6.8 (est.)	.67 (est.)	None Reported	Two legs lifted 2 BM while not walking
AirHopper	1.29	34.6	None Reported	None Reported	Jumps 1.6 BL high, 1.4 BL/s wheeled speed
Dante II	3.7	770	0.02	0.17	Tethered 2kW Power Draw
Adaptive Suspension Vehicle	5.8	3175	0.16	0.08	Pulled sled weighing .34 body masses
Scout II	0.84	21.7	1.55	None Reported	On board power, galloping gait
Titan XI	3.4	6800	2.2×10^{-3}	None Reported	Carries one person, on board power
Silo4	0.3	30	0.06	0.33	
Lauron III	0.7	18	0.43	0.56	
GE Truck	4	1300	0.23	0.17	
HuboDog	0.8	42	0.69	0.57	
Asimo	1.2	52	0.37	0.02	On board power, 1 hr run time

The relevant summary of the data in Table 1 (compiled from [3,4,12,15,17,18,23,25-33]) is that very few robots described in the literature have documented the ability to simultaneously carry some non-trivial payload and self-locomote. This is a significant gap in the state of the art in mobile robotics since a robot who cannot carry a payload is of little practical utility even if it has a high degree of mobility and dexterity.

Of those robots that claim the capability to simultaneously self-locomote and carry a payload, fewer still are able to operate untethered, i.e. they do not carry an on-board power source. Of particular note is that several of those robots who claim to have a nontrivial normalized output power (product of normalized output force and normalized velocity) and operate untethered are fluid powered, i.e. either pneumatically or hydraulically actuated (Titan XI, Adaptive Suspension Vehicle, BigDog).

A thorough study of the power densities of possible actuation choices for mobile robots was conducted by Kuribayashi [24]. It is abundantly clear from the conclusions of this paper that the power densities of pneumatic and hydraulic actuators are vastly superior to those of electromagnetic actuators. However, while fluid power maintains this significant advantage in actuation, energy storage solutions that are well matched to these forms of actuation have remained elusive. One standard approach is to include a compressor or pump on board the robot to supply pressure to the fluid actuator. This method allows a very energy dense hydrocarbon to serve as the fuel source (since an internal combustion engine can be employed to drive the pump or compressor) but suffers from a high component count (and thus a low reliability), a large payload overhead in the mass of the energy generation system (i.e. the maximum achievable

payload is reduced by the weight of the IC engine, compressor, etc.), as well as the introduction of a significant number of drops in efficiency in the energy transduction path from chemical potential energy in the fuel to compressed air or hydraulic fluid that can ultimately be used by the actuator. In other words, there is some inefficiency associated with each of the stages of energy transfer in this scheme (e.g. incomplete combustion, heat loss in engine, heat loss in compressor, frictional losses within engine and compressor, theoretically low maximum efficiencies of both engine and compressor, etc.), and so there is a large gross energy loss. Alternatively, a battery/electric motor combination (which is considerably more efficient than an IC engine) could be employed to drive the pump or compressor, but this does not eliminate some of the principal inefficiencies, such as those in the compressor. Further, this scheme is not likely to be competitive because the energy density of the battery is far less than that of a hydrocarbon fuel.

A second standard approach is to outfit the robot or mobile machine with a tank of compressed air. While this method allows for a more appropriately matched delivery of stored energy to the actuator (i.e. transfer of energy from the storage medium to the actuator is direct and fewer opportunities for energy loss exist), the energy density of typical gas storage mediums (e.g. liquid CO_2 or compressed gaseous N_2) is very low compared to either batteries or hydrocarbon fuels. Therefore, the efficacy of the device is severely limited either because the compressed fluid will be rapidly exhausted or because the robot will be overburdened by the extreme size and weight of a reservoir required to have a longer useful life.

The approach championed by Goldfarb et al [34] is to employ hydrogen peroxide (H_2O_2) used as a monopropellant as the compressed gas storage medium. In this approach, the monopropellant is catalytically decomposed into high temperature oxygen and steam in the presence of a precious metal catalyst. Common catalysts are silver, palladium, and iridium. Decomposition happens very quickly, especially relative to the timescales of a pneumatically actuated system. The use of a energy generation system such as this allows for a much higher energy density and specific volume in the storage of the gas than in compressed gasses as it is accessed through a chemical reaction rather than through a phase change or simple expansion. Further, the monopropellant has a greater potential to do useful work when compared to traditional gas storage mediums as the products of decomposition are more energetic, due to their high temperature, than are compressed gasses.

The monopropellant actuated systems first designed in [34] and deployed in [35,36] are ideally suited to mobile robotics applications as they pair a proven high power density actuation mechanism with a novel energetically dense fuel that is well suited to power the actuators.

The comparison between state of the art electromagnetic actuated systems and the proposed actuation methods is perhaps best made via the device of a Ragone plot. A line on a Ragone plot represents all the possible machines that can be made with a particular energy storage medium and a particular power delivery device, i.e. actuator. One end of the line represents the limit where the machine is dominated by the energy storage medium (e.g. an R/C airplane IC engine with a tanker truck sized fuel tank). The other end of the line represents the limit where the machine is dominated by the actuator (e.g. a

jet engine for a commercial aircraft with a fuel tank holding one drop of fuel). The lines on a Ragone plot generally have a knee where the transition from energy storage dominant machines to power output dominant machines is made. Most physically realized (and useful) systems fall near this knee.

Fig. 1 shows a Ragone plot with lines for a variety of possible energy storage/actuator pairings. In the figure, P2A denotes a monopropellant powered hot gas vane motor driving a hydraulic pump/motor and P2B denotes a propane fired free piston air compressor (see section I.C for further elaboration) driving a pneumatically actuated system. The line marked “Monopropellant + Pneumatic” refers to the hydrogen peroxide systems referred to in the preceding paragraphs. In general, the further from the origin of a Ragone plot that an individual machine's power and energy densities fall, the more capable the machine will be. For the comparison shown in the figure, it seems clear that there is an advantage to using a fluid powered system as the three options shown (red, blue, and green lines in Fig. 1) have distinct advantages over the more common DC motor/battery and IC engine/hydraulic pump combinations (black lines in Fig. 1).

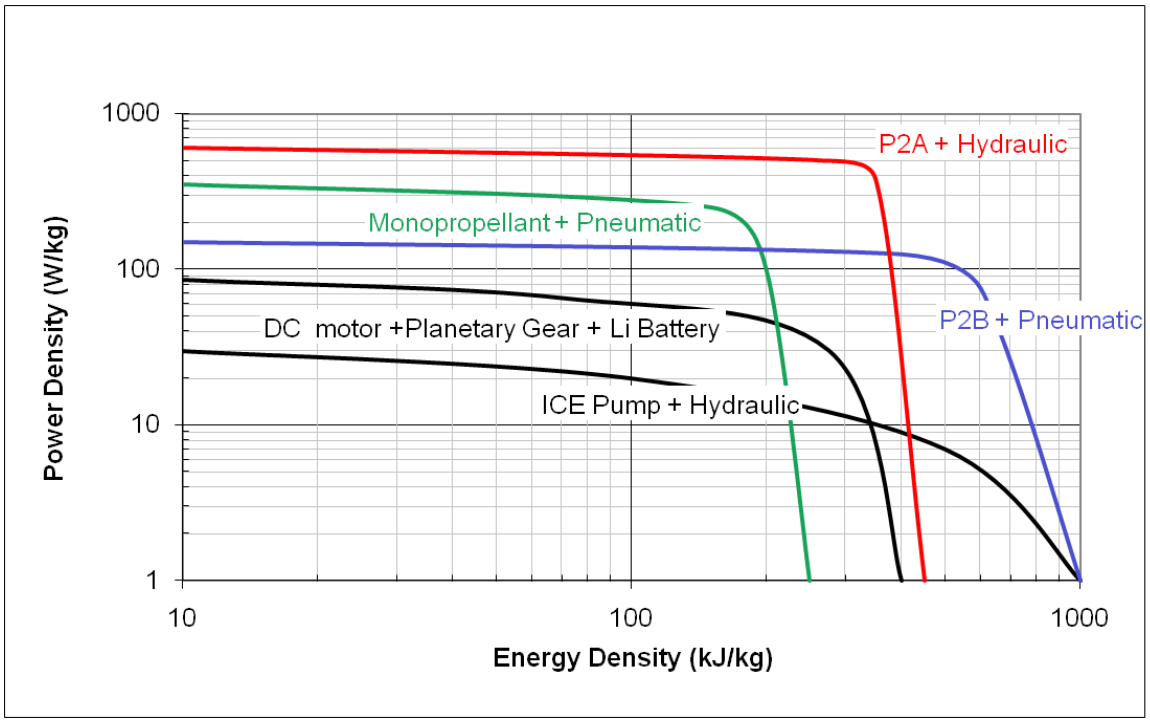

Fig. 1. Ragone plot comparing power storage and delivery approaches

It is believed that a mobile robotic system using pneumatic actuation and either the highly energy dense monopropellant or the novel free-piston air compressor as its source of working fluid will fill the aforementioned gap in the state of the art in mobile robotics. That is, the robot in question will, using a self-contained power source, be able to carry as payload a significant portion of its own weight (≥ 50%) while walking at a reasonable speed (≥ 1 body length per second).

I.C Possible Energy Storage Mediums for the Robot

This robot is part of a wider collaborative effort facilitated by the NSF's Engineering Research Center for Compact and Efficient Fluid Power (CCEFP). Within this collaboration, the walking robot is a project designed to demonstrate the efficacy of a number of fluid power supplies in a compact human-to-sub-human scale setting. Three

sources for supplying fluid power to the walking robot are targeted as part of this collaborative framework. The first two power sources are suited for the present, pneumatic version of the robot and are direct injection of hot gas byproducts of monopropellant decomposition [35,37] and a propane-fired liquid slug free piston air compressor [38,39]. The third power source is a hot gas (hydrogen peroxide monopropellant fired) vane motor that drives a hydraulic pump. This source is intended for a future iteration of the device described in this document that would, ostensibly, utilize a hydraulic actuation system.

This work aims to document the process through which the ultimately constructed and fielded robot was conceived, to show the design of the quadrupedal robot, and to describe the methods used for controlling walking locomotion of the robot. Demonstrated walking results will also be presented that were obtained using tethered power supplies that mimic the pressures and flow rates of the intended power supply targets. The use of off-board pneumatic power is intended to validate the design of both robot hardware and control systems. Integration of the on-board power supplies as listed above will occur and be evaluated as the respective systems become mature.

I.D Organization of this Work

The text of this work is divided into seven chapters and several sections. Chapter I is this introduction and motivation to the actual work described.

Chapter II gives a description of the initial work undertaken to characterize the possible performance of the robotic system as well as to guide its detailed design work. This chapter is composed of two subsections, each of which are reprintings of two previously published works. Section II.B is reprinted from [40] and Section II.C is reprinted from [41].

Chapter III details the methods through which meaningful locomotion and work are achieved with the constructed physical robot. Note that Section III.B is reprinted from [42].

Chapter IV provides a detailed description of the final mechanical construction of the robot platform and Chapter V describes the accompanying electrical and actuation systems.

Chapter VI describes the experiments that were carried out using the system developed in Chapters III, IV, and V, as well as a comparison of the output power metrics described above for previously documented robots with those of the robot documented herein.

Finally, Chapter VII outlines the lessons learned during the execution of this project and offers conclusions and recommendations on the outcome as well as the process undertaken to arrive at final results.

CHAPTER II

EXPLORATION OF WALKING ROBOT DESIGN

II.A Initial Design Considerations

Designing a robot is in general a difficult problem. The difficulty is compounded when the design space is not constrained by performance targets, weight limitations, form factor specifications, etc. (as is the case with the present robot). The only goal at the start of this project was to build a walking robot approximately the size of a small dog that would be able to traverse obstacles approximately the size of a standard American cinder block (a rectangular prismatic envelope measuring 20.3 cm x 20.3 cm x 40.6 cm). This single constraint in the highly open design space for walking robots did little to guide the design. As a first act, the assumption was made that a six-legged vehicle would be both dexterous and robust and so the robot was initially designed as a hexapod. In order to further guide the process of designing the physical structure of the robot, simulations were undertaken to estimate joint output forces and speeds required to achieve self locomotion. Further, it was discovered in literature searches that one of the most challenging problems in polypedal locomotion relates to how the several legs should be coordinated. Simulation was used to address this problem. These simulations are described in Section II.B.

Based on these simulations, a prototype robot was constructed and fielded. While the results of the simulation and some early testing in hardware indicated that a purely position based approach to the control of the leg joints would be both appropriate and

easily tractable, further testing with this prototype provided contradicting results. The results of the testing with this prototype, including hardware design, joint control issues, and extension of the inter-leg coordination algorithms are described in Section II.C.

II.B Simulation for Design Guidance

Many research groups have developed approaches for the control of locomotion in hexapedal walking robots [10]. The motivation to pursue this kind of locomotion rather than any other is that the hexapedal platform is by its physical nature extremely stable. The two principle gaits of this kind of walker, the tripod and tetrapod gaits, are both statically stable, since the hexapod maintains at least three points of ground contact at all time, which eliminates the need for active balancing in such platforms. Additionally, since the hexapod has redundant legs compared to the also naturally stable quadruped walker, it is theoretically possible for this sort of vehicle to be able to continue operation in the event of disabled limbs.

The various approaches for the control of locomotion in hexapods (and other multipedal robots) can be roughly categorized into three categories, which include central pattern generation approaches, finite state approaches, and coordination-based approaches. In the central pattern generation approaches, a gait is pre-selected by the designer and a central pattern generator is used that provides each leg with a trajectory signal. This signal corresponds to the solely internal representation of the robot‘s desired walking motion. Most approaches to locomotion in hexapedal walking devices follow this paradigm, as represented by the work of Lee and Lee [43], Zielinska et al. [44], Clark et al. [45], and others. Unlike the central pattern approaches, the finite-state approaches incorporate a set of conditions that place the robot into one of several states, as

determined by a predetermined rule set for various types of environmental interaction (i.e., stair climbing, walking over flat terrain, etc.). Examples of this work include that of Tanaka and Matoba [46], Saranli et al. [47], and others.

The third major category, coordination-based approaches, is one in which the gait is not statically specified, but in which it is an emergent behavior resulting from some sort of coordination system. This type of system is theoretically able to more easily traverse arbitrary and possible hostile terrain since, as Klavins et al. [48] point out, the difference between the central pattern generator approach and that of the coordination system is akin to the difference between open-loop and closed-loop control.

This kind of approach has had some following, including the works of Chiel and Quinn et al. [49,50], Calvitti and Beer [51], Svinin et al. [52], Pfeiffer et al. [53], and others.

Cruse et al. [54,55] thoroughly investigated the neural control structure utilized for control of locomotion in the stick insect *Carausius morosus*. Specifically, by sequentially and selectively isolating various components of the insect's neural circuitry and by utilizing microelectrodes to measure neural activity during various phases of locomotion, Cruse et al. in essence "reverse-engineered" the neural circuitry of the *Carausius morosus*. Based on their investigations, they proposed a system of interconnected neural networks (collectively termed WalkNet) that emulates the circuitry that coordinates locomotion in the insect. As described subsequently, one of the interesting aspects of WalkNet, one that is patterned directly after the biological system, is the use of positive feedback (i.e., unstable feedback) in the stance phase of locomotion. Cruse et al. further demonstrated the promise of their approach via a series of

simulations. One significant shortcoming of their validation, however, is that their simulations did not consider gravitational effects, inertial dynamics, or contact dynamics between the legs and the ground. In the case of a stick insect, one can argue that such (inertial) dynamics are not significant. At the scale of a typical hexapedal robot, however, such effects are significant, and have a significant bearing on the stability of a closed-loop system. In fact, as discovered by the authors, WalkNet (as presented by Cruse et al.) does not provide stable locomotion in the presence of dynamic effects. Motivated by this issue, the authors propose a modified version of WalkNet that is based on its biological paradigm, but that provides stable locomotion in the presence of dynamics, while still enabling the significant benefits (i.e., self-selecting, robust, emergent behavior) of the WalkNet approach.

II.B.1 Synopsis of WalkNet

Cruse's neural network that achieves synthetic stick insect walking consists of three main subsystems, namely the swing net (which generates a leg's trajectory during swing phase), the stance net (which does the same for the stance phase), and the selector net (which decides for each leg which of the two trajectories to use).

The swing net is a neural network that has been trained using data from in vivo motion measurements of the stick insect, the results of which are subsequently massaged using a non-linear multiplier and a bias input so as to very closely mimic the swing trajectory of the animal.

For stance, Cruse propounds the idea that positive feedback of joint velocity can be used along with a few modifications to reliably and simply generate a stance trajectory. That is, if one of the important functions of the stance phase is to propel the body forward, such propulsion can be achieved (and apparently may be achieved in the stick insect) by using positive feedback in the thoracic-coxal (α) and femur-tibia (γ) joints, which simply push back against the ground while in contact with it.

One of the most significant benefits to the method proposed by Cruse is that, rather than use a central pattern generator as many hexapedal robots do, the gait is evolved due to the fact that each legs has the capacity to independently choose whether to execute a swing or a stance motion by following a set of simple rules. These rules are enumerated as six "coordinating influences" by Cruse and are implemented in WalkNet as the selector net subsystem. These coordinating influences are summarized in Fig. 2, which is reprinted from[54].

These influences work primarily by altering the "posterior extreme position," or the leg "point-of-no-return" position, beyond which a leg will transition from a stance phase motion into a swing phase motion. The end of swing phase is detected by sensing a ground impact. The selector net relies on these coordinating influences to evolve a stable walking gait.

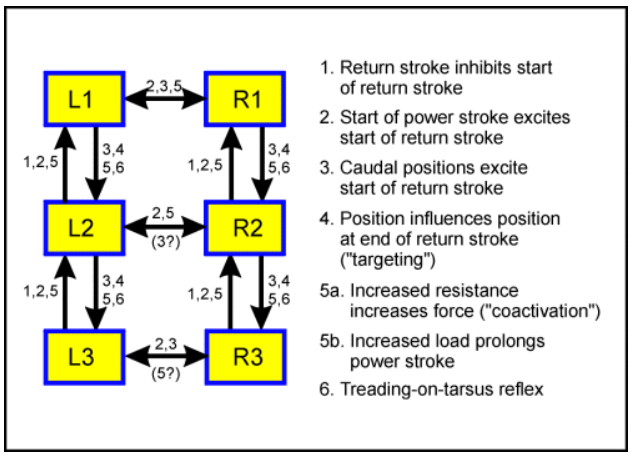

Fig. 2. Coordinating influences of WalkNet's selector net.

Another interesting aspect of the WalkNet structure is that both the swing and stance trajectory generators generate joint velocity commands rather than joint position commands in contrast to traditional robot controllers which in general are structured in terms of desired position trajectories. Note that biology's use of velocity based control is quite sensible, since the main objective of locomotion is to keep the body moving forward at a desired rate of speed. Velocity control is also generally simpler and more stable than position control, since velocity control in the presence of inertial dynamics generally involves only a single integration from (actuator) force.

II.B.2 Problems with WalkNet for Robot Locomotion

As previously indicated, some difficulties exist with the realization of WalkNet in a hexapedal robot. The most significant is that no mechanism is described in WalkNet that maintains stability in the lateral direction, which is particularly significant in the presence of dynamic effects. Specifically, since WalkNet is by its nature a joint-level control approach (i.e., operates in the joint space rather than in the task space), the

unstable behavior generated in the joint space by the use of positive feedback during stance phase may propel the body forward, but since the joint angles generally show up in all task space directions, the (intentionally) unstable behavior also propels the body laterally, which results in falling to the side. One could apply this notion of positive feedback in the task space and separate the forward and lateral dynamics (i.e., positive feedback in the forward direction, negative feedback in the lateral direction), but such an approach requires task space control, which in turn sacrifices much of the biologically inspired paradigm, and with it many of the most significant assets, such as emergent behavior and self-selected gait patterns. Additionally, the positive feedback concept relies on each stance leg remaining in contact with ground during the entire stance phase, which cannot be guaranteed in a real world trial. For example, a slippery substrate or a loose substrate that falls away as force is applied may cause the leg to lose contact with the ground. Once the stabilizing influence of the ground is no longer present, the positive feedback generates exponentially increasing velocity and hence an undesirable stance response.

II.B.3 Proposed Walking Algorithm

A block diagram of the proposed approach is shown in Fig. 3. The portion of the block diagram most integral to the proposed approach is enclosed by the dashed box and labeled “Trajectory Generation.” The structure of this subsystem is based largely on that of the Cruse system in that there are independent blocks that generate the swing and stance trajectories and a third block that chooses which of the two trajectories to use

based on the state of an individual leg and those of the neighboring legs. Unlike Cruse's system, however, the swing and stance phases are calculated through mathematical formulations, as subsequently described, rather than by neural networks.

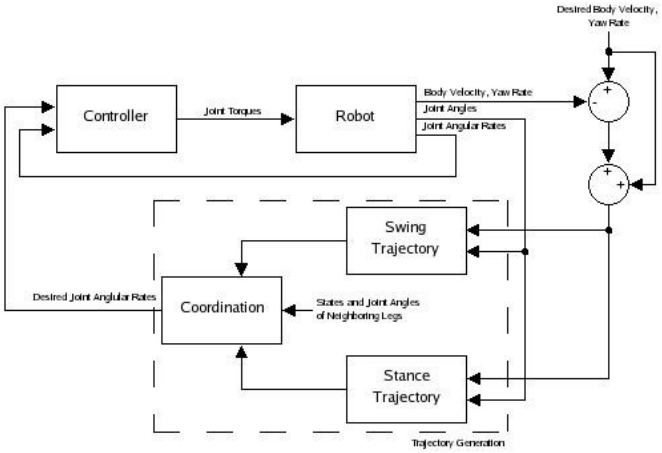

Fig. 3. Block diagram of proposed gait control structure.

II.B.3.a Stance Phase

The stance trajectory is conceptually defined as being able to simultaneously meet the following criteria. First, the trajectory must cause the body to follow some desired linear and angular velocities (i.e., the desired inputs into the system are the desired linear and angular (or yaw) velocities of the body center of mass). This selection of inputs will allow the robot to be commanded in the same manner in which one is accustomed to driving an automobile. This criterion then consists of describing a straight line path of the foot parallel to the body axis with velocity equal to the desired body linear velocity. This path is then modulated using the desired angular velocity and the instantaneous

distance from the body center of mass to the end point of each leg. Note that it is also possible to supply a desired lateral linear velocity to allow the vehicle to side-step or walk crabwise, although this is not included in the present implementation.

Secondly, the stance trajectory should maintain the robot body at some constant (vertical) distance from the ground, duplicating the function of the "height net" block in the WalkNet structure. Fundamentally, this amounts to a virtual suspension system with function and performance similar to that of a wheeled vehicle. However, the stiffness of the virtual spring in this system will vary depending on how many of the legs are in contact with the ground at a given time. In order to use this criterion, a desired height is required to simulate the free length of the virtual spring. Currently, this height is selected as some suitable constant, but could vary continuously if necessary or desired.

Finally, a third stance phase criterion keeps the robot body from falling laterally to one side by serving as a feedback loop that performs error correction in the lateral direction, a feature which does not appear to be present in WalkNet. The addition of this criterion has the added effect of maintaining the robot's heading more accurately than solely through the yaw rate feedback loop.

II.B.3.b Swing Phase

The swing trajectory block takes the current position of an individual leg and calculates a set of joint angular velocities that causes the foot of that leg to follow a parabolic trajectory in the sagittal plane. Two important features govern the character of this trajectory. The first feature is that the expected foot-ground impact point must be selected in order to maximize the "sure-footedness" of the robot. This is a declaration of

the inclusion of the fourth Cruse coordination influence or the so-called "targeting influence." The idea behind this influence is that if the next rostral (when walking forward) leg has a satisfactory foothold, then placing a foot near its rostral foot will also result in a satisfactory foothold and the avoidance of a possible gap. Of course, some allowance needs to be made in order to keep the two legs from contacting. This is done by locating the target end-point of the swing movement some small distance behind the current position of the next rostral foot.

For the most rostral (i.e., most forward) legs, no such information exists, so the target points are chosen arbitrarily. This raises a concern pertaining to the behavior of the leg if intersection with the ground does not occur as expected. Should this occur, following the described parabolic trajectory is problematic because the leg will eventually reach a singular configuration. While this scenario is not possible in the current simulation because of the simple environment chosen, Durr [56] has conducted research extending that of Cruse and has identified a stereotypical searching trajectory that the stick insect executes in order to find a foothold. It is expected that continuing the biological analogy by using this method will result in successes similar to those described by Durr. Note finally that use of velocity rather than position control will in general result in less precision in foot placement than position control. However, reasonable proximity can be attained by allowing the trajectory generator to use feedback information from the current leg position when determining desired joint velocities.

The second feature that governs the nature of the swing trajectory is that the vertical velocity when the foot is expected to impact ground should be kept small in order to minimize impact forces and the ensuing rapid body height fluctuations (i.e.,

vibrations), which dictates that the parabolic trajectory be “shallow.” Note that a shallow trajectory will in general increase the likelihood of a possible collision between a leg and some environmental obstruction. However, this possibility is not of great concern since the current simulation is focused solely on level walking in an ideal environment and also since Cruse describes methods observed in the stick insect to recover from such collisions.

From the above criteria, this parabolic trajectory is constructed so that it passes through two points: the leg's current position and the desired target. Also, it is desired to pass through some maximum height and in the absence of additional constraints, we force this maximum to occur at the transverse plane passing through the leg's basal joint. Finally, since velocities are to be the result, the parabolas are mathematically formulated as in (1) and (2). Here, x is the body axial direction with positive values being rostrally directed, z is the vertical axis with positive values being upward, y is the lateral axis with positive values being anatomically sinister (left), and k_1 and k_2 are constants.

$$\begin{aligned} \dot{x} &= k_1 \cdot v_{body,des} \\ \dot{y} &= k_2 \cdot \left(y_{target} - y \right) \end{aligned} \tag{1}$$

$$\begin{aligned} \dot{z} &= 2 \cdot A \cdot x \cdot \dot{x} \\ A &= \frac{z - z_{max}}{x^2} \forall \left\{ x < 0 \cup x \geq x_{target} \right\} \\ A &= \frac{z_{target} - z}{x_{target}^2 - x^2} \forall \left\{ 0 \leq x < x_{target} \right\} \end{aligned} \tag{2}$$

II.B.3.c Leg Coordination

The coordination block shown in Fig. 3 is implemented using the set of coordination influences from the work of Cruse et al. Currently, influences 5 and 6 are not in the present implementation, as they relate to non-ideal environments, which have not been considered in the work herein, although will be integrated in future work. Additionally, the authors have found that allowing influence 1 to act on all neighboring legs (non-diagonal) rather than caudal-only causes the robot to easily and stably change speeds, since such an allowance appears to evolve gaits more quickly than without. Finally, the gains used in the modified version presented herein use a different set of gains than those utilized in Cruse's WalkNet, and in particular were empirically tuned in order to achieve a satisfactory performance for the robot dynamics that include inertial, gravitational, and ground contact effects.

II.B.4 Simulation

The previously described walking algorithm has been implemented in a software simulation that includes robot dynamics and simulates ground contact using the open source Open Dynamics Engine library. Ground contact is modeled using the collision detection features built into the library and essentially amounts to a spring-damper connection between colliding bodies. For the purpose of collision detection, the ground is modeled as an infinite flat plane and the leg segments as spherically capped cylinders. The torque control at each joint is simulated as a local proportional velocity control loop, wherein the generated torque is proportional to the error in joint velocity. Actuator dynamics were not simulated at this point, since they were assumed to be fast relative to

the frequencies of locomotion, although joint torques were saturated at representative levels. Body and leg segments are considered to be point masses with values as documented in Table 2 and defined as shown in Fig. 5, reprinted from [54].

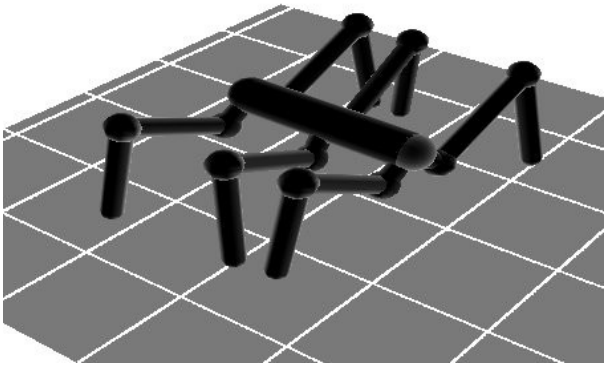

Fig. 4. Sample screenshot of simulation as run.

Table 2
Summary of Body Segment Values

Segment	Mass (kg)	Length (cm)
Coxa	0.36	5
Femur	0.28	15
Tibia	0.28	15
Thorax	2.3	20

Information used by the walking algorithm is limited to that which would be available via the sensors on the robot, namely the individual leg joint angular positions, the body linear and angular velocities, and the axial load on the distal leg segments.

Using the described walking method, the robot is able to conduct forward walking with and without simultaneous turning and is capable of starting from and coming to a stop. Also, the simulation permits the user to continuously change the input linear and angular velocities. Note that backwards walking and turning in place are not currently implemented, though the method does not preclude the possibility of these features, both of which are topics of future work.

The simulation is indicative of an in-progress physical robot which the authors are currently designing. The legs of the simulated system and the eventual physical system are modeled after the stick insect's legs in terms of joint orientation and relative leg segment lengths. A sketch of the insect's limb is shown below, and segment lengths used are listed along with their projected mass in Table 2.

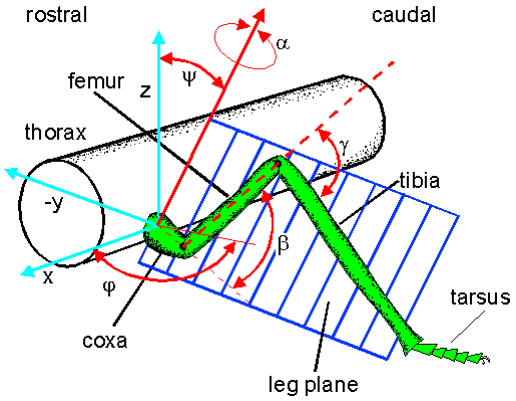

Fig. 5. Definition of leg geometry using biological inspiration.

In the current simulation, ψ is set to 45º and φ to 90º. On-going work is determining optimal values for these two angles that will evenly distribute joint power contributions and that will also promote gait stability. The other three angles shown in the diagram are those which are actuated and controlled to perform the described leg motions.

II.B.5 Results

The emergent coordination between the legs can be seen in Fig. 6, which depicts the position along the body axis of all feet relative to their individual hip locations. The result is the stereotypical tripod gait with a phase separation of approximately .4 seconds.

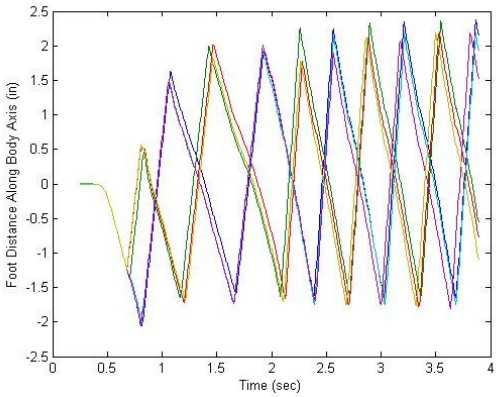

Fig. 6. Emergence of tripod gait using coordination influences.

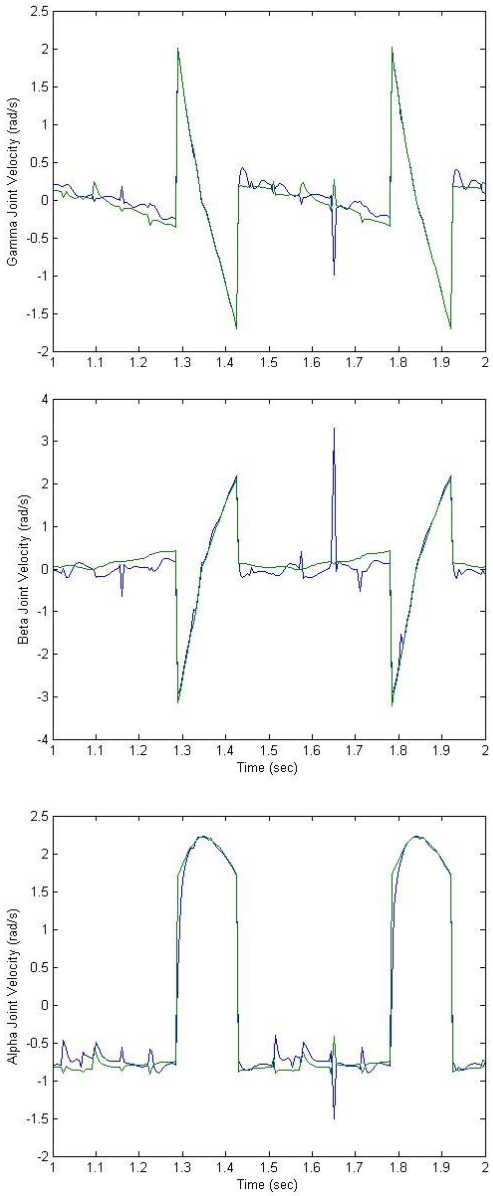

Fig. 7. Joint velocity tracking for all joints in one leg.

The joint level velocity commands, and resultant velocity tracking is shown in Fig. 7 for the three joints of one leg. From these plots, one can observe that the velocity tracks easily during swing motions, while the higher impedance of the ground interaction during stance motions creates a sufficient disturbance to generate noticeable tracking error.

A time history of an individual leg's trajectory in the sagittal plane is shown in Fig. 8, which shows the development of a single leg's trajectory over time as the coordinating influences act to shorten or lengthen the duration of the stance phase of the leg as well as showing the character of the parabolic swing phase trajectory.

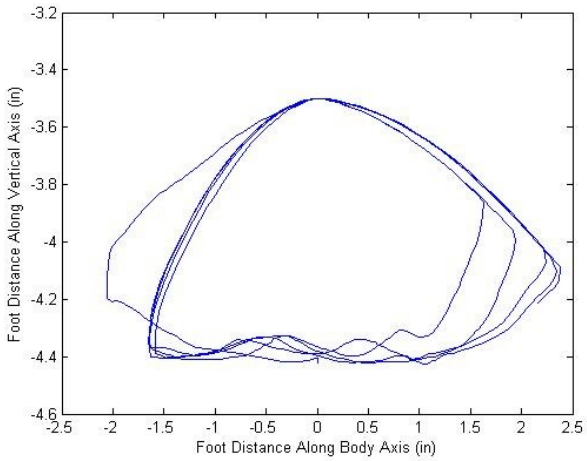

Fig. 8. Time history of a single foot trajectory as viewed in the sagittal plane.

When a non-zero desired yaw rate is introduced to the system, as in Fig. 9, the resulting gait pattern becomes somewhat chaotic. Here, the yaw command is made non-zero starting at approximately 5.7 seconds. Thereafter, the well-ordered gait pattern

dissociates into a seemingly disordered, but still stable and functional gait pattern. Although this gait cannot be classified as either a standard tripod or tetrapod gait, it is able to propel the robot along while reasonably following the desired linear and angular velocities.

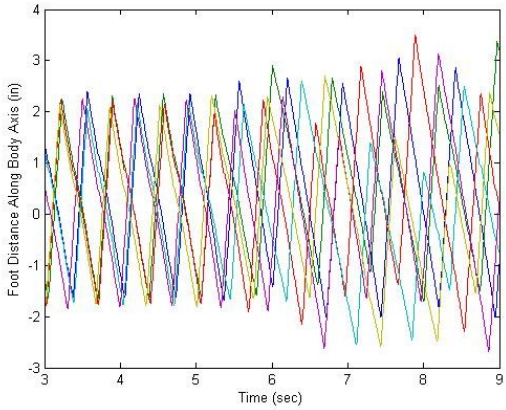

Fig. 9. Gait time history with non-zero yaw command introduced at ~5.7s.

II.B.6 Conclusions

The foundation laid by Cruse with respect to emergent stable walking gaits allows rapid development of a complete walking algorithm. Using simple trajectory generation and joint control combined with the coordinating influences as described, a dynamic simulation has been implemented which can guide a hexapedal robot through arbitrary curvilinear paths.

On-going work includes the implementation of purely lateral motion, turning-in-place, and walking backwards. Additionally future work includes testing the approach with non-ideal environments, especially those which include uneven (rocky) terrain and slippery substrates.

II.C Hardware and Control Structure

The path of legged robot development is well trod. A vast array of walking machines have been the subject of extensive research over the last several years and many, if not all, of these efforts have involved biologically inspired or biomimetic design. It is only natural that this should be so as the world abounds with highly capable legged creatures each of whom are successful exemplars of this form of locomotion.

The authors are currently developing a monopropellant-powered, pneumatically-actuated hexapod robot. While legged locomotion has self-evident benefits in traversing non-regular terrain, the specific benefits of hexapedal walking include inherent static stability in most tripod or tetrapod gaits, and that the failure of up to two legs should not cause total failure of the robot. In this case the nominal hexapod becomes a quadruped, whose gaits have also been well studied. This redundancy extends operation of a hexapod relative to walkers with fewer legs when operating in potentially hazardous or unstable environments.

The robot described herein is designed and controlled using an array of biological analogies all of which aspire to provide effective locomotion and natural interaction with the robot's environment. First, a liquid monopropellant-as-a-gas-generator approach is intended to provide the robot with greater power density relative to battery-powered,

electric motor actuated approaches [37,57,58]. The use of monopropellants as a power source retains the benefits of pneumatic actuation, such as compliant interaction with environments while dramatically improving power and/or energy density over phase change or compressed gas storage methods. These low impedance dynamics have been shown by others [47,59,60] to be beneficial, if not critical, for good performance in walking robots and to more closely approximate the dynamics of biological walkers. In contrast, many robots use electromagnetic actuators due to their abundance and ease of use. However, these actuators generally require high transmission ratio gearheads and result in unnaturally high output impedance, characterized by non-backdriveable joint dynamics, which are at odds with the dynamics of biological locomotion.

Secondly, the design of the robot's structure is inspired by the stick insect *Carausius morosus*. This is a well-studied animal and has provided the basis for a number of other walking machines . The authors' intention was not to design a robot that was a strict scaling of an existing animal's morphology. Instead, the mechanical design loosely mirrors that of the animal and is guided by the results of a dynamic simulation [40] to achieve optimal performance with regard to a torque distribution metric.

Thirdly, the control of each individual leg utilizes an impedance approach. Controlling impedance rather than directly controlling position and velocity of the legs further integrates the notion of acting in a low impedance fashion into robot operation. In this scheme, the precise position and velocity of the robot's limbs are byproducts of the interaction of the robot and its environment and are principally dictated by the environment rather than the controller. The nominal equilibrium trajectories incorporated

into the impedance controller are designed as minimum jerk trajectories. This control construct in which impedance is directly controlled along a trajectory that minimizes jerk has been shown [61,62] to be employed in human arm movements.

The final biological paradigm in use by the robot's control architecture lies in the coordination of the robot's six legs. As reported earlier by the authors [40], the decentralized coordinating mechanisms developed by Cruse [55] are effective in causing a stable gait in a simulation of the designed robot. In contrast to centralized approaches, these coordinating influences incorporate the effects of the environment on the robot into the generation of the robot's gait.

This paper describes the progress to date in the development of the robot, which includes the design of the robot, the design of leg, and coordination-level controllers, and the experimental implementation of the leg-level controllers on a pair of legs. The robot on two legs demonstrates the ability to walk in a robust manner at a speed of approximately 15 cm/sec.

II.C.1 Robot Design

Rather than use batteries as the source of locomotive power, the robot is designed to use the liquid monopropellant hydrogen peroxide (H_2O_2) as a gas generator to supply pneumatic-type actuators. This approach, which is described in [35], has been shown to provide system-level power densities similar to biological systems. Fig. 10 shows a schematic of the actuation system. The liquid propellant is pressurized by a CO_2 cartridge, and is pushed through a catalyst pack by the opening of one or more servovalves downstream. As the liquid propellant passes over the catalyst contained in

the catalyst pack, the liquid exothermically decomposes and becomes gas, which serves as the working fluid for the gas servovalves and pneumatic actuators. Note that the servovalves have been developed by the authors, and are described in [35,63].

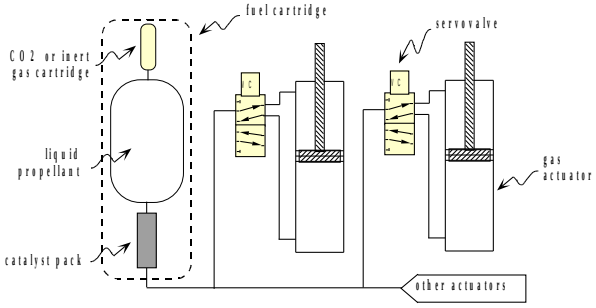

Fig. 10. Hexapod power and actuation configuration.

The robot design is shown in Fig. 11. The design is patterned loosely after the morphology of the stick insect *Carausius morosus*. As subsequently described, and as reported in [40], the locomotive control is similarly patterned after the same insect. Unlike the stick insect, the robot is designed to be the size of a medium-sized dog, such that it can more easily negotiate human-scale terrain. Specifically, the hexapod occupies a volume 64.7 cm in axial length, 55.9 cm wide, and 22.5 cm high in a nominal stance.

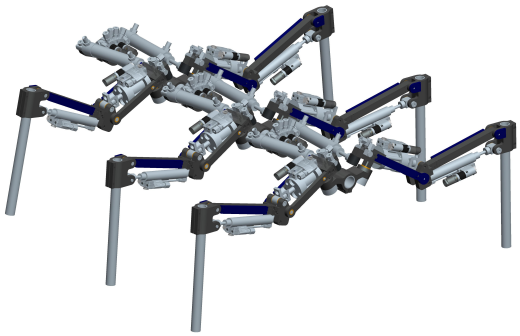

Fig. 11. Solid model of hexapod robot.

Attached to the central "spine" of the hexapod are three modular leg pairs (rear-, mid-, and fore-legs). Each leg pair consists of a left and right leg, their associated pneumatic actuators, and the common central brackets from which these legs and actuators originate. Additional brackets are located on the spine and provide further structure and alignment for the routing of fluid lines, mounting of an on-board fuel tank and additional valves, actuators and electrical hardware. In the animal, each of the leg pairs departs from the central body axis in the horizontal plane at unique angles (φ), while all angles of departure in the robot are 90° as noted in Table 4. The legs of the hexapod each consist of three segments and three joints as illustrated in Fig. 12, (reproduced from [53]). Each of these joints is actuated by a pneumatic cylinder (α: Bimba 041.75-DXPV, β: Bimba FO-041.25-2RV, γ: Bimba 021.75-DXPV) mounted to either the preceding segment or the central spine. The lengths of these segments are designed primarily to accommodate the dimensions of off the shelf pneumatic actuators and not to exactly scale the insect's dimensions. However, the robot approximates a 15:1 scale insect, excluding the most proximal leg segment, as noted in Table 3. Animal typical values in Table 3 are taken from [64].

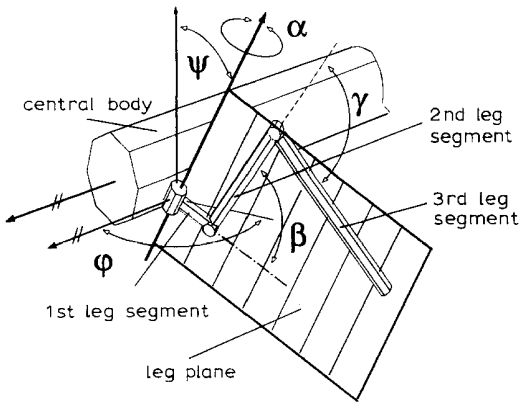

Fig. 12. Model of single leg.

Table 3
Length Comparison to *Carausius morosus* Animal

Quantity	Animal Value (Typical)	Robot Value	Scale
Segment 1	1.5(mid/rear) to 1.6 (front, mid) mm	97.7 mm	65.1 to 69.8
Segment 2	11.4 (mid) to 14.7 (front) mm	159.2 mm	10.8 to 14.0
Segment 3	10.7 (mid) to 13.7 (front) mm	207.9 mm	15.2 to 19.4
Leg Separation	17.5 mm (front/mid) to 10.9 mm (mid/rear)	215.9 mm	12.34 to 19.8

At each leg joint, integrated potentiometers (ALPS RDC503013A) measure joint angle and are protected and secured to the robot by plastic covers. Load cells (Measurement Specialties ELFM-T2E-100L) are placed between the pneumatic actuators and the structure of the robot to provide force signals for the force controllers around

each joint. Wiring is either routed through channels in the leg segments or through the spinal tube. The position and force signals are transmitted to the control computer via a 3m umbilical.

Liquid hydrogen peroxide from the fuel tank is fed downstream via flexible tubing to catalyst packs filled with iridium coated alumina granules. These catalyst packs then feed hot gas (steam and oxygen) directly into manifolds and their associated servovalves. These servovalves are either mounted directly or adjacent to their corresponding gas actuators.

The servovalves are powered and controlled by custom on-board microcontroller (Microchip PIC16F690) based electronics designed by the authors. The circuits sample valve position at 1 kHz and are capable of delivering .75 amps at 15 volts to the motors (Faulhaber 1319T006SR) that drive the valves using on-board servoamplifiers (Apex PA75CD). Position of the valve is sensed via the motor's integrated encoder (IE2-400), decoded into up/down counter signals on the board which are then sensed by the microcontroller's counter modules. The controller boards are 2.5 by 3.75 cm. Desired position commands are sent from the computer are sent as current commands to the on-board servocontrollers. Fig. 13 shows a stereotypical actuator assembly.

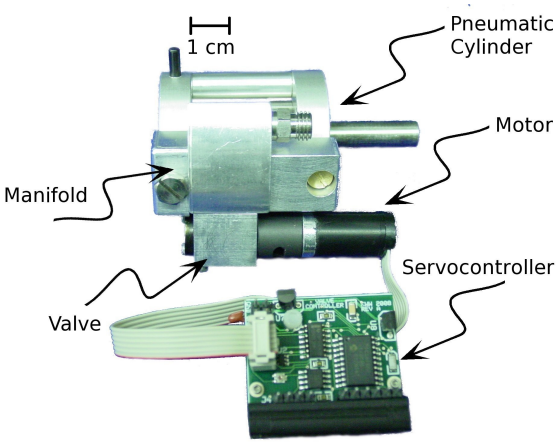

Fig. 13. Valve/actuator assembly with custom servocontroller electronics.

As in the stick insect, each leg of the hexapod contains three degrees of freedom, as shown in Fig. 12. The angular ranges of each of the degrees of freedom is restricted by the choice of pneumatic actuators but very closely mimic the angular ranges observed in the stick insect animal [64,65], as noted in Table 4. Rather than adopt the kinematic configuration directly from the biological insect, an exhaustive search was conducted to select the proximal joint angle ψ and the nominal body height to best distribute the torque load throughout the leg actuators. Specifically, the proximal joint angle and nominal body height were independently varied, and a full dynamic gait simulation (and coordination level control) was performed for each combination until the hexapod either converged to or departed from a limit cycle. For each combination, the torque distribution between joints was quantified by computing the two-norm of the vector consisting of the differences between each joint torque. In the case that the norm of the joint torque differences is zero, the torques are regarded as perfectly evenly distributed between leg joints. The results of all simulations are plotted in Fig. 14. As indicated in

the figure, the minimum norm (i.e., most even torque distribution) occurs at a body-carrying height between approximately 17.5 and 22.5 cm (7 and 9 inches), and at proximal joint angles between 15 and 45 degrees. As the nominal body height can be easily varied in the control system software but the proximal joint angle is fixed by the design of the hardware brackets, the robot was designed with a proximal joint angle of 30 degrees to be centered in the optimal range and therefore robust to inaccuracies in the simulation. The robot is intended to nominally carry its body at a height of approximately 18 cm (7 in) above the ground which places the operating point near the center of the lowest strata in Fig. 14. Note that, interestingly, the resulting proximal joint angle of 30 degrees is comparable to the angle found in the biological insect as noted in Table 4.

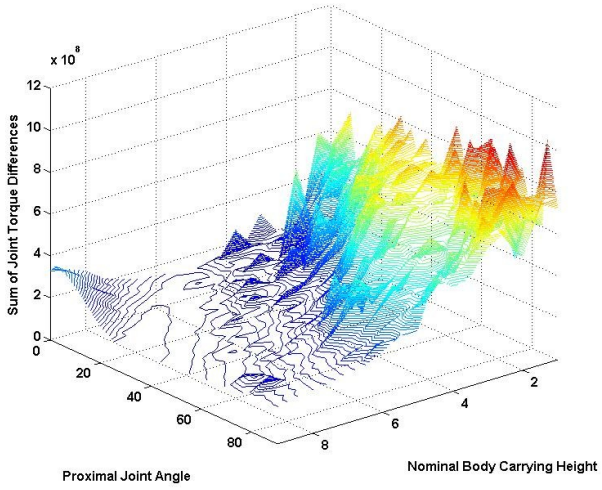

Fig. 14. Exhaustive search of body-carrying height (x) and proximal joint angle (y) to minimize the sum of joint torque differences (z) indicating a minimum around 30° and 18 cm.

Table 4
Angular Comparison to *Carausius morosus* Animal

Dimension	Animal Value (Typical)	Robot Value
α Range	-50° to 50° (mid)	-44.34° to 59.55°
β Range	25° to 75° (rear)	-17.18° to 119.83°
γ Range	25° to 110° (front and rear)	29.79° to 133.5°
φ	75° (front) 85° (mid) 135° (rear)	90°
ψ	29° to 50°	30°

Based on simulations with a projected mass of 10 kg, the average power consumed by all 18 actuated joints is 34W at a walking speed of 0.15 m/s over level ground. A 70% solution of hydrogen peroxide will produce 273 kJ/L of usable pneumatic energy. If we assume 50% efficiency in the pneumatic system, then the pneumatic power requirement is 70 W, or 250 kJ/hr. As such, an hour of operation will require somewhat under a liter of peroxide at the given concentration. Note that while Fig. 11 does not depict the robot with a fuel tank, the design can comfortably accommodate a tank two liters in capacity which is included along with a battery that provides power to the electrical components of the robot over a similar time in the weight estimate. This quantity of hydrogen peroxide will then power the robot for two hours, over which time it will traverse a distance of 1.1 km. By way of comparison, the well-known RHex robot runs for up to 15 minutes and covers a distance of 477m on a full battery charge [47] and the also well-known iSprawl robot runs for up to 5 minutes and covers a distance of 690m on a full battery charge [25]. It should be noted, however, that both RHex and iSprawl are considerably smaller than the robot described here.

II.C.2 Control Architecture

The locomotive control architecture for the hexapod robot consists of low-level joint torque controllers, mid-level leg impedance controllers, and high-level leg coordination controllers. The latter are based largely on the work of Cruse [55]. In order to validate the hardware and actuator design, the low-level joint torque controllers, and the mid-level leg impedance controllers, two (front) legs were fully implemented, as shown in Fig. 15. As shown in the figure, the four caudal legs were omitted and replaced by a wheeled cart mounted to the rear of the robot. It should be noted that, while the robot is designed to be powered by the hydrogen peroxide monopropellant, it is currently supplied with compressed air in the form of Nitrogen gas. This is done to permit testing of the robot without the added complexity of hydrogen peroxide and to validate the control systems, which are independent of the medium used to transmit power.

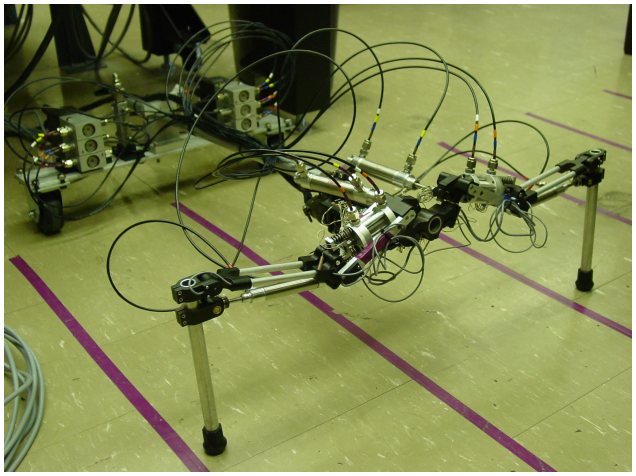

Fig. 15. Experimental setup consisting of two legs and two wheels for stability purposes.

Since the coordination-level control (described in [40]) requires multiple sets of legs, a rudimentary coordination mechanism was instead implemented in which at most one leg was permitted to be in the swing phase at a given time.

II.C.2.a Mid-Level Leg Impedance Control

The legs of a robot repeatedly interact with the ground during locomotion. High output impedance (i.e., position controlled) approaches locomote in a stiff, and not particularly biomimetic, fashion. Most biological systems incorporate impedance-type controllers, and have been shown to "track" motion through a series of via points, where the motion between via points follows a minimum jerk trajectory [61,62,66,67]. Further, it has been shown that the forces moving the limb toward these points are achieved by regulating the impedances of the muscles of the limb used in its motion toward the via-points rather than attempting to regulate the position itself. These findings suggest that so-called impedance control strategies are being employed in vivo by at least some animals.

Impedance control allows for position control-like performance when the manipulator acts in the absence of a stiff environment and for force control-like performance when such an environment is present as well as for a smooth transition between these two. Given the ability of impedance controllers to stably interact with hard constraints, and given the fact that pneumatic actuators are well suited to impedance type control, impedance controllers were implemented to guide the motion of each leg.

The impedance trajectory generator designed and used consists of a finite state machine (FSM) that specifies impedance gains and equilibrium positions for each state, a mode transition logic that specifies how the FSM moves between states, and a minimum jerk smoothing function that acts on the equilibrium position when a finite state transition takes place. The smoothing function is a specially designed filter that causes the equilibrium position to move in a biomimetic manner rather than as an instantaneous step motion.

The designed impedance trajectory was implemented in hardware and is shown in Fig. 16. Here, the equilibrium position of the impedance controller (which guides the leg forces acting on the environment) is shown as a dashed line, while the measured foot trajectory is shown as a solid line. Vertical dotted lines are used to denote mode transitions within the finite state machine.

Beginning from the leftmost mode transition, the controller enters the swing phase. During this phase, a minimum jerk transition brings the impedance equilibrium position in the z-direction (normal to the ground) above ground level and begins to cause axial movement of the foot. Note that, although there is a discontinuity in the x-direction (along primary robot body axis) equilibrium, this is an intended behavior that starts the minimum jerk motion at the foot's actual position when the mode transition occurs. If the equilibrium position trajectory were continuous, the loss of ground contact and associated resistance would result in a rapid and undesired motion in the x-direction. That is, the discontinuity in the x-direction equilibrium position serves to ensure a smooth and continuous motion of the leg.

At the moment when the foot passes the zero mark in the x-direction, the mode transition logic begins the equilibrium position motion downwards to re-establish ground contact over a span of 1 second. This occurs at approximately 1 second in Fig. 16.

When the downward minimum jerk transition of the equilibrium position has completed, the controller enters the stance phase. In Fig. 16, this occurs at approximately 2 seconds. Again, the x-direction equilibrium position discontinuity is intended in order to prevent a force being applied to the ground that would be counter to the desired direction of motion. In the stance phase, the stiffnesses of the impedance controller are modestly increased in anticipation of the increased resistance observed because of ground contact. A minimum jerk transition of longer duration is executed in the x-direction while the equilibrium position in the z-direction is maintained at a constant. This phase continues until the foot passes through the plane where the x-direction displacement is 12.7 cm caudal of the leg's base joint at which point the controller transitions back to the swing phase.

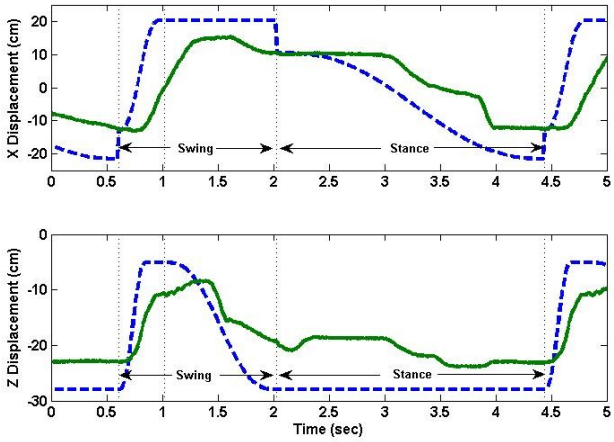

Fig. 16. Single gait cycle of implemented impedance trajectory

II.C.3 Improving High Level Control

The most prevalent form of affecting a gait in hexapedal robots appears to be that of using central pattern generators. In this construct, each of the legs is made to transition between stance and swing phases at a time prescribed by a clock [47]. This transition is made independent of any information regarding the states of the legs or their interaction with the substrate. While the success of the CPG method is not in question, the benefit of using a decentralized algorithm for developing a gait cycle is thought to be that the interaction with the environment is not only considered when determining swing/stance transitions, it is a critical portion of this decision. To this end, the authors have chosen to implement a decentralized pattern generator based on the efforts of Cruse [55] that culminated in the development of a neural network that approximated the walking of the *Carausius morosus* animal.

Cruse's neural network consists of three main subsystems, namely the swing net (which generates a leg's trajectory during swing phase), the stance net (which does the same for the stance phase), and the selector net (which decides for each leg which of the two trajectories to use).

In the neural network, the gait is evolved due to the fact that each leg's selector net has the capacity to independently choose whether to execute a swing or a stance motion by following a set of simple rules. These rules are enumerated as six "coordinating influences" by Cruse.

These influences work primarily by altering the "posterior extreme position," beyond which a leg will transition from a stance phase motion into a swing phase motion. The end of swing phase is detected by sensing a ground impact. A stable walking gait is evolved through the effects of the individual selector nets. The influences are summarized in Fig. 17.

These coordination influences require a set of weights, which in the work conducted by Cruse, were trained with a neural network to mimic the motion of the *Carausius morosus* animal. Since the dynamics of the pneumatic robot differ in important ways from those of the stick insect, selecting the weights in such a way is not appropriate. Instead, an exhaustive search optimization was used, somewhat similar to that used to select the proximal joint angle and nominal body height. That is, the influence weights were determined by exhaustively searching combinations of weights, while repeatedly running the dynamic simulation of walking for each combination, and selecting the set that resulted in the least tracking error of desired body velocity. The search space was four dimensional, with values being sought for the first three

coordinating influences in Fig. 17, as well as the base, unmodified posterior extreme position. The possible values for each parameter were suggested by Roggendorf [68], after being scaled by the robot's body length and using estimates based on iterative tuning of each parameter.

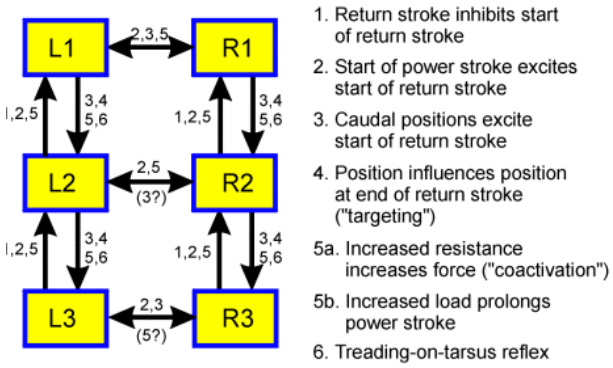

Fig. 17. The coordinating influences of Cruse

While exhaustive searching is not an efficient optimization method, the effect of the influence weights on the comprehensive performance is difficult to model analytically (i.e., solution of the resulting motion requires numerical simulation) and there is no guarantee that the objective function is smooth.

The specific objective function that was minimized is the average error from a reference trajectory. That is, the simulation is provided with a constant desired body velocity and turning rate. The influence weighting parameters are varied and the simulation is allowed to run for sufficient time such that the robot should have reached a

gait limit cycle (if not, the given set of weights would not be of interest). The trajectory of the body center of mass at the conclusion of the run time is compared to the ideal trajectory consisting of the integrated velocity and turning rate commands.

The specific velocity commands given are 14.9 cm/s (the fastest walking achieved in the two-legged prototype to date) and 30.5 cm/s each at 0, ±2.5, and ±5 deg/s for a total of 10 unique body trajectory parameter searches. The simulation is run for a simulated time of 10 seconds at each iteration. Although the simulation time is chosen to limit required processing time for the optimization, it is believed that this distance is an adequate space for assessing the motion.

The procedure calculated relative deviations from ideal trajectories for 238,140 parameter sets. Over the ten trials described, the minimum average deviation was 4.9% and was achieved by a single parameter set. In the case that this minimum deviation parameter set is unsatisfactory when used in hardware experiments, 24 parameter sets that deviated ≤ 7% on average and 174 sets that deviated ≤ 10% on average are available for testing.

It should be noted that the results of this search may not be valid over a global range of velocity or turning rate commands and may be unique to the particular commands given. This qualifier will be tested in hardware after construction of additional leg pairs has been completed, but the optimal parameters found should be adequate to attempt hexapedal walking in hardware in the defined speed and turning rate ranges.

II.C.4 Conclusion

The authors have designed a monopropellant powered pneumatically actuated hexapedal robot. The proximal joint angle of each leg and the nominal body height (which are two of the significant parameters of the geometric configuration of the robot) were found based on an exhaustive search optimization that attempted to achieve a completely even distribution of joint torques during walking. Interestingly, the optimal proximal joint angle of 30 degrees is comparable to that found in the walking stick insect. The authors additionally implemented two of the six legs, and showed that the use of impedance-based controllers with minimum jerk set-point trajectories provided robust walking at a speed of 15 cm/sec. Finally, another exhaustive search was performed to select a set of coordination influence weights (to coordinate leg movement for the six-legged robot) that minimized the body velocity tracking error. Future work includes the completion of the remaining four legs, and experimental implementation of the coordination level controller with the optimized set of influence weights.

CHAPTER III

FINAL CONTROL DESIGN

III.A Motivation of Design Changes

During the conceptual phase of this robot (in parallel with the simulation work of Section II.B), experimental control of a single rotary pneumatically actuated joint was carried out. In these experiments, a prototype femur-tibia joint was mounted to travel in a horizontal plane (i.e., parallel to the ground). These experiments indicated that valve commands derived solely from joint rotational position error (i.e., without velocity, acceleration, pressure, force, or other information) were sufficient to achieve stable controlled motion of the prototype joint with presumably adequate bandwidth and disturbance rejection to be usable in the finished walking robot.

Fig. 18. Initial, position controlled two-legged prototype

The first prototype (Fig. 18) used this method to attempt to walk. While this prototype failed for a variety of reasons (e.g. poor frictional interface with substrate, excessively long pneumatic lines between valves and actuators, gravitational effects not present in the initial experiments, etc.), the elimination of many of these problematic characteristics failed to sufficiently correct the qualitatively poor legged locomotion observed.

It was surmised at this point in development that position based control was fundamentally defective for two principal reasons.

First, position control results by its very nature in a stiff (i.e., high impedance) output system. It is well known within the field that position control is unable to interact with the naturally high input impedance of many environments [67]. In general, for good impedance matching it is desirable to have low output impedance coupled with high input impedance. It was theorized based on extensive prior research by other investigators (e.g. [60,67,69]) that having low stiffness control of the robot legs would enable much more natural motion and interaction with the ground.

Second, the models that characterize the dynamics from valve command to actuator position are nonlinear but are at least third order. In contrast, the dynamics from valve command to actuator force are at most first order and the dynamics from actuator force to actuator force are approximately second order. By measuring and using force information from each pneumatic actuator, the control problem could be recast from a difficult problem into two easily tractable ones. That is, control of first or second order dynamics is relatively easy, while control of third order ones is possible but usually difficult.

Experiments were carried out (as documented in section II.C) in which force information from each actuator was available and a low impedance controller was implemented. While these experiments were highly successful, the reliability of the force sensors was quite poor. With an eye to enhancing the reliability of the system while retaining the dramatically improved system level performance offered by impedance control, valve commands derived solely from joint position level feedback were revisited.

Additionally, the high number of actuated degrees of freedom in a hexapedal robot implies a large number of overall components and therefore a very low reliability or system availability (i.e., the reliability of the system is a product of the reliability of all its component parts). To address this, the basic morphology of the robot was reconsidered. Rather than continue to develop a hexapedal robot, a pair of legs was omitted so that the device becomes a quadruped. In addition to rendering the Cruse algorithm for leg coordination deprecated, this significant design change requires a fundamentally different approach because four legged gaits are highly dissimilar to six legged ones. Instead of the approaches outlined in Chapter II, a new method for both individual leg motion planning and inter-leg timing and motion is needed and developed.

III.B Enhancing PVA Control of Pneumatic Systems

A typical pneumatic servoactuator consists primarily of a proportionally controllable four-way spool valve and a pneumatic cylinder, as depicted in Fig. 19. The control objective for such a system is to command the valve spool position to achieve a desired trajectory tracking of the pneumatic cylinder piston (and load) motion. Though various control approaches have been developed for the motion control of pneumatic servoactuators (for example, see [70-82]), the industry standard approach is the position-

velocity-acceleration (PVA) control structure, in which the servovalve command is a weighted sum of the position error and its first and second derivatives, respectively (i.e., it is the pneumatic equivalent of proportional-derivative control for an electric servomotor). PVA control is generally the preferred approach because it enables motion control without the need for pressure or force feedback, which if required, adds cost and complexity to the pneumatic servoactuator. Pneumatic servosystems often compete against electric servomotors, which typically provide robust stability based only on motion (i.e., position) feedback. Unlike an electric servomotor, a pneumatic servoactuator (such as that depicted in Fig. 19) is characterized by nonlinear third-order dynamics from the valve spool position to the load motion. Though most accurately characterized by a nonlinear model, the essential dynamic behavior of a PVA-controlled pneumatic servoactuator can be described using a linear description. In a linear systems context, an ideal PVA controller adds two zeros to the third-order open-loop dynamics of the servoactuator, which yields an open-loop system with a relative order of one, which at a high gain would provide high-bandwidth tracking and robust stability (i.e., an infinite gain margin). A realistic PVA controller, however, must be causal and attenuate noise at high frequencies, and as such realistically includes (at least) three poles. It should be noted that velocity and acceleration could be derived from a linear tachometer and accelerometer, respectively, but (like the use of pressure or force sensors) the additional sensors add cost and complexity to the servoactuator, and still realistically require filtering (which will similarly add poles to the compensator). As such, a standard PVA-controlled pneumatic servoactuator is characterized by six poles and two zeros in the open-loop dynamics, and thus is characterized by a relative order of four. Rather than

improve in performance while remaining stable (as does the ideal system with relative order one), the realistic system will become unstable as the gain is increased. This problem is compounded by the fact that such systems are often subject to significant Coulomb friction (particularly as the seals are pressurized), and achieving good tracking in the presence of such friction requires a high gain. The use of a high gain in a relative-order-four system results in a low gain margin, which is particularly problematic given the nonlinearities present in the pneumatic servoactuator. The issue of unstable behavior at large input amplitudes due to the nonlinearities present in the dynamics of a pneumatic servoactuator is discussed in the 1965 paper by Vaughan [83]. In particular, he presents an analysis that indicates that "within the framework of a linear-design procedure," the presence of choked flow "will create instability for certain large-amplitude commands." As such, PVA-controlled systems often operate at the border between acceptable tracking performance and instability. This issue is further exacerbated in the presence of a highly varying load (e.g., pick-and-place task), since significant variation in the plant dynamics can cause a stable system with a small gain margin to go unstable. As previously mentioned, control approaches based on full state feedback (such as sliding mode control) offer improved performance and stability, but require additional sensors (which increases cost and decreases reliability).

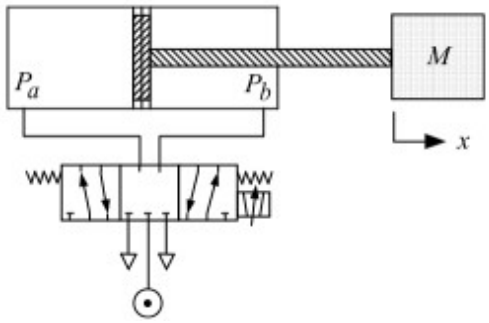

Fig. 19. Schematic representation of a typical pneumatic servoactuator.

In order to enhance the performance of a pneumatic servosystem without pressure, force, velocity, or acceleration sensing, the authors consider the use of a hydraulic damper placed in parallel with the pneumatic servoactuator. The authors show that supplementing the open-loop actuator with a simple, low-cost damper can enhance considerably the performance (i.e., the stability robustness, tracking accuracy, disturbance rejection, and in some cases the energetic efficiency) of a PVA-controlled pneumatic servo system. The damper is both a low cost and high reliability component, and thus provides advantages relative to approaches that require additional sensors, especially in a commercial or industrial context in which cost is a major consideration.

Note that the use of a hydraulic damper in parallel with a pneumatic actuator is discussed in at least three United States patents, including the patent by Huff [84], Crosby [85], and McCormick [86]. A hydraulic damper was used in combination with a pneumatic actuator in Klute et al. [87], although in that paper the authors utilized a McKibben actuator (rather than a pneumatic cylinder actuator), and they incorporated the hydraulic damper primarily for purposes of emulating the functional characteristics of biological muscle.

This paper formalizes some of the performance and stability benefits provided by the use of supplemental mechanical damping in pneumatic servosystems, and (unlike these related prior works) presents an analysis that illustrates the benefits of such damping with respect to the gain margin, tracking accuracy, and disturbance rejection of the servoactuator, and provides an experimental validation of these analytical results.

III.B.1 Linear Model of a Pneumatic Servoactuator

Although the behavior of a pneumatic servoactuator is most accurately described with nonlinear dynamics, the essential dynamic character of a PVA-controlled pneumatic actuator can be captured with a linear model, which is derived in this section. The motion dynamics provided by the (double-acting, single-rod) pneumatic servoactuator depicted in Fig. 19 is driven by the pressure differential in the cylinder chambers and can be written as

$$M\ddot{x} + B\dot{x} = P_a A_a - P_b A_b - P_{atm} A_r \tag{3}$$

where M is the payload plus the piston and rod assembly mass, B is the viscous friction coefficient, P_a and P_b are the absolute pressures in chambers a and b, respectively, P_{atm} is atmospheric pressure, A_a and A_b are the effective areas of each side of the piston, and A_r is the cross-sectional area of the piston rod. Coulomb friction forces from the piston and rod seals are lumped into the viscous friction term. Assuming air is a perfect gas undergoing an isothermal process, the rate of change of the pressure inside each chamber of the cylinder can be expressed as:

$$\dot{P}_{(a,b)} = \frac{RT}{V_{(a,b)}} \dot{m}_{(a,b)} - \frac{P_{(a,b)}}{V_{(a,b)}} \dot{V}_{(a,b)} \tag{4}$$

where $P_{(a,b)}$ is the pressure inside each side of the cylinder, $\dot{m}_{(a,b)}$ are the mass flow rates into (or, if negative, out of) each side of the cylinder, R is the universal gas constant, T is the (constant) fluid temperature, and $V_{(a,b)}$ is the volume of each cylinder chamber. Assuming the isentropic flow of an ideal gas through a converging nozzle, the mass flow into or out of each cylinder chamber can be written as a linear function of the signed valve area as follows:

$$\dot{m}_a = A_v \Psi_a = \begin{Bmatrix} A_v \Psi_a(P_s, P_a) \forall\ A_v \geq 0 (charge\ a) \\ A_v \Psi_a(P_a, P_{atm}) \forall\ A_v < 0 (discharge\ a) \end{Bmatrix} \tag{5}$$

$$\dot{m}_b = -A_v \Psi_b = \begin{Bmatrix} -A_v \Psi_b(P_s, P_b) \forall\ A_v < 0 (charge\ b) \\ -A_v \Psi_b(P_b, P_{atm}) \forall\ A_v \geq 0 (discharge\ b) \end{Bmatrix} \tag{6}$$

where A_v is the signed valve area (positive for charging chamber a and discharging b, negative for charging b and discharging a), P_s is the (absolute) supply pressure, P_{atm} is atmospheric pressure, and ψ is a function that describes the flow condition as follows:

$$\Psi(P_u, P_d) = \begin{Bmatrix} \dfrac{C_1 C_f P_u}{\sqrt{T}} & if\ \dfrac{P_d}{P_u} \leq C_r (choked) \\ \dfrac{C_2 C_f P_u}{\sqrt{T}} \left(\dfrac{P_d}{P_u}\right)^{\left(\frac{1}{\gamma}\right)} \sqrt{1 - \left(\dfrac{P_d}{P_u}\right)^{\frac{(\gamma-1)}{\gamma}}} & otherwise (unchoked) \end{Bmatrix} \tag{7}$$

where C_f is the discharge coefficient of the valve, P_u and P_d are the pressures upstream and downstream of the valve, respectively, T is the air temperature at the valve area A_v, γ is the ratio of specific heats, C_r is the pressure ratio that divides the flow regimes into unchoked and choked flow (approximately 0.5 for air), and C_1 and C_2 are constants defined as:

$$C_1 = \sqrt{\frac{\gamma}{R}\left(\frac{2}{\gamma+1}\right)^{\frac{(\gamma+1)}{(\gamma-1)}}} \tag{8}$$

and

$$C_2 = \sqrt{\frac{2\gamma}{R(\gamma-1)}} \tag{9}$$

The full nonlinear dynamics from the valve area input to the motion output are thus given by the time derivative of (3) combined with the expressions in (4) through (9).

A linear description of the servoactuator dynamics can be obtained by assuming equal areas on both sides of the piston, given by:

$$A_p = \frac{1}{2}(A_a + A_b) \tag{10}$$

and by linearizing the pressure dynamics of (4) about a nominal chamber pressure and volume, P_o and V_o, respectively, so that the motion dynamics expressed by the first time-derivative of (3) can be rewritten as:

$$M\ddot{x} + B\ddot{x} = \frac{A_p}{V_0}\left(RT_s\left(\dot{m}_a - \dot{m}_b\right) - 2P_0\dot{V}\right) \tag{11}$$

where T_s is the temperature of the air supply. Given the assumption of equal piston areas, the rate of change of volume can be expressed as

$$\dot{V} = A_p\dot{x} \tag{12}$$

As such, the dynamics of (11) can be rewritten as

$$M\ddot{x} + B\ddot{x} + K\dot{x} = \frac{A_p RT_s}{V_0}u \tag{13}$$

where

$$K = \frac{2 P_0 A_p^2}{V_0} \tag{14}$$

and the control input

$$u = \dot{m}_a - \dot{m}_b \tag{15}$$

Assuming the flow resides primarily in the choked regime, and recalling that the signed valve area is positive when charging a and discharging b and negative when charging b and discharging a, the mass flow rates can be written based on (5) through (9) as

$$\dot{m}_a = \begin{Bmatrix} C_m P_s A_v \; \forall \; A_v \geq 0 \, (charge\, a) \\ C_m P_a A_v \; \forall \; A_v < 0 \, (discharge\, a) \end{Bmatrix} \tag{16}$$

$$\dot{m}_b = \begin{Bmatrix} -C_m P_s A_v \; \forall \; A_v < 0 \, (charge\, b) \\ -C_m P_b A_v \; \forall \; A_v \geq 0 \, (discharge\, b) \end{Bmatrix} \tag{17}$$

where

$$C_m = \frac{C_1 C_f}{\sqrt{T}} \tag{18}$$

and where, for the assumed condition of choked flow, the temperature at the valve area is a constant given by:

$$T = \frac{2 T_s}{\gamma + 1} \tag{19}$$

As such, the control input can be written as

$$u = \begin{Bmatrix} C_m (P_s + P_b) A_v \; \forall \; A_v \geq 0 \, (charge\, a, discharge\, b) \\ -C_m (P_s + P_a) A_v \; \forall \; A_v < 0 \, (charge\, b, discharge\, a) \end{Bmatrix} \tag{20}$$

Since, for the linearized pressure dynamics it was assumed the chamber pressures operate about a nominal pressure P_o, the control input can be written in a single expression as

$$u = C_m (P_s + P_0) A_v \tag{21}$$

Thus, the linearized dynamics of the pneumatic servoactuator can be expressed as

$$\dddot{x} + a_2 \ddot{x} + a_1 \dot{x} = b_0 u \tag{22}$$

where

$$a_1 = \frac{K}{M} = \frac{2 P_0 A_p^2}{M V_0} \tag{23}$$

$$a_2 = \frac{B}{M} \tag{24}$$

and

$$b_0 = \frac{A_p R T_s}{M V_0} \tag{25}$$

In transfer function form, the model is expressed as:

$$G_p(s) = \frac{X(s)}{U(s)} = \frac{b_0}{s\left(s^2 + a_2 s + a_1\right)} \tag{26}$$

III.B.2 Linearized Dynamics of a PVA-Controlled Pneumatic Servoactuator

III.B.2.a Root Locus

As expressed by (26), the linearized pneumatic servoactuator is characterized by three poles between the valve command and the piston/load motion. One of these poles is at the origin of the s-plane, while the location of the other two poles is determined by the model parameters a_1 and a_2 (equations (23) and (24), respectively) according to:

$$s_{2,3} = \frac{1}{2}\left(-a_2 \pm \sqrt{a_2^2 - 4a_1}\right) \tag{27}$$

Based on (23), (24), and (27), and assuming the model is linearized about the mid-stroke of the cylinder such that:

$$V_0 = \frac{A_p L}{2} \tag{28}$$

where L is the length of the cylinder, the two non-zero poles (i.e., the two not located at the origin) will be an imaginary pair when:

$$B < 4\sqrt{\frac{P_0 A_p M}{L}} \tag{29}$$

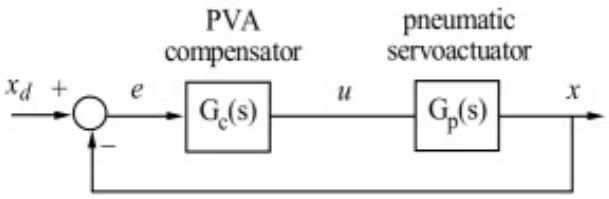

Fig. 20. Block diagram of typical closed loop pneumatic servoactuation with PVA compensator

Most pneumatic systems are characterized by condition (29), and in fact the damping coefficient is typically much smaller than the right-hand-side of (29), such that the pole pair is commonly lightly-damped (see, for example, [70,75,81]). In a PVA controller, which is shown in Fig. 20, the compensator ideally takes the form:

$$G_c(s) = \frac{U(s)}{E(s)} = k_a s^2 + k_v s + k_p \tag{30}$$

which introduces two zeros into the open-loop. Assuming the gains are chosen such that these zeros lie on the real axis, the root-locus of the PVA-controlled pneumatic servoactuator is as shown in Fig. 21. The relative order of this system is one, and as the loop gain is increased, the system will remain stable, and at a sufficiently high loop gain the control bandwidth will be limited by the location of the PVA zeros. In the presence of noise, however, realistic implementation of a PVA controller requires that the compensator incorporate three poles in addition to the two zeros, which will attenuate the high-frequency noise. These poles will in general be placed to the left of the compensator zeros. Assuming the zeros are real and the poles are real and repeated, the PVA compensator will take the form:

$$G_c(s) = \frac{k(\tau_1 s + 1)(\tau_2 s + 1)}{(\tau_3 s + 1)^3} \tag{31}$$

where τ_1 and τ_2 determine the location of the open-loop zeros, k is the loop gain, and τ_3 determines the location of the compensator roll-off poles. Combined with the plant transfer function, this compensator will reshape the “ideal” root locus of Fig. 21 into the more realistic locus shown in Fig. 22. As the loop gain is increased in the realistic system, the closed-loop will exhibit an increasingly oscillatory response until the dominant poles cross into the right-half-plane and the closed-loop becomes unstable.

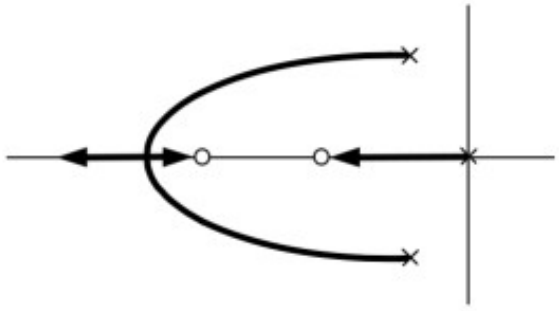

Fig. 21. Root locus of typical pneumatic servoactuator with idealized PVA controller.

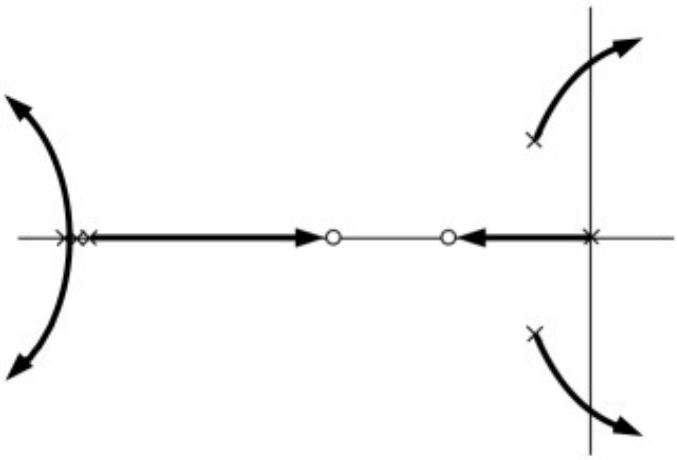

Fig. 22. Root locus of realistic PVA-controlled pneumatic servoactuator, including the effect of compensator poles (i.e., effect of filtering).

In order to achieve better performance, the open-loop can be "reshaped" with the introduction of a mechanical damper to the open-loop system. Specifically, based on (26), the two non-zero plant poles will be located on the real-axis when:

$$B \geq 4\sqrt{\frac{P_0 A_p M}{L}} \tag{32}$$

With an appropriate choice of damping, the open-loop poles can be re-oriented as shown in the root locus in Fig. 23. As shown in the root locus, the poles and zeros of the compensator have not changed, but due to the relocation of the open-loop poles, the root locus remains stable in a much larger region of the s-plane, and in fact can provide a closed-loop response with a larger bandwidth and (as subsequently shown) gain margin relative to the non-modified system shown in Fig. 22.

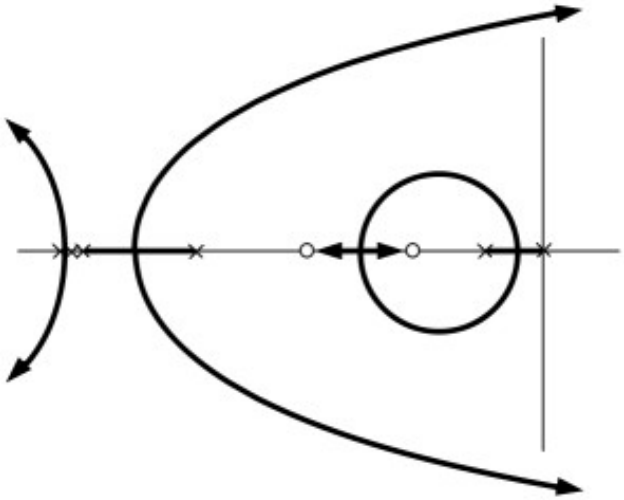

Fig. 23. Root locus of PVA-controlled pneumatic servoactuator with the addition of a damper in the open-loop.

It should be noted that the relative-order-one compensator described by (11) can be replaced with a slightly less conservative relative-order-zero PVA compensator, which will contribute less phase lag to the loop, at the expense of somewhat more high-

frequency noise. Specifically, rather than filter all the components of the PVA, one can filter only the differentiators (such that the velocity and acceleration components are each relative-order-one), so that the form of the compensator is:

$$G_c(s)=\frac{k_a s^2}{(\tau_3 s+1)^3}+\frac{k_v s}{(\tau_3 s+1)^2}+k_p= \frac{k_p\tau_3^3 s^3+(3k_p\tau_3^2+k_v\tau_3+k_a)s^2+(3k_p\tau_3+k_v)s+k_p}{(\tau_3 s+1)^3} \tag{33}$$

This form of the compensator will add three zeros and three poles to the open-loop. The shape of the root locus without and with open-loop damping remains similar to Fig. 22 and Fig. 23 respectively, with the primary difference being that three poles leave along asymptotes rather than four (relative order of open-loop is now three), and the asymptotes are oriented at ±60° and -180° rather than at ±45° (i.e., one pole moves to the left along the real axis, while the poles that become unstable move across the imaginary axis at ±60° rather than at ±45°). Aside from these minor differences, the nature and influence of open-loop damping on the root locus remains the same (i.e., remains as illustrated by Fig. 23).

III.B.2.b Gain Margin

When considering the gain margin of the PVA-controlled pneumatic servoactuator (i.e., the two-zero, six-pole combination of the PVA compensator and the plant dynamics), the closed-form analytical solution is too complex to provide concise insight (i.e., the solution occupies several pages). The essential effect of the open-loop damping on the gain margin, however, can be illuminated by separating the contributions from the PVA compensator and the plant, which will both contribute multiplicatively to

the open-loop gain. Since the PVA compensator does not explicitly include the damping term, the general trend between plant damping and gain margin can be elucidated by assessing the gain margin of the plant only. Based on (26), one can show that the phase will cross -180° at a frequency of:

$$\omega = \sqrt{a_1} \tag{34}$$

and that, at this frequency, the inverse of the gain (i.e., the gain margin for the plant) will be:

$$k_g = \frac{b_0}{a_1 a_2} = \frac{2 P_0 A_p B}{M R T_s} \tag{35}$$

As such, the gain margin of the portion of the open-loop dynamics directly affected by the damping is directly proportional to the plant damping. Though the actual gain margin will be different when combined with the PVA compensator, it is clear that the addition of plant damping has a positive influence on the gain margin of the closed-loop system.

III.B.2.c Disturbance Rejection

A force disturbance to the load motion can be modeled as shown in Fig. 24, where $G_p(s)$ is as defined in (26), $G_c(s)$ is of the form (31) or (33), and $G_d(s)$ is:

$$G_d(s) = \frac{1}{s(Ms + B)} \tag{36}$$

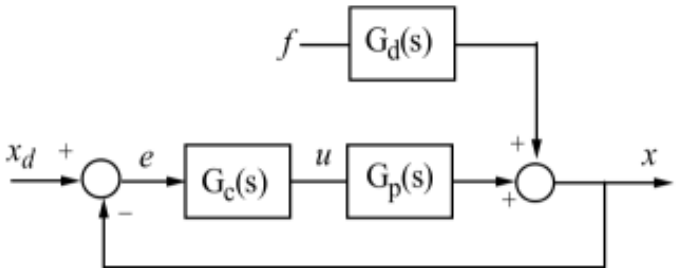

Fig. 24. Model of a force disturbance on the output of a PVA-controlled pneumatic servoactuator.

For the PVA compensator (31), the disturbance transfer function from the force-based disturbance to the output motion is given by:

$$D(s)=\frac{F(s)}{X(s)}=\frac{1}{Ms+B}\left[\frac{(\tau_2 s+1)^3(s^2+a_1 s+a_2)}{k b_0(\tau_1 s+1)^2+(\tau_2 s+1)^3(s^2+a_1 s+a_2)}\right] \tag{37}$$

and the steady-state response to a step input in the disturbance force given by:

$$x(t\to\infty)=\frac{V_0}{k(C_m A_p R T_s(P_s+P_0))} \tag{38}$$

As such, the disturbance rejection for a step input in force is inversely proportional to the loop gain, *k*. Since the addition of open-loop damping enables an increase in gain margin, it similarly enables a larger loop gain, and thus provides improved disturbance rejection. Note also that the most significant impediment to accurate tracking in a pneumatic servoactuator is typically the presence of Coulomb friction in the piston and rod seals. Since Coulomb friction can be considered a force disturbance in the control loop, and since the addition of open-loop damping enables an

increased loop gain and corresponding increase in disturbance rejection, the inclusion of added open-loop damping also serves to increase the tracking accuracy of the pneumatic servoactuator.

III.B.3 Experimental Validation

Experiments were performed on a single degree-of-freedom pneumatic servoactuator to validate the (analytically) prescribed benefits of supplemental damping. Specifically, experiments compared the achievable gain and the resulting performance for a PVA-controlled pneumatic servoactuator, with and without supplemental mechanical damping. The experimental setup, which is shown in the schematic of Fig. 19 and in the photograph of Fig. 25, consists of a 2 cm (3/4 in) inner diameter, 10 cm (4 in) stroke single-rod, double-acting pneumatic cylinder (Bimba model 044-DXP), which is connected to a 1 kg mass affixed to a linear slide. Displacement of the slide (and actuator) was measured with a linear potentiometer (Midori LP-150F). Actuator motion was controlled via a four-way servovalve (FESTO MPYE-5-M5-010-B). The PVA controller was digitally implemented at a sampling rate of 1 kHz on an Intel Core 2 Duo processor via the real-time interface provided by Matlab/Simulink (The MathWorks, Inc.). Supplemental mechanical damping was added via a linear hydraulic damper (Integy model MSR8 Savage with spring removed) filled with 80-weight silicone oil, which was connected to the linear slide as shown in Fig. 25. The damping constants present in the pneumatic actuator and provided by the supplemental damper were measured to be B_{nom} = 28.3 kg/s for the pneumatic actuator, and B_{sup} = 652 kg/s for the supplemental damper. Other model parameters corresponding to the experimental setup were measured or found

as given in Table 5. Note that the nominal chamber volume V_o was selected at the mid-point of the cylinder stroke, and the nominal pressure P_o approximately half of the supply pressure.

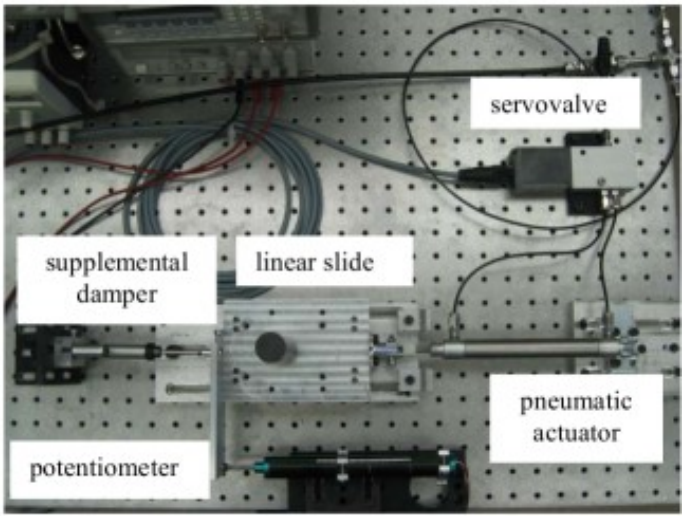

Fig. 25. Single degree-of-freedom experimental setup (shown with supplemental damper attached to slide).

Table 5
Model parameters corresponding to the experimental conditions.

Parameter	Value
T_S	297 K
P_S	690 kPa
R	.297 kJ/kg-K
V_0	1.37 x10-5 m^3
A_a	5.7 x10-4 m^2
A_b	5.2 x10-4 m^2
M	1.0 kg
B_{nom}	28.3 kg/s
B_{sup}	652 kg/s
P_0	335 kPa

The controller used in the experiments was the relative-order-zero PVA controller described by (33) where the real, repeated polls were located at $\tau_3 = 3.2\text{x}10^{-3}$ s (which corresponds to a filter roll-off frequency of 50 Hz). The roll-off frequency was chosen to be as large as possible without introducing significant noise into the control output. In order to reduce the number of controller parameter choices, the three (proportional, velocity, and acceleration) gains were reduced to two through the following relationship:

$$k_a s^2 + k_v s + k_p = k\left(\tau_1 s + 1\right)^2 \tag{39}$$

where the parameter k is the loop gain and the parameter τ_1, which establishes the location of the real repeated zeros in an ideal PVA controller, was experimentally selected as $\tau_1 = 9.1\text{x}10^{-3}$ s (which corresponds to a break frequency of 17.5 Hz). As with

the roll-off frequency, the break frequency was chosen to be as large as possible, without introducing significant noise into the control output. The experiment PVA compensator therefore was of the form:

$$G_c(s) = k\left(\frac{\tau_3^3 s^2 + \left(3\tau_3^2 + 2\tau_1\tau_3 + \tau_1^2\right)s^2 + \left(3\tau_3 + 2\tau_1\right)s + 1}{\left(\tau_3 s + 1\right)^3}\right) \tag{40}$$

where the loop gain k was varied between experiments, while the controller parameters τ_1 and τ_3 remained at the previously indicated values ($\tau_1 = 9.1\text{x}10^{-3}$ s and $\tau_3 = 3.2\text{x}10^{-3}$ s) for all cases.

III.B.3.a Gain Margin

As mentioned in the introduction, nonlinearities present in the pneumatic servoactuator can create instability for large-amplitude commands (e.g., a command that would result from a step input to a PVA controller). In the servoactuator, the “instability” predicted by the linear analysis manifests as sustained large-amplitude, high-frequency oscillations. At a low loop gain, the stability margin is sufficient to prevent this behavior, but at a sufficiently high loop gain, the stability margin decreases to a point that is insufficient to guard against the limit cycle behavior. For the nominal experimental setup (i.e., without supplemental damping), a loop gain at or below k = 40 g/m-s will maintain stable tracking behavior, while a loop gain at or above k = 44 g/m-s will result in sustained large-amplitude oscillations when subjected to a step command. The respective responses to a step command corresponding to a loop gain of k = 40 g/m-s and k = 53 g/m-s are shown in Fig. 26 and Fig. 27, respectively. Note that the stable response (Fig. 26) is somewhat asymmetric, due primarily to the asymmetry in piston area, which is

characteristic of a single-rod type cylinder. Note that, in all figures, a step in the positive direction indicates rod retraction, while a step in the negative direction indicates rod extension. The “unstable” response (Fig. 27) clearly illustrates the aforementioned sustained large-amplitude oscillations. Note that, at a gain of k = 44 g/m-s, only the step from positive to negative displacement (rod extension) exhibits sustained oscillations, while at a gain of k = 53 g/m-s, the sustained oscillations are present in both directions (recall the piston asymmetry).

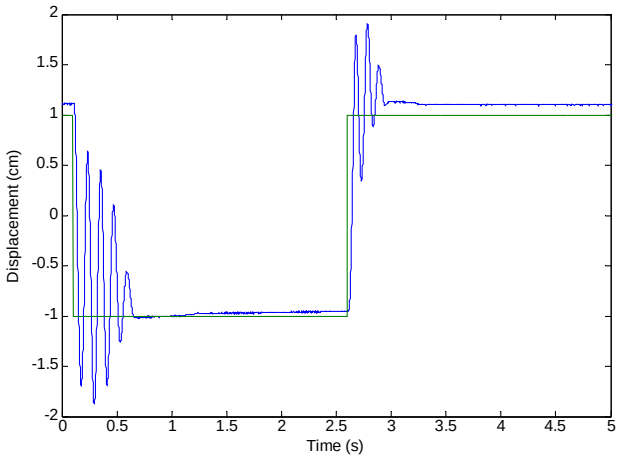

Fig. 26. Nominal servoactuator plant at maximum loop gain for stable tracking (k=40 g/m-s).

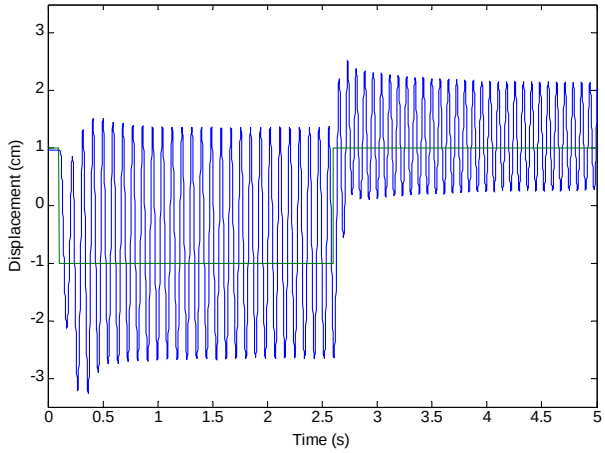

Fig. 27. Nominal servoactuator at loop gain of k=53 g/m-s, demonstrating oscillatory limit cycling behavior.

When supplemental damping is added to the PVA-controlled servoactuator, the corresponding maximum loop gain that will maintain a stable response to a step command (i.e., will not induce a limit cycle of oscillations) can be increased to k = 293 g/m-s. The motion tracking corresponding to this gain is shown in Fig. 28. Note that, despite the fact the response is not particularly oscillatory, a gain higher than k = 293 g/m-s will induce an oscillatory limit cycle, similar in nature to Fig. 27. As discussed in section III.B.2.b and indicated by expression (35), the increase in damping from B = 28.3 kg/s to B = 680 kg/s enables an increase in loop gain from 40 to 293 g/m-s, and thus experimentally increases the gain margin of the servoactuator by a factor of 7.3 (which corresponds to an increase of approximately 17 dB).

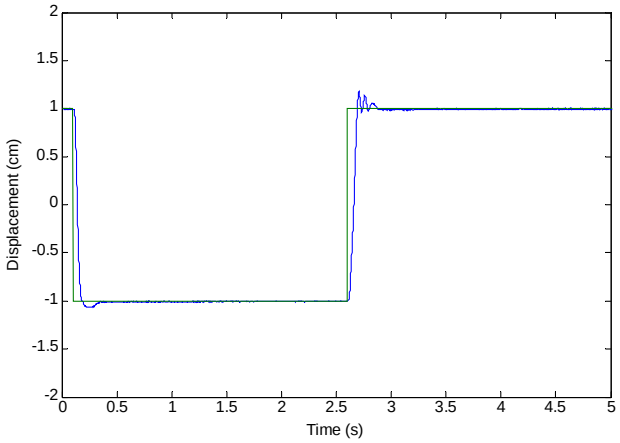

Fig. 28. Servoactuator with supplemental damping at maximum loop gain for stable tracking (k = 293 g/m-s).

III.B.3.b Tracking Accuracy and Disturbance Rejection

As discussed in section III.B.2.c and indicated by expression (38), the (steady-state) disturbance rejection is proportional to the loop gain. As previously mentioned, since Coulomb friction (in the piston and rod seals) generally limits the tracking accuracy in a pneumatic servoactuator, and since this friction can be regarded as a disturbance in a PVA-controlled actuator, the tracking accuracy is directly related to the disturbance rejection characteristics of the closed-loop system, which is directly proportional to the loop gain. Since the addition of supplemental damping enables a significantly higher loop gain, one would expect a corresponding significant improvement in steady-state tracking accuracy. Fig. 29(a) shows the response of the PVA-controlled servoactuator with and without supplemental damping, both at 90% of their respective maximum loop gains (i.e., the nominal system at k = 40 g/m-s and the system with supplemental damping at k = 264 g/m-s). Fig. 29(b) and Fig. 29(c) show close-ups of Fig. 29(a) during the steady-state

segments of both steps. As indicated in the figures, the steady-state error improves from an average of 0.33 mm to an average of 0.05 mm for the extension step (Fig. 29(b)), and improves from an average of 0.5 mm to an average of 0.05 mm for retraction step (Fig. 29(a)). As such, the average tracking accuracy improves from 420 microns without the damper to 50 microns with the supplemental damping, or a factor of 8.4 times. Thus, the experimental results validate the projection given in equation (38) that the steady-state disturbance rejection (and thus the tracking accuracy) improves essentially in proportion to the increase in loop gain (i.e., a factor of 7.2 increase in gain resulted in a factor of 8.4 increase in accuracy).

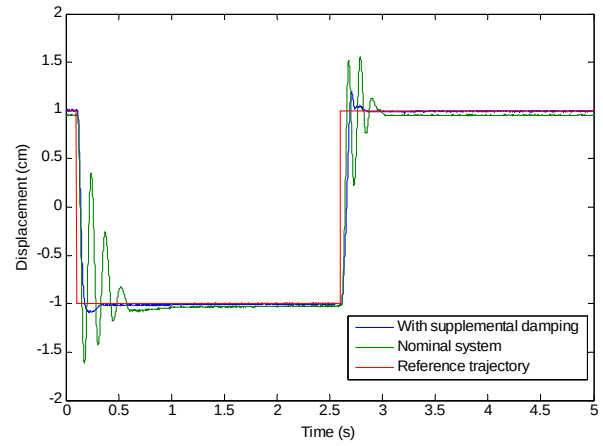

(a)

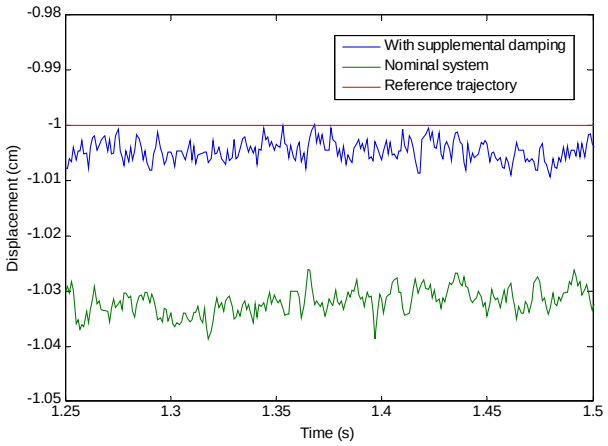

(b)

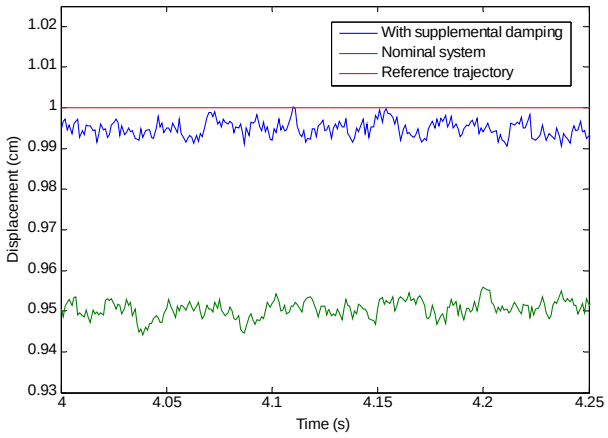

(c)

Fig. 29. (a) Step response for PVA-controlled servoactuator with and without supplemental damping, both at 90% of maximum loop gain; (b) close-up of steady-state tracking for downward step; and (c) close-up of steady-state tracking for upward step.

Improvement in disturbance rejection was additionally validated by another comparison experiment in which a 9 kg (20 lb) mass was connected to the linear slide by a cable, which was routed over a pulley, so that the mass could hang vertically by the side of the table. As such, the mass imposed an 88 N (20 lb) steady-state force on the servoactuator rod in the extension direction. In addition to the steady-state disturbance, the hanging mass alters significantly the mass of the system, and also introduces the somewhat nonlinear properties of the cable transmission (i.e., stiff in tension, compliant in compression). As in the previous experiment, both the nominal system and the system with supplemental damping were controlled with a loop gain that was 90% of their respective maximum gains (i.e., loop gains were set to k = 40 g/m-s and k = 264 g/m-s, respectively). Fig. 30(a) shows the step responses for the respective systems when subjected to the hanging mass, while Fig. 30(b) and Fig. 30(c) show close-ups of the steady-state portions in extension and retraction, respectively. The average steady-state error for the nominal system is approximately 2.5 mm, while the average steady-state error for the system with supplemental damping is approximately 0.4 mm. As such, the system with supplemental damping demonstrates an improvement of approximately 6.3 times in steady-state disturbance rejection, relative to the nominal servoactuator (Fig. 31).

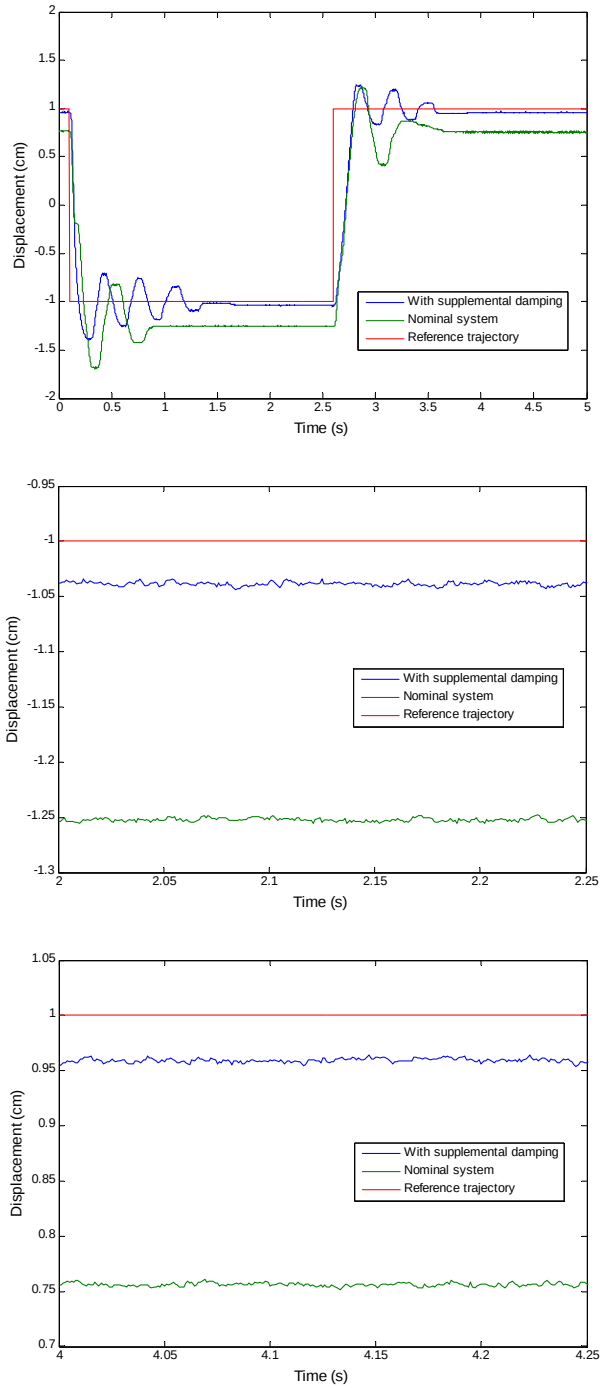

Fig. 30. (a) Step response for PVA-controlled servoactuator with and without supplemental damping, both at 90% of maximum loop gain, when subjected to a 9 kg hanging mass disturbance; (b) close-up of steady-state tracking for downward step; and (c) close-up of steady-state tracking for upward step.

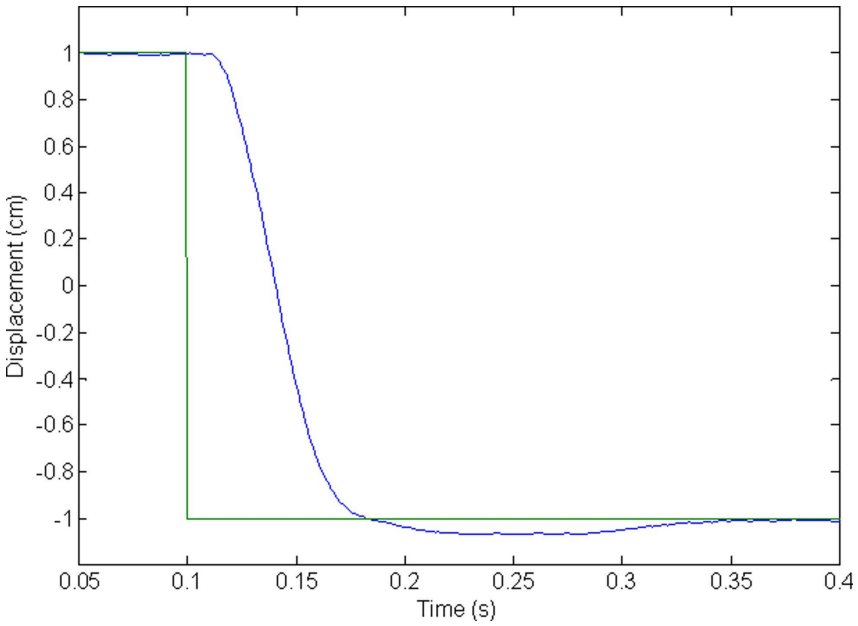

Fig. 31. Close-up of step response of servoactuator with supplemental damping at maximum loop gain for stable tracking (k = 293 g/m s)

III.B.4 Conclusion

The authors present an analysis of supplemental mechanical damping in a PVA-controlled pneumatic servoactuator. The analysis indicates that added mechanical damping can significantly increase the gain margin of the servoactuator, and that the higher loop gain that results from the improvement in gain margin will provide improved steady-state accuracy in the controller, and improved steady-state disturbance rejection. An energetic analysis indicates that these improvements in performance do not require additional actuator energy expenditure. Experiments on a single degree-of-freedom system demonstrate the assertions of the model based analysis; namely that the addition of a damper provides significant improvements in gain margin and corresponding significant improvements in tracking accuracy and disturbance rejection.

III.C Planning Robot Leg Motions

Based on the descriptions (or “gait formulas”) of [88], a solely time based approach (i.e. neglecting inertial and force measurements) is chosen to encode the desired motion of the present robot's legs. In other words, an internalized clock will run and each of the robot's legs will be put into swing or stance modes as that clock repeatedly cycles through the desired gait's formula. Note that this approach greatly simplifies the problem of generating walking motion, but is potentially unstable as the robot's dynamics are totally absent from the locomotion formulation. However, the notion of using a freely running clock as an open-loop gait generator is not without precedent in both nature and engineering [1,9,48,89,90]. So, while the approach is seemingly basic and ignores some problems, it is appropriate to be used in this application.

It then remains to both construct the gait formulas for those quadrupedal gaits that are either shown or thought to be suitable for the robot's morphology and dynamics as well as to plan the trajectory of an individual leg in both swing and stance. These two data sets fully define the ambulatory locomotion of the robot. A gait formula is merely a combination of the phase differences between the (in this case identical) motions of each of the legs as well as a duty factor that is the ratio of the amount of time each leg spends in a supporting phase versus in a retraction phase. A summary of the possible forms of locomotion that using this definition of a gait formula allows a quadruped to take on is given in Appendix B. For the purposes of this work, only the walk and trot are of interest (i.e. dynamic gaits are omitted for simplicity and because the requisite sensing for such gaits is absent).

To plan the individual leg motions, it is worth investigating the reachable workspace of an individual foot. The reachable workspace for an individual leg can be visualized as some geometric solid that is fixed in space relative to the robot's thorax. Note again that, because of the symmetry of the robot and the equivalent construction of all of its legs, the reachable workspaces are all also equivalent. However, a special condition arises because the rear legs are reflections of the fore legs across the robot's transverse plane. That is, for any single leg, both a given trajectory and the front-to-back reflection of that trajectory must be wholly contained within the reachable workspace of that leg. This ensures that all legs (fore and hind) are able to execute the planned trajectory and can work as an ensemble to cause the robot to walk forward. As an added benefit, this condition allows the robot to walk equivalently both forward and backward.

A three-dimensional visualization of the designed leg's reachable workspace is found by exhaustively searching through the Cartesian space surrounding the robot. At each point in that space, the inverse kinematics (equations (50),(53), and (54) found in Appendix A) are interrogated to see if a solution exists and, if one exists, that the solution falls within the achievable range of all joints (Table 8). Using this method, such a visualization was created, and is shown in Fig. 32.

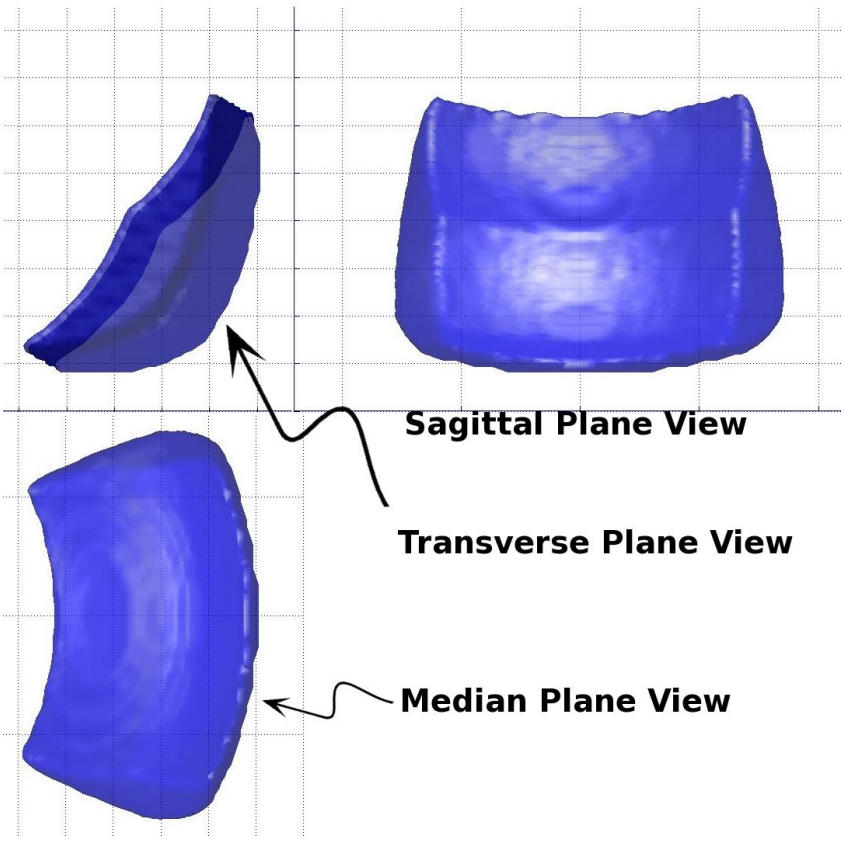

Fig. 32. Plan view of reachable workspace of a single leg (front left).

A foot path then must have the necessary features so that, when it is followed, ambulatory locomotion will result. These are relatively obvious, but include that the path has some region where it moves on a line parallel to the body axis in the direction opposite the robot's direction of travel (stance phase motion) and that there is some region in which the foot returns from its most posterior extreme position to its most anterior extreme position in some space above the stance phase motion line so that the foot clears the ground (swing phase motion). Further, a foot path must also (as noted earlier) fall totally within the reachable workspace (Fig. 32) of the robot's foot.

There is an infinite number of possible paths that can be constructed that meet these simple criteria. Other helpful but not strictly necessary features are that the stance phase motion is as long as possible (otherwise the robot is not fully utilizing its available leg workspace). Also, for higher speed gaits, it seems (through empirical observation) to be important that the swing phase motion terminate with motion in the direction of the impending stance motion. This feature helps to alleviate the high accelerations and jerks required to transition from swing to stance, but does have the unfortunate side effect of shortening the maximum possible swing phase motion. This is because what would have been the most anterior portion of the stance phase motion is absorbed by the swing phase motion. Along the same line of reasoning, it is helpful for the stance-to-swing transition to have the same smoothness features as the swing-to-stance transition.

Early iterations of these motion constructs for the present robot were created by stringing minimum jerk motions in the *x*-*z* plane together so that the motion was smooth. The use of minimal jerk as the objective function in trajectory planning has some foundation in the biomechanical literature as [61] demonstrated that such a criterion is apparently used in arm movements of monkeys. While the use of these trajectories worked well for low speeds, the difficulty of using this idea increased dramatically at high speeds, mostly due to the discovery that the smoothness criteria mentioned above increases in importance at higher walking rates.

Instead, the Simulink “Signal Builder” tool was used to manually draw paths that have all the necessary features. This is somewhat crude and relies more on intuition and experience with the particular robot rather than any kind of mathematical construct or optimality criterion. To assist in guiding the creation of these foot paths, the same quantities from the canine [91] were used as a starting point.

It should be noted that the present work is unconcerned with thoroughly investigating the dynamics of the robot and developing a walking method that has some robust stability characteristics or other such goals. The task is instead merely to characterize the normalized output power metrics of the robot; this requires only a rudimentary walking method. Therefore, the formulation of these foot paths (as well as the gait formulas and other characteristics of the walking mode) through intuition and manual tuning is acceptable and adequate.

A time history for some arbitrary clock rate of the *x*- and *z*-direction foot trajectories as planned by the above method (the *y*-direction trajectory is equivalent to the z-direction trajectory as the workspace shape of Fig. 32 angles away from the robot body in that sense) is shown in Fig. 33 and these trajectories are compiled into a three dimensional space in Fig. 34. Note that these are normalized versions of the foot trajectories and are scaled and translated (both temporally and spatially) when used by the robot in ambulatory locomotion.

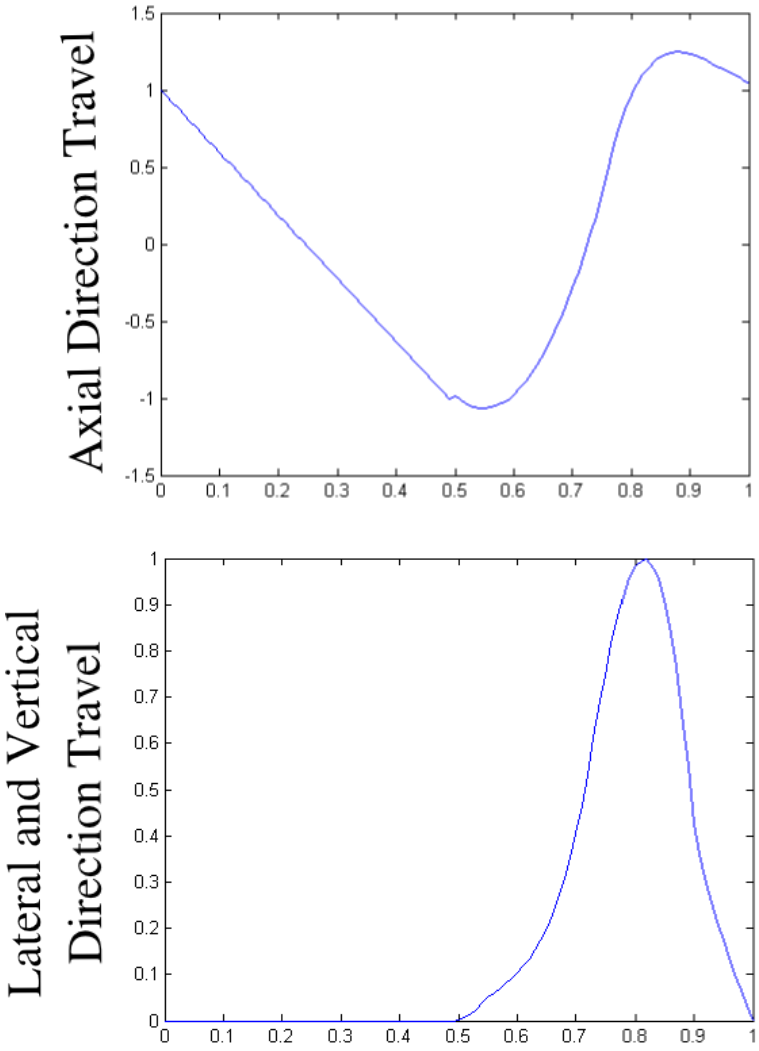

Fig. 33. Time history of manually defined foot trajectory

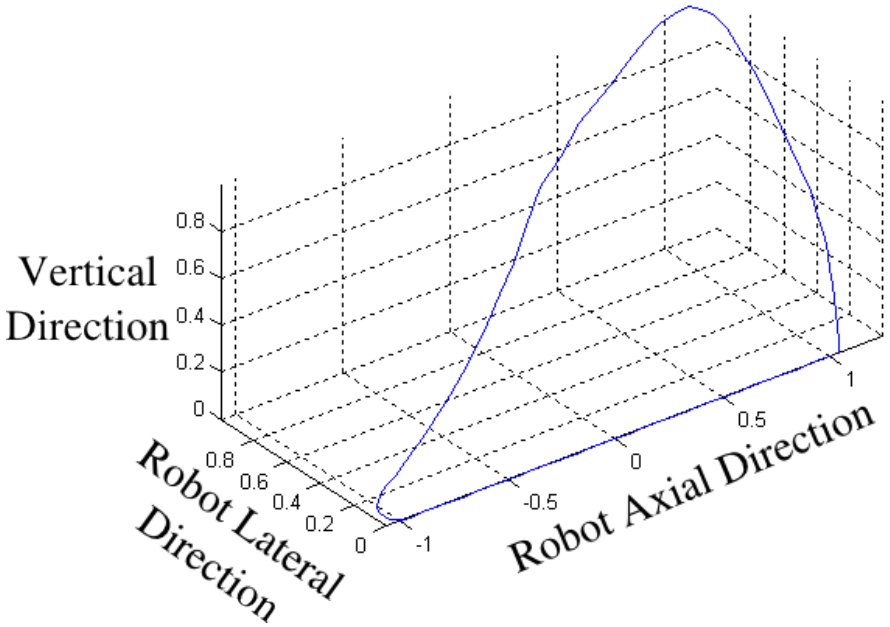

Fig. 34. Manually derived foot path developed over time and viewed in robot's sagittal plane

III.C.1 Increasing Static Stability of the Walk Gait

In the most common implementation of the walk or crawl gait (see Appendix B), the walking entity has a constant forward body velocity. Because of this and the order and timing of when legs transition from stance phase to swing phase, there are two instants in every cycle of the walker's gait where its static stability margin momentarily drops to zero. This margin is simply the minimum distance from the robot's center of mass to one of the edges of the convex hull whose vertices are the feet that are supporting the weight of the walker when the center of mass position is projected onto the horizontal plane. In fact, the static stability margin is constantly decreasing during the swing motion of two legs and increasing during the swing motion of the other two.

A simple method of improving the static stability margin used in this work is to cause the center of mass of the robot to be farther inside the support triangle during its walking motion. This is done here by the purposeful addition of lateral and axial oscillatory motions to the previously described motion of the robot's feet. The oscillations present in each foot are in phase with each other and are of equal magnitude so that they resolve into a body mass center movement. The frequency of these oscillations is an integer multiple of an individual foot's gait frequency. These sinusoidal motions are identical in nature to those used in [92,93] and serve to increase the static stability of the gait by shifting the robot's center of mass farther into the support polygon than would be the case in their absence. The body center's motion, then, becomes the superposition of straight line, constant speed (i.e. that of the unmodified walk/crawl gait) with a figure-eight oscillatory motion to enhance stability. This second portion of the motion is idealized in Fig. 35. This same motion is shown in Fig. 36 as the actual realized center of mass motion viewed from an inertial reference frame moving at a constant speed equal in magnitude to the average speed of the robot's body center. The robot's body center motion viewed from a stationary reference frame is shown in Fig. 37. In both Fig. 36 and Fig. 37, the robot's direction of travel is to the right. Note that this change does not eliminate the two instants in which static stability drops to zero, but the velocity of the center of mass through these two points is increased and the static stability margin is made higher for a greater portion of the gait by the change.

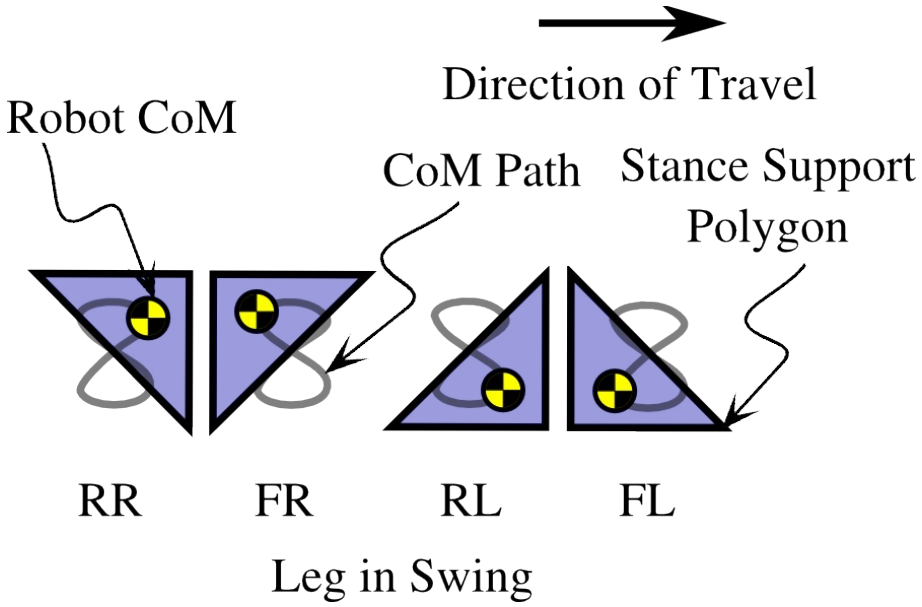

Fig. 35. Center of mass figure-eight oscillatory motion for stability enhancement. Leg in swing is denoted by F/R (front/rear) followed by R/L (right/left).

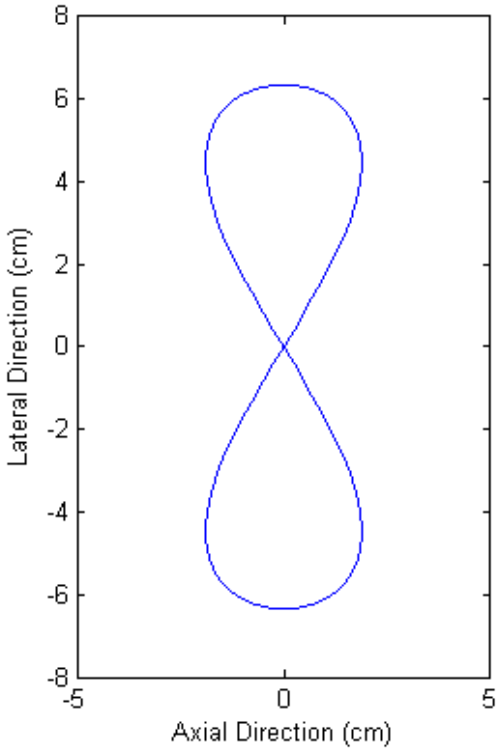

Fig. 36. Center of mass stability enhancing motion viewed relative to an inertial reference frame moving at the average forward speed of the robot

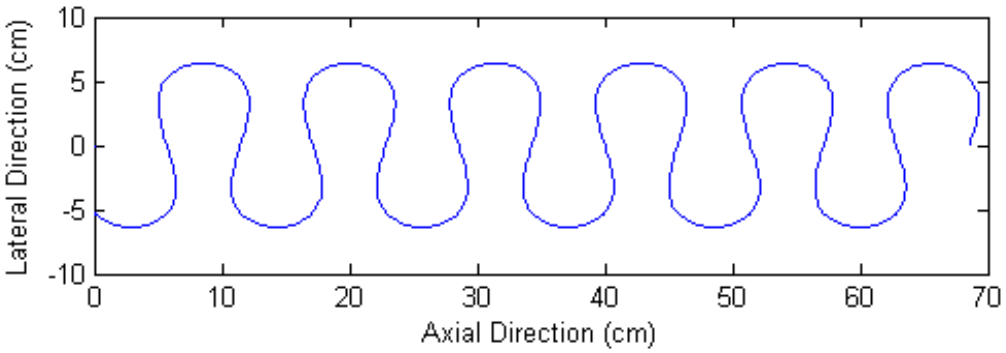

Fig. 37. Robot body center motion including the addition of a stability enhancing modification viewed from a stationary reference frame

Finally, a phasing diagram depicting the exact way in which the motion of the four legs are timed relative to each other is shown in Fig. 38. Here, the highlighted portions denote swing phase motion. The duty cycle of the walk shown is .75 (the minmum for a statically stable walk) and the legs are identified by F/R (front/rear) followed by R/L (right/left). Note that, while the direction of motion of the rear legs appears to be counter to that of the front legs, this is because of the convention for the positive direction of the thorax-coxa joint is reversed for the rear legs.

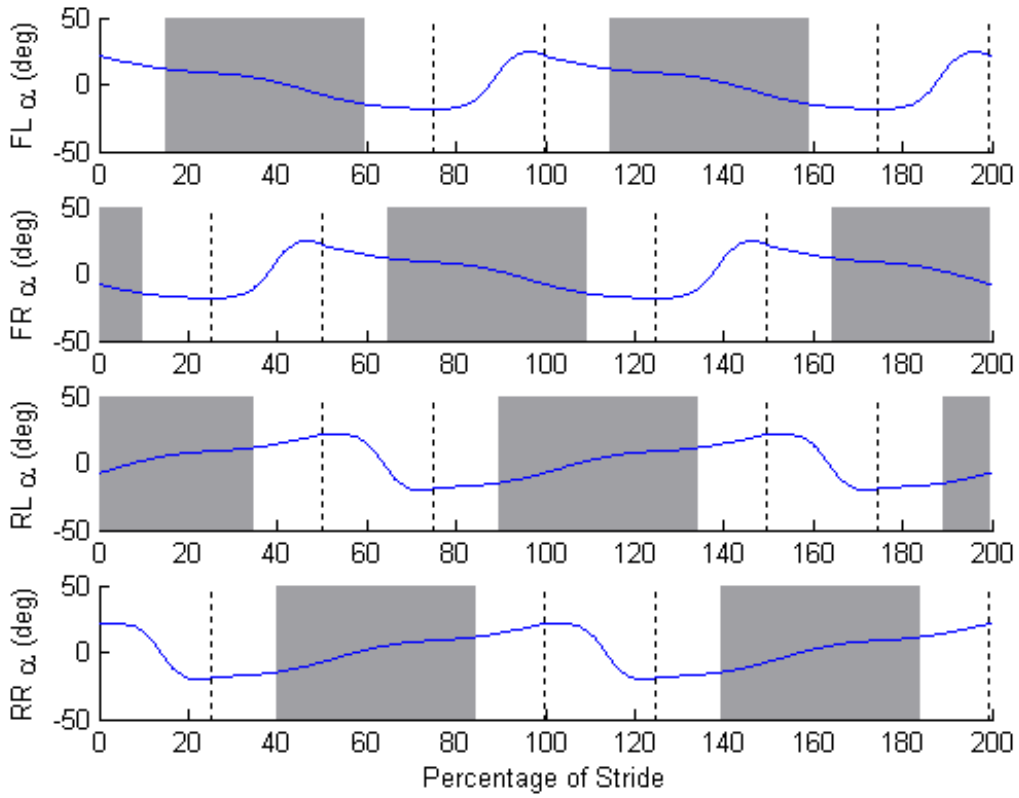

Fig. 38. Walk gait phasing diagram

III.D Gain Scheduling

A complication arises when attempting to implement the PVA controller of section III.B to control a foot in the walking robot. This is that the plant that the controller acts upon changes dramatically when the leg makes a transition from stance to swing or vice versa. Effectively, the mass term present in equations (23)-(26) jumps by a large factor when the foot gains contact with the ground (Fig. 39). A leg operating in swing phase (top of Fig. 39) is exposed to its mass only, while a leg operating in stance phase (bottom of Fig. 39) acts upon not only its mass, but some share of the overall body mass. Further, because of joint position errors throughout the body (irrespective of

magnitude), each joint in a stance phase leg experiences additional loading emanating from the actuators of its colleagues. These loads add to the effective mass experienced by stance phase joints. These increases in mass cause the plant poles of Fig. 22 to move significantly. While the addition of the damping that is the focus of section III.B attenuates this effect, it is not totally eliminated.

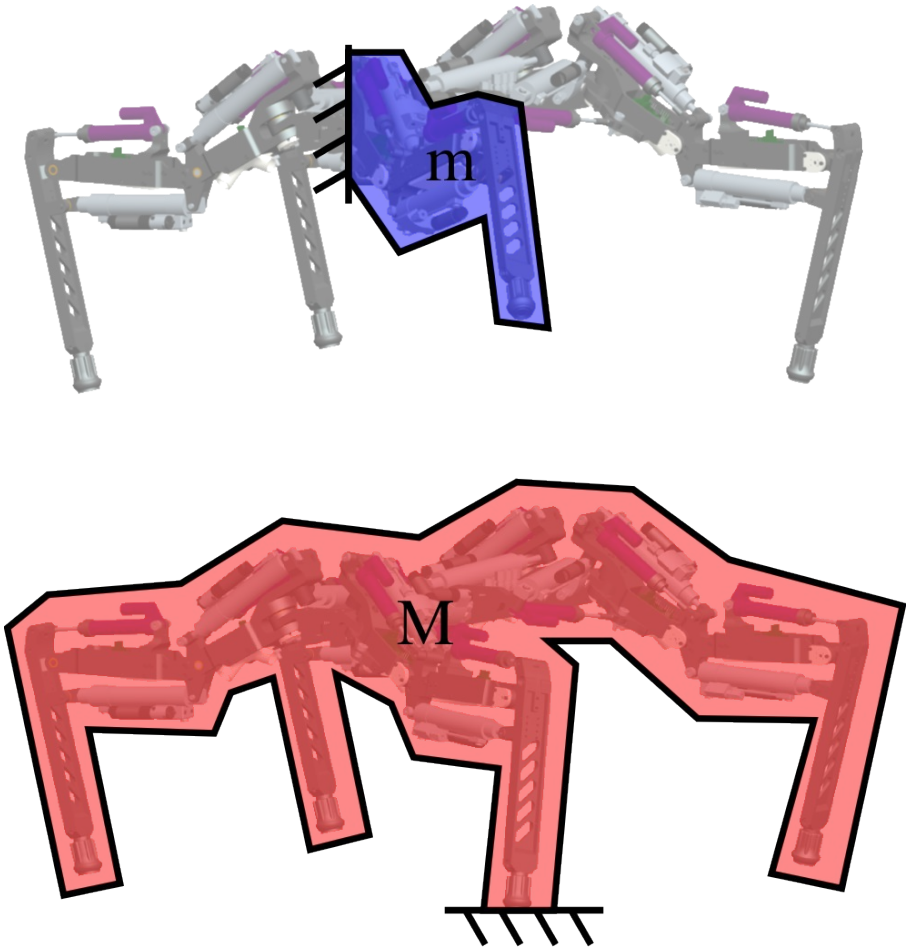

Fig. 39. Illustration of the change in effective inertia when ground contact state changes

This drastic change in plant manifests itself in two types of oscillation when the PVA compensator is used to achieve closed loop position control. When the controllers are tuned for the foot moving in the air (i.e. swing phase), the robot is unable to stand on its feet. The damping imposed by the controller on the joints that is required for stability in the air is insufficient to resist the inertial movements of the robot's body. What results is a full body oscillation of approximately .5 Hz that is never attenuated by the joint controllers.

Therefore, for stance phase motion, the controller gains (especially the velocity and acceleration terms that effectively provide increased damping) must be increased to eliminate this relatively slow full body oscillation. Note that, in a root locus perspective, these changes in gain correspond to both an increase in loop gain as well as a movement in the compensator zeros. However, attempting to use these increased gains on a leg that has no contact with the ground results in a different kind of problem. In this case, high frequency noise in the joint position is amplified by a large factor when the acceleration and velocity measurements are computed from the noisy position signal. When ground contact is present, these high amplitude transients are masked by the slow dynamics of the robot's inertia, but when ground contact is absent, they cause very violent, high frequency oscillations of the robot's joints.

To compensate for the dramatic change in the plant, the idea of a gain scheduler is employed. In a gain scheduler, the parameters of a compensator are discretely varied based on some a priori known variation in the environment (e.g. a linearized model of a nonlinear plant where the linearization is computed for several values throughout the

active region). The actual values that the parameters of the compensator take on are found by tuning the controller for desired performance within each discretized regime of the environment.

In general, some measurements are used to detect when a different regime has been entered. In the present case, however, there is no need to do so because the trajectory defines the change in regime, at least for level ground walking scenarios (which are the sole focus of this effort). That is, the trajectory has a defined portion in which the foot will contact the ground (stance) and a defined portion in which this contact will be lost (swing). Therefore, the gain scheduler is set to change the parameters of the PVA controller when the trajectory changes from stance to swing (and vice versa) and it is assumed that this transition physically happens when it is commanded to. This scheme is sufficient to cause the PVA controller to achieve good and stable position control of the robot's joints throughout the gait cycle.

The normalized travel of Fig. 33 is scaled for a duty cycle of .75 with the actual spatial magnitudes used in the robot's walking experiments then converted into joint motions using the kinematics of Appendix A in Fig. 40. This is still given in normalized time as a percentage of the gait cycle. In the figure, the stance portion of the motion occurs to the left of the dotted vertical line and the swing motion is to the right. The highlighted portion of the gait is that portion where stance phase gains are used while swing phase gains are used elsewhere. The swing phase gains are used beyond the borders of the actual swing phase gain motion to compensate for uncertainty in the time of substrate contact acquisition. That is, using stance phase gains before ground contact occurs is a worse outcome than using swing phase gains after ground contact occurs (due

to the nature of the undesirable oscillations described above). The time in which swing phase gains are used is extended to exploit this fact. The gains used in the walking experiments of Chapter VI are given in Table 6.

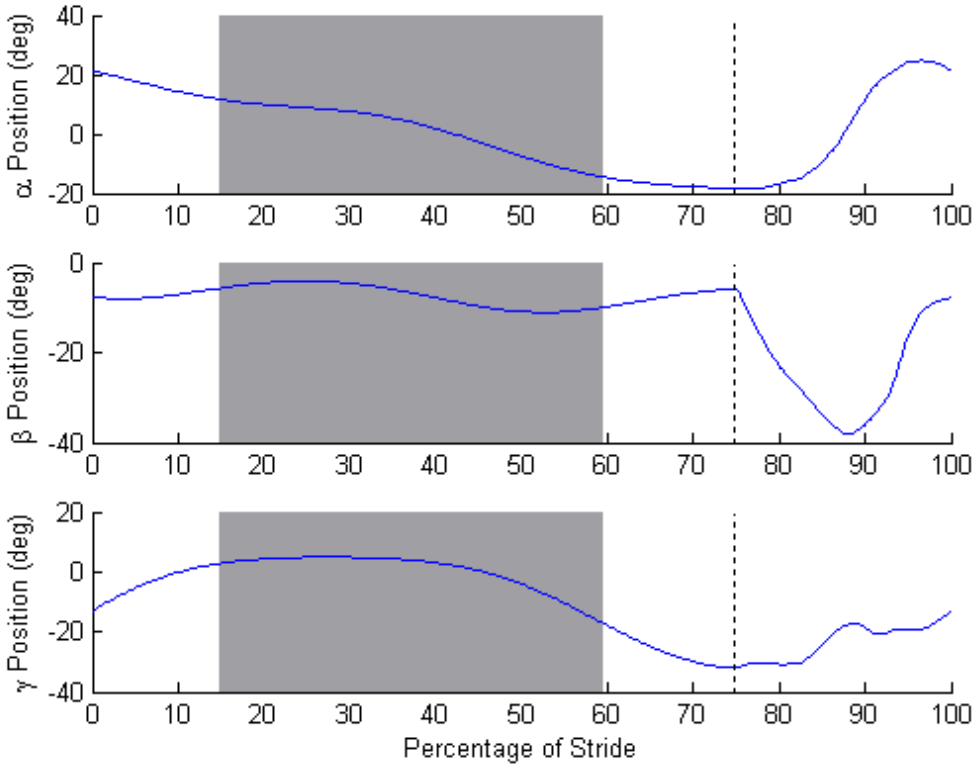

Fig. 40. Joint angular trajectory for a .75 duty cycle motion in normalized time with gain scheduling and swing/stance phase marked

Table 6
PVA Gains Used in Walking
(Gains are in units of valve degrees per robot joint [degree degree/s, degree/s^2])

Gait Phase	Gain Type	θ_1	θ_2	θ_3
Stance	Position	1.87	2.49	2.49
	Velocity	0.198	0.156	0.156
	Acceleration	5.26×10^{-3}	4.67×10^{-3}	4.67×10^{-3}
Swing	Position	2.18	2.18	2.49
	Velocity	93.4×10^{-3}	93.4×10^{-3}	0.125
	Acceleration	1.56×10^{-3}	1.56×10^{-3}	1.56×10^{-3}

CHAPTER IV

MECHANICAL DESIGN

IV.A Motivation to Design Changes

After having gone through the initial development process described in Chapter II and the refinement of control process described in Chapter III, a finalized approach was settled on that addressed a number of the problems observed in the implementation of the prototype robot.

First, the prototype robot utilized commercial, off the shelf valves. While these valves are fast, robust, and simple to deploy, they are not appropriate for the present application because of their size, weight, and lack of support for high temperature and high pressure working fluids, such as the byproducts of a hydrogen peroxide catalytic decomposition as proposed for the present robot. The tethered version of the final design (i.e. the design does not include those components necessary for computation and energy storage to be supplied on board the robot) is shown in Fig. 41 and incorporates customized valves controlled and powered by customized electronics that possess all of the necessary attributes for integration into a small, highly mobile robot.

Fig. 41. Final, as-built design of quadrupedal robot. Shown without fuel tank, batteries, or on-board high level computation.

Second, early prototypes of the robot robot were controlled using an impedance based approach that, in general, requires force or pressure information. The load cells deployed on the prototype robot provided this information but were prone to mechanical failures either due to the application of excessive bending loads that plastically deformed the load cell, thus destroying it, or due to the wires from the load cell becoming snagged on any of the various moving parts of the robot or on some external obstacle and subsequently torn away from the load cell body. Further, the load cells (because of the high number of actuated degrees of freedom that require them) necessitate the inclusion

of a large number of electrical components and connections, thus further reducing the reliability or availability of the overall system. Pressure data were not used because it was not possible to find sufficiently compact sensors that were compatible with hot gases.

Rather than revising the design of the robot or replacing the unacceptable sensors to lessen the likelihood of catastrophic failure, a revised control method, described in Section III.B, was found and integrated into the robot design that permitted the removal of both the impedance approach and its requisite load cells while still achieving acceptable motion of the robot's limbs.

Third, as noted in the introduction to Chapter III, it is advantageous from a reliability standpoint to have as few legs as possible, thereby eliminating as many unique mechanical electronic components (i.e. potential failure points) as possible. Since walkers with legs numbering fewer than four must include some type of balancing considerations (i.e. four legs is the fewest in which statically stable walking is possible), a quadrupedal morphology was decided upon and the mechanical design altered to reflect this new reality.

Finally, the mechanical structure of the robot has been improved over that of Fig. 11 to be more robust, easier to maintain, and to more completely integrate with the pneumatic and electrical systems of the robot, while the overall geometry (i.e., kinematics and basic morphology) of the robot's leg that was proven in the early testing and development phases was maintained. The full set of drawings required to reconstruct the robot are given in Appendix D.

IV.B Leg Design

The initial design called for a six-legged robot [41] with the logic that having two legs beyond the four minimum legs required for a statically stable walker would provide the robot with redundancy, increase the stability of the robot, and provide additional forward motive force. The previous hexapedal robot design (that was never fully realized) featured 18 actuated degrees-of-freedom (DOFs) and a miniature load cell at each DOF. This design allowed for joint-level force control loops and very good walking performance (as demonstrated in the two legged variant of Section II.C), but was extremely complex and prone to failure because of the high number of critical components.

To reduce the complexity of the robot, two fundamental changes to the walking robot's design have been made. First, the robot is now quadrupedal rather than hexapedal. This removal of two legs eliminates six actuated DOFs and increases the overall system reliability significantly due to their absence.

Secondly, the load cells at each actuated DOF were removed because of the frequency at which they failed mechanically. This necessitated the development of a method for low level control of the joint motion without the aid of force information. In this vein, it was discovered (as shown in Section III.B) that a substantial increase in viscous damping was able to dramatically increase the stability margin and disturbance rejection characteristics of a PVA controlled pneumatic actuator. This discovery was incorporated into the design of the robot's legs as shown in the following discussion.

The leg design is guided by observation of the *Carausius morosus* insect, but there is no strict scaling of insect measurements into robot design parameters. Rather, the basic configuration of the leg, including number, placement, and orientation of joints are drawn from insect measurements. Several other noteworthy walking robot projects have also looked to this particular animal for inspiration [4,94,95]. The morphology of the insect as well as that of the present robot are compared in Fig. 42 (partially reprinted from [96]). Note that the robot in this figure is that of [41] and not the final robot, but, as noted, the final robot retains the form and kinematics of the original.

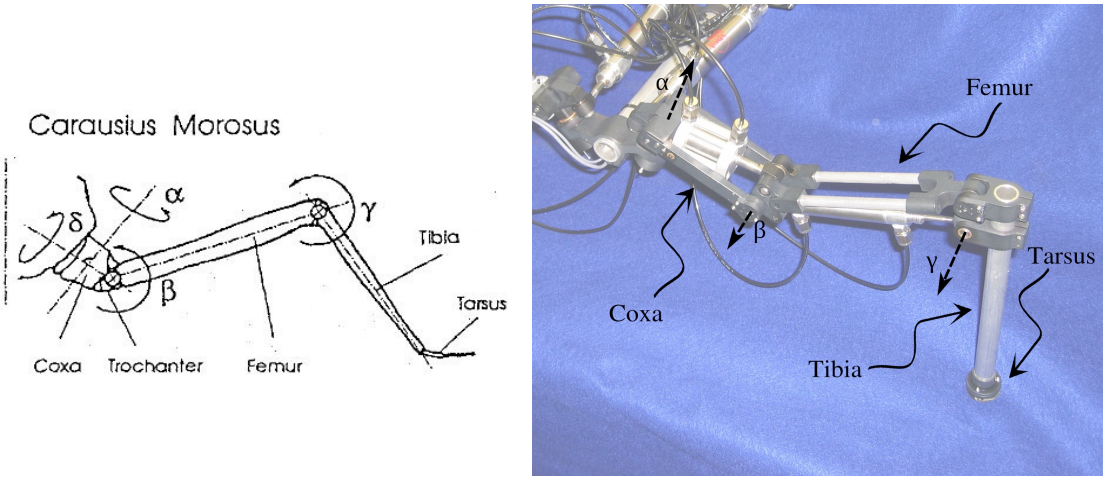

Fig. 42. Morphological comparison of the Carausius morosus insect with the present robot

The salient features of a single leg, are shown in Fig. 43 without the robot's thorax. Note that the incorporation of three DOFs in each leg leads to the robot's potential ability to walk in axial and transverse directions and turn in place as well as any superposition of these three types of motion, although these capabilities are not

investigated in the present work. That is, the robotic manipulator that is a single leg of the robot is holonomic in the sense that its number of degrees of freedom is equal to its number of controlled degrees of freedom. This is significant as some noteworthy robots [1,3] lack the ability to move in a true holonomic sense (i.e. to move from one arbitrary position and orientation in a 2D setting to any other arbitrary position and orientation regardless of path taken).

Each actuated DOF consists of some portion of the robot's structure, a hydraulic damper, a joint angle sensor, and an actuation unit. The actuation unit is a custom servo valve (extensively described in [35] and in Chapter V) mounted onto a standard commercial pneumatic cylinder and electrically connected to a small custom servocontroller. An assembled actuation unit is shown in Fig. 44. The pneumatic actuator drives its joint of the robot in a conventional slider-crank configuration. The servovalve is mounted onto a manifold assembly that is tailored to the specific pneumatic cylinders used in the robot's design. Note that this set of components for each joint is required to implement the PVA controller as above. A stereotypical servovalve assembly is shown in Fig. 45 in an exploded view.

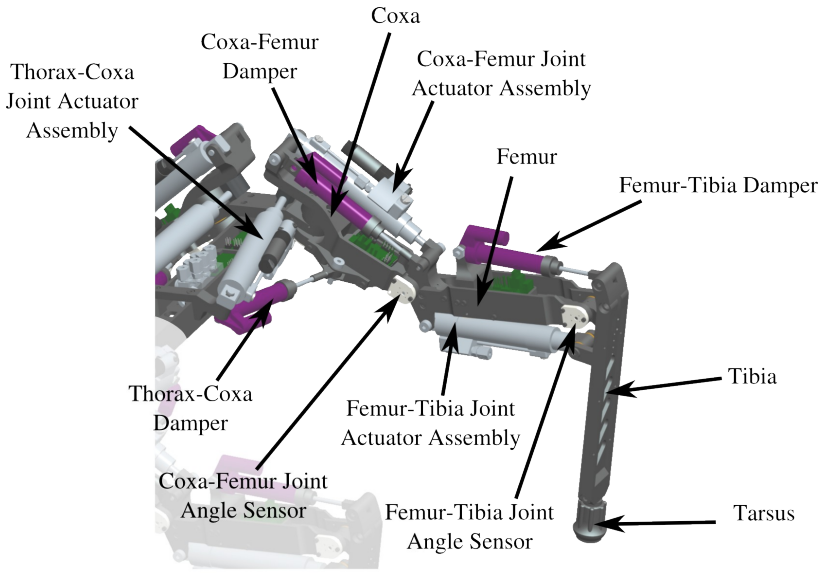

Fig. 43. Design of leg structure and component placement

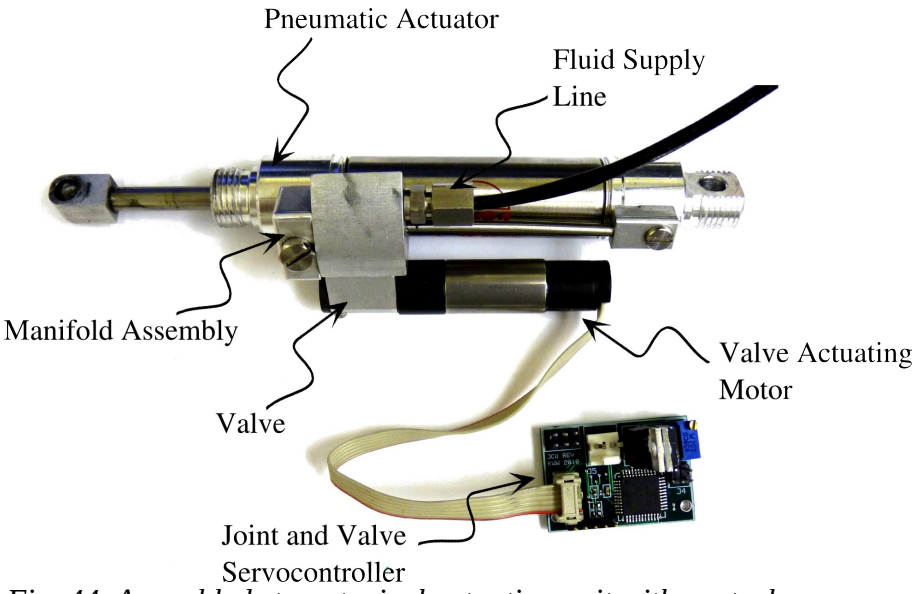

Fig. 44. Assembled stereotypical actuation unit with control electronics

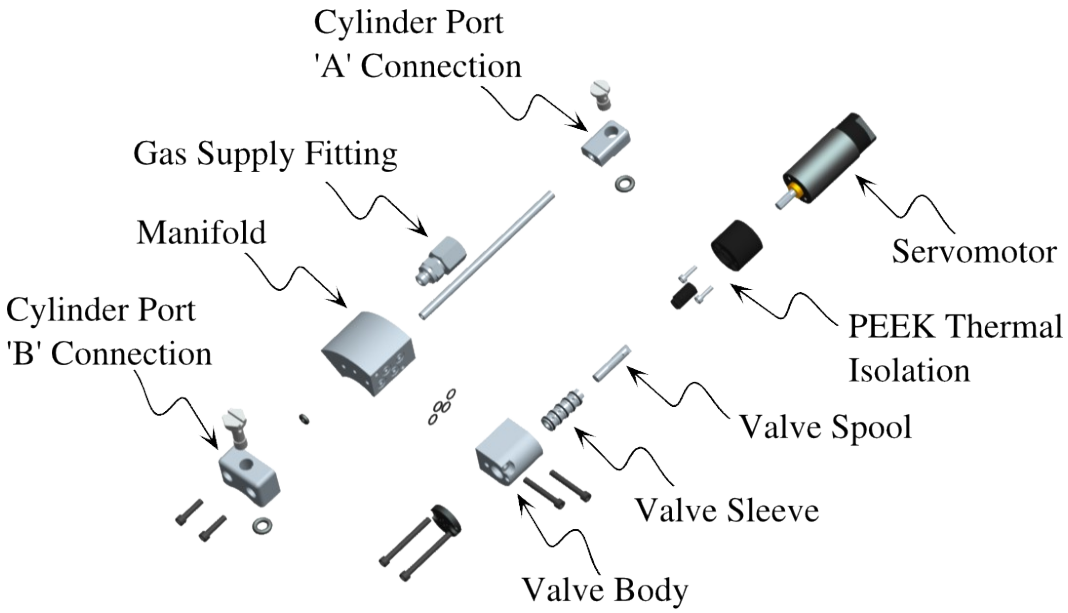

Fig. 45. Exploded view of custom servo valve and manifold assembly.

Actuator selection was made based on the results of a dynamic simulation of the previous, hexapedal robot [40], as well as on iterative testing and reconfiguration with two- and four-legged prototypes [41]. Damping values used in each of the three actuated joints were varied by filling the hydraulic dampers with different weights of oil so that the experimental position tracking performance of the joint was qualitatively acceptable. Measured values of the damping for each joint are given in Table 7.

Table 7
Experimentally Measured Damping Values for Each Joint

Joint	Damping Value Used (N·s/m)
θ_1	1100
θ_2	2400
θ_3	1300

Each link of the robot structure of which the leg is composed has an asymmetric I-beam cross-section. This shape is selected to provide a convenient, mostly enclosed mounting location for the valve control electronics required for each valve. The larger of the two channels created by the asymmetric cross section is sized to accommodate the dimensions of the electronics (Fig. 46). Further, the smaller of the channels created by the I-beam shape are utilized for the routing of wires carrying electrical signals to and from each DOF in the legs.

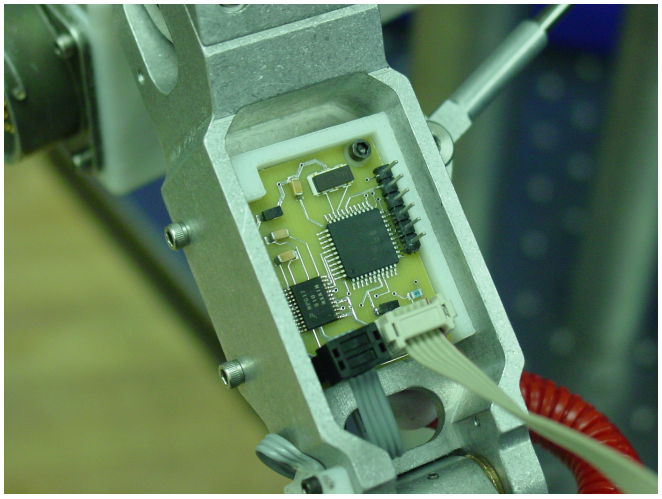

Fig. 46. Asymmetric I-beam structure provides enclosure of servovalve control electronics (coxa-femur actuator and damper removed for visibility)

The kinematic equations of the leg, which are necessary to permit path planning in a Cartesian sense while allowing the PVA controller to work on joint trajectories as well as to aid in the design of the leg by showing the effect of the ranges of each of the joints on the overall leg motion, have been determined and are fully described in

Appendix A. Joint ranges, using the conventions established in Appendix A, are given in Table 8, as are maximum torque values achievable by the actuators of the joints. These torque maxima are given at a gas supply pressure of 2.07 MPa, which is the pressure used in the walking experiments described in Chapter VI.

Table 8
Joint Ranges of Motion and Maximum Torques

Joint	Max Angle Value (degrees)	Min Angle Value (degrees)	Max Torque (N·m)
θ_1	41.25	-38.18	25.48
θ_2	6.36	-48.03	16.46
θ_3	24.22	-28.59	16.85

IV.C Foot switches

The tarsus (i.e., foot) of each leg robot contains a mechanical assembly, shown in Fig. 47, that houses a force sensing resistor (FSR). These FSRs can be used to sense when the robot gains and loses contact with the ground at each foot. Each FSR is mounted using its adhesive backing directly to the foot body, a component that is rigidly connected to the tibia, or most distal leg structural component. As recommended by the manufacturer, a soft rubber disk is used to actuate the foot switch sensor and is adhered to a small aluminum disk. This disk is inserted into a commercially available crutch tip that serves as the ultimate interface between the robot and the substrate and (as is its original design intent) provides significant friction.

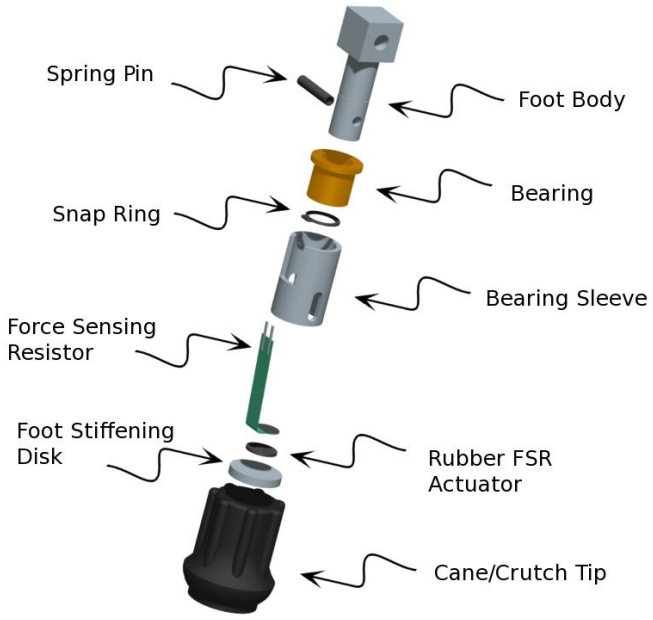

Fig. 47. Assembly housing FSR foot switches

A bearing is press fit into a bearing sleeve and this assembly is allowed to slide over very short distances (< .25 mm) along the shaft of the foot body. The bearing sleeve provides stiffening to the naturally compliant rubber crutch tip to prevent it from buckling, and the permitted sliding motion serves to ensure that the FSR is in the load path of nearly all of the axial force that the environment applies to the robot. The bearing and bearing sleeve are constrained to the foot body by a snap ring in the axial direction and a spring pin that prevents rotation of the bearing sleeve and, by extension, the crutch tip relative to the foot body.

Note that, while the foot switches were mechanically designed and constructed and electrically tested to verify function, they are not electrically connected to the actuator control systems. This description of their design is supplied as an aid to future extensions of this work where foot contact information or possibly leg loading information would be valuable to the choice of locomotive control.

IV.D Thoracic Design

The thorax, or spine, of the quadrupedal robot consists of a monocoque structure along with brackets that allow for attachment of the legs and the thorax-coxa joint actuators. The thorax also supports the manifolds from which all pneumatic actuators of the robot are supplied with working fluid and can support the centralized components required for untethered operation of the robot. This last class of components includes the pneumatic working fluid supply or source, various electronics necessary for the robot to function autonomously, and the battery that provides electrical power to both the servovalves, and these electronics.

The structure of the thorax is a simple slender beam with an asymmetric cross section identical to that used in the structure of the legs. In the thorax, the larger channel accommodates the control electronics for the thorax-coxa servovalves and the smaller channel again serves as a conduit for the routing of electrical wires throughout the robot. The space in the larger channel not occupied by the control electronics is used to house small pneumatic manifolds. These manifolds receive a fluid supply from some pressure source (varying depending on whether the robot is tethered for testing and debugging or

is operating untethered with a local supply from some onboard source). The manifold directly connects this fluid supply to each of the actuation units. The thorax is depicted in Fig. 48.

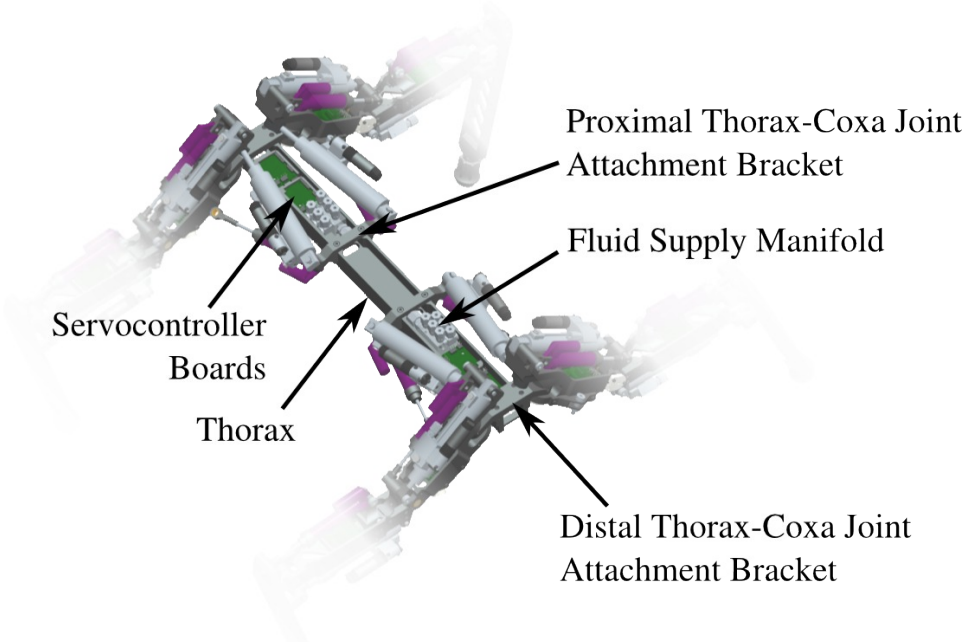

Fig. 48. Thorax portion of robot with important features labeled

The final design of the robot, as constructed, is shown in Fig. 49. The robot, when in a normal standing position, is approximately 46 cm in length, 64 cm wide, and stands 38 cm high. By way of contrast, Boston Dynamics' LittleDog is 34 cm in length, 18 cm wide, and stands 14.3 cm high, according to its user guide. Further, the present robot has a mass of 6.9 kg, while LittleDog is advertised as having a mass of 3 kg.

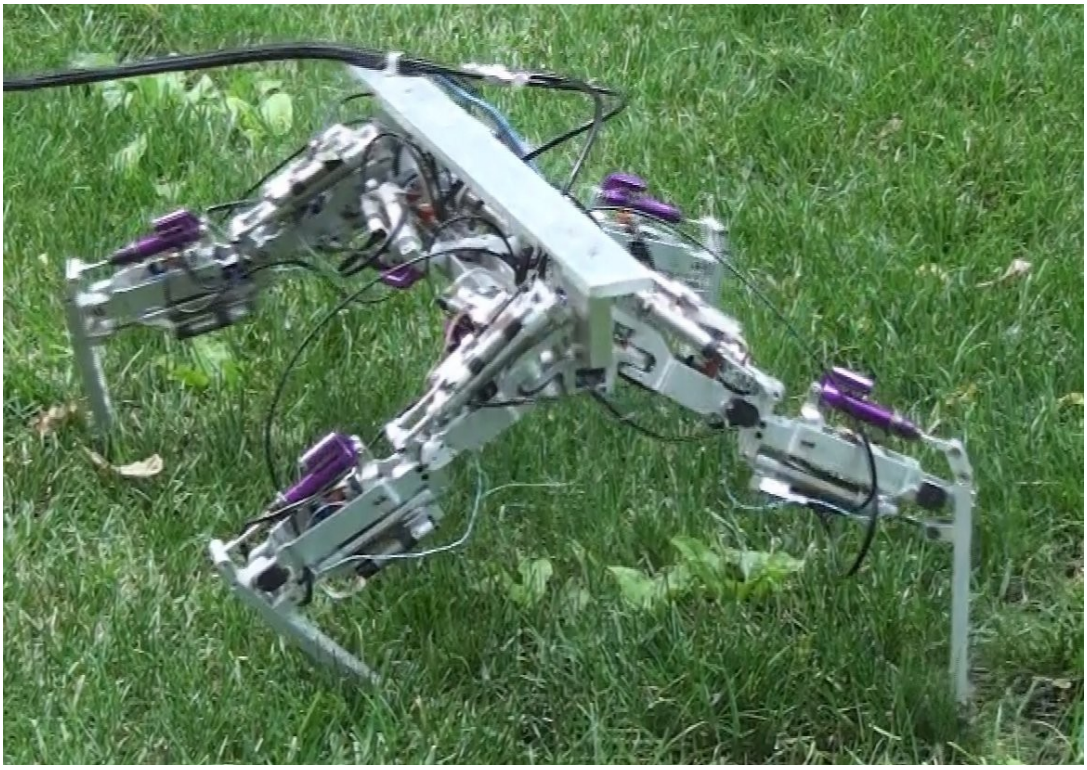

Fig. 49. Final design and construction of the quadrupedal pneumatic robot traversing a grass substrate.

IV.E Achieving Pneumatic Autonomy

In the present work, the pneumatic energy source consists of an offboard compressed Nitrogen gas tank. While compressed gas is not one of the power targets of the device (Section I.C), it is a convenient way to test the untethered operation of the robot. In other words, operation of the robot using compressed gas is much easier than with its defined power targets because the technologies of the power targets are either not yet fully mature (vane motor and free piston compressor) or are difficult to work with (monopropellant direct injection). Further, the use of compressed gas is justified because the control systems should not be affected by the source of the working fluid so long as the pressure and flow rate provided by each of the fluid sources are consistent. Note that,

while a cold compressed gas is used, the preceding design studies have ensured that all components of the system are usable with high temperature, high pressure fluid sources (such as the byproducts of catalytic hydrogen peroxide decomposition). That is, nothing in the physical and control designs precludes the use of such sources in the future.

CHAPTER V

ACTUATOR AND ELECTRICAL DESIGN

V.A Overview and Motivation

The power delivery and control apparatus for the robot is such that the most basic building-block component in the overall system is an individual valve. That is, neither a pneumatic actuator, nor a joint or leg level system is directly controllable by a computer. Instead, the output of the actuator (and, by extension, the higher level systems which build upon the pneumatic actuator) is directly dependent upon the action of its valve.

The valves used are custom, 4/3 proportional rotary valves and are actuated by use of a simple, DC motor. The position control of such a motor is extremely simple and has been thoroughly studied. However, because of the manner in which the valve has heretofore been employed, the physical manifestation of the control logic for this motor must be entirely rethought.

Again, because the valve used is truly the most fundamental unit in the entire robot's design, it is imperative that its characteristics be well understood. This need is compounded by the reformulation of the control circuitry. Because of these two factors, an effort was made to characterize the pneumatic aspects of the valve, as well as the electrical power requirements of the valve while under the authority of the newly designed control apparatus.

Finally, the eventual need to have an untethered system for the most versatile performance of the robot as possible makes its own demands upon the electrical system of the robot. These demands manifest themselves in nearly every aspect of the robot's electronics and are dealt with in as neat a fashion as possible.

V.B Embedded Controllers

During the development phases and tethered walking experiments, the motor that drives the valve is normally controlled and supplied with electrical power by a small electronics board, measuring 2.7 cm by 3.8 cm (Fig. 50). The development and design of this servocontroller is fully explored in the following sections.

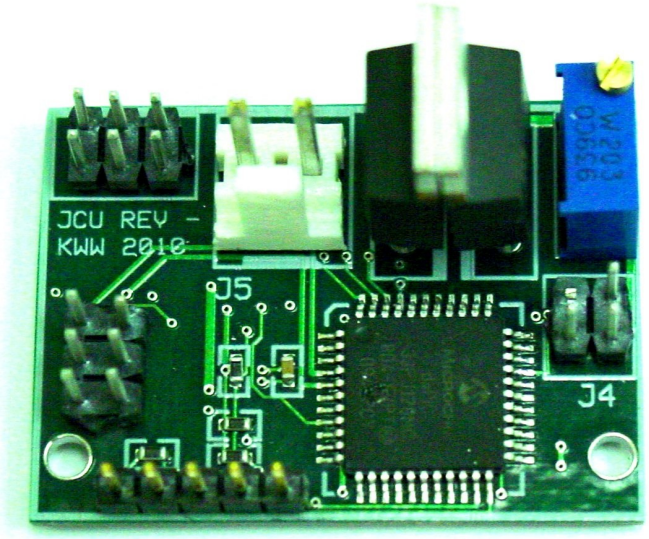

Fig. 50. Valve servocontroller electronics

V.B.1 Motivation and IC Selection for Embedded Controller

The valve itself is extensively described in [35,63] and was previously controlled using a Matlab Real Time Windows Target model running on a PC that required a data acquisition card with a quadrature encoder input for each valve that was to be operated. While this method was robust and easy to deploy and debug, previous projects [35] required multiple computers to support high degree-of-freedom devices. The multiple PC arrangement was only possible in these projects because of the decoupled nature of the operation of the respective devices. This arrangement is not appropriate for the quadrupedal robot of this work as the several actuated DOFs are required to operate in unison with one another for reasonable walking to be achieved. Further, it was not possible to find a set of data acquisition cards limited in number to the typical number of PCI slots available on a PC that would have sufficient quadrature encoder inputs (for sensing valve position), analog inputs (for sensing joint angle position, etc.), and analog outputs (for control of the several actuators) and would be supported with minimal software development effort in Matlab Real Time Workshop.

Experimentation with various possibly appropriate computing platforms (such as PC/104 and Matlab's xPC Target) for untethered operation of the robot was conducted. During this exploration, it was found that the extensive use of analog signals traveling along conductors of moderate length (such as the references to the embedded valve servocontrollers and the joint angular positions), the limited ability to communicate bidirectionally with the servocontrollers, as well as the presence of power electronics used to supply both the valve motors and a centralized computing platform with power made the system highly unreliable. Specifically, with regard to the limited

communications channels with the servocontrollers, early prototype joint controller boards were unable to relay valve tracking data to an operator or debugger and could not receive commands beyond a desired valve position.

Because of these limitations, an effort was undertaken to develop an embedded system to contain all of the necessary hardware and software to fully control both a joint's position and the valve's position that is the output of the joint controller. Therefore, the proposed embedded system must sport a number of features to successfully perform these functions, First, it must sense and maintain an accurate measure of the valve position from the incremental quadrature encoder that is integrated into the valve's motor actuator. It must also sense its joint's position from a potentiometer and be capable of outputting bidirectional power of sufficient magnitude to cause stable and relatively high bandwidth control of the valve to the small DC motor that drives the valve.

Further, because the valve position sensor is an incremental encoder, its absolute position must somehow be established. A hard stop in the valve design is used in this capacity by requiring that, at start up, the controller force the valve to follow a predefined trajectory that uses the hard stop's a priori known position to determine the absolute position of the valve spool.

Also, in early prototypes of the embedded servocontroller system, the desired joint position was communicated to the controller through an analog voltage signal. Because this afforded a very limited amount of information that could be conveyed to and from the controller and because the accuracy of these transmitted signals was quite degraded by noise, it was determined that a digital communications protocol was needed.

The use of a bidirectional digital communications channel allows for debugging operational modes to be set and for both valve and joint position tracking data to be displayed to the developer.

Finally, the embedded servocontroller must have sufficient computational power to execute a PD controller (identical to that used by the proven Matlab controller) for valve control as well as a PVA controller for joint control, as described above, at a sufficient sampling rate for closed loop control. For reference, in the PC-controlled experiments, a sampling rate of 1 kHz was used. The method used in the embedded servocontrollers for realizing the continuous time controllers in a digital setting is fully described in Appendix C.

These requirements drove the selection of a handful of ICs which compose the embedded controller. The first IC is a Microchip dsPIC33F128GP804, a microcontroller that features multiple on-board analog inputs, an on-board quadrature encoder input, the capability of executing 40 million instructions per second (MIPS), several on-board digital I/O ports, a small number of PWM outputs, and compatibility with CAN-bus, SPI, and I^2C digital communications protocols, as well as many features not required for the servocontroller at hand. Further, the PIC series of microcontrollers has a significant online support community and is widely used among electronics hobbyists.

The second IC used is a Freescale 17510 H-Bridge that can output 1.2 A continuously and 3.8 A peak at a maximum voltage of 15 V, can operate at PWM frequencies of up to 200 kHz, and can operate in forward, reverse, brake, and high impedance modes. Additional ICs on the board include a CAN-bus line driver, a quad

op-amp for the analog circuitry associated with joint position sensing, and a pair of voltage regulators that provide power to the ICs on the board. The schematic of the joint control unit (JCU) electronics is shown in Fig. 51.

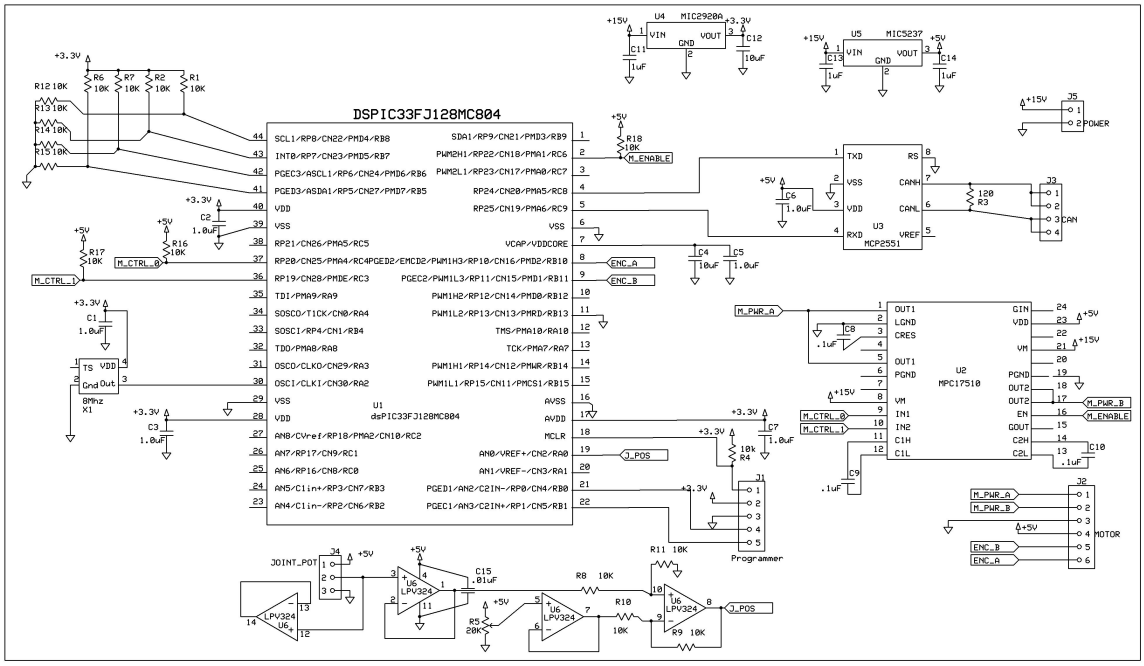

Fig. 51. Schematic of JCU electronics

Note that, because the PVA controllers have been implemented in the distributed JCUs (rather than in a centralized PC as was originally intended), the only task that must be carried out by a central processor is the generation of joint trajectories. In the overall design, then, a node (e.g. a PC or a second microcontroller board design) on the communications bus sends out joint reference commands to each of the 12 JCUs. The use of a single emitter of joint commands ensures that all of the legs remain in sync (and do not drift because the distributed processors' clocks are not precisely matched to each

other). The command emitting node can also carry out non-crucial tasks such as collecting tracking data from the JCUs and presenting them to the user, notifying a JCU that it should re-calibrate its valve after a failure, and various other functions.

The block diagram of the control elements that are programmed into the JCU's firmware are depicted in Fig. 52.

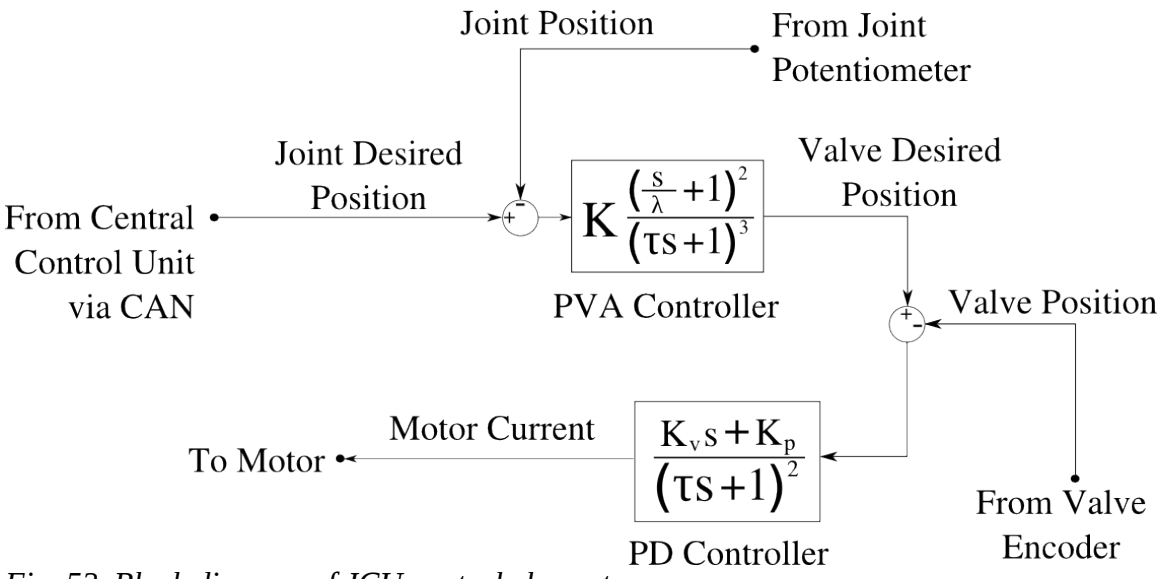

Fig. 52. Block diagram of JCU control elements

V.B.2 Joint Controller Digital Communications Protocol

CAN-bus is a mature, two-wire digital communications bus that was originally conceived for the automobile industry and is widely deployed in this capacity. This mode of digital communications over any of the other options supported by the dsPIC microcontroller because of the ease of adding additional nodes on the network (e.g. useful sensors not currently present or not used in the current robot such as

accelerometers and foot switches), a high, 1 Mbit/s bandwidth, the need for only two wires to access every node on the network, and because it allows experience within the research group to be effectively leveraged.

By using a digital communications channel in the present application (rather than using analog signals, which is perhaps more common in mechatronic systems because of ease of deployment), a wealth of additional data can be communicated on the network (not to mention the gain in transmission accuracy relative to analog). Because of this flexibility, the operator of the robot can exert finer control over how the valves and joints function. For example, power to the motors can be either supplied or withheld on command (e.g. for troubleshooting and development) and the gains of both the joint and valve controllers can be tuned without the need for reprogramming the microcontroller.

However, the use of digital signals is complicated by the need for a description of a communications protocol, i.e. a CAN-bus message specification. That is, the CAN-bus specification mandates that a message must include certain features (e.g. an identifier frame, a data frame, a CRC hash, etc.), but makes no prescriptions about what the content of some portions of the message should be.

A portion of the standard CAN-bus message format is an 11-bit identifier. CAN-bus hardware embodiments are able to filter on a portion of, or the entirety of this 11-bit identifier. That is, all devices on a CAN-bus receive all messages that are transmitted over the bus, because of the manner in which all of the device son the CAN-bus are connected, as shown in Fig. 53. To ensure that a device only acts upon messages that are intended for it and reduce computational load, the filter module of a CAN-bus enabled device is programmed to discard any message whose identifier does not match one of the

user-defined forms. The forms that the identifier may take are not defined by the CAN specification, but are instead left to the designer of a particular system. Therefore, some portion of the identifier can be used to not only prescribe the device that should receive and interpret the message, but also to specify what the contents of the message may be.

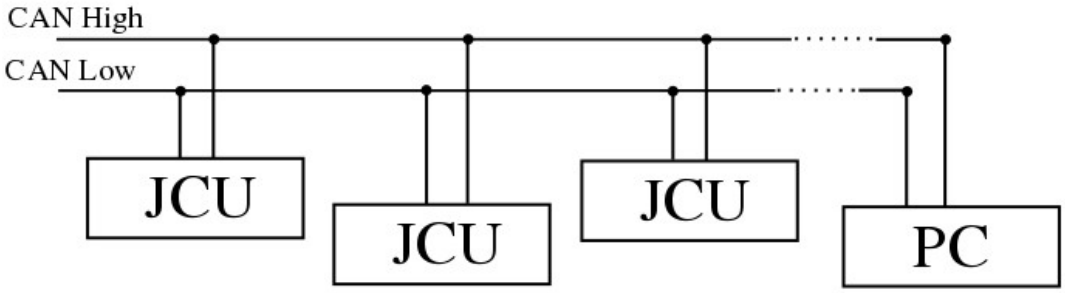

Fig. 53. CAN-bus connection layout

This is done in the present CAN implementation by defining the 11-bit identifier as in Fig. 54. As shown in the figure, the first 6 bits of the identifier fully describe both the sender and the intended recipient of the message (since two JCUs currently have no need to communicate with each another). For example, one bit indicates whether the message is destined for a JCU or the coordinating PC, one bit indicates that the target JCU is located on a fore (not aft) leg, etc.

The last 4 bits of the identifier are used to specify what sort of message is being transmitted. Because of this new flexibility, the operator of the robot can exert finer control over how the valves and joints function. For example, power to the motors can be either supplied or withheld on command and the gains of both the joint and valve controllers can be tuned without the need for reprogramming the microcontroller.

Note that, because one bit remains unused in the defined protocol and because five possible message types remain used, the protocol is highly extensible to allow for additional node types (e.g. the sensor nodes alluded to earlier) as well as other data not currently shared on the robot's data network.

Standard Identifier

Bit #	10	9	8	7	6	5	4	3	2	1	0
	From/To PC	Leg ID		Broadcast	Joint ID			Message Type Identifier			

Bit #	Bit Name	State	Description
ID {10}	From/To	0	Message is from the PC to the JCUs
		1	Message is from a JCU to the PC
ID {9:8}	Leg ID	11	Sender/Recipient is a Left Front Joint
		10	Sender/Recipient is a Front Right Joint
		01	Sender/Recipient is a Left Rear Joint
		00	Sender/Recipient is a Right Rear Joint
ID {7}	Broadcast	1	Message is directed to all joints on the leg specified in the Leg ID
		0	Message is directed to the joint specified in the Leg ID and Joint ID
ID {6:5}	Joint ID	11	Reserved
		10	Sender/Recipient is a Gamma Joint
		01	Sender/Recipient is a Beta Joint
		00	Sender/Recipient is an Alpha Joint
ID {4}		-	Reserved
ID{3:0}	Message Type	0000	Set Desired Joint Position
		0001	Set Joint Control Gains (1/4)
		0010	Set Joint Control Gains (2/4)
		0011	Set Joint Control Gains (3/4)
		0100	Set Joint Control Gains (4/4)
		0101	Set Valve Control Gains (1/2)
		0110	Set Valve Control Gains (2/2)
		0111	Set Operating Modes
		1000	Set Desired Valve Position
		1001	Set Valve Zero Location Relative to Hard Stop
		1010	-
		1011	-
		1100	-
		1101	-
		1110	-
		1111	Send Tracking Data

Fig. 54. JCU CAN-bus identifier specification

The balance of the standardized CAN message that concerns this project is the data frame. This is an 8-byte segment of the message that contains the payload, or the actual content of, the message. For the purposes of this project, the contents of the data frame can vary based on the type of message. Fig. 55 describes the contents of the data frame for each message type defined in Fig. 54. Note that, in Fig. 55, 8-bit (1 byte) values are unsigned integers, 16-bit (2 byte) values are signed integers, and 32-bit (4 byte) values are of single precision floating point data type.

				Data Frame							
Bit #	**Bit Name**	**State**	**Description**	**Byte 0**	**Byte 1**	**Byte 2**	**Byte 3**	**Byte 4**	**Byte 5**	**Byte 6**	**Byte 7**
ID{3:0}	**Message Type**	0000	Set Desired Joint Position	Alpha Desired		Beta Desired		Gamma Desired		DATA REQ	
		0001	Set Joint Control Gains (1/4)	PVA K (e0)				PVA K (e1)			
		0010	Set Joint Control Gains (2/4)	PVA K (e2)				PVA K (e3)			
		0011	Set Joint Control Gains (3/4)	PVA K (u1)				PVA K (u2)			
		0100	Set Joint Control Gains (4/4)	PVA K (u3)							
		0101	Set Valve Control Gains (1/2)	PD K (e0)				PD K (e1)			
		0110	Set Valve Control Gains (2/2)	PD K (u1)							
		0111	Set Operating Modes	PWR_EN	RESET	DATA REQ		CTRL MOD	VALVE REV	JOINT REV	
		1000	Set Desired Valve Position	Alpha Valve Desired		Beta Valve Desired		Gamma Valve Desired		DATA REQ	
		1001	Set Valve Zero	Valve Zero Angle							
		1010	-								
		1011	-								
		1100	-								
		1101	-								
		1110	-								
		1111	Send Tracking Data	Joint Desired Position		Joint Actual Position		Valve Desired Position		Valve Actual Position	

PVA K* and PD K* are the gains used on the terms in the digital PVA and PD controllers

Value	**Description**
PWR_EN	Motor Power On (PWR_EN = 1), Off (PWR_EN = 0)
RESET	JCU executes valve zeroing routine (RESET = 1)
DATA REQ	JCU responds to message by sending tracking data to PC (DATA REQ = 1)
CTRL_MOD	JCU uses CAN-bus supplied valve desired position (CTRL_MOD = 1), uses valve reference computed from joint controller (CTRL_MOD = 0)
VALVE REV	Valve reference command is multiplied by -1 (VALVE REV = 1), 1 (VALVE REV = 0) before use in digital controller
JOINT REV	Joint measured position is multiplied by -1 (JOINT REV = 1), 1 (JOINT REV = 0) before use in digital controller

Fig. 55. JCU CAN-bus data frame specification

With the JCU developed as described, the robot can trivially be made electrical autonomous in a few different ways. In one scenario, a commercially available wireless CAN-bus bridge is deployed with one node affixed to the robot and the other located near to the PC. The bridge is such that neither the PC nor the JCUs is aware that the bus is abnormal. Because all control is performed on-board the robot and only joint reference

commands are supplied from the PC, a breakdown in wireless communications or in the normal operation of the PC will cause the robot to merely hold its last commanded position. Only a battery need be added to the robot so that electrical power for the JCUs, valve motors, and the bridge is not supplied through a tether. Alternatively, an onboard trajectory source can be implemented as another MCU node on the CANbus, as previously described.

V.C Valves

V.C.1 Description of Valve

The valve used in each actuated DOF of the quadrupedal robot is a custom, miniature, proportional, 4/3 rotary valve. The valve has an active mechanical range of ±45º, and was originally driven by a Faulhaber 1316 motor with integrated shaft encoder position sensing and a custom built, two stage, cable-capstan transmission with a total reduction ratio of 9:1. The cable used is a PEEK monofilament, and the capstan components and the transmission housing are all made of PEEK as well. An exploded model of the valve with motor and transmission is shown in Fig. 56, and the assembled valve is shown in Fig. 57. The valve itself is approximately 6 mm in diameter and 17 mm in length, but lengthens to approximately 73 mm when assembled with the servomotor.

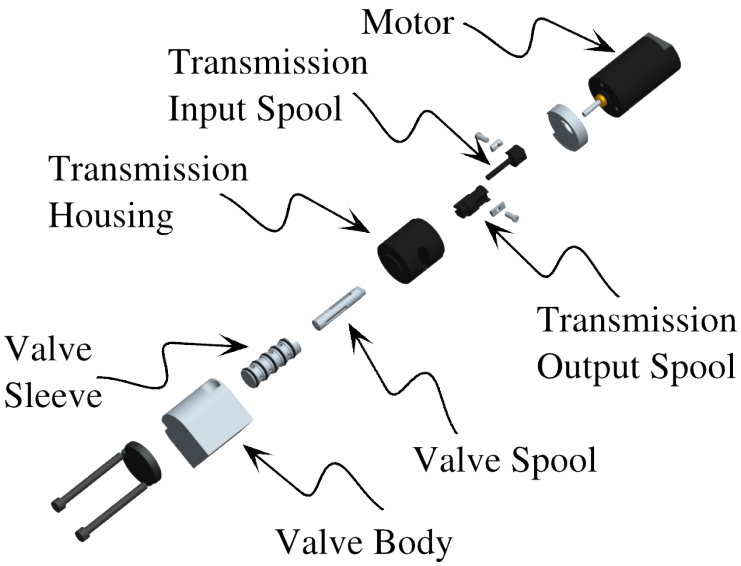

Fig. 56. Exploded view of valve and transmission

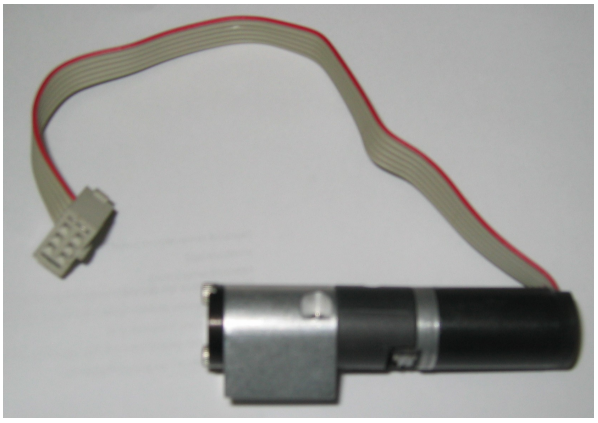

Fig. 57. Assembled valve

V.C.2 Characterization

Although previous work [63] characterized the performance of the valve, it was desired to verify that the embedded controller (Section V.B) developed for this specific application did not affect the documented performance and that the performance was repeatable across multiple permutations of the valve/controller pairing. Further, it was

desired to characterize the power consumption of the valve when driven by the embedded control electronics for the purpose of selecting a battery for untethered operation of the robot. The measurements to be taken were power consumption of the motor alone and of the embedded system alone when the reference input was sinusoidal, as well as the quasistatic flow rate through the valve as a function of the valve angle. Other desirable information to be measured was the valve's performance with regard to both repeatability and hysteresis.

V.C.2.a Methodology

For the purposes of the testing described hereafter, only one side of the valve was used. The mechanical range of the valve used in the test was 0º (both ports fully closed) to 45º (port A to supply fully open, port B to exhaust fully open). The working fluid was compressed, medical grade nitrogen regulated to a pressure of 92±5 psi (approximately 6 bar). The pneumatic system is shown in Fig. 58.

The actual experimental setup is shown in Fig. 60. A U.S. quarter is shown in the figure for scale.

Two types of tests on the valves were carried out. In the first set of tests, the valve was commanded to hold a given position and the flow rate out of the valve was measured. This process was carried out at twenty-five evenly spaced positions on the valve angular range 0-45º, inclusive. Measurements were taken for increasing flow rate (0º to 45º) and for decreasing flow rate (45º to 0º). Three trials each of increasing and

decreasing flow rates were performed. Volumetric flow rate was measured using a Festo SFE1-LF-F200-HQ8-P2U-M12 flow meter, and data was collected through manual reading of the flow meter's integrated LED screen.

In the second set of tests, the valve was commanded to track a sinusoidal reference trajectory at frequencies of 1 and 2.5 Hz at maximum valve deflection (22.5º amplitude) with the same pressure as above applied to the valve. Power consumption for both the motor and electronics were independently measured using the circuit shown in Fig. 59. In this figure, the variable resistor was used to manually specify the command during flow rate measurement and was switched to a computer generated profile for power measurement.

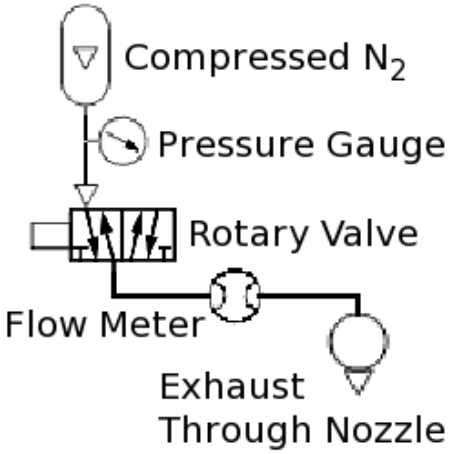

Fig. 58. Pneumatic system for flow rate and valve power consumption measurement

Voltage and current data was recorded at a sampling rate of 1 kHz over a period of 20 seconds in each trial. These quantities were multiplied together to arrive at power consumption. The data acquisition system was a Matlab/Simulink Real Time Workshop model running on a Pentium 4 computer and using a Sensoray 626 analog I/O board. The manner in which the reference command to the valve control electronics was supplied by the computer system as well as the measurement points to which the computer were connected are as shown in Fig. 59.

The results of these tests are given in Section V.C.2.b.

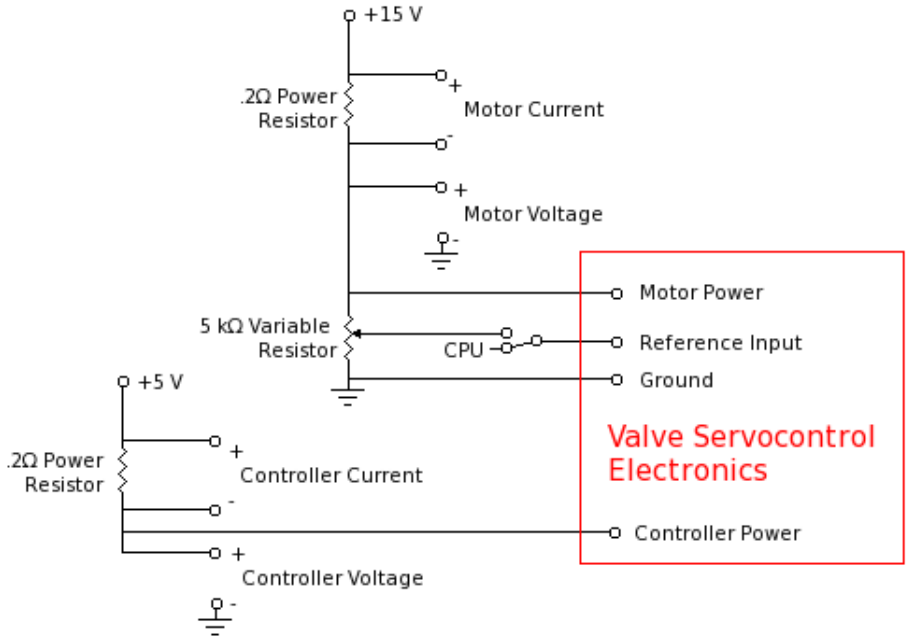

Fig. 59. Circuit diagram for valve control and power measurement

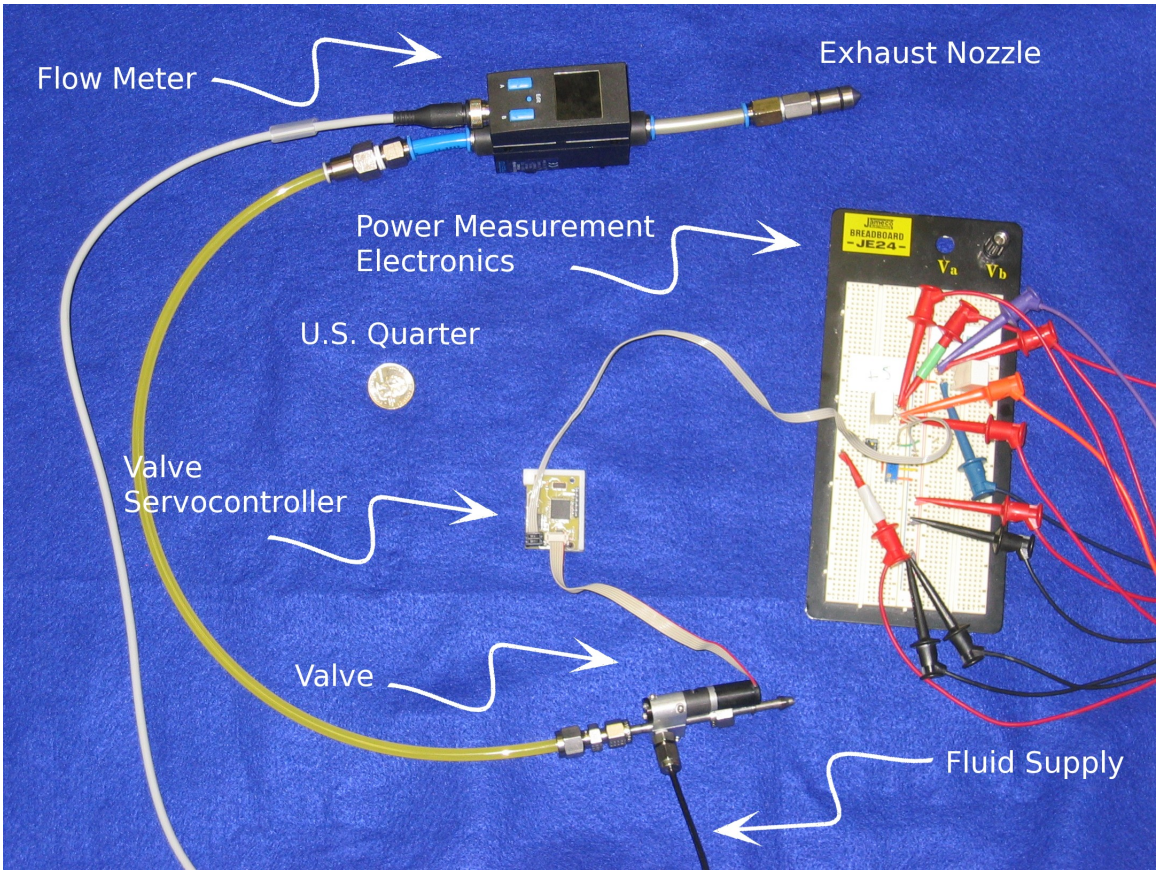

Fig. 60. Experimental setup for measurement of desired quantities

V.C.2.b Results

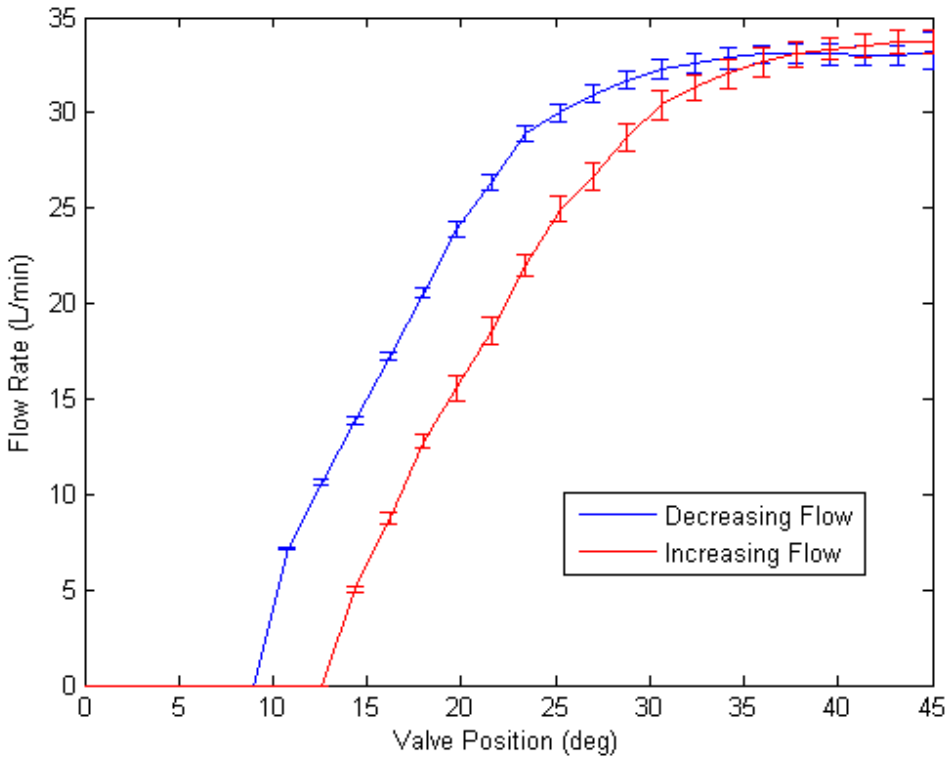

Fig. 61. Flow rate as function of commanded position for increasing and decreasing flow

Input commands were within ±.09º of nominal value and measured flow rates were within ±.1 L/min of the values recorded. Error bars in Fig. 61 denote the range of measurements taken over the three trials performed.

Table 9
Time Averaged Power Consumption

Input Frequency (Hz)	Motor Power (W)	Total Power (W)
1	1.500	1.730
2.5	1.631	1.871

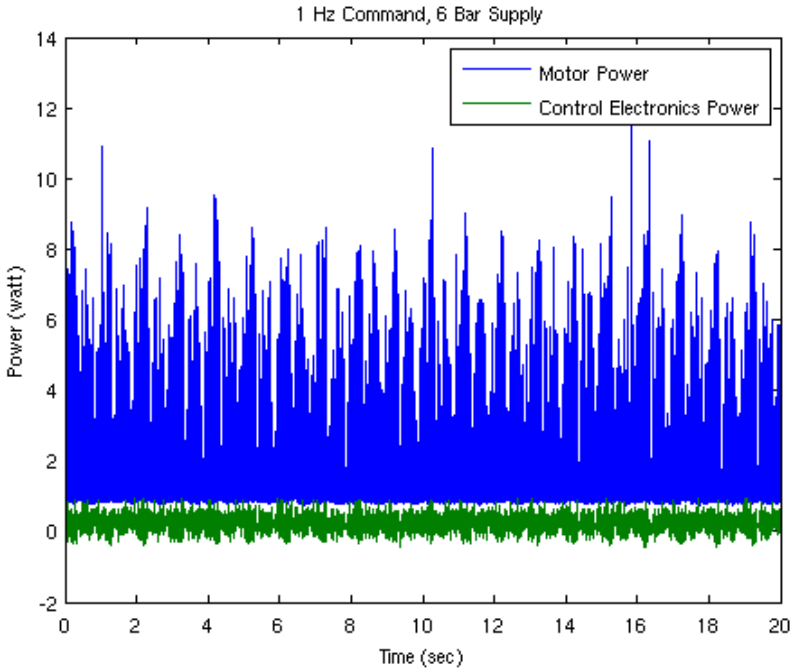

Fig. 62. Power consumption time history for a 1 Hz sinusoidal input

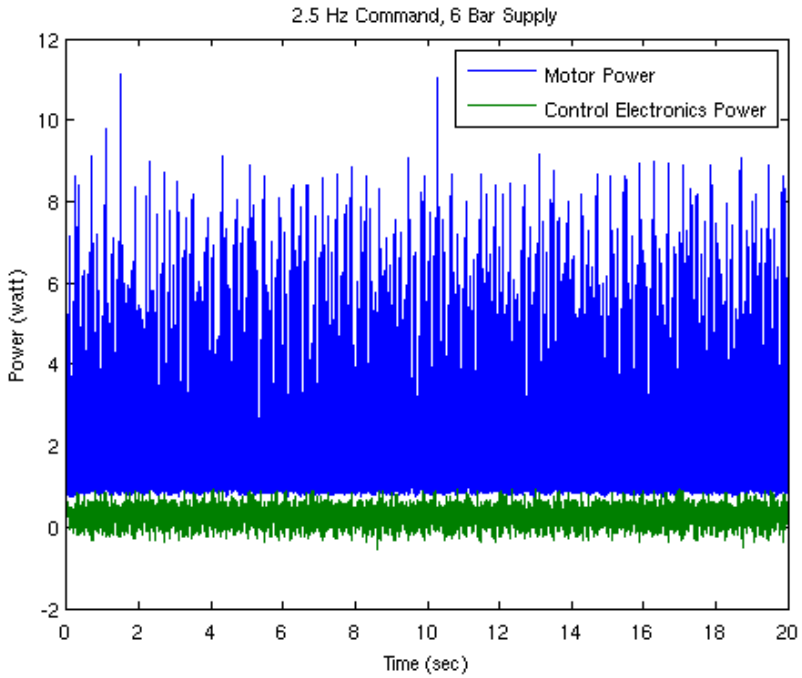

Fig. 63. Power consumption time history for a 2.5 Hz sinusoidal input

V.C.2.c Discussion and Conclusions

During the tests to measure flow rate through the valve, it was observed that, although the flow meter reported no flow when the embedded controller was commanded to position the valve in the range of 0 to 9 degrees, there was audible air flow through the exhaust nozzle. This is without a doubt due to the range of the flow meter used, which is 10 to 200 L/min (i.e., flow rates between 0 and 10 L/min are not measurable using the sensor). Previous testing of this valve under other pressure conditions and with other flow meters has shown that the flow asymptotically approaches no flow as the valve position is brought to 0° (fully closed).

Further, while the flow data exhibits some significant hysteresis, it is worth noting that it is very likely that this effect is largely due to the compliance of the gearhead. As noted in Section V.C.1, the gearhead used is principally composed of a PEEK monofilament, which has some intrinsic compliance. This compliance, coupled with the static friction present in the valve, especially when pressurized, gives rise to the hysteresis effects in the common Maxwell slip model. The hysteresis is estimated to be 26% of the maximum flow rate through the valve, accounting for the lower measuring limit of the flow meter as above, and is believed to be strongly due to the polymer cable-capstan transmission. This transmission is present to isolate the valve actuator from high temperatures due to the high temperature working fluid required in the application for which this valve was originally designed.

Further, it should be noted that the although the supply pressure to the valve was regulated to 6 bar, the actual supply pressure was observed to fluctuate during the course of the test procedure up to a maximum of 7 bar. This appears to be a large factor in the

seemingly poor repeatability of the flow rate measurements. When this was noticed, the regulated pressure was brought back to 6 bar. Therefore, a better sense of repeatability can be gained by comparing the first and third decreasing flow rate measurement sets, in which the supply pressures were most nearly equal to 6 bar (and to each other). These are shown in Fig. 64. In this figure, the measured flow rates are much closer to each other than the spread shown in Fig. 61 and differ from each other by less than 3% throughout the entire measured range of the valve.

Next, as there was some concern that the observed flow rate through the valve was lower than anticipated, a number of steps were taken to verify that the maximum output flow observed (34.7 L/min) was, in fact, accurate. First, the pressure gauge was verified to be regulating the supply pressure at 6 bar. The gauge used (ACSI 1200-0300) does not support metric units, but the measured pressure was verified to be approximately 87 psi (6 bar). Next, the valve was removed from the experimental setup shown in Fig. 60. That is, the nozzle was connected directly to the pressure supply through the flow meter. In this configuration, the air flow was limited by the nozzle to 110 L/min. Therefore, neither the nozzle nor the flow meter were the limiter in the maximum flow observed. Finally, to eliminate the possibility that the servocontroller used to position the valve may have been faulty, the valve was replaced into the experimental setup, but the valve actuator was removed. The valve was then manually turned through a full 360º of rotation (4 cycles through its active range). The flow meter indicated a maximum flow of 35.0 L/min, or approximately equal to the maximum flow found during the course of the testing. It seems clear that the measured flows are accurate and that the valve is the most significant limiter of flow in this pneumatic system.

Finally, a linear range of the valve was estimated to exist between the valve positions 9º and 25.2º for the decreasing case and between 12.6º and 28.8º for the increasing case. A linear best fit curve was applied to these regions and gave a linear flow coefficient of approximately 1.7 L/min per degree of valve position. The linear best fit is superimposed onto the data of Fig. 61 in Fig. 65.

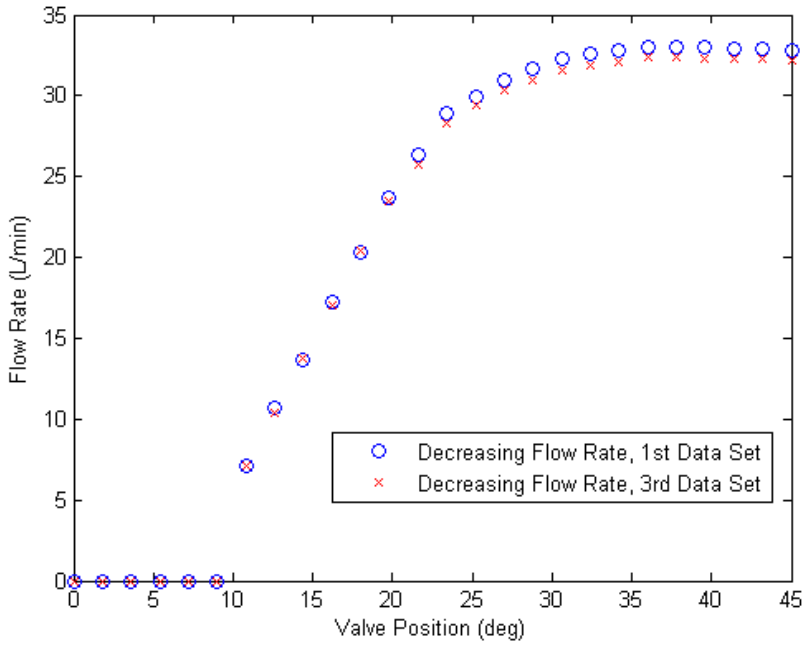

Fig. 64. Repeatabilty of measurements

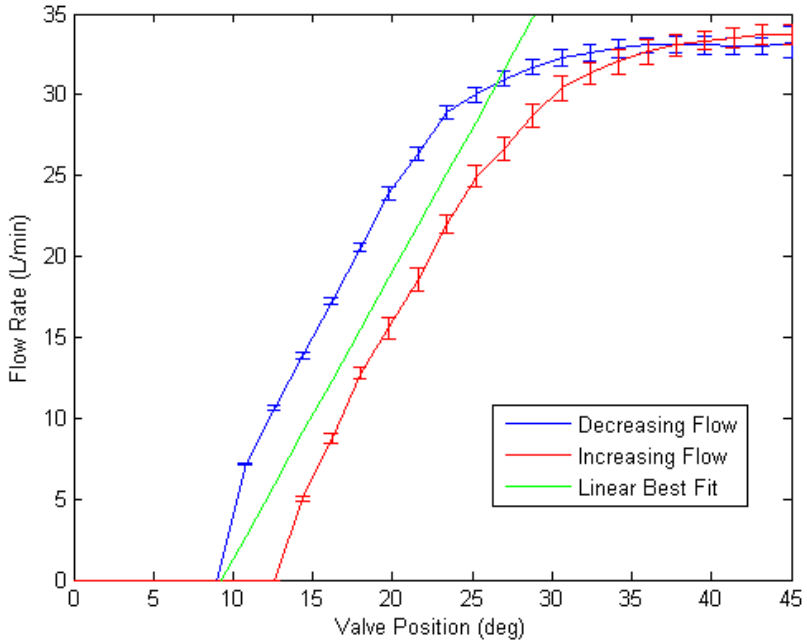

Fig. 65. Linearity of valve

V.C.3 Improvements to the Valve

Based on the flow and power measurements taken, it was determined that the exceptional amount of observed hysteresis needed to be addressed. As noted above, the presence of non-trivial compliance in the transmission coupled with the Coulomb friction that is commonly observed in pressurized valves leads to a phenomenon described by the so-called Maxwell slip model.

In the Maxwell slip model, a system whose input is a position is modified to incorporate the observed behavior by inserting an idealized spring element and including a Coulomb friction element.

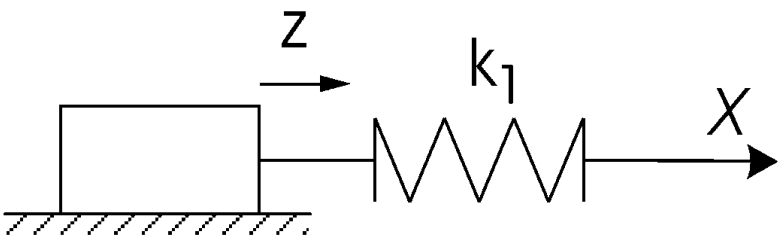

Fig. 66. Maxwell slip model

As the input (*x* in Fig. 66) increases, the force exerted by the spring at the output (*z* in Fig. 66) increases until it exceeds that of the Coulomb friction force. After the appropriate displacement of the spring is reached, the output tracks the input. The overall result is that an offset in tracking of the input occurs anytime the input position is near (relative to the spring constant) zero.

The means for removing the offending phenomenon in the valve at hand is simply to eliminate the compliance in the transmission. This will eliminate the tracking offset, or more appropriately, the hysteresis observed due to Maxwell slip. To accomplish this, a commercial gearhead was purchased with nearly the same reduction ratio as the custom cable-capstan transmission (14:1 and 9:1, respectively). While the previous transmission was made from PEEK in order to insulate the valve servomotor from possible high temperatures due to the use of hydrogen peroxide decomposition products in the valve, the commercial gearhead is a metallic planetary gearhead which will efficiently conduct heat and potentially lead to the destruction of the motor. Temperature isolation is trivially recovered by attaching PEEK components both to the gearhead output shaft and to the motor body. An exploded view of the valve assembly with PEEK isolation components and the commercial transmission is shown in Fig. 45. The penalty paid for

this change is a modest increase in the length of the valve actuator (i.e., transmission and motor). While this increase in length was intolerable in previous projects that used this valve, there is ample space in the quadrupedal robot to accommodate the change.

The presence of the commercial gearhead allows for the use of substantially higher control gains because the metallic gears are far more robust and unlikely to break compared to the PEEK cable used in the custom transmissions. Empirically measured bandwidth of the valve while pressurized at 20.7 bar (300 psi) under the influence of the increased gains is shown in Fig. 67. The higher gains, along with the nearly eliminated compliance in the transmission, attenuate the magnitude of the hysteresis in the valve's output flow rate (from 26% of full scale flow rate to 7%), as shown in Fig. 68. This figure was constructed by repeating the experiments of Section V.C.2.a using the commercial gearhead rather than the custom one.

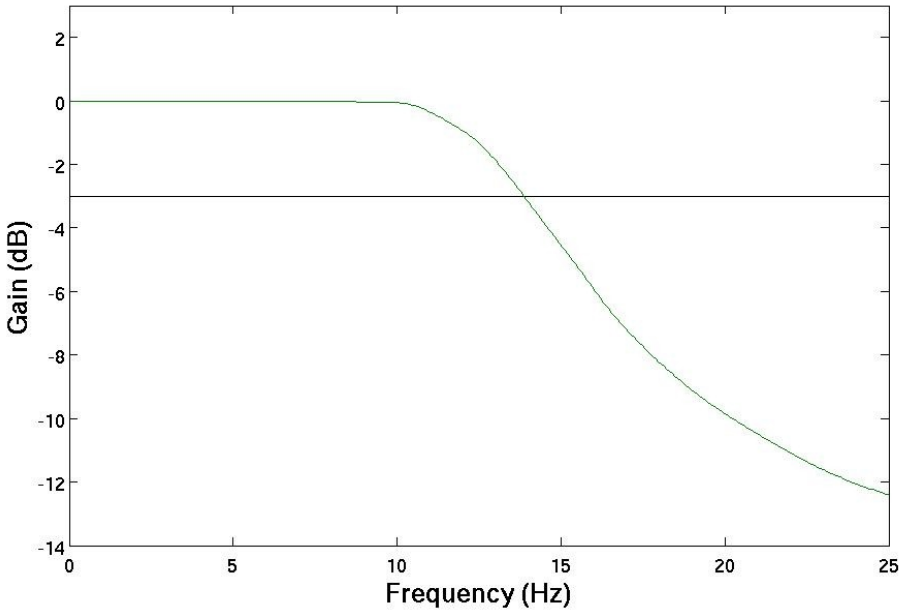

Fig. 67. Valve bandwidth using commercial transmission and custom servocontroller

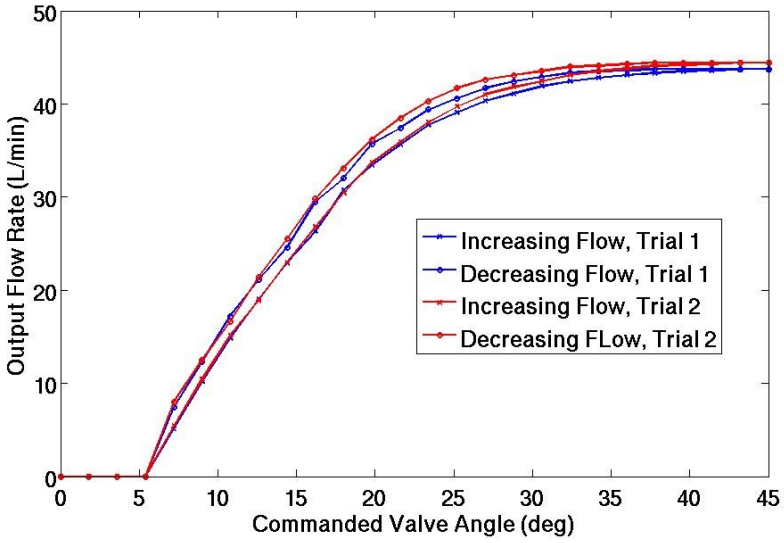

Fig. 68. Hysteresis in valve flow rate attenuated through improvement of servomotor transmission

Raising the gains has the unfortunate side effect of requiring somewhat more power to drive the valve servomotors. However, it was experimentally determined that the increase in power is only weakly a function of reference signal frequency. That is, the power consumed (approximately 2 W) is nearly constant regardless of the speed at which the valve is driven.

In addition to replacing the inadequate custom cable-capstan transmission with a more robust commercial option, the valves were modified to correct a relatively severe oversight in their original design. As depicted in Fig. 56, the angular orientation of the valve sleeve within the valve body is maintained solely through the friction of the o-ring on both the valve sleeve and valve body.

With the original, cable-capstan transmission, it is possible that this frictional interface was adequate to resist torques applied to the valve sleeve by the valve's actuating motor. However, the commercial gearhead can apply more torque because the reduction ratio is increased from 9:1 to 14:1. In addition, the cable-capstan transmission was limited in its maximum travel by the manner in which the cable ends were terminated. That is, the transmission was not free-running and the output of the transmission was limited in travel to only slightly more (approximately 15°) than the operational range of the valve itself. Because the commercial gearhead does not suffer from either of these limitations, it is possible for the valve to fall out of calibration during operation.

A possible and likely scenario for how the calibration can be lost follows. When the valve and controller are powered on, the controller drives the motor so that the hard stop of the sleeve is engaged with its mating surface on the PEEK transmission output.

Then, the controller commands the valve to back away from the hard stop so that the valve spool is aligned with the spool's no output flow angular orientation (nominally 0°). Assuming that the sleeve does not change angular orientation relative to the valve body, the valve will perform as expected at this point. However, if a step in valve position towards the hard stop is commanded while the transmission output impacts the valve sleeve's hard stop (or if there is some overshoot when following a smaller magnitude command), the motor can potentially move the valve spool. Then, the valve's zero-flow location that was determined at start up has been lost and the valve will not perform as expected.

What is needed to correct this design flaw is a locking feature that maintains the valve sleeve's orientation relative to the valve body in the presence of potentially considerable applied forces. Because the valve spool and sleeve are made of hardened 440 stainless steel and are precision ground to have approximately 10 microns of diametral clearance, the options for introducing the needed features are limited.

The modifications actually performed on the valve assembly are to grind .75mm diameter scallops at diametrically opposite locations on both the valve sleeve and the valve body. Then, .75mm diameter and 3.2mm long dowel pins are pressed into holes drilled into the valve endplates (shown, but not marked in Fig. 56) that align with the new scallops. When assembled, the dowel pins engage with the scallops of the valve sleeve and prevent it from rotating. The modified portions of the valve assembly are shown in Fig. 69.

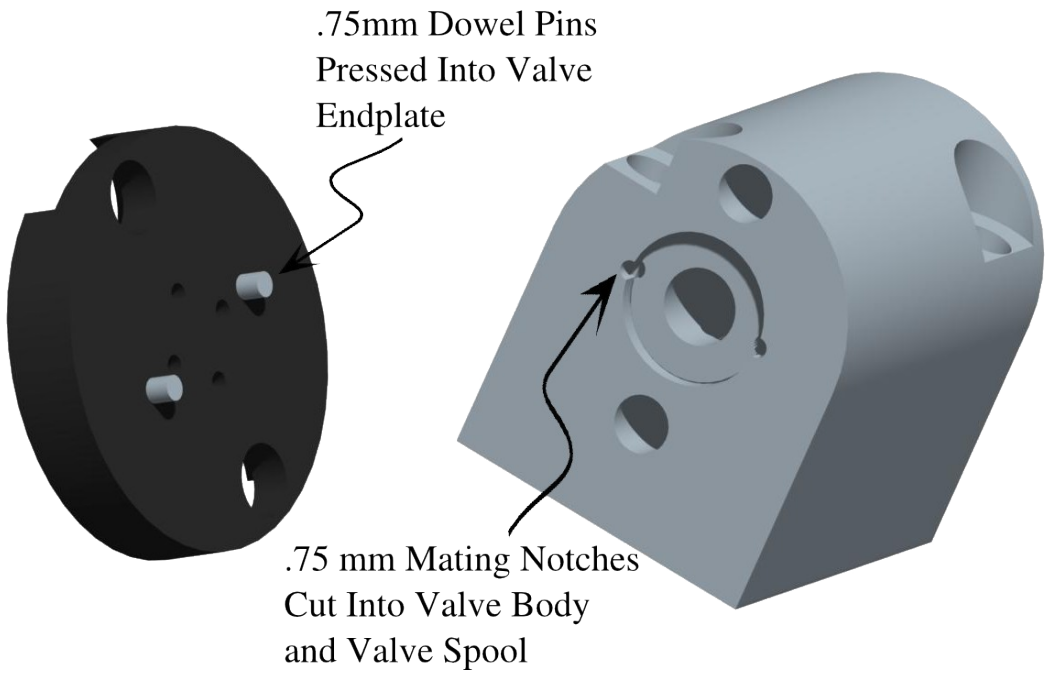

Fig. 69. Valve modifications to eliminate causes of calibration loss

CHAPTER VI

RESULTS

As noted in Chapter II, walking was first achieved in the robot using a position control scheme. This robot (depicted in Fig. 18) featured two legs instrumented only with angular position sensors and valves separated from the pneumatic actuators that they controlled by approximately 3 m long tethers. Also, only two legs of the robot were manufactured and the aft portion of the robot was supported instead by a pair of non-holonomic caster wheels. Self-locomotion was difficult due to a number of unforeseen difficulties in the design and control of this prototype, but was possible and was demonstrated as in the frame sequence of Fig. 70.

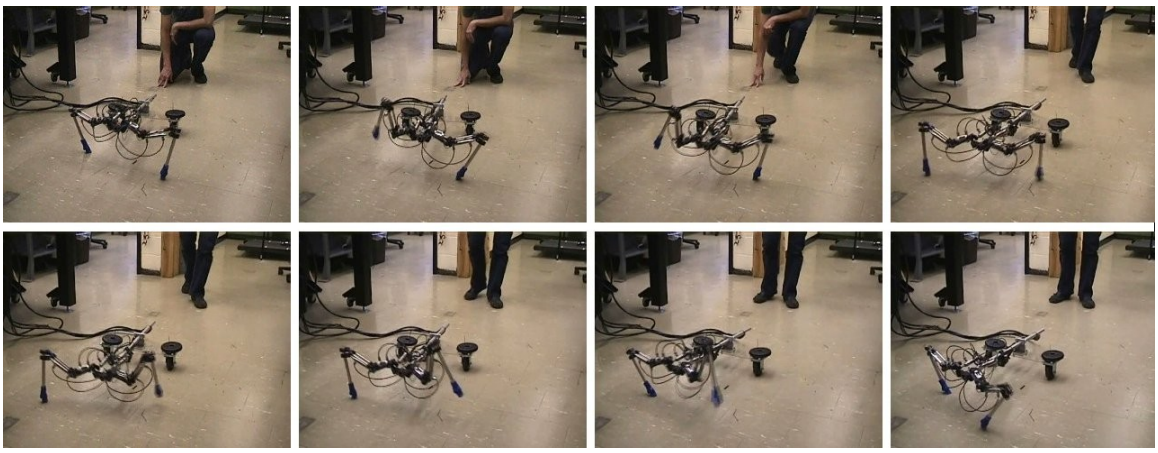

Fig. 70. First achievement of any kind of walking by the robot. Execution captured in frame sequence uses position control and valves at a distance of 3 m from the robot

Having determined that position control was either not appropriate to the particular problem or that it was not correct in its implementation, the robot was modified and reconfigured (as described in Section II.C) to include load cells in its sensor package for each joint. Further, the control scheme was replaced with an impedance control method operating in the workspace frame. However, the same, off the shelf, valves were used in this prototype but were moved to a closer distance of roughly .5 m from their respective pneumatic actuators. Also, only the front two legs were again tested and the aft portion of the robot was again supported by nonholonomic casters. Using this altered prototype robot, very smooth walking motion was achieved, as depicted in the frame sequence of Fig. 71. Additionally, a maximum speed of approximately 35 cm/s, measured by a frame-by-frame analysis of captured video, was achieved using this prototype and the described control methods. This represents a normalized speed of approximately .55 body lengths per second for the designed thorax length of the (then assumed and designed) hexapedal robot.

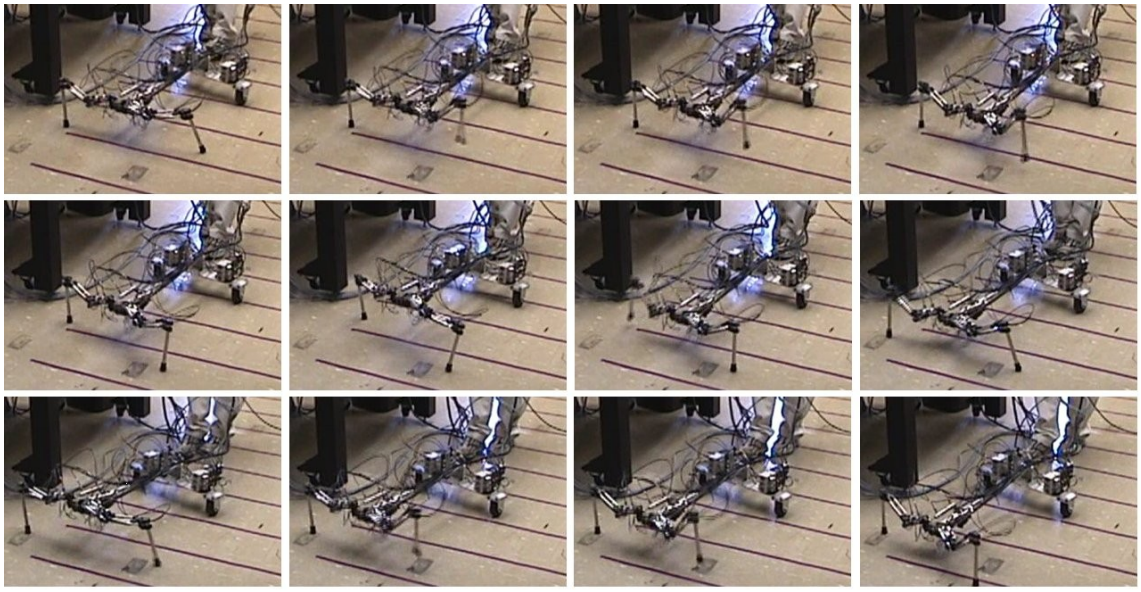

Fig. 71. Two-legged prototype demonstrating walking under impedance control

Many tests and demonstrations were conducted using the prototype and methods of Fig. 71. During these trials, many difficulties were encountered with the load cells (as noted in the introduction of Chapter III) that were introduced to make operation of the device using the impedance control approach possible. Because of this, the robot was again redesigned (as in Chapter IV) to use the PVA control method of Section III.B. This robot was manufactured in a four-legged form.

In initial testing, the walk (or crawl) gait, described in Appendix B, was programmed into the control software driving the tethered robot. The gait parameters used were those of McGhee and Frank [97] because of their optimal quasistatic stability properties. This mode of locomotion was successfully demonstrated as shown in the frame sequence of Fig. 72.

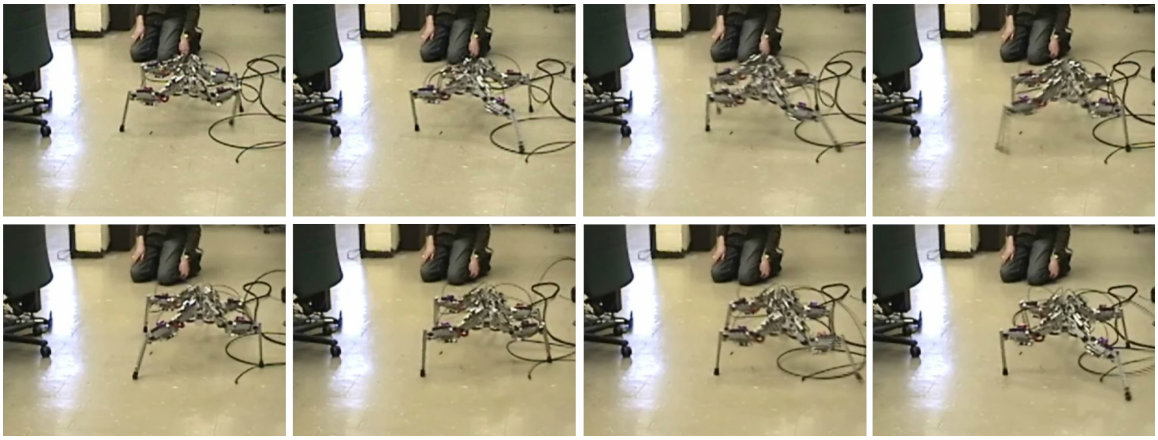

Fig. 72. First achieved walking by the quadruped robot. The walk or crawl gait is used in the frame capture.

A number of problems were again encountered when attempting trials of the quadrupedal robot using the walk gait. These were thought to be mainly due to the apparently very small margin of static stability (as in Fig. 86) that was a product of the robot's specific geometry and the specifics of the walk gait. Motivated by this, the so-called intermittent crawl gait of Tsukagoshi et al [98] was implemented in the robot's control software. This was successfully demonstrated as illustrated in Fig. 73.

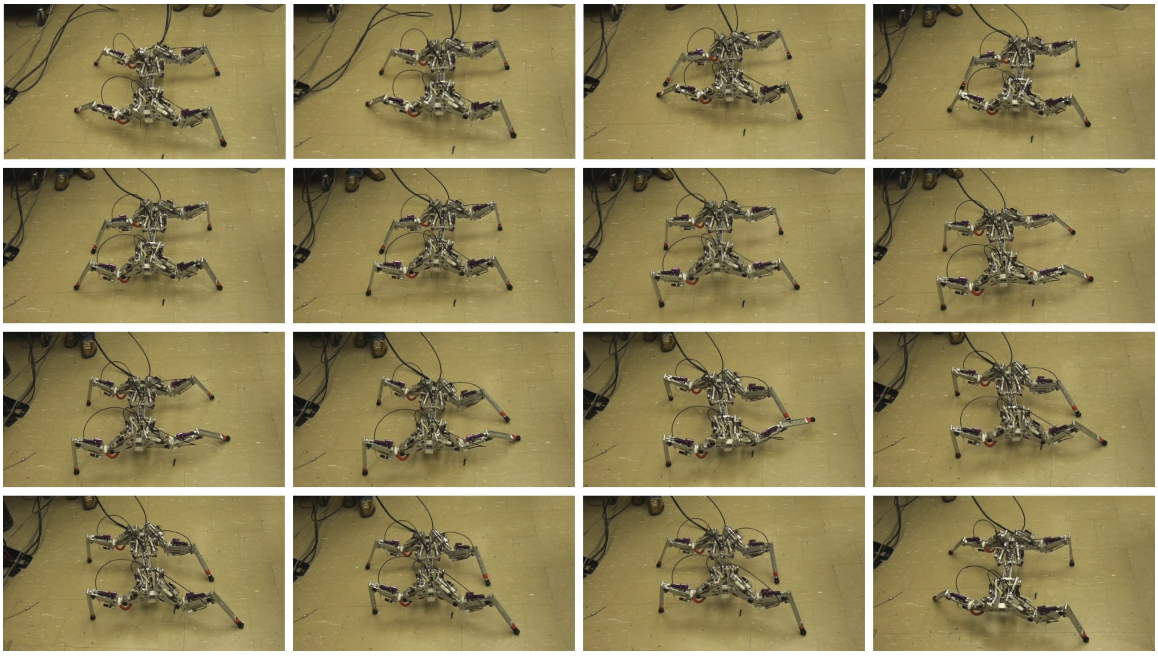

Fig. 73. Quadrupedal robot locomoting using the intermittent crawl gait

After observing the robot operating using the intermittent crawl gait, it was verified that the guarantees of static stability implied in [97,98] are only valid when the speed of travel is extremely slow. This problem is exacerbated by the weight distribution implicit in the design of the robot. Specifically, the majority of the components (valves, actuators, dampers, electronics) are mounted to the legs and the structure of the legs has been made somewhat more robust than that of the thorax to compensate for this component placement. Because of this, the majority of the robot's weight is distally located and the inertial effects of moving the robot's legs are non-negligible except in excessively slow speeds.

Rather than either attempt to achieve static stability in the presence of these non-idealities or to develop a model and control structure that incorporated them, it was decided to attempt faster, dynamic, gaits such as the trot and to ignore the fact that

nothing in the totally clock-driven (as noted in Section III.C) control scheme is able to detect or compensate for dynamic effects. Surprisingly, this approach was quite successful and is a testament to the applicability and robustness of the central pattern generator (CPG)-like approach. The results of operating the robot under the influences of this method are depicted in Fig. 74.

The most clear difference of the walking robot described in this work relative to others documented in the literature is that it uses pneumatic actuation. As described in Section I.B, this implies that the robot should be more capable than its peers when comparing its power metrics (maximum speed and maximum payload capacity) with theirs. To demonstrate that the benefits of fluid powered actuation are, in fact, achievable and have been realized by the robot at hand, two types of experiment were conducted.

First, using the trot gait as described above, the robot demonstrated a maximum speed of approximately 1 body length per second using this method and observation of this experiment seems to indicate the possibility that greater speeds can be achieved with the described architecture.

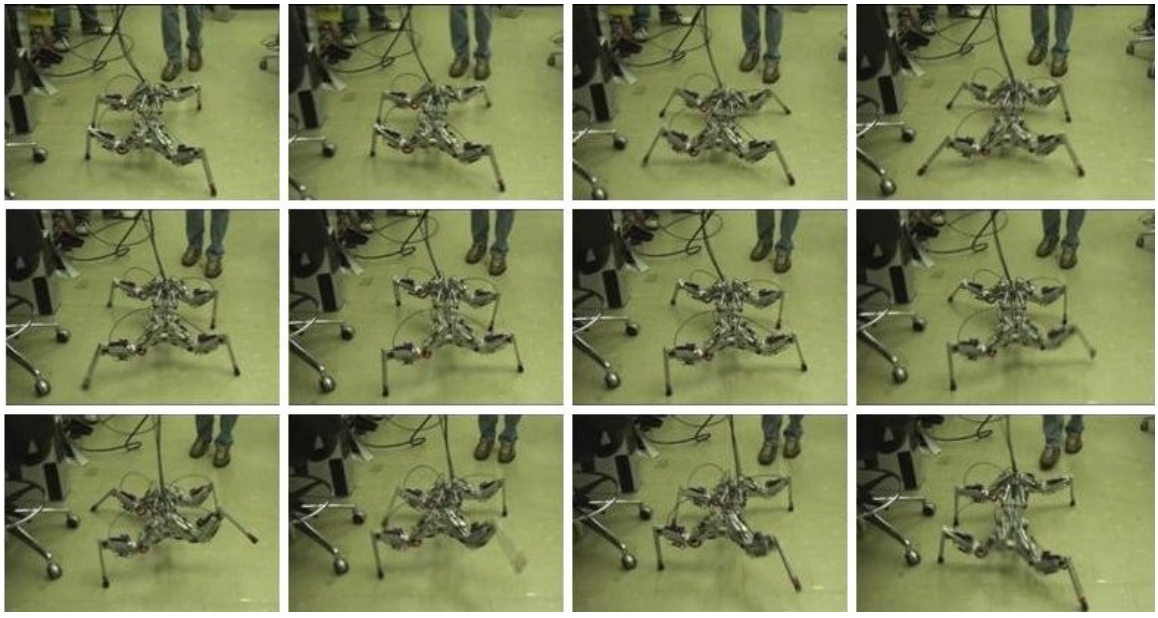

Fig. 74. Tethered quadruped demonstrating trot gait

Buoyed by the success of these trials in validating that walking and trotting were possible with the given design and control methods, steps were taken to quantify the maximum normalized payload carrying capacity (measured as a percentage of robot body mass).

In the next set of experiments, the robot was commanded to travel using a walk or crawl gait. While doing so, the robot was loaded with weights. Because the robot is not only blind (as robots who lack vision systems are commonly referred to in the literature), but lacks a kinesthetic sense of force and a vestibular sense of balance, the parameters of the joint controllers and of the gait (e.g. duty cycle, walking speed, etc.) were manually tuned to give a qualitatively good walk. Through this process, a maximum payload of 20 lb (representing 130% of the robot's 6.9 kg mass) was carried. This achievement is depicted in Fig. 75.

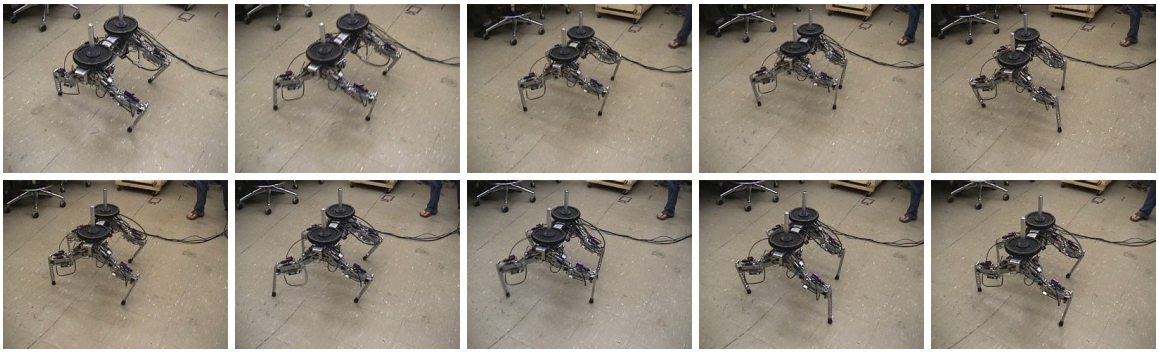

Fig. 75. The robot locomoting while supporting 130% of its own mass.

At this extreme payload mass, the duty cycle of the walk is increased to 0.96 (i.e. the stance phase lasts 96% of the gait cycle), and the walking speed is reduced to ~0.1 body lengths per second. Even greater weights can be supported by the robot while it merely stands. However, the relatively extreme height at which the payload masses are set on this robot makes the task particularly difficult. Indeed, the very large duty cycle used in this experiment is required because large amplitude, low frequency body oscillations result from a single leg's swing motion (i.e. the removal of one of the four supporting legs induces such an oscillation). The relatively large amount of time in which all four legs are simultaneously in a stance phase is required to attenuate these oscillations and fully stabilize the robot before the next leg begins its swing motion.

At higher speeds, the duty cycle can be decreased so that the walking gait is more fluid and “natural;” however, the robot is unable to support as great magnitudes of payload at greater velocities. In support of this claim, the speed of the robot was increased to .5 body lengths per second and was again made to locomote while carrying a payload. At this speed, the maximum supportable payload was 66% of the robot's mass.

As the tracking performance of the various levels of control of the robot may be of interest, such data was taken during many of the experiments. One of these is depicted below. The test from which these data were taken was one conducted on a tile floor using a walking gait with a duty cycle of .75 and a body speed of .5 body lengths per second. The figure eight motion was incorporated with a lateral amplitude of 6.4 cm and an axial amplitude of 1.9 cm. Fig. 76 shows tracking of the joint angles of the robot's front left leg using the angle naming convention of Fig. 42. Fig. 77 shows the tracking of the robot's front left foot in Cartesian space. Note that this is merely a transformation of the data from Fig. 76 using the kinematics of Appendix A. Fig. 78 depicts tracking of the valve spool positions for the valves that drive the actuators of the robot's front left leg. The reference positions given for the valve tracking result from application of the PVA controllers of Section III.B on the joint data of Fig. 76.

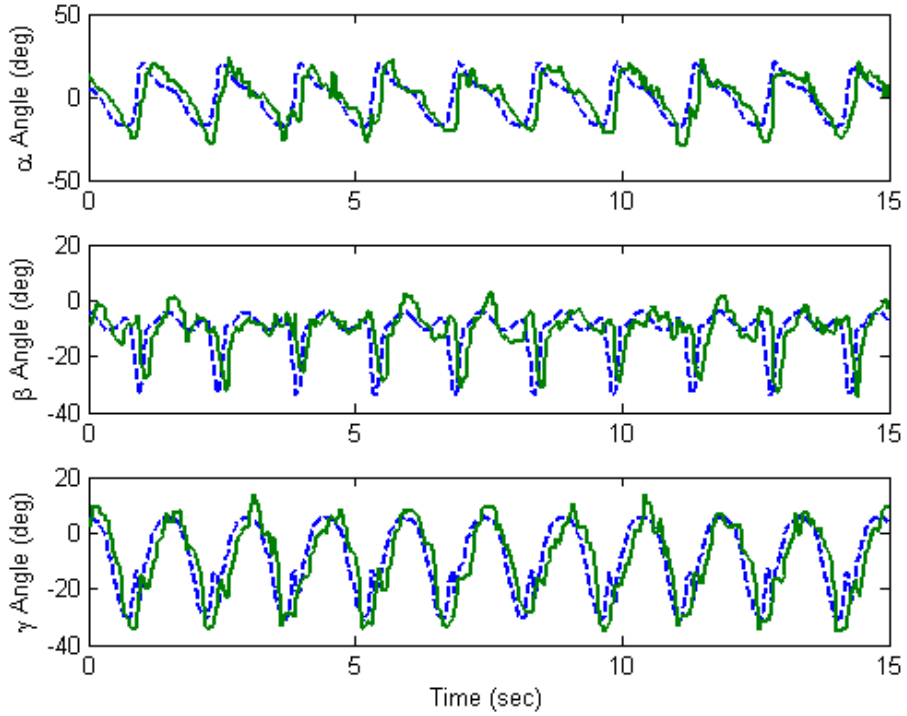

Fig. 76. Tracking of robot front left leg joint angles

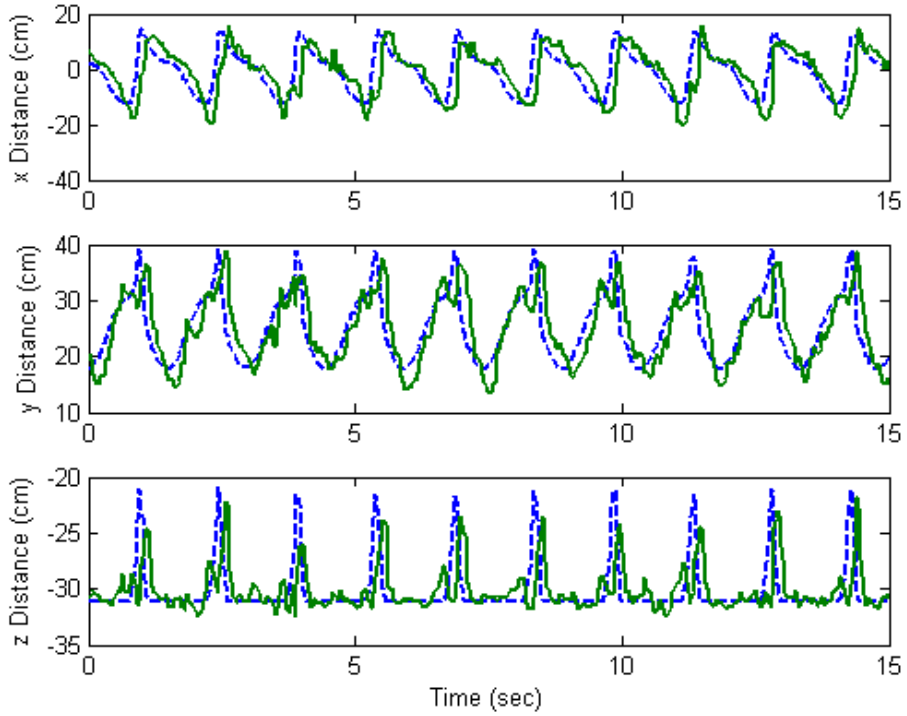

Fig. 77. Tracking of robot front left foot in Cartesian space

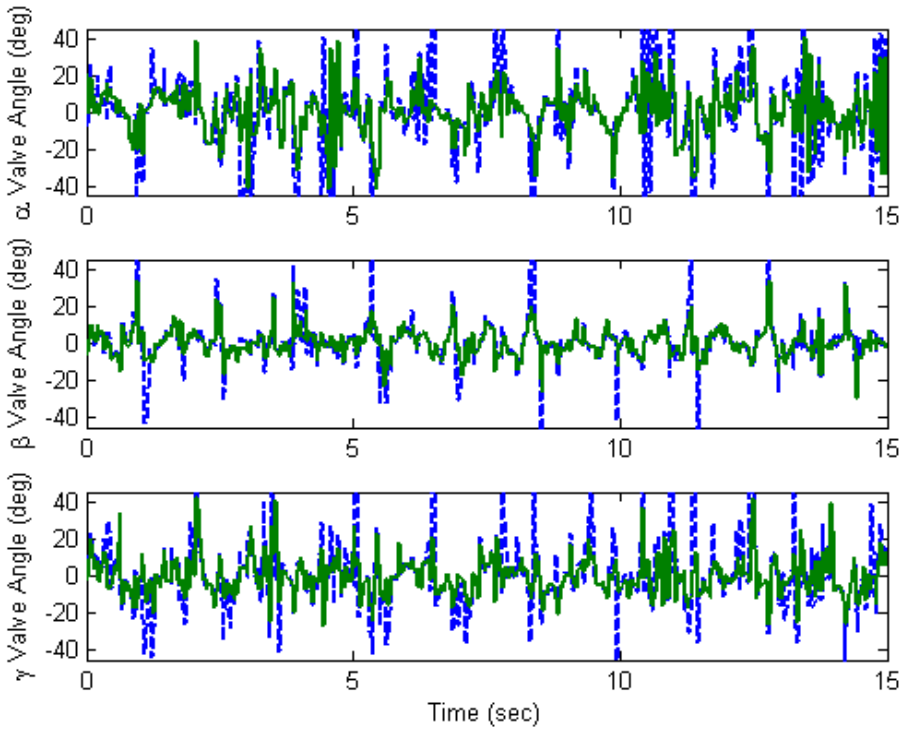

Fig. 78. Tracking of robot front left valve spool positions

A final set of experiments were carried out in which the robot walked over a few types of substrate beyond the tiled floor used in all of the experiments heretofore described. These were all outdoor experiments and included substrates such as concrete, brick, soil densely covered with pine straw, and wet soil sparsely covered with grass. Throughout these cases, various rates (ranging from approximately .1 to .6 body lengths per second) and both the walk and trot gaits were successfully achieved. The only caveat worth mentioning is that, because these were outdoor experiments, a much longer tether was needed (due to placement of electrical outlets relative to the substrates). Specifically, the tether was increased from approximately 6 meters to 30.5 meters. This has the unfortunate consequence of causing the supply pressure at the robot's valves to

fluctuate somewhat due to the time lag of pressure waves traveling from the supply tanks to the actuators. This was somewhat mitigated by using multiple lines for the transmission of compressed air, but still had the effect of making the tracking of joint positions considerably less precise and determinate. Despite this, as noted above, walking was possible (although more qualitatively poor) on each of the substrates. One such experiment on a grassy substrate is shown in Fig. 79.

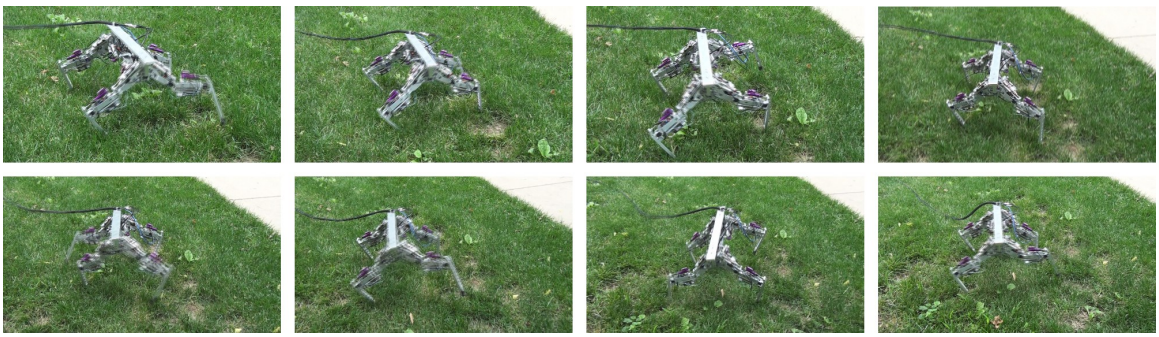

Fig. 79. Outdoor walking test of robot on grassy substrate

Attempts were made to cause the robot to move forward at a rate exceeding the 1 body length per second mark that was achieved using the trot. These tests proved that the robot is easily capable of moving its leg joints at speeds that can support body velocities in excess of 1.5 body lengths per second. The proof of this was that the position controller maintains tracking (similar in quality to that of Fig. 76) of the fixed walking trajectory at frequencies that were sufficiently high to reach this body velocity mark (i.e. the bandwidth of the pneumatic actuators apparently exceeds that necessary to meet this mark). However, the robot's postural stability at speeds in excess of the demonstrated 1 body length per second speed is questionable. Specifically, the robot tends to overturn

within a short period of it starting from rest when commanded to travel at such rates. This failure is not intrinsic to the design of the robot, or of the servocontrollers used in the actuation of the joints, but rather it is a failure of the rudimentary walking methods and a lack of sensory information that would permit the robot to perceive impending postural failures. As such, it can be said with certainty that the robot demonstrates a maximum normalized velocity of 1 body length per second and a maximum payload carrying capacity of 130% body mass.

These demonstrations validate the premise that pneumatic actuation confers an advantage in the output power of the robot relative to its peers or competitors. Fig. 80 makes this comparison visually. In the figure, diagonal lines are lines of constant normalized power (product of normalized speed and normalized payload capacity). Traversal of one of these diagonal lines is analogous to selection of a different transmission ratio (i.e. trading force for velocity). The human mark on the figure is taken from various estimates of average human performance, while performance of the robots other than the current one is taken from Table 1.

It is apparent from the figure that the current robot (labeled as VU Quad) is second only to Boston Dynamics' BigDog among state-of-the-art robots and vastly exceeds all other efforts to date in this metric. Indeed, it is probable that, with more advanced walking algorithms and with a more complete sensor package, the robot of this work can match the impressive marks set by BigDog as the speed of the current robot seems to be limited only by gait software and a lack of sensory information.

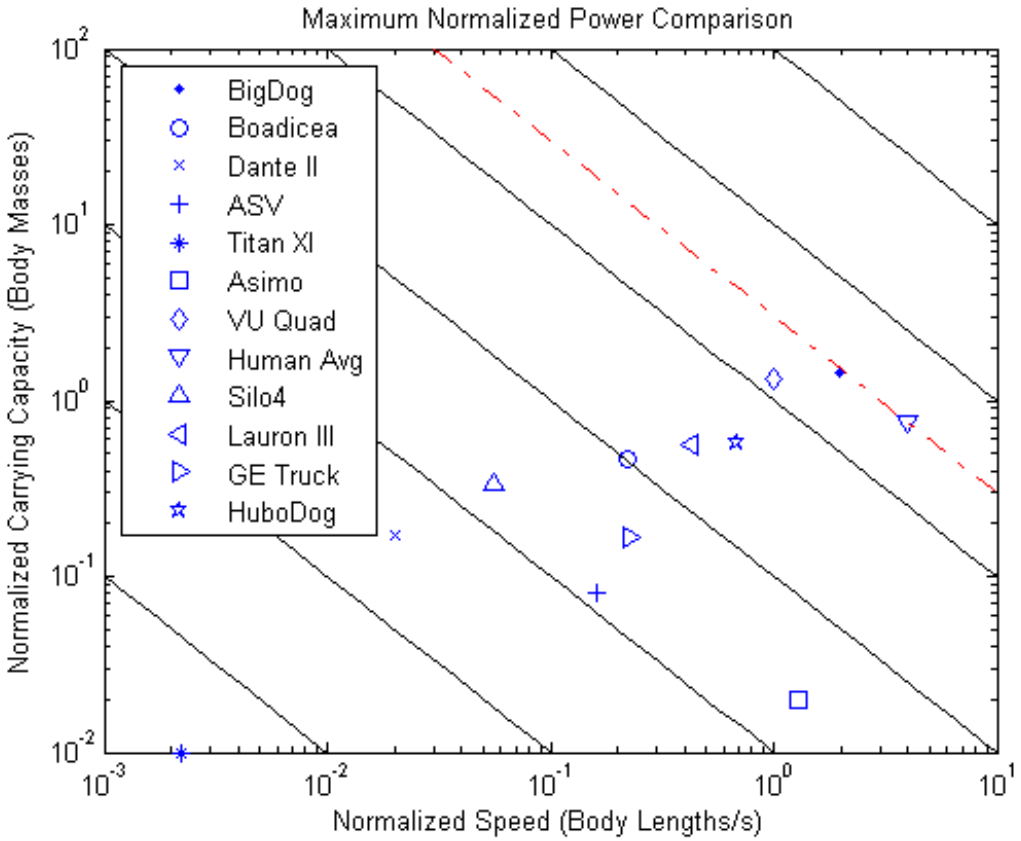

Fig. 80. Normalized output power comparison of current robot with other state-of-the-art walking robots and human average.

CHAPTER VII

CONCLUSIONS AND POSSIBILITIES FOR FUTURE WORK

The most critical lesson to be learned from this work is that it is important to learn from the lessons of others before embarking on a project of this magnitude. The global robotics research community has largely moved away from the development of new forms of legged robots and has instead gravitated towards higher level, computational efforts like simultaneous localization and mapping (SLAM), artificial intelligence (AI), and autonomous operation. The evolution of quadrupedal legged robots essentially ended with the remarkably capable quadruped described by Raibert in [99] and its direct successors [12]. These robots also use fluid power and so have the significant advantages associated with its use, but pair this power with a sophisticated and capable control methodology that uses a dynamic model and clever insights of dynamic walking to achieve its robustness.

The present work uses a very simple control scheme that performs, by comparison, somewhat poorly (with respect to gait robustness). The major advantage of this robot over the Raibert-derived ones is that, because of the valve technology used, it can be made much smaller than the earlier efforts. Indeed, the miniaturized descendant of BigDog is LittleDog and it has become the de facto standard for legged autonomous robot research [100-103]. LittleDog has a body size similar in scale to the robot of this work, but is electrically instead of fluid powered, effectively proscribing it from attempting the kinds of payload lifting feats that BigDog is known for.

Persons who choose to continue this line of work need to first confront a few very difficult problems. First, as the robotics community is, in general, no longer interested in this type of work, the large amount of time and money that must be put into a project such as this will largely be futilely spent if academic fruits are sought. That is, it is very difficult to create something that has novelty over the countless efforts that have been documented before and to generate the interest and excitement that is needed to publish prolifically on it.

Second, since the robot is notionally to be used for search and rescue (according to the goals of the CCEFP), it is worth considering the needs of the community who might actually field this robot in this capacity. In a search and rescue situation, these persons will, of course, need something that works reliably and simple so that it is robust against failures due to hazardous conditions. Life or death situations are not not tolerant of fickle hardware. Because of this, almost all research robots that are intended for search and rescue are tracked and not legged. With such a trend in mind, it is likely that this demographic, in addition to the academic one, will also be largely uninterested in a device such as that described in this document. Preparing the current robot for search and rescue missions is well within the realm of possibility, but will require a great deal of redesign as well as significant effort to understand the mission profiles that first responders are interesting in applying the robot to. It may be that the search and rescue mission is inappropriate to the current robot, but in any case it is worth determining the robot's primary goal and adjusting the design and abilities to be specific to this goal.

An additional conundrum facing future extensions of this work is that the primary advantage of this robot is also a great challenge and possibly a weakness. Specifically, it is asserted in Section I.B that pneumatic systems have certain advantages over electromagnetic competitors. While the force and power density of pneumatic actuators will vastly exceed those of electromagnetic actuators for the foreseeable future, this advantage is not without cost. First, electromagnetic systems are extremely efficient, especially compared to pneumatic systems [34], a limitation which is fundamental in nature and unlikely to ever be addressed. Indeed, repeating the analysis of [34] using battery energy densities for modern lithium polymer technologies indicates that an electrically actuated system using these types of batteries is superior (with respect to energy density) to the 70% hydrogen peroxide powered one due mostly to the efficiencies of electromagnetic actuation. Second, energy dense sources of compressed gas to run this robot introduce their own complexities (especially the causticity and reaction temperature of hydrogen peroxide). It is possible that the free piston compressor of [39] will be able to achieve adequate energy densities while supplying gas at a cool and easy to work with temperature, but it is not yet clear that it will be able to deliver sufficient power for the robot of this work. This is not a judgment on that device but rather an admission that the power consumption of the present robot has not been measured. Finally, electromagnetic systems are extraordinarily easy (nearly trivial) to control and do not require nonlinear or esoteric methods (such as that in Section III.B) to achieve good performance.

Supposing that the issues cited above can be adequately addressed, the most important future work on the present device should be to make it become more “Raibert like.” The Raibert-derived robots are essentially the only polypedal (i.e. more than two) legged robots that have been shown to work in a variety of environments reliably and robustly. To make the robot of this work approach or exceed the robust performance of BigDog, etc., pressure sensors or force sensors must be integrated into the design at an earlier stage so that the challenges of fragility and complexity can be addressed at the most basic level. The presence of these sensors will allow for a large number of improvements. First, impedance control, which is in general much more successfully used in legged locomotion than stiff position control schemes (such as that used in the present work) can be employed. Indeed, the robot (by this author's estimation) appeared to move the most controllably and deliberately when under the command of the impedance controller. Pressure or force sensors will enable the robot to again use this sort of control method. The robot should also be more robust against noise since the necessity of a twice-differentiated potentiometer signal (as in the PVA controller) is no longer present.

Finally, the robot's current performance regarding the speed metric is limited only by a lack of sensors and by the rudimentary control algorithm used. Enhancing both of these aspects of the present robot should yield great rewards both in its qualitative attributes (such as postural robustness) as well in the quantitative metric of normalized speed. That is, the inclusion of inertial measurements into the control algorithms should abate the postural stability problems observed in the robot when higher speed trotting was attempted.

Next, while the mechanical design of the robot is more or less sound, the strategy for moving to an untethered mode of operation is quite tenuous. Specifically, the notion of designing a robot for tethered operation and then attempting to simply add all of the additional components needed for untethered opeartion to it is a poor idea. The mechanical hardware of the device should be revisited so that the electronics needed for autonomous operation as well as the mobile fluid power source can be more suitably integrated into the design. Further, the allowances made in the current design for wiring are inadequate. The stiff and thick wires needed to daisy chain the JCUs are far more substantial than the structure has been designed to accommodate. Connectors were not treated beyond a cursory search through existing stocks. Unfortunately, the problem of selecting a connector is quite a bit more complicated, involving the characteristic impedance of the electrical connection (especially in the case of the CANbus wires), locking features, polarizing features, etc. The present iteration of the robot has intermittent electrical failures because the selection of connectors is non-optimal. While the electrical system works more often than not, the random nature of these failures is extremely annoying. Future incarnations of the robot should address these problems earlier rather than later.

While the mechanical design of the robot as demonstrated is effective, it is possible that its legacy is hindering its efficacy. That is, the sprawling kinematics of the robot are quite different from almost all natural quadrupeds (the notable exceptions being animals such as the gecko family and the salamander family). The BigDog and LittleDog robots as well as most (if not all) mammalian quadrupeds feature a 2 DOF ball joint hip as well as primarily vertically oriented legs. This is quite different than the large

horizontal component of the present robot's leg kinematics. Intuitively it would seem that the mammalian-like leg design has advantages in limiting the static forces needed to hold the leg upright (i.e. the large moment arm developed by placement of the robot's feet quite far from its center of mass is eliminated). Concretely determining that the mammalian-like leg kinematics are, in fact, superior requires further simulation and analysis, but may yield some important improvements.

Finally, a statics-based approach to the control scheme used is almost totally inadequate for a walking robot as its whole purpose is in being in motion. Successful future efforts to extend this robot framework must carefully consider full body dynamics in motion planning if they hope to be as resilient as biological quadrupeds or as the most capable of the state of the art legged robots. This will by necessity introduce significant new burdens in the modeling of the robot's inertial properties as well as other effects of interest, such as friction and the highly non-linear factors in pneumatic actuation. However, the failure to incorporate these factors early into the all aspects of the design of the robot will lead to unforeseen difficulties in the process of implementation. Further, the robot must sport a much greater number and variety of sensors to enable dynamic kinds of motion. Specifically, inertial measurement using accelerometers and/or gyroscopes are a necessity, as are pressure or force sensors at the actuators or joints of the robot. The latter will not only improve the controllability of the pneumatic actuators, but also enable better interaction of the robot with its environment, as previously noted. Three-axis load cells, or at the very least single-axis load cells, located at the feet of the robot to get weight distribution measurements are also probably a necessity. Many other researchers use vision sensors or LIDAR to good effect in navigating difficult terrain, so

it is possibly desirable to incorporate these elements into the robot's sensor suite. In general, it is not reasonable to assume that the robot can perform at the maximum level supported by the high-power actuators when it is essentially anesthetized against its environment.

At a most basic level, the primary lesson to be learned from this effort is that it is important to have a thorough plan for constructing a highly complex system. This plan should have a basis for each of its steps that is not pure conjecture or intuition. Rather, concrete proofs for why something is to be done (based in the use of mathematics and scientific principles) should be established as early as possible in the planning phases and certainly before any electrical circuitry is constructed or before metal is cut. For example, while single degree of freedom tests of the pneumatic PVA control structure were undertaken to ensure that this scheme would work appropriately, these experiments did not come close to authentically representing the end scenario that the joint under test was to be used for (i.e. the robot's inertia, loading during locomotion, actuator size, supplementary damping, etc. were not replicated in the 1-DOF experiments). It was assumed based on the results of these simplistic experiments that the proposed system would perform in most environments as it did in the single tested environment. This assumption was eventually shown to be false.

The difficulties encountered as a result of this poor planning were eventually overcome, but might have been avoided altogether if proper unit testing or simulation was conducted ahead of time.

APPENDIX A

ROBOT LEG FORWARD AND INVERSE KINEMATICS

A.1 Development of Forward Kinematics

Controlling the position of the leg while walking (or in the case of impedance control, establishing a set point trajectory) relies on the ability to plan a reference trajectory for the leg to follow. In this context, each of the legs can be viewed as an individual robotic arm whose end effector is a foot of the robot. When walking (e.g. in a straight line), the principal tasks that the legs must carry out are to support the robot's weight and to supply force in the direction of travel. These two tasks are, by definition, in a task (i.e. Cartesian) space rather than in the joint space of the leg.

Because of this, it is appropriate and desirable to formulate the forward and inverse kinematics of each leg. Note that, since each of the legs is identical in morphology and construction and because the robot is quadrilaterally symmetric, it is necessary only to derive kinematics for a single leg. The kinematic equations for the other legs differ merely by the inclusion of some offset (i.e., spacing between forward and rear leg pairs) and the changing of some signs (i.e., reflection across the robot's mid-sagittal and mid-transverse planes).

In the following discussion, L_c, L_f, and L_t designate the lengths of the coxa, femur, and tibia of the robot, respectively. L_B is the length of the body from front to back (measured from forward leg pair origin to aft leg pair origin). Fig. 81 along with Fig. 82 give the location and orientation of the base coordinate frame of the robot as well as a graphical representation of the various link lengths.

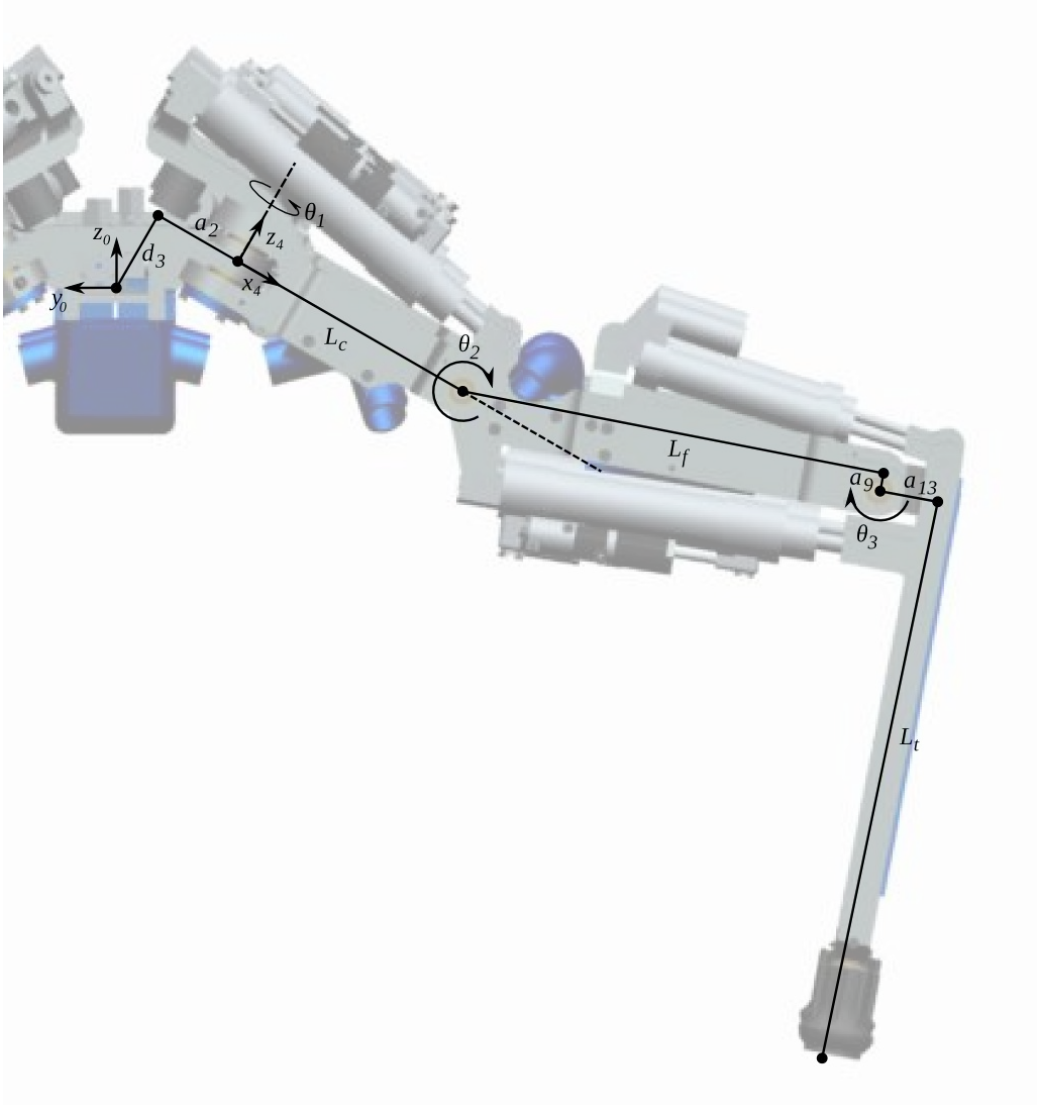

Fig. 81. Aft (looking forward) view of the robot, showing basic coordination frame position and orientation as well as showing link length definition.

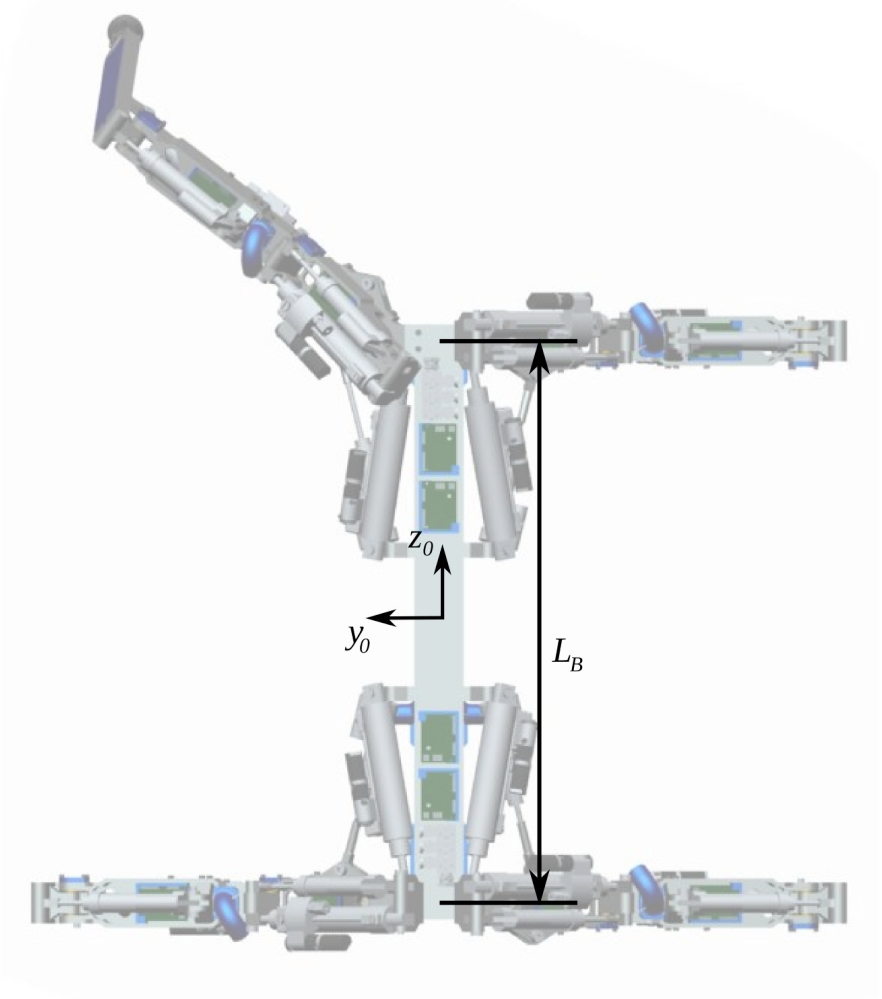

Fig. 82. Top (looking down) view of the robot, showing basic coordination frame position and orientation.

Each line of Table 10 gives Denavit-Hartenberg parameters for the leg structure and defines a kinematic transformation matrix using the equation from Craig [104].

$$T_{i-1,i}=\begin{bmatrix} \cos\theta_i & -\sin\theta_i & 0 & a_{i-1} \\ \sin\theta_i\cos\alpha_{i-1} & \cos\theta_i\cos\alpha_{i-1} & -\sin\alpha_{i-1} & -\sin\alpha_{i-1}d_i \\ \sin\theta_i\sin\alpha_{i-1} & \cos\theta_i\sin\alpha_{i-1} & \cos\alpha_{i-1} & \cos\alpha_{i-1}d \\ 0 & 0 & 0 & 1 \end{bmatrix} \quad (41)$$

Table 10
Forward Kinematic Parameters of Robot Leg

i	α_{i-1}	a_{i-1}	d_i	θ_i
1	ψ	$L_B/2$	0	0
2	0	0	0	$-\pi/2$
3	0	a_2	d_3	0
4	0	0	0	θ_1
5	0	L_c	0	0
6	$-\pi/2$	0	0	0
7	0	0	0	θ_2
8	0	L_f	0	0
9	0	0	0	$\pi/2$
10	0	a_9	0	0
11	0	0	0	θ_3
12	0	L_t	0	0
13	0	0	0	$-\pi/2$
14	0	a_{13}	0	0

To derive the forward kinematic transformation matrix from leg base to foot (end-effector) position, each of the matrices resulting from the application of (41) to each row of Table 10 is sequentially multiplied. For the case of a foot (as compared to a hand, gripper, or other type of end effector), the orientation is of no interest, so the first three columns of the final matrix are discarded, leaving the position of the foot relative to its base as (given for the front right leg, as shown in Fig. 81 and Fig. 82):

$$x = \sin\theta_1\left(L_c + L_f\cos\theta_2 + a_{13}\cos\left(\theta_2+\theta_3\right) - a_9\sin\theta_2 - L_t\sin\left(\theta_2+\theta_3\right)\right) + \frac{L_B}{2} \tag{42}$$

$$y = \cos\psi\left(a_2 + \cos\theta_1\left(L_c + L_f\cos\theta_2 + a_{13}\cos\left(\theta_2+\theta_3\right) - a_9\sin\theta_2 - L_t\sin\left(\theta_2+\theta_3\right)\right)\right) + \\ -\sin\psi\left(-d_3 + a_9\cos\theta_2 + L_t\cos\left(\theta_2+\theta_3\right) + L_f\sin\theta_2 + a_{13}\sin\left(\theta_2+\theta_3\right)\right) \tag{43}$$

$$z = \cos\psi\left(d_3 - a_9\cos\theta_2 - L_t\cos\left(\theta_2+\theta_3\right) - L_f\sin\theta_2 - a_{13}\sin\left(\theta_2+\theta_3\right)\right) + \\ -\sin\psi\left(a_2 + \cos\theta_1\left(L_c + L_f\cos\theta_2 + a_{13}\cos\left(\theta_2+\theta_3\right) - a_9\sin\theta_2 - L_t\sin\left(\theta_2+\theta_3\right)\right)\right) \tag{44}$$

A.2 Development of Inverse Kinematics

The inverse kinematics cannot be found by the algebraic method (i.e., algebraic manipulation of equations (42)-(44) to arrive at expressions for θ_1, θ_2, and θ_3 in terms of the foot position x,y,z). Instead, the geometric method must be used as follows. For reference, a representation of the robot's front right leg with relevant dimensions and definitions is shown in Fig. 81.

To start, we introduce the convenience variables L_1 and L_2. The definitions for these variables are shown in Fig. 83. In the figure, the portion of the leg shown is viewed parallel to the plane containing the coxa, femur, and tibia of the leg. Note that y' and z' are rotations of y and z to be aligned perpendicular to the axis of θ_1 and with the fixed offsets a_2 and d_3 removed. The value y'' is similarly oriented but subtracts the value L_c from y'.

$$L_1 = \sqrt{L_f^2 + a_9^2} \tag{45}$$

$$L_2 = \sqrt{L_t^2 + a_{13}^2} \tag{46}$$

$$y' = y\cos\psi + z\sin\psi + a_2 \tag{47}$$

$$z' = -y\sin\psi + z\cos\psi - d_3 \tag{48}$$

$$y'' = \sqrt{x^2 + y'^2} - L_c \tag{49}$$

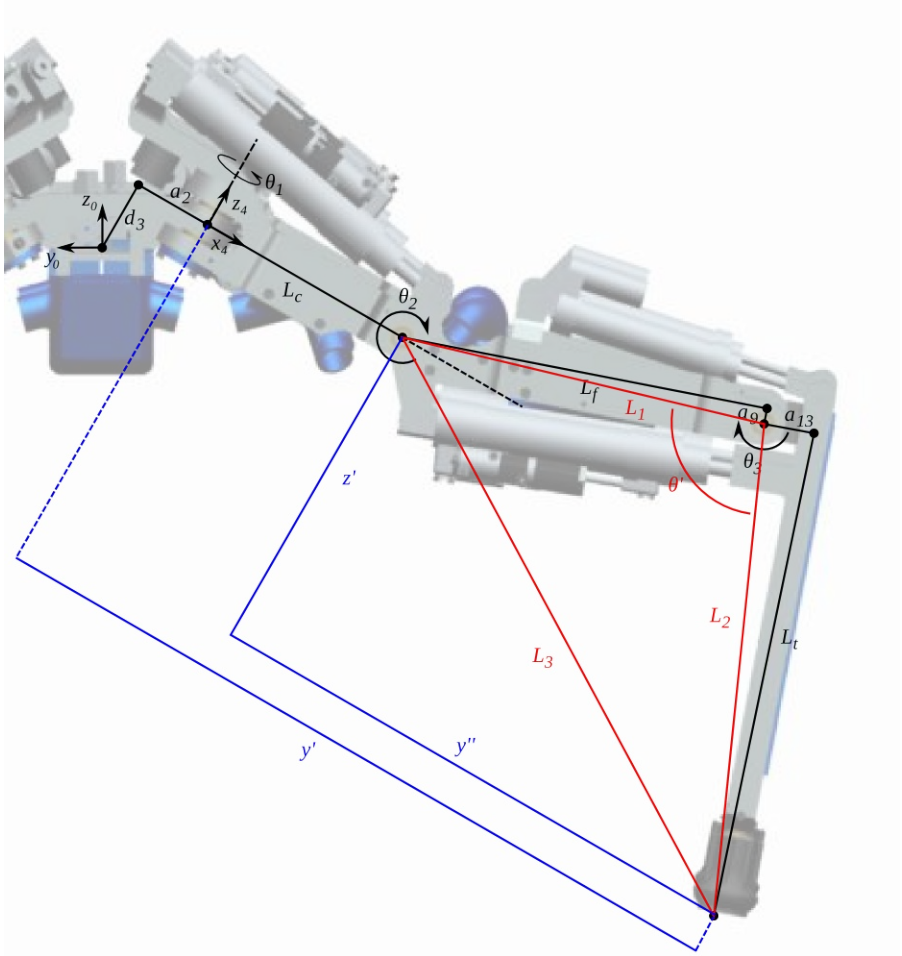

Fig. 83. Stick figure representation of leg showing convenience variables

With these definitions, the value of θ_1, the most proximal joint, is solved for trivially as is shown in Fig. 84 below. This figure is the leg depicted from a view perpendicular to the axis of rotation of θ_1. Therefore, the expression for θ_1 is:

$$\theta_1 = \tan^{-1}\left(-\frac{x}{y'}\right) \tag{50}$$

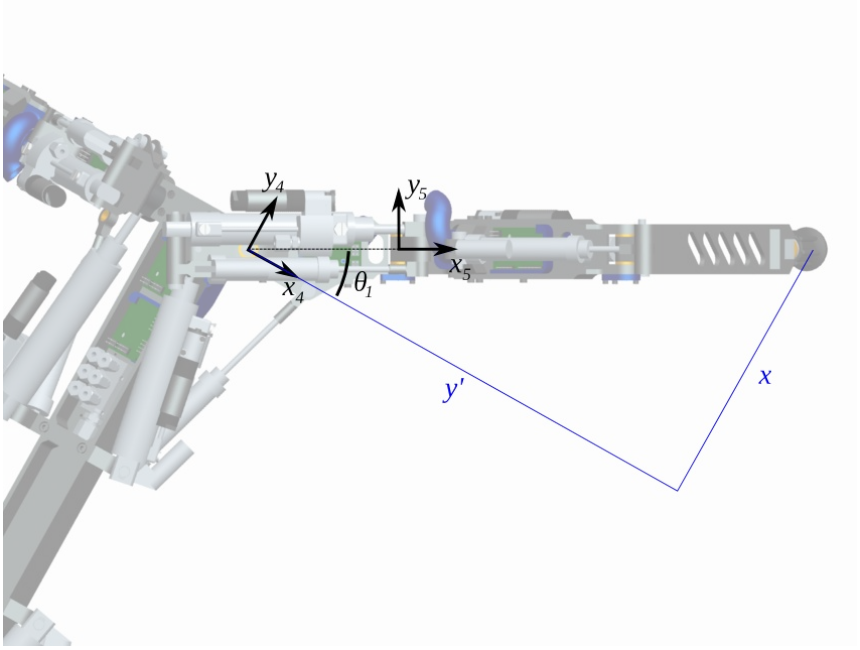

Fig. 84. Graphical depiction of θ_1 as viewed in plane perpendicular to axis of θ_1

The value for the most distal joint is solved for next. The quantity L_3 is introduced as the line forming a triangle with L_1 and L_2.

$$L_3 = \sqrt{y''^2 + z'^2} \tag{51}$$

Additionally, θ' is defined as the angle between L_1 and L_2 and is solved for using the law of cosines.

$$\theta' = \cos^{-1}\left(\frac{L_3^2 - L_1^2 - L_2^2}{-2 L_1 L_2}\right) \tag{52}$$

Using this definition, the value for the most distal joint is given as a sum of its constituent components from Fig. 83 above.

$$\theta_3 = \pi - \tan^{-1}\left(\frac{L_t}{a_{13}}\right) + \tan^{-1}\left(\frac{a_9}{L_f}\right) - \theta' \tag{53}$$

Finally, the value for θ_2 is found from its constituent components using the law of sines to determine the value of one of the components.

$$\theta_2 = \frac{\pi}{2} - \tan^{-1}\left(\frac{-y''}{z'}\right) - \sin^{-1}\left(\frac{L_2}{L_3}\sin\theta'\right) - \tan^{-1}\left(\frac{a_9}{L_f}\right) \tag{54}$$

Equations (47)-(54) completely define the inverse kinematics and were automatically verified to be correct using symbolic manipulation software. This was done by substituting equations (47)-(54) into equations (42)-(44) and showing that equality is maintained. Although these equations are specific to the front right leg, simple transformations (as for the forward kinematics) can be used to recover inverse kinematics for all of the robot's legs.

Note that, while potential singularities exist in the given inverse kinematics, the ranges of motion allowed by the structure and actuators of the as-built robot are such that the given equations for the inverse kinematics are valid for the entire reachable workspace of the robot.

APPENDIX B

A SURVEY OF QUADRUPEDAL GAITS

B.1 Introduction and Definitions

Quadrupeds are multitudinous in nature, and each species has evolved a style of walking that is unique to its natural form. As nature has a head start of several millennia over the present work in developing walking gaits or methods for four legged bodies, and as a great deal of work has been put into studying, classifying, and describing the naturally occurring categories of quadrupedal gait, it is highly redundant to start from scratch when specifying the way that the robot should walk. Rather, it is wise to at least take cues from quadrupeds in nature when designing the walking methods for the robot, if not exactly mimicking outright some four legged animal that most closely resembles the device.

The modern study of animal and human gaits begins with the pioneering work of Edward Muybridge in the late 19th century. His work utilized the then new invention of mechanical shutters and a large number of automatically triggered cameras to take a rapid succession of photographic frames of horses locomoting at a variety of speeds (as well as other motion studies of various species) as depicted in his seminal work, *Animals in Motion* [105]. Through Muybridge's and later researchers' work, a number of different motion primitives for natural quadrupeds were identified. A comprehensive overview of quadrupedal gaits used in nature was compiled by Hildebrand [88].

By way of definition, a gait cycle refers to the minimum sequence of motions or events that each leg executes and, when repeated ad infinitum, defines the continuous motion of the leg during locomotion. Duty factor, then, refers to the percentage of the gait cycle in which a leg is in a weight supporting (or ground contact) mode, while phase refers to the gait cycle percentage which temporally separates one leg from another. In other words, phase is defined between two individual legs and describes the time (expressed as a percentage of the gait cycle) between the same gait motion or event (e.g. beginning of swing phase) being executed by those two legs. A particular mode of locomotion can then be uniquely described by a duty factor value (sometimes the duty factor takes on a unique value for each leg), three phase values (some leg will serve as an index and a phase value is only needed for the other three legs relative to the index), as well as a motion description (e.g. joint trajectory) for a single gait cycle for each leg. Since the present robot is quadrilaterally symmetric, a single motion description is used for all of the legs.

B.2 Gait Studies

The slowest mode of quadrupedal locomotion is known as walking (or crawling). In this mode, some combination of three of the four legs remain in contact with ground for close to 100% of its gait cycle. The appeal of this particular gait is that it is unique among the quadrupedal gaits in that it is potentially statically stable. Static stability requires that, when viewed in a plane perpendicular to local gravity, the center of gravity of the walking robot or creature falls inside of the convex hull whose vertices are the points of contact between the robot and ground. In a four-legged robot, this requirement means that only one leg at a time can be in a swing state (i.e. retraction, or not in contact

with the ground), since three stance (i.e. protraction, or supporting the robot's weight and in contact with the ground) legs are required to encapsulate the center of gravity in a support triangle. An equine walk is depicted in a series of photos by Muybridge in Fig. 85.

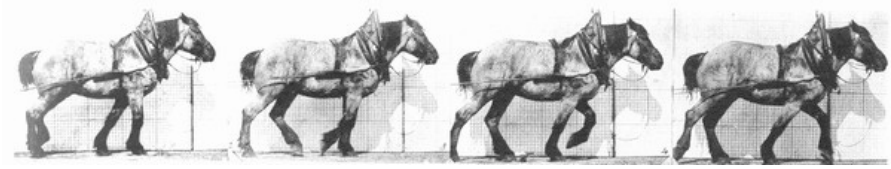

Fig. 85. Equine walk as captured by Muybridge.

McGhee and Frank, in an early study of quadrupedal robot locomotion [97], offered a mathematical proof of the static stability of these gaits (referred to by them as “creeping” gaits while they are known in biological or veterinary circles as “walking” gaits). They showed that a particular sequence of the unique swing phase legs was optimally stable and further defined phase offsets and duty factor for optimal static stability. They note that their optimal sequence is used by a large number of naturally occurring quadrupeds (confirmed by [88]). However, their optimal duty factor is quite high (91.67%) which implies that the robot must have a body speed (equal in magnitude but counter in direction to the foot stance speed) that is very slow to prevent the swing motions from being excessively fast. This slow speed is also required in order for the primary assumption made when employing the walk as formulated by McGhee to be true (i.e. that the body behaves quasistatically or that inertial effects are vanishingly small).

For all but the slowest walking speeds, the inertial effects of the body and the moving legs are considerable and will violate this assumption, rendering the carefully constructed gait sequences worthless for all practical purposes.

Tsukagoshi et al [98] noted that, in the crawling gait formalized by McGhee, the static stability of the walking body is at a minimum (and approaches instability) when the center of mass of the body passes over the so-called stability admitting lines (those lines projected onto the substrate that join the fore left and aft right feet, as well as the fore right and aft left feet). In the crawl gait, this transition happens very nearly simultaneously with the point in the gait where support is exchanged from a fore triangle to an aft triangle. To avoid this potential instability, Tsuakogshi et al introduce a modification of the crawl gait. In their modification, the walking body shifts its center of mass in a purely lateral direction to be more nearly in the center of its instantaneous support triangle. This lateral motion is conducted both before and after the points at which the body's center of mass passes over a stability admitting line. Further, the walker is stationary during any leg's swing phase while the walker's body is in motion when all four legs execute stance phase motions simultaneously. A graphical comparison of the standard walk/crawl and intermittent crawl gaits is depicted in Fig. 86. In the figure, the circles drawn surrounding the center of mass indicate the minimum distance from the center of mass to a boundary of the quasistatic convex support hull. Or, in other words, the body is more statically stable as the size of the circle surrounding the center of mass increases. This distance is greatly increased with the lateral movement and halting modifications that create the intermittent crawl gait.

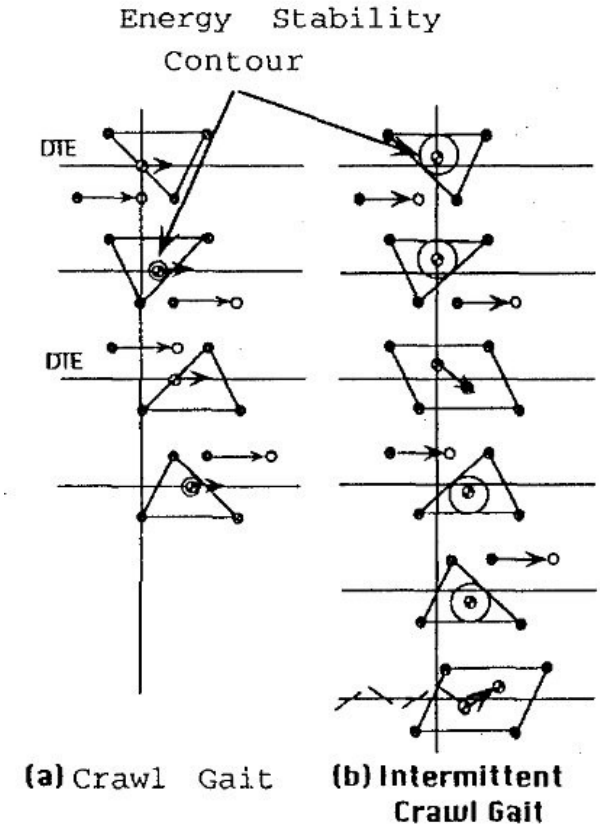

Fig. 86. Comparison of standard crawl and intermittent crawl gaits

In equines (and other animal quadrupeds), the mode of locomotion nearest in velocity to the walk (but more rapid) is the trot. The trot, unlike the walk, is a dynamic gait in which only two legs are most often in contact with the ground. Until the work of Muybridge, it was commonly assumed among horse experts that two legs were always in stance. However, his high speed photographs clearly demonstrated that, at least in equines, there is a free flight phase in which no legs are in a ground contact state.

The trot is characterized by diagonally opposite pairs being in synchrony. That is, an animal's left fore and right hind feet move with zero relative phase and equal speed while the right fore and left hind feet move at the same speed but with approximately 50% phase difference from the first pair. The duty factor of a trot is also approximately 50%.

Because at most two feet are in contact with the ground at any instant, the static stability criteria described above cannot possibly be fulfilled in a trot (i.e. a convex hull cannot be constructed with only two points). Instead, the momentum of the trotting robot or animal is required to carry the body through locomotion. The equine trot is depicted in a series of Muybridge's photos in Fig. 87.

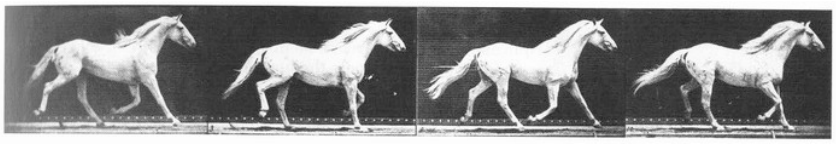

Fig. 87. Equine trot as captured by Muybridge.

An alternative to the trot (similar in form and in speed) is known as the pace. A pacing animal moves leg pairs in unison; however, unlike the diagonal pairs used in the trot, the pairs used in a pace are a fore and hind foot on one side of the body. The pace is apparently favored by long legged animals because it avoids the situation where a hind foot moving forward would impact its next rostral neighbor. However, the pace is

apparently avoided by short legged animals because there is an inherent increase in lateral instability when using this gait. Animals that are known to use this gait are camels and some large slender dogs [88].

The gallop (depicted in Fig. 88), unlike the walk and trot, is known as an asymmetric gait. That is, in the walk and trot, the duty factor is identical for all four legs. In the gallop, however, the fore legs spend much less of the gait cycle touching the ground relative to the hind legs. The gallop is, of course, a much faster motion than either the walk or the trot. This speed, along with the associated low duty factors and greater time spent in free flight, makes the gallop highly dynamic and apparently requires significant preparation to ensure stability while in motion.

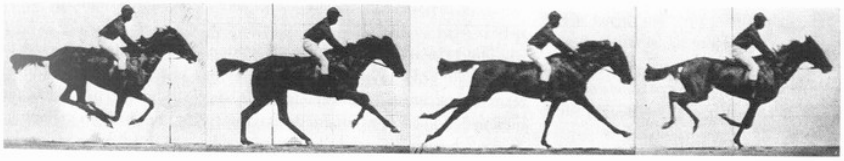

Fig. 88. Equine gallop as captured by Muybridge.

In the gallop, the fore legs have a relatively small phase difference between each other, while the phase difference between fore and aft legs is much greater. Gallops are classified as either transverse or rotary depending on what side (left or right) leg transitions to stance first within this scheme. If the leading fore leg is on the same side as the leading hind leg, the gallop is transverse. Otherwise, the gallop is rotary.

A gait that is similar to the gallop is known as the bound. The bound is asymmetric (as is the gallop); however, in a bound, the two fore feet move in near synchrony and have relative zero phase difference, as do the two hind feet. Whereas in a gallop, there is some non-zero phase difference between the two front (or rear) legs. In the special case where a bounding animal has zero phase difference among all four legs, the gait is known as a pronk rather than a bound.

One issue that is not addressed by this simple categorization system is how and when an animal or robot walker should make a transition from one walking gait to another. That is, what is the criterion that should exist before a walking body makes the change from a trotting gait to a gallop, for example. Hoyt and Taylor [106] have performed experiments in which they trained horses to, on command, walk, trot, or gallop rather than use a self-selected gait. These animals were then placed on a treadmill and made to ambulate at a variety of speeds while their metabolic energy consumption was measured. Next, the animals were allowed to walk freely on a marked grid and their speed and selected gait were measured. Through these experiments, it was shown that the horses would self-select that gait (walk, trot, or gallop) which was the most energy efficient at any given speed. Alexander [107] expanded somewhat on this observation by noting that a large number of animals will make gait mode transitions at similar values of the dimensionless Froude number:

$$Fr = \frac{v^2}{g\,L} \tag{55}$$

Where v is the locomoting speed, g is the acceleration due to gravity and L is the walker's leg length (measured as hip height to ground). Alexander notes that many creatures, regardless of size, will change from walking to trotting at a Froude number of 0.5 and from trotting to galloping at a Froude number value of 2.5.

APPENDIX C

DISCRETE CONTROLLER FORMULATION

As noted above, the valves used to deliver pneumatic power to the actuators of the robot had previously been controlled successfully using a Matlab Real-Time Workshop model of PD type. The transfer function form of a theoretical PD controller is:

$$\frac{U}{E} = K_D s + K_P \tag{56}$$

Because this transfer function is acausal (i.e., the derivative term requires future information and can therefore not be implemented in real-time operation), a practical PD controller must incorporate some filter when computing the derivative term. While multiple choices for this filter exists, the Matlab implementation uses the form:

$$\frac{U}{E} = K_D \frac{s}{\tau s + 1} + K_P = \frac{\left(K_P \tau + K_D\right) s + K_P}{\tau s + 1} \tag{57}$$

This can be transformed into a lumped parameter model:

$$\frac{U}{E} = \frac{A \cdot s + B}{C \cdot s + D} \tag{58}$$

where

$$A = K_p \tau + K_D \tag{59}$$

$$B = K_p \tag{60}$$

$$C = \tau \tag{61}$$

$$D = 1 \tag{62}$$

Before being implemented in software within the embedded system, the PD compensator of (57) must be taken from the Laplace domain (continuous time) into a discretized time domain. This is performed using a Z-Transform, of which there are several. The specific Z-Transform used here is the bilinear, or Tustin approximation:

$$\frac{1}{s} = \frac{T}{2}\left(\frac{z-1}{z+1}\right) \rightarrow s = \frac{2}{T}\frac{z+1}{z-1} \tag{63}$$

Here, T denotes the sample time used by the processor performing the numerical computation required for execution of the compensator. Substituting expression (63) for the Laplace variable, s, into expression (58) for the lumped parameter, continuous time PD compensator above and performing algebraic manipulation to eliminate acausal terms yields an equivalent, discrete time compensator.

$$u_k = e_k \frac{2 \cdot A + B \cdot T}{2 \cdot C + D \cdot T} + e_{k-1} \frac{B \cdot T - 2 \cdot A}{2 \cdot C + D \cdot T} - u_{k-1} \frac{D \cdot T - 2 \cdot C}{2 \cdot C + D \cdot T} \tag{64}$$

Here, the subscript k denotes the value of the variable at the discrete time value, k. A zero value for k signifies the value of the variable at the current time step, negative values signify the value of the variable at previous time steps, and positive values signify future values of the variable.

With this formulation of the discrete time compensator, it is possible to both implement the desired control strategy with a fixed sampling time in software and to tune the control gains as if the controller was operating in continuous time (by using the expressions for A, B, C, and D in (59)-(62) above).

Note that the PVA controller described in Section III.B is integrated into the JCU as noted above. The discrete PVA controller is derived identically to the method of this section and subsequently implemented in the JCU's firmware.

APPENDIX D

MECHANICAL DRAWINGS

NOTES:
1. ALIGN LN # SO THAT FLAT FACE OF PROTRUSION FACES PROXIMALLY
2. INSERT LN # THROUGH LNs # & #

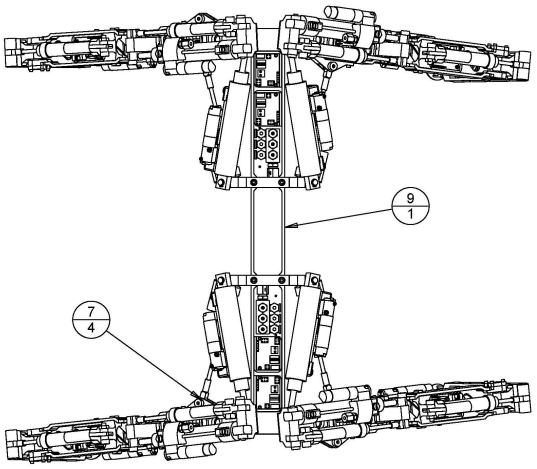

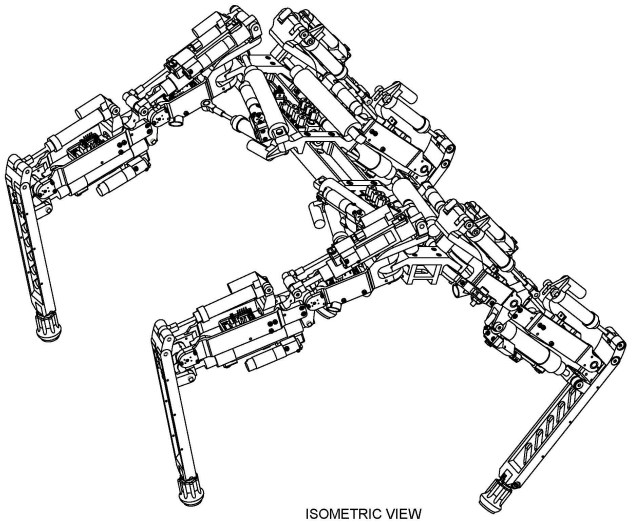

ISOMETRIC VIEW
FOR REFERENCE ONLY

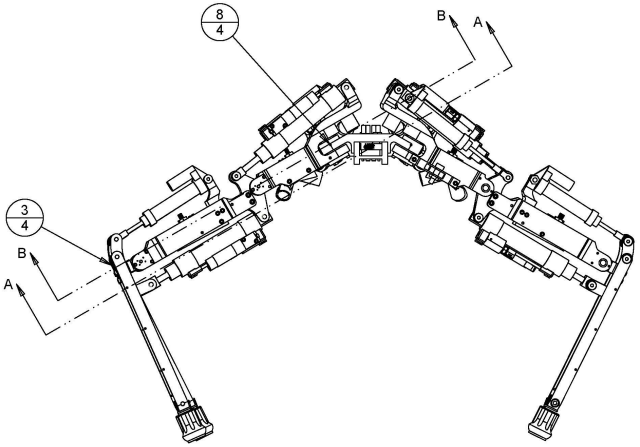

LN	QTY	CAGE	P/N	DESC
9	1	48UA4	1100	THORAX_ASSY_4_LEG
8	4	2V507	98296A027	SPRING_PIN_1_16OD_1_2L
7	8	2V507	92012A535	SHLDR_SCREW_1_4OD_3_8SHLDR
6	12	2V507	91251A079	SHCS_2_56_3_8L
5	4	2V507	90480A195	NUT_10_32
4	4	1JN02	688-RDC503013A	MOUSER_POT
3	4	48UA4	1200	LEG_ASSY_REVB
2	4	48UA4	1305	ALPHA_SHAFT
1	4			ALPHA_POT_COVER

UNLESS OTHERWISE SPECIFIED:
ALL DIMENSIONS IN INCHES
AND APPLY AFTER FINISH
DIMENSION TOLERANCES
.X: ± .02
.XX: ± .01
.XXX: ± .005
ANGLE: ± .5°

REMOVE ALL SHARP EDGES AND BURRS
INTERPRET PER ANSI Y14.1

SCALE 0.330 : 1

CENTER FOR INTELLIGENT MECHATRONICS
VANDERBILT UNIVERSITY, NASHVILLE, TENNESSEE

DESCRIPTION
QUADRUPED_TOP_ASSY

CAGE CODE 48UA4 | 1000 | SIZE C

DRAWN BY K. WAIT | &todays_date | SHEET 1 OF 2

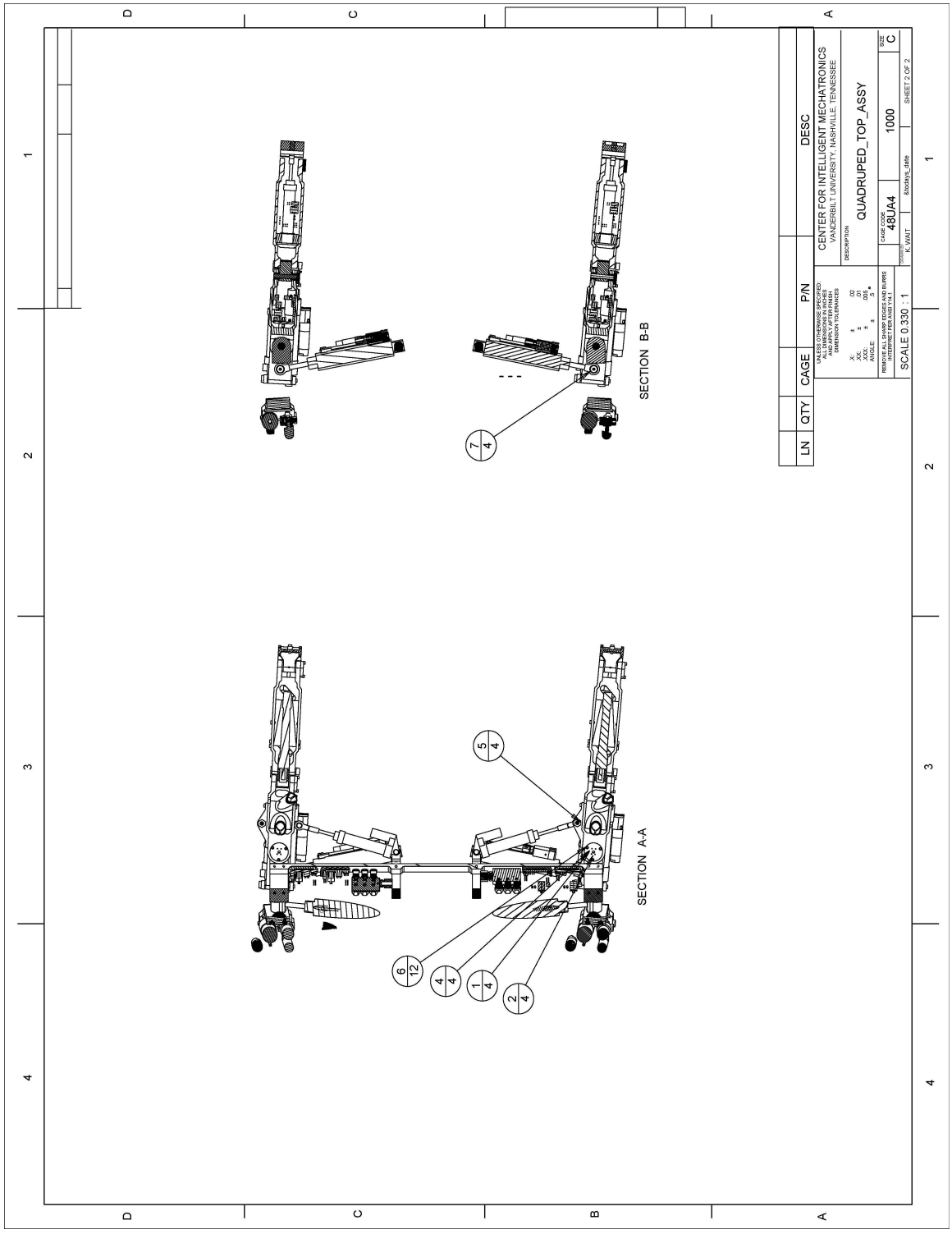
SECTION B-B
SECTION A-A
LN
QTY
CAGE
P/N
DESC
CENTER FOR INTELLIGENT MECHATRONICS
VANDERBILT UNIVERSITY, NASHVILLE, TENNESSEE
QUADRUPED_TOP_ASSY
48UA4
1000
C
K_WATT
SCALE 0.330 : 1
SHEET 2 OF 2

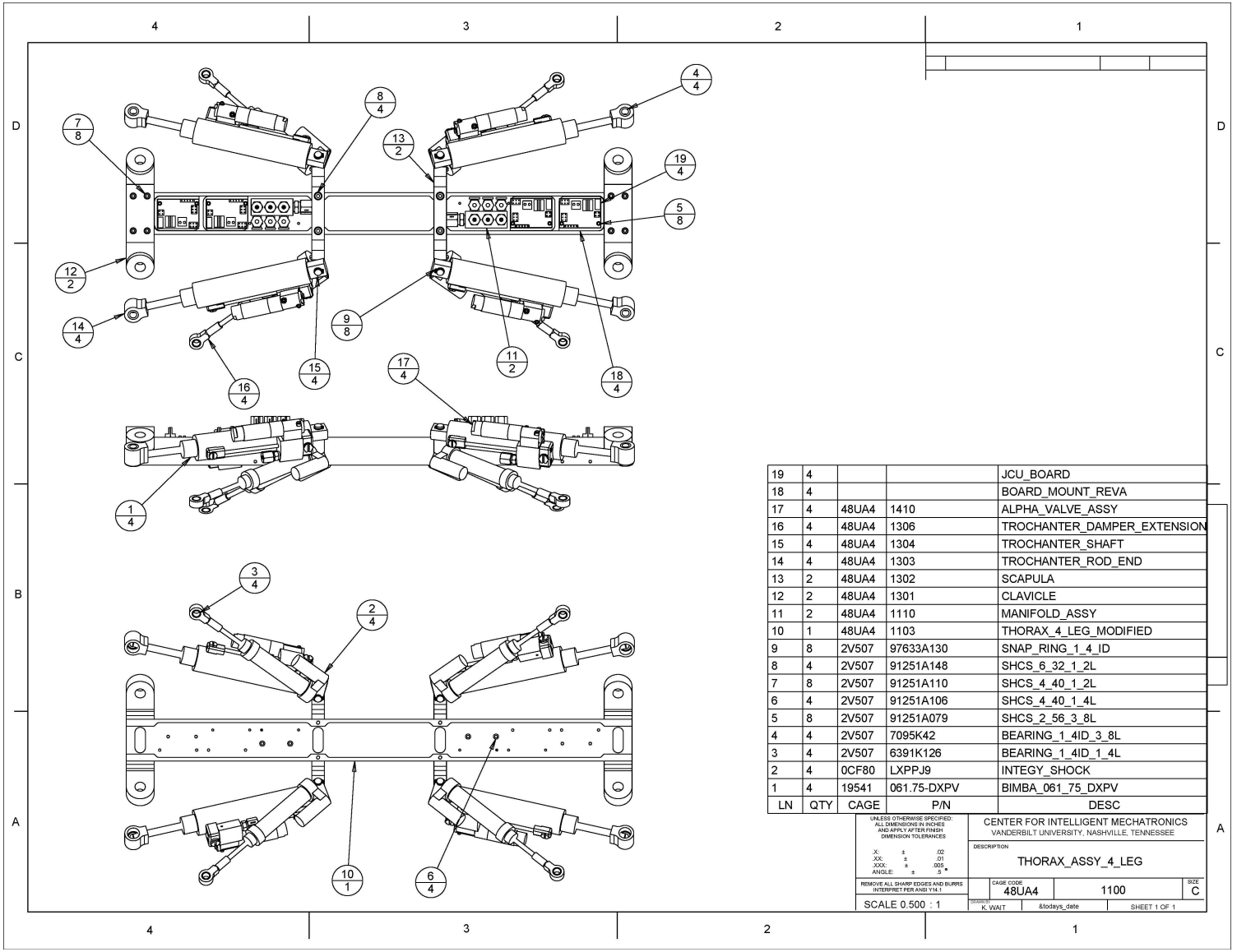

LN	QTY	CAGE	P/N	DESC
19	4			JCU_BOARD
18	4			BOARD_MOUNT_REVA
17	4	48UA4	1410	ALPHA_VALVE_ASSY
16	4	48UA4	1306	TROCHANTER_DAMPER_EXTENSION
15	4	48UA4	1304	TROCHANTER_SHAFT
14	4	48UA4	1303	TROCHANTER_ROD_END
13	2	48UA4	1302	SCAPULA
12	2	48UA4	1301	CLAVICLE
11	2	48UA4	1110	MANIFOLD_ASSY
10	1	48UA4	1103	THORAX_4_LEG_MODIFIED
9	8	2V507	97633A130	SNAP_RING_1_4_ID
8	4	2V507	91251A148	SHCS_6_32_1_2L
7	8	2V507	91251A110	SHCS_4_40_1_2L
6	4	2V507	91251A106	SHCS_4_40_1_4L
5	8	2V507	91251A079	SHCS_2_56_3_8L
4	4	2V507	7095K42	BEARING_1_4ID_3_8L
3	4	2V507	6391K126	BEARING_1_4ID_1_4L
2	4	0CF80	LXPPJ9	INTEGY_SHOCK
1	4	19541	061.75-DXPV	BIMBA_061_75_DXPV

UNLESS OTHERWISE SPECIFIED:
ALL DIMENSIONS IN INCHES
AND APPLY AFTER FINISH
DIMENSION TOLERANCES
.X: ± .02
.XX: ± .01
.XXX: ± .005
ANGLE: ± .5°

REMOVE ALL SHARP EDGES AND BURRS
INTERPRET PER ANSI Y14.1

SCALE 0.500 : 1

CENTER FOR INTELLIGENT MECHATRONICS
VANDERBILT UNIVERSITY, NASHVILLE, TENNESSEE

DESCRIPTION
THORAX_ASSY_4_LEG

CAGE CODE 48UA4 | 1100 | SIZE C

DRAWN BY K. WAIT | &todays_date | SHEET 1 OF 1

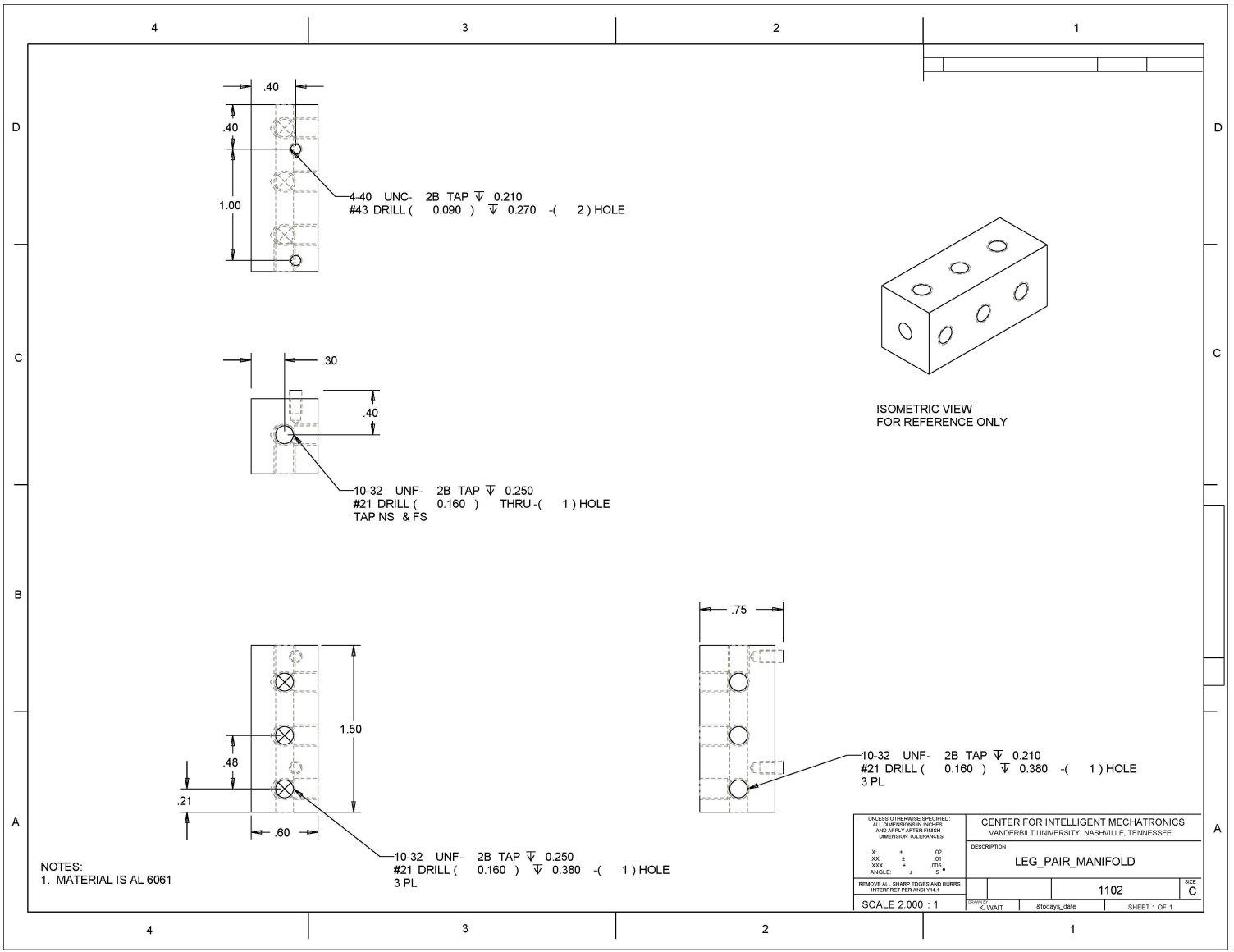
.40
.40
1.00
4-40 UNC- 2B TAP ↧ 0.210
#43 DRILL (0.090) ↧ 0.270 -(2) HOLE
.30
.40
10-32 UNF- 2B TAP ↧ 0.250
#21 DRILL (0.160) THRU -(1) HOLE
TAP NS & FS
ISOMETRIC VIEW
FOR REFERENCE ONLY
.75
1.50
.48
.21
.60
10-32 UNF- 2B TAP ↧ 0.250
#21 DRILL (0.160) ↧ 0.380 -(1) HOLE
3 PL
10-32 UNF- 2B TAP ↧ 0.210
#21 DRILL (0.160) ↧ 0.380 -(1) HOLE
3 PL
NOTES:
1. MATERIAL IS AL 6061
UNLESS OTHERWISE SPECIFIED:
ALL DIMENSIONS IN INCHES
AND APPLY AFTER FINISH
DIMENSION TOLERANCES
.X: ± .02
.XX: ± .01
.XXX: ± .005
ANGLE: ± .5 °
REMOVE ALL SHARP EDGES AND BURRS
INTERPRET PER ANSI Y14.1
SCALE 2.000 : 1
CENTER FOR INTELLIGENT MECHATRONICS
VANDERBILT UNIVERSITY, NASHVILLE, TENNESSEE
DESCRIPTION
LEG_PAIR_MANIFOLD
1102
SIZE
C
DRAWN BY
K. WAIT
&todays_date
SHEET 1 OF 1

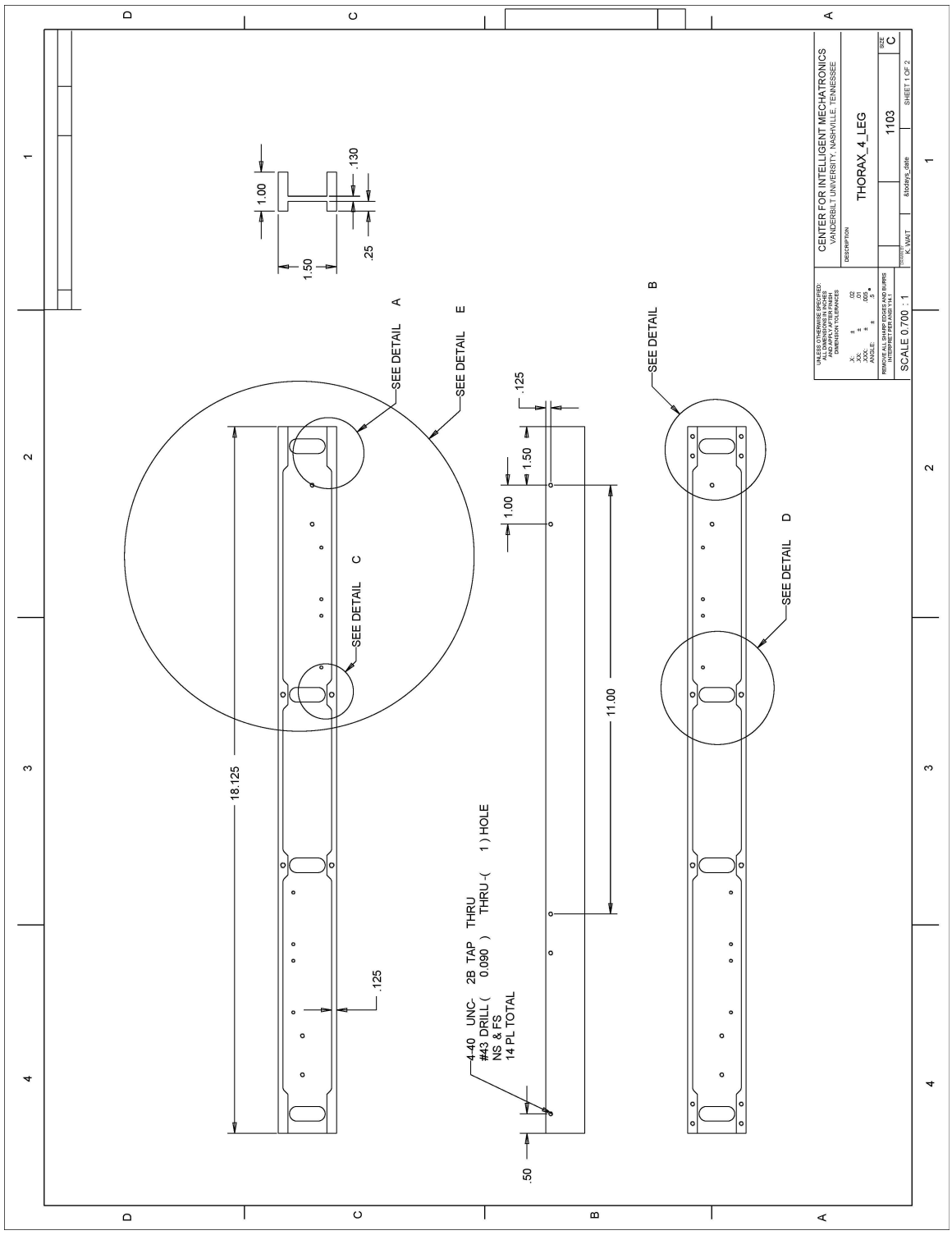
CENTER FOR INTELLIGENT MECHATRONICS
VANDERBILT UNIVERSITY, NASHVILLE, TENNESSEE
DESCRIPTION
THORAX_4_LEG
1103
SIZE C
SHEET 1 OF 2
K_WATT
&tolsharp_date
SCALE 0.700 : 1
UNLESS OTHERWISE SPECIFIED:
ALL DIMENSIONS IN INCHES
AND APPLY AFTER FINISH
DIMENSION TOLERANCES
REMOVE ALL SHARP EDGES AND BURRS
BREAK ALL EDGES .XX
SEE DETAIL A
SEE DETAIL E
SEE DETAIL C
SEE DETAIL B
SEE DETAIL D
18.125
.125
1.00
.130
.25
1.50
.125
1.50
1.00
11.00
.50
4-40 UNC- 2B TAP THRU
#43 DRILL (0.090) THRU -(1) HOLE
NS & FS
14 PL TOTAL

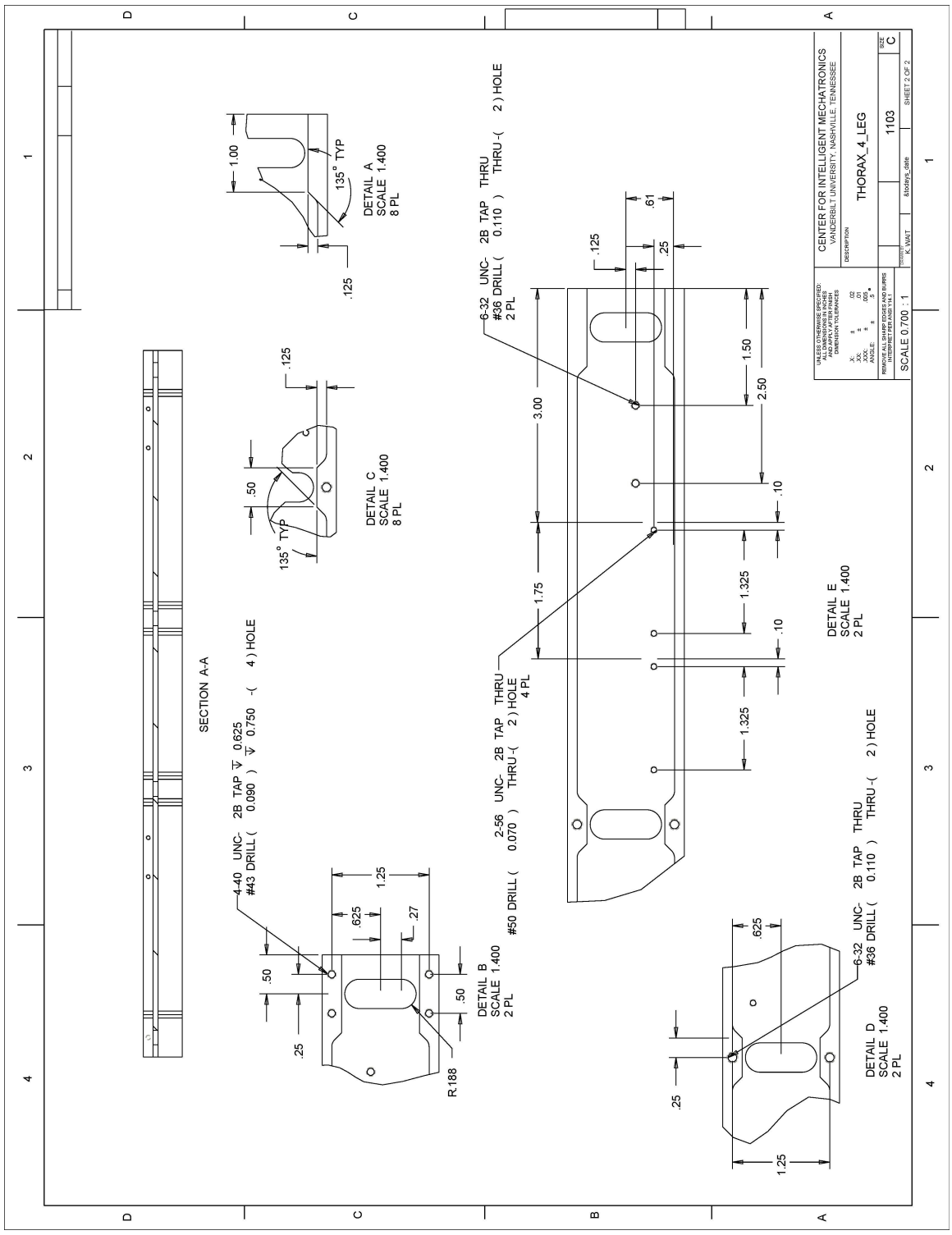
CENTER FOR INTELLIGENT MECHATRONICS
VANDERBILT UNIVERSITY, NASHVILLE, TENNESSEE
THORAX_4_LEG
1103
C
SCALE 0.700
SHEET 2 OF 2
K. WATT
SECTION A-A
DETAIL A
SCALE 1.400
8 PL
DETAIL B
SCALE 1.400
2 PL
DETAIL C
SCALE 1.400
8 PL
DETAIL D
SCALE 1.400
2 PL
DETAIL E
SCALE 1.400
2 PL
#50 DRILL (0.070) THRU-(2) HOLE
4 PL
2-56 UNC- 2B TAP THRU
#43 DRILL (0.090) ↧ 0.750 -(4) HOLE
4-40 UNC- 2B TAP ↧ 0.625
#36 DRILL (0.110) THRU-(2) HOLE
6-32 UNC- 2B TAP THRU
#36 DRILL (0.110) THRU-(2) HOLE
6-32 UNC- 2B TAP THRU
135° TYP
R.188

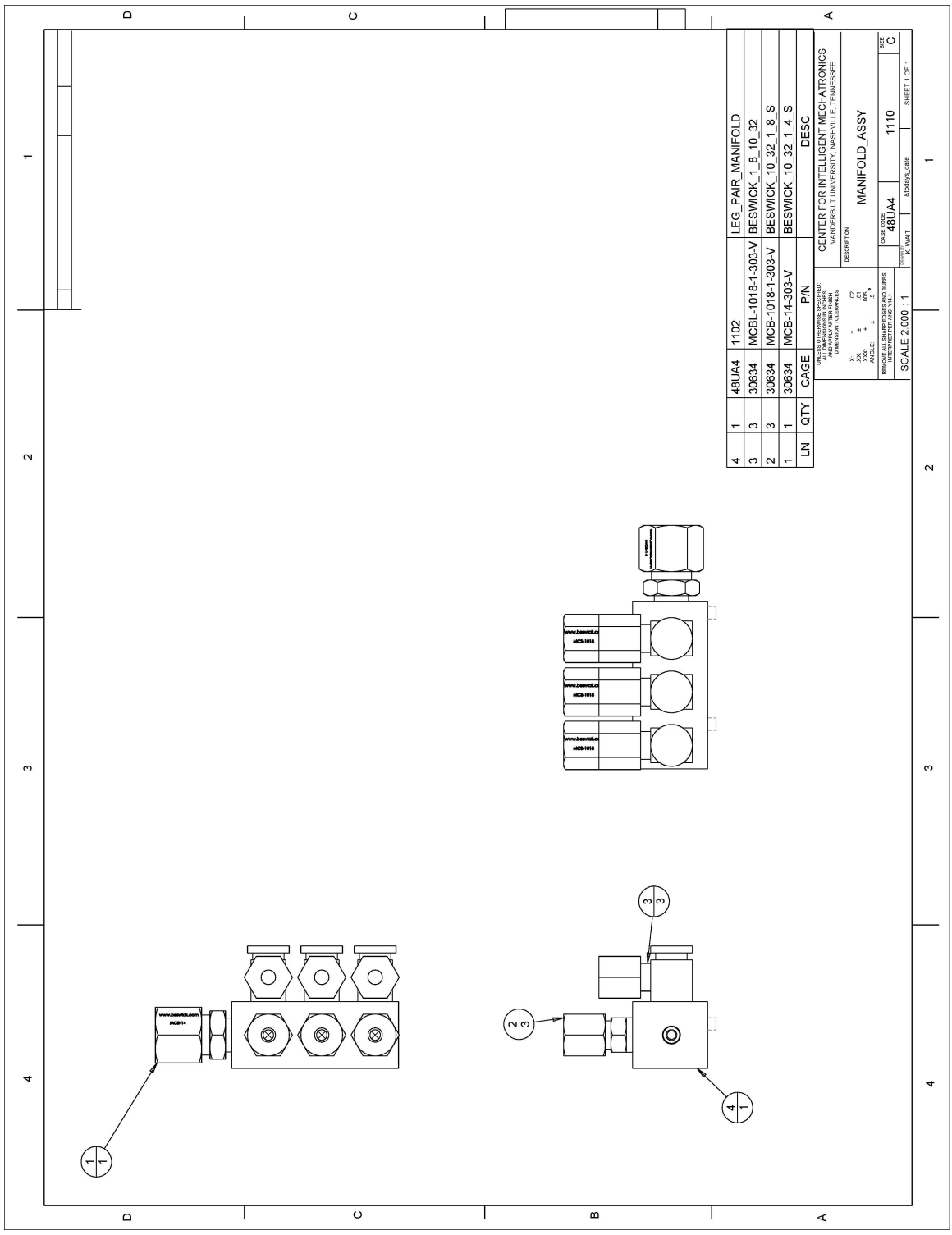
LEG_PAIR_MANIFOLD
BESWICK_1_8_10_32
BESWICK_10_32_1_8_S
BESWICK_10_32_1_4_S
DESC
MCBL-1018-I-303-V
MCB-1018-I-303-V
MCB-14-303-V
P/N
1102
48UA4
30634
30634
30634
CAGE
4
3
2
1
LN
1
3
3
1
QTY
CENTER FOR INTELLIGENT MECHATRONICS
VANDERBILT UNIVERSITY, NASHVILLE, TENNESSEE
MANIFOLD_ASSY
48UA4
1110
C
K. WATT
SCALE 2.000 : 1
SHEET 1 OF 1

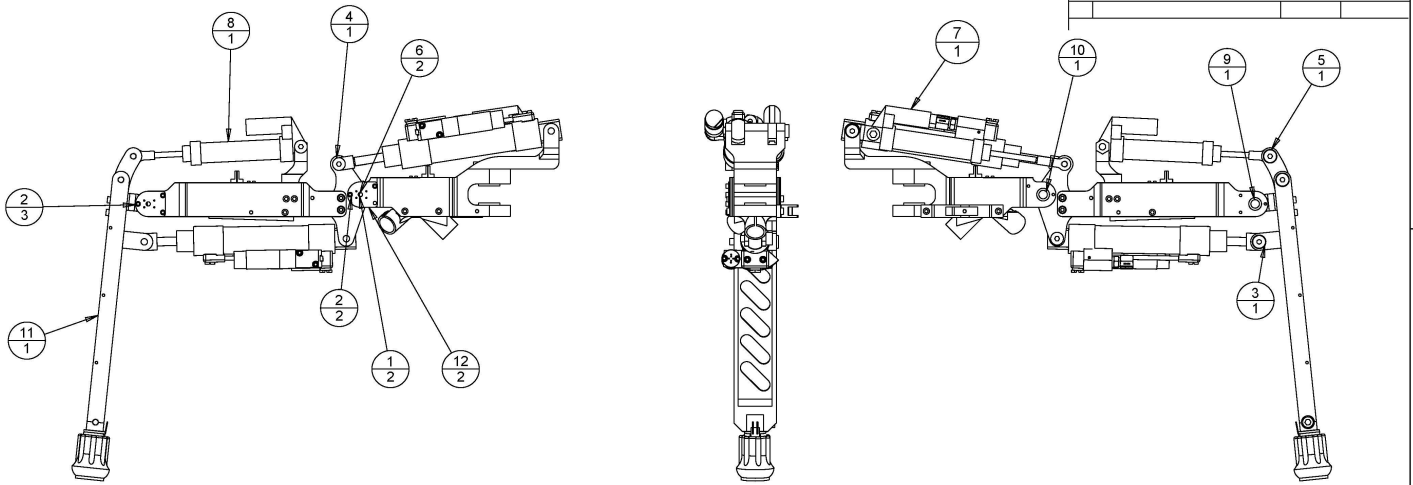

LN	QTY	CAGE	P/N	DESC
12	2			BETA_POT_COVER
11	1	48UA4	1700	TIBIA_ASSY_REVA
10	1	48UA4	1608	FEMUR_COXA_SHAFT
9	1	48UA4	1604	FEMUR_TIBIA_SHAFT
8	1	48UA4	1600	FEMUR_CHANNEL_ASSY_REVB
7	1	48UA4	1500	COXA_ASSY_REVA
6	2	2V507	98296A027	SPRING_PIN_1_16OD_1_2L
5	1	2V507	94035A537	SHLDR_SCREW_1_4_OD_1_2_L
4	1	2V507	92012A542	SHLDR_SCREW_1_4_OD_1_L
3	1	2V507	91259A541	SHLDR_SCREW_1_4_OD_7_8_L
2	5	2V507	91251A079	SHCS_2_56_3_8L
1	2	1JN02	688-RDC503013A	MOUSER_POT

NOTES:
1. INSERT LN 1 INTO LN 12 BEFORE ATTACHING
2. ALIGN LN 9 AND LN 10 SO THAT FLAT FACE OF PROTRUSION FACES DISTALLY
3. INSERT LN 6 THROUGH ALIGNED HOLES IN LNs 8 & 10 AND LNs 9 & 11 RESPECTIVELY
4. LNs 1, 9, 10, AND 12 SHOULD ATTACH TO SIDE OF ASSEMBLY SHOWN FOR FRONT RIGHT AND REAR LEFT LEGS AND THE OPPOSITE SIDE OF THE ASSEMBLY FOR FRONT LEFT AND REAR RIGHT LEGS

UNLESS OTHERWISE SPECIFIED: ALL DIMENSIONS IN INCHES AND APPLY AFTER FINISH
DIMENSION TOLERANCES
.X: ± .02
.XX: ± .01
.XXX: ± .005
ANGLE: ± .5°

REMOVE ALL SHARP EDGES AND BURRS
INTERPRET PER ANSI Y14.1

SCALE 0.500 : 1

CENTER FOR INTELLIGENT MECHATRONICS
VANDERBILT UNIVERSITY, NASHVILLE, TENNESSEE

DESCRIPTION
LEG_ASSY_REVB

CAGE CODE		SIZE
48UA4	1200	C

DRAWN BY		
K. WAIT	&todays_date	SHEET 1 OF 1

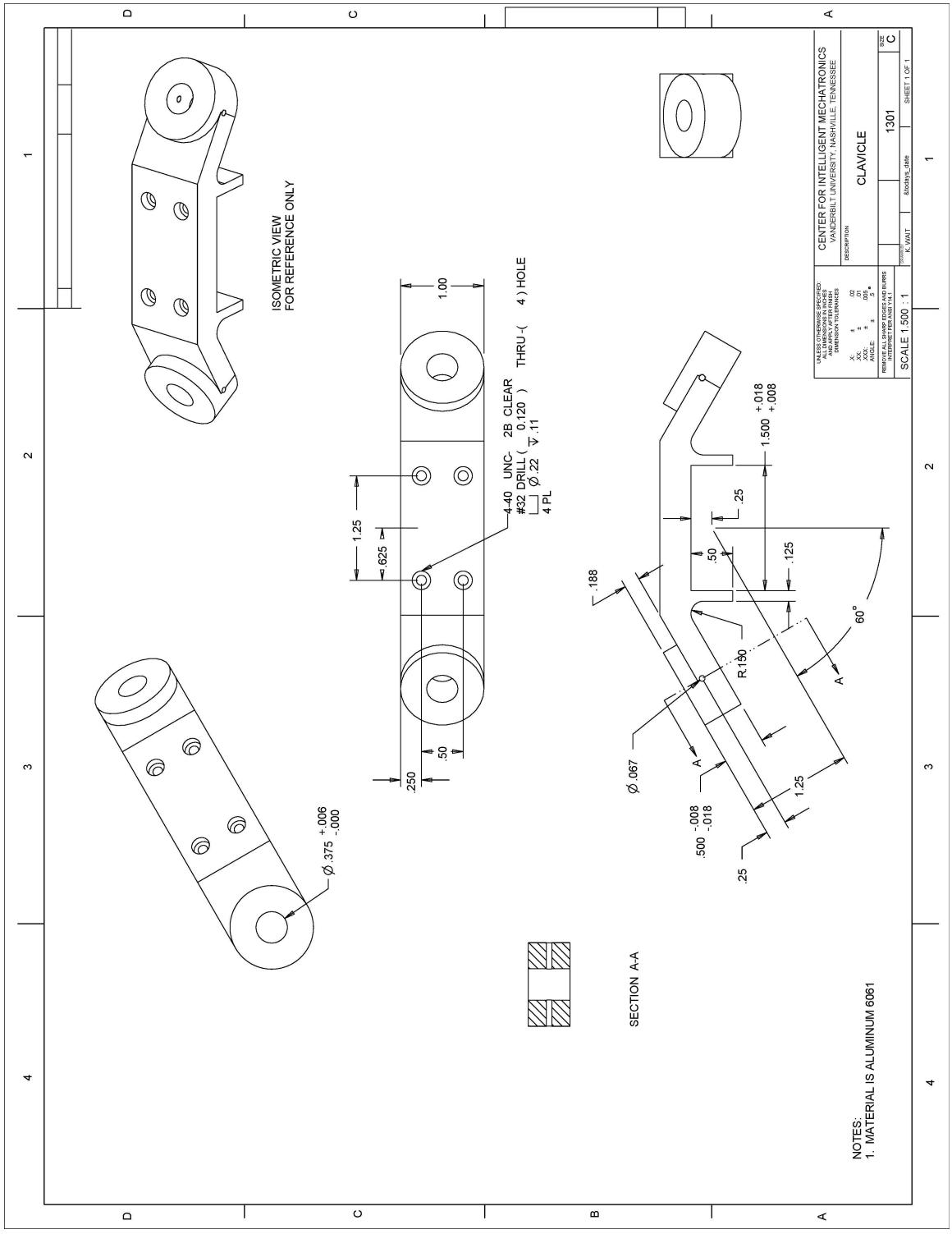
ISOMETRIC VIEW
FOR REFERENCE ONLY
4-40 UNC- 2B CLEAR
#32 DRILL (0.120) THRU -(4) HOLE
⌴ Ø.22 ↧.11
4 PL
1.00
1.25
.625
.250
.50
Ø.375 +.006 -.000
SECTION A-A
.188
Ø.067
.500 -.008 -.018
.25
1.25
R.130
60°
.50
.25
.125
1.500 +.018 +.008
NOTES:
1. MATERIAL IS ALUMINUM 6061
CENTER FOR INTELLIGENT MECHATRONICS
VANDERBILT UNIVERSITY, NASHVILLE, TENNESSEE
DESCRIPTION
CLAVICLE
1301
SIZE C
SCALE 1.500
SHEET 1 OF 1
K. WATT
&thickness_date
UNLESS OTHERWISE SPECIFIED:
ALL DIMENSIONS IN INCHES
AND APPLY AFTER FINISH
DIMENSION TOLERANCES
REMOVE ALL SHARP EDGES AND BURRS
FINISH: ANODIZE ALL

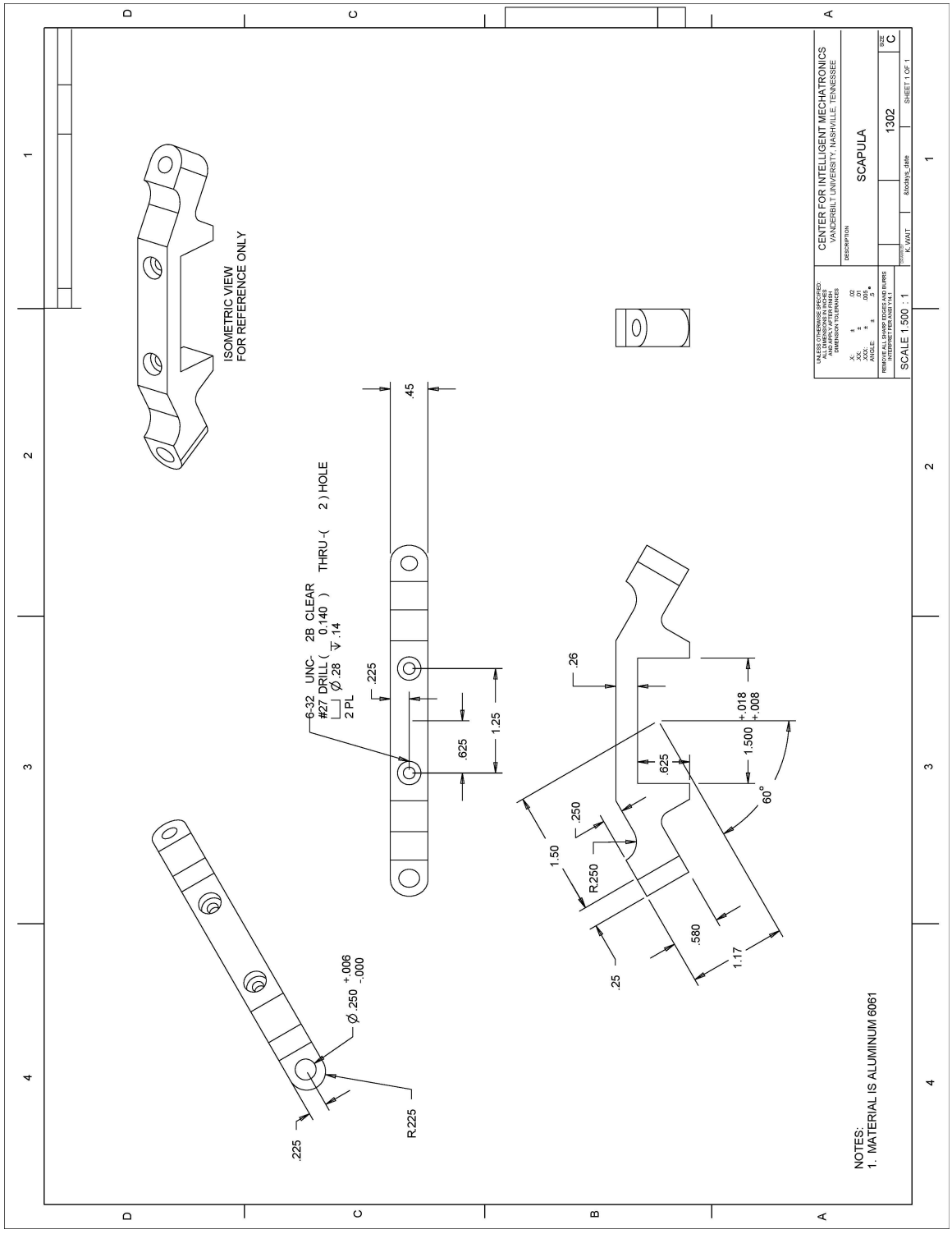
ISOMETRIC VIEW
FOR REFERENCE ONLY
6-32 UNC- 2B CLEAR
#27 DRILL (0.140) THRU -(2) HOLE
2 PL
Ø .28 ↧ .14
.225
.45
.625
1.25
.26
.625
1.500 +.018 -.008
60°
1.50
.250
R.250
.580
1.17
.25
Ø .250 +.006 -.000
R.225
.225
NOTES:
1. MATERIAL IS ALUMINUM 6061
CENTER FOR INTELLIGENT MECHATRONICS
VANDERBILT UNIVERSITY, NASHVILLE, TENNESSEE
DESCRIPTION
SCAPULA
1302
SIZE C
SCALE 1.500
SHEET 1 OF 1
K. WATT
&todays_date
UNLESS OTHERWISE SPECIFIED:
ALL DIMENSIONS IN INCHES
AND APPLY AFTER FINISH
DIMENSION TOLERANCES
REMOVE ALL BURRS AND SHARP EDGES
BREAK SHARP EDGES .XX
A
B
C
D
1
2
3
4

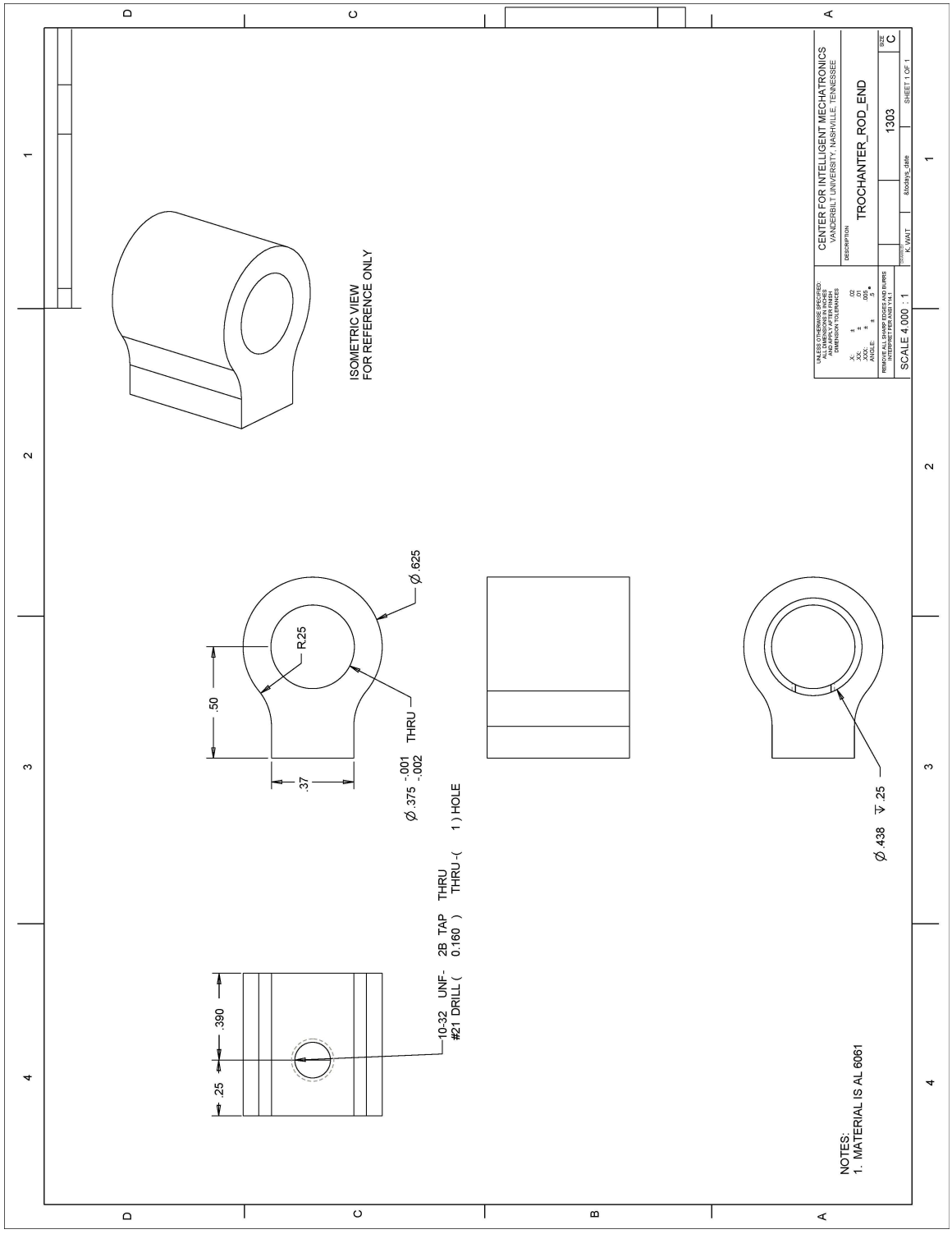
ISOMETRIC VIEW
FOR REFERENCE ONLY
R.25
.50
.37
Ø.625
Ø.375 -.001 -.002 THRU
10-32 UNF- 2B TAP THRU
#21 DRILL (0.160) THRU -(1) HOLE
.25
.390
Ø.438 ⩛ .25
NOTES:
1. MATERIAL IS AL 6061
CENTER FOR INTELLIGENT MECHATRONICS
VANDERBILT UNIVERSITY, NASHVILLE, TENNESSEE
TROCHANTER_ROD_END
1303
SIZE C
SCALE 4.000
SHEET 1 OF 1
K. WATT

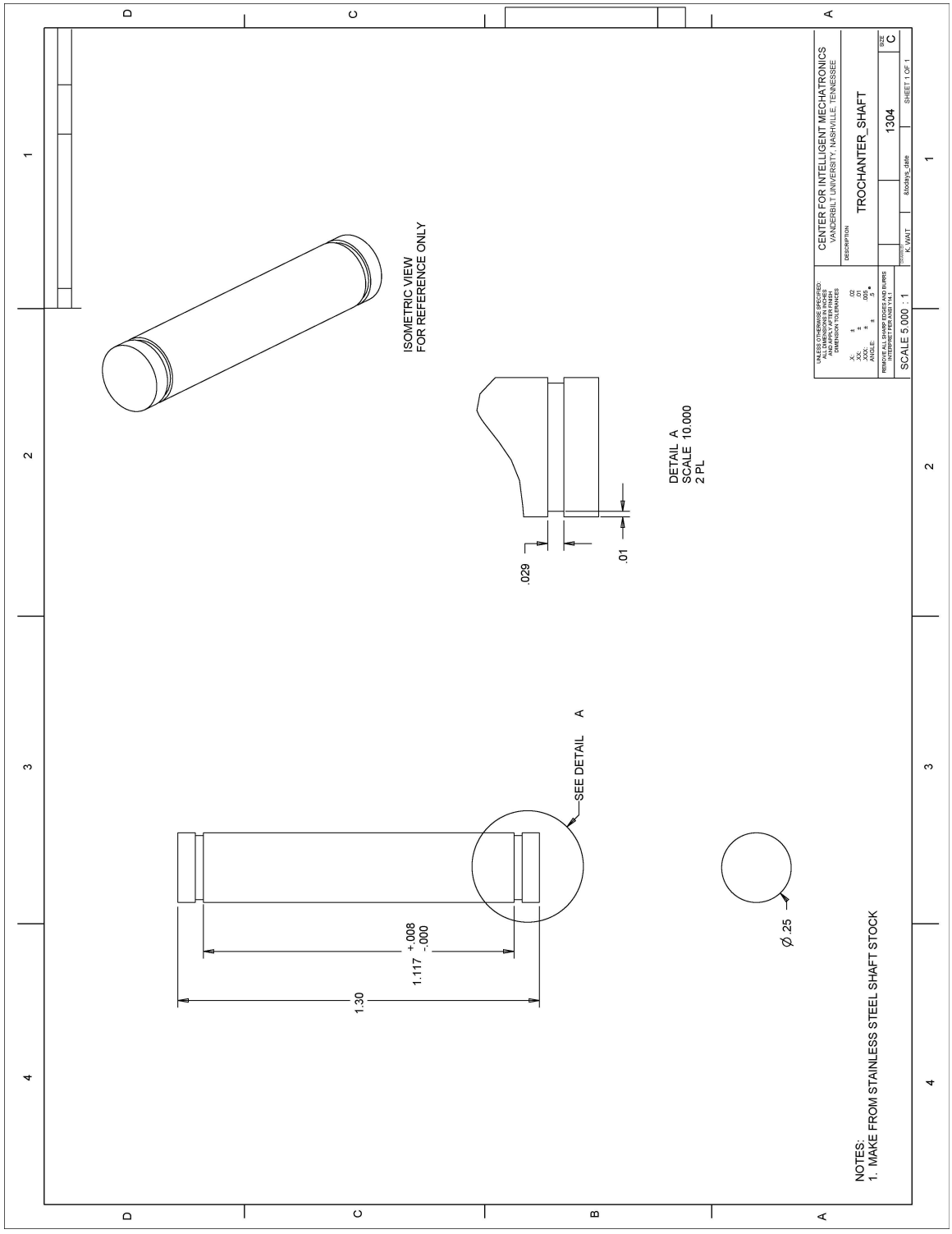
CENTER FOR INTELLIGENT MECHATRONICS
VANDERBILT UNIVERSITY, NASHVILLE, TENNESSEE
TROCHANTER_SHAFT
1304
SIZE C
SCALE 5.000 : 1
SHEET 1 OF 1
K. WATT
&tocharp_date
ISOMETRIC VIEW
FOR REFERENCE ONLY
DETAIL A
SCALE 10.000
2 PL
.029
.01
SEE DETAIL A
1.30
1.117 +.008 -.000
Ø.25
NOTES:
1. MAKE FROM STAINLESS STEEL SHAFT STOCK

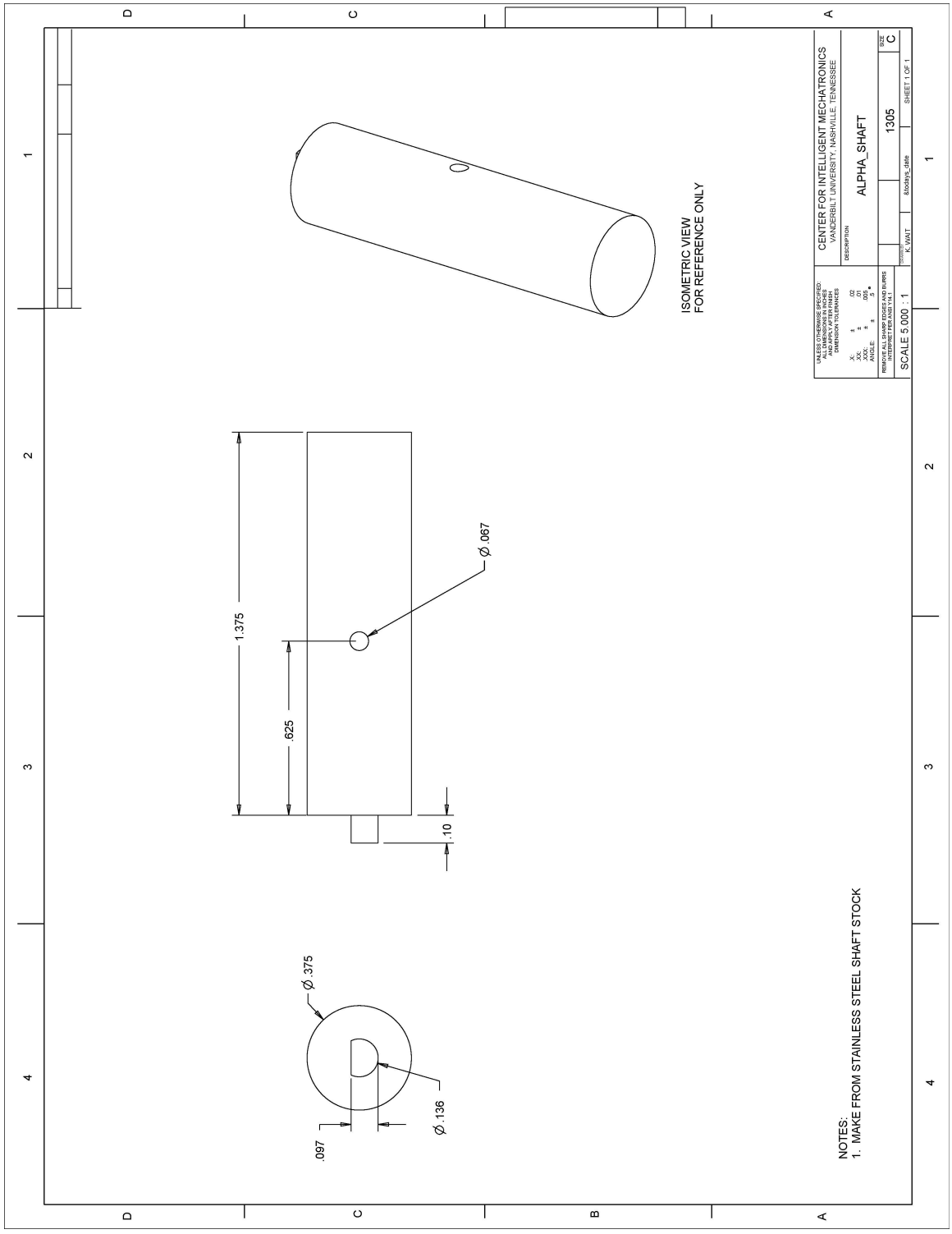
ISOMETRIC VIEW
FOR REFERENCE ONLY
1.375
.625
Ø.067
.10
Ø.375
Ø.136
.097
NOTES:
1. MAKE FROM STAINLESS STEEL SHAFT STOCK
CENTER FOR INTELLIGENT MECHATRONICS
VANDERBILT UNIVERSITY, NASHVILLE, TENNESSEE
ALPHA_SHAFT
1305
SCALE 5.000 : 1
SHEET 1 OF 1
K. WATT

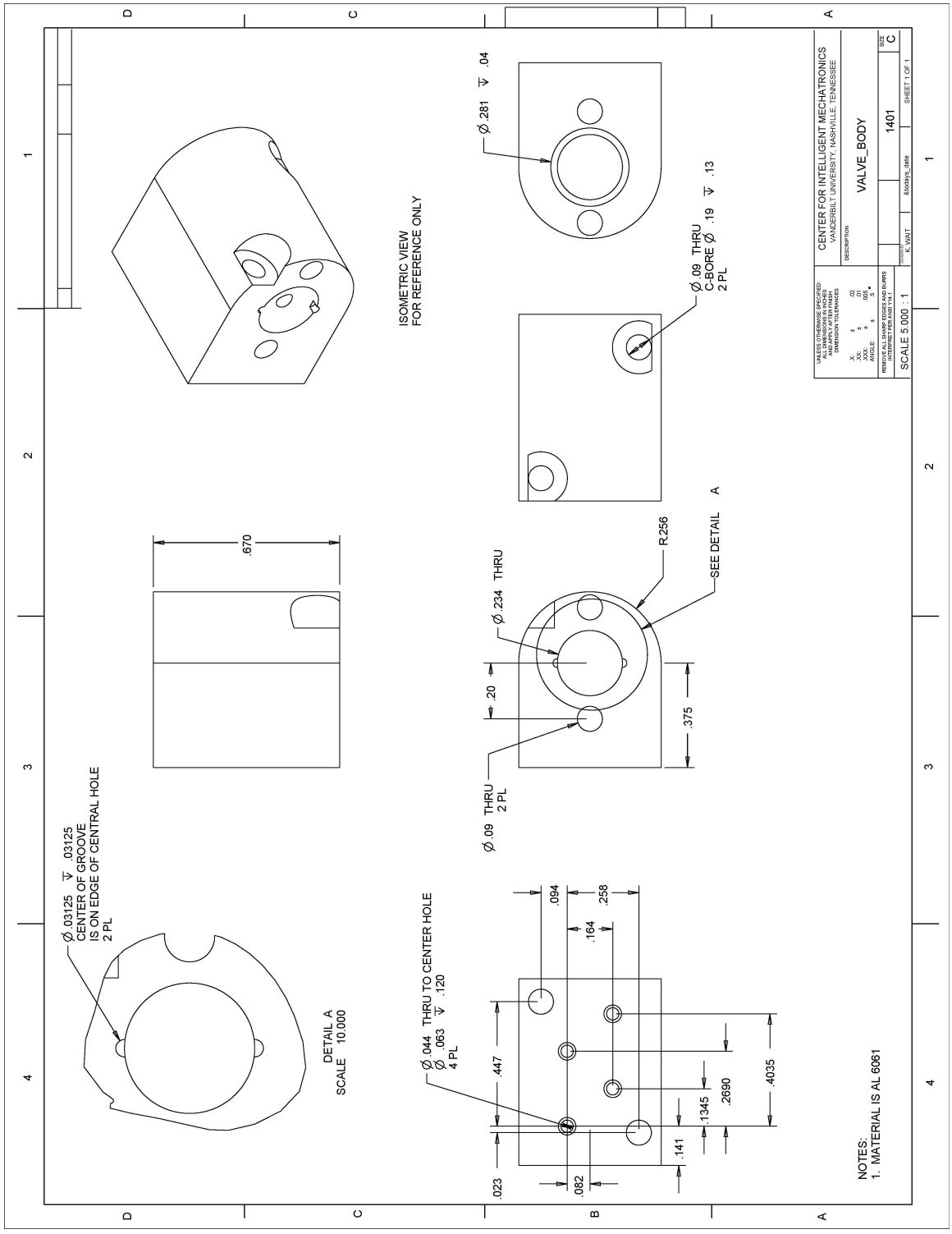
Ø .03125 ⊽ .03125
CENTER OF GROOVE
IS ON EDGE OF CENTRAL HOLE
2 PL
DETAIL A
SCALE 10.000
.670
ISOMETRIC VIEW
FOR REFERENCE ONLY
Ø .281 ⊽ .04
Ø .09 THRU
C-BORE Ø .19 ⊽ .13
2 PL
Ø .234 THRU
R.256
SEE DETAIL A
.20
.375
Ø .09 THRU
2 PL
Ø .044 THRU TO CENTER HOLE
Ø .063 ⊽ .120
4 PL
.094
.258
.164
.447
.1345
.2690
.4035
.141
.023
.082
NOTES:
1. MATERIAL IS AL 6061
CENTER FOR INTELLIGENT MECHATRONICS
VANDERBILT UNIVERSITY, NASHVILLE, TENNESSEE
DESCRIPTION
VALVE_BODY
1401
SIZE C
SCALE 5.000
SHEET 1 OF 1
K. WATT
&todays_date

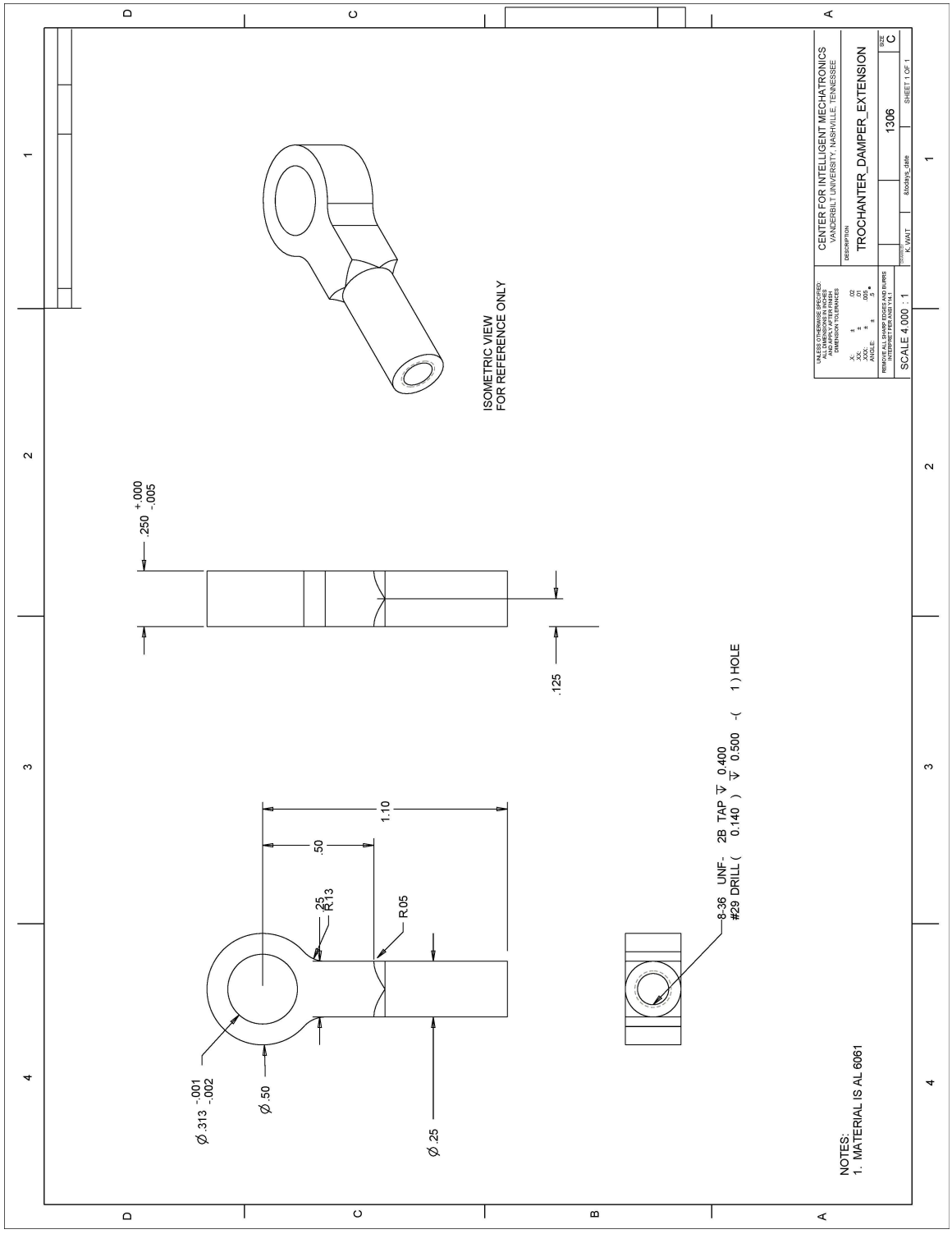
CENTER FOR INTELLIGENT MECHATRONICS
VANDERBILT UNIVERSITY, NASHVILLE, TENNESSEE
DESCRIPTION
TROCHANTER_DAMPER_EXTENSION
1306
SIZE C
SCALE 4.000 : 1
SHEET 1 OF 1
K_WATT
&tolsharp_date
ISOMETRIC VIEW
FOR REFERENCE ONLY
.250 +.000 -.005
.125
1.10
.50
.25
R.13
R.05
Ø .313 -.001 -.002
Ø .50
Ø .25
8-36 UNF- 2B TAP ⌀ 0.400
#29 DRILL (0.140) ⌀ 0.500 -(1) HOLE
NOTES:
1. MATERIAL IS AL 6061

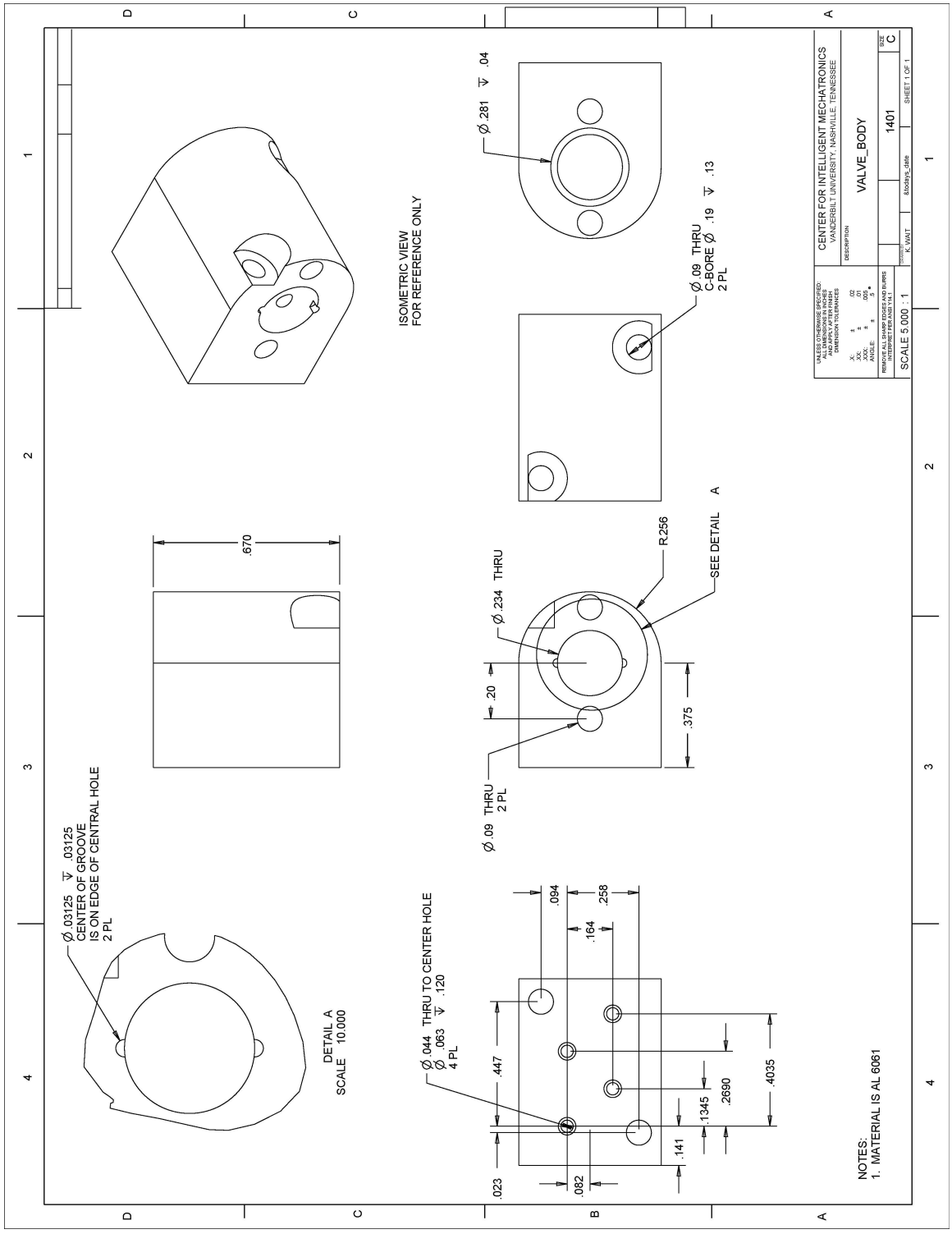
ISOMETRIC VIEW
FOR REFERENCE ONLY
Ø .03125 ⩛ .03125
CENTER OF GROOVE
IS ON EDGE OF CENTRAL HOLE
2 PL
DETAIL A
SCALE 10.000
.670
Ø .044 THRU TO CENTER HOLE
Ø .063 ⩛ .120
4 PL
.094
.258
.164
.447
.2690
.4035
.1345
.141
.023
.082
Ø .09 THRU
2 PL
Ø .234 THRU
.20
.375
R.256
SEE DETAIL A
Ø .281 ⩛ .04
Ø .09 THRU
C-BORE Ø .19 ⩛ .13
2 PL
NOTES:
1. MATERIAL IS AL 6061
CENTER FOR INTELLIGENT MECHATRONICS
VANDERBILT UNIVERSITY, NASHVILLE, TENNESSEE
VALVE_BODY
1401
SIZE C
SCALE 5.000
SHEET 1 OF 1
K. WATT
&todays_date

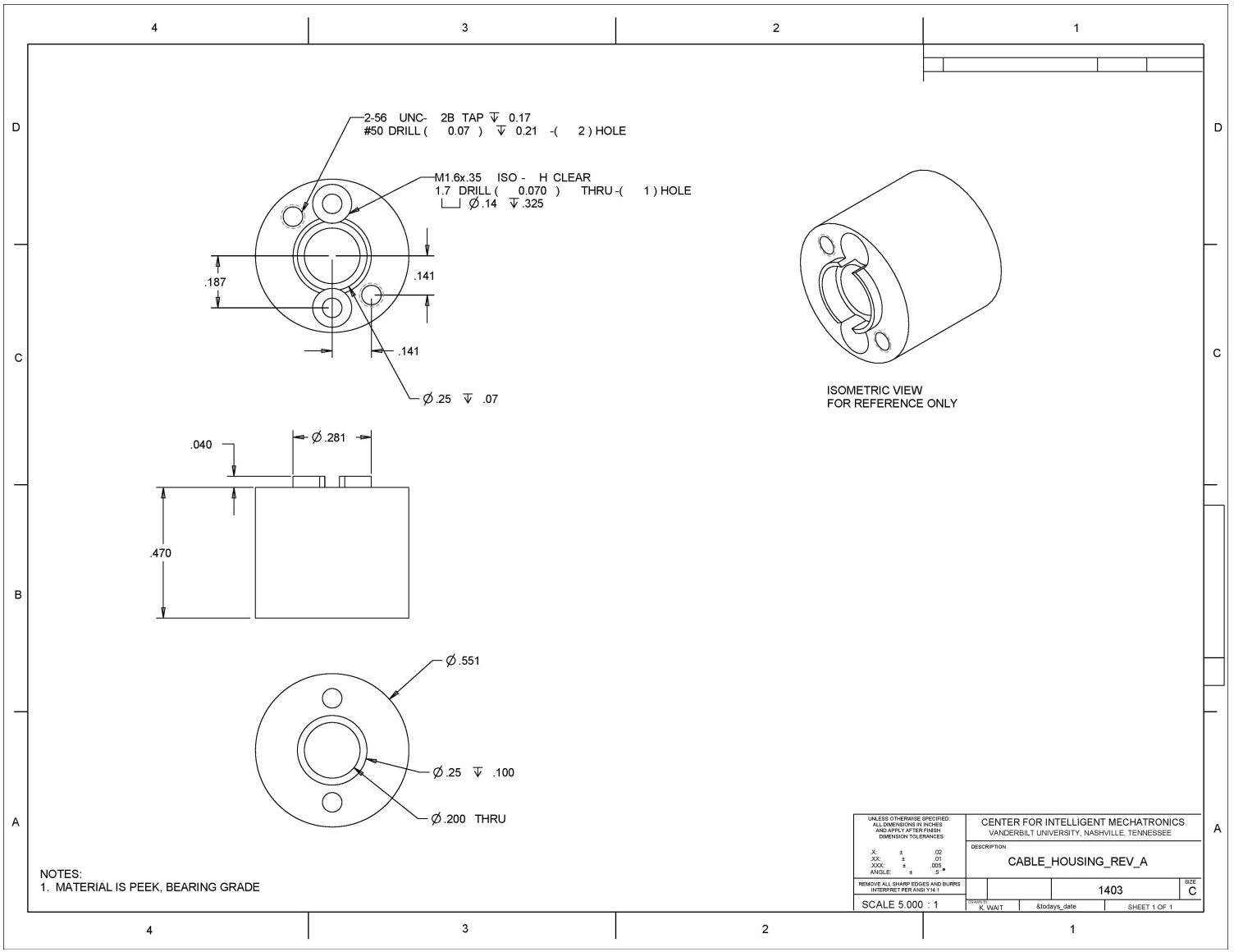
2-56 UNC- 2B TAP ↧ 0.17
#50 DRILL (0.07) ↧ 0.21 -(2) HOLE
M1.6x.35 ISO - H CLEAR
1.7 DRILL (0.070) THRU -(1) HOLE
⌴ Ø .14 ↧ .325
.187
.141
.141
Ø .25 ↧ .07
ISOMETRIC VIEW
FOR REFERENCE ONLY
.040
Ø .281
.470
Ø .551
Ø .25 ↧ .100
Ø .200 THRU
NOTES:
1. MATERIAL IS PEEK, BEARING GRADE
UNLESS OTHERWISE SPECIFIED:
ALL DIMENSIONS IN INCHES
AND APPLY AFTER FINISH
DIMENSION TOLERANCES
.X: ± .02
.XX: ± .01
.XXX: ± .005
ANGLE: ± .5 °
REMOVE ALL SHARP EDGES AND BURRS
INTERPRET PER ANSI Y14.1
SCALE 5.000 : 1
CENTER FOR INTELLIGENT MECHATRONICS
VANDERBILT UNIVERSITY, NASHVILLE, TENNESSEE
DESCRIPTION
CABLE_HOUSING_REV_A
1403
SIZE C
DRAWN BY
K. WAIT
&todays_date
SHEET 1 OF 1

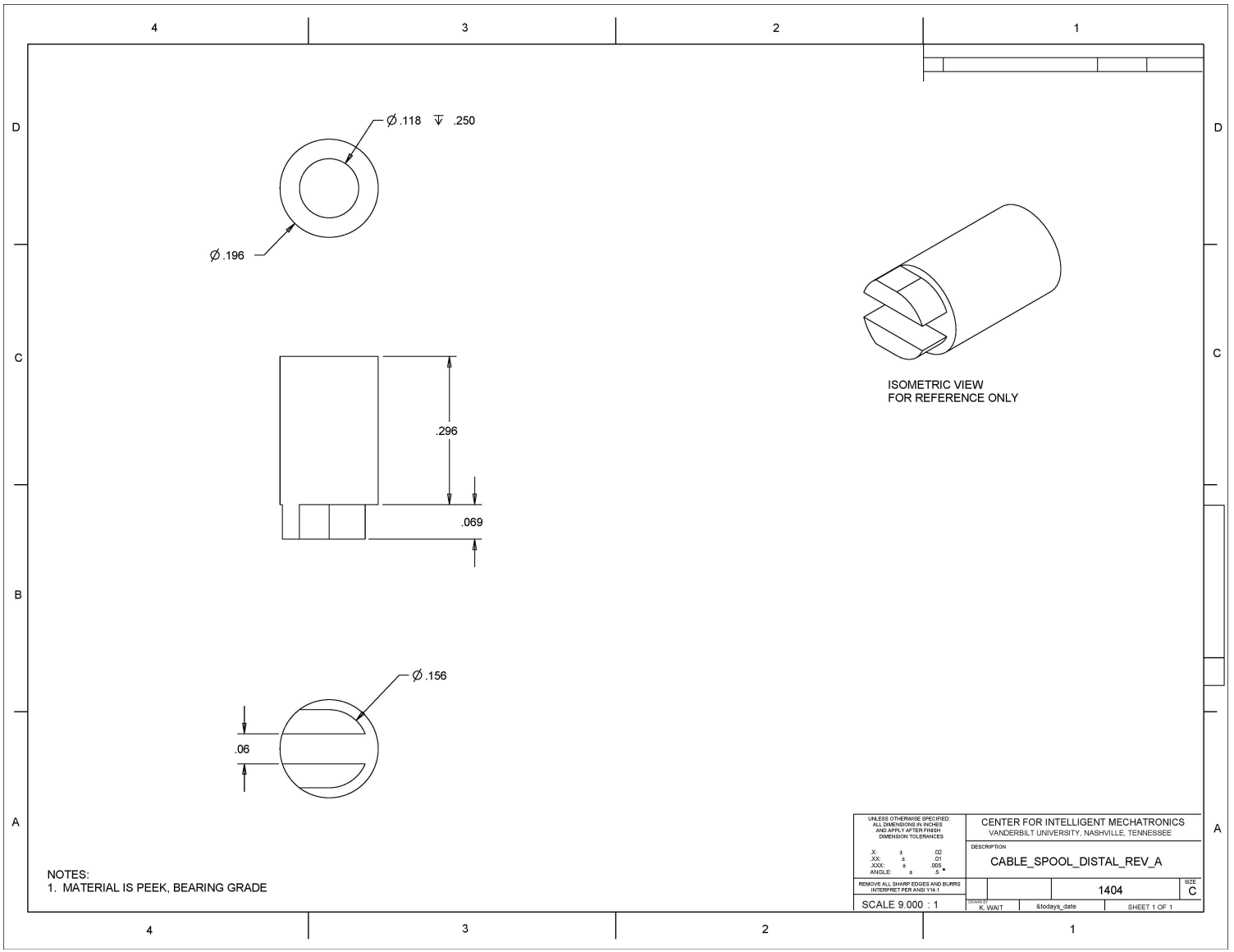
4
3
2
1
D
C
B
A
Ø .118 ⌀ .250
Ø .196
.296
.069
Ø .156
.06
ISOMETRIC VIEW
FOR REFERENCE ONLY
NOTES:
1. MATERIAL IS PEEK, BEARING GRADE
UNLESS OTHERWISE SPECIFIED:
ALL DIMENSIONS IN INCHES
AND APPLY AFTER FINISH
DIMENSION TOLERANCES
.X ± .02
.XX ± .01
.XXX ± .005
ANGLE ± .5°
REMOVE ALL SHARP EDGES AND BURRS
INTERPRET PER ANSI Y14.1
SCALE 9.000 : 1
CENTER FOR INTELLIGENT MECHATRONICS
VANDERBILT UNIVERSITY, NASHVILLE, TENNESSEE
DESCRIPTION
CABLE_SPOOL_DISTAL_REV_A
1404
SIZE
C
DRAWN BY
K. WAIT
&todays_date
SHEET 1 OF 1

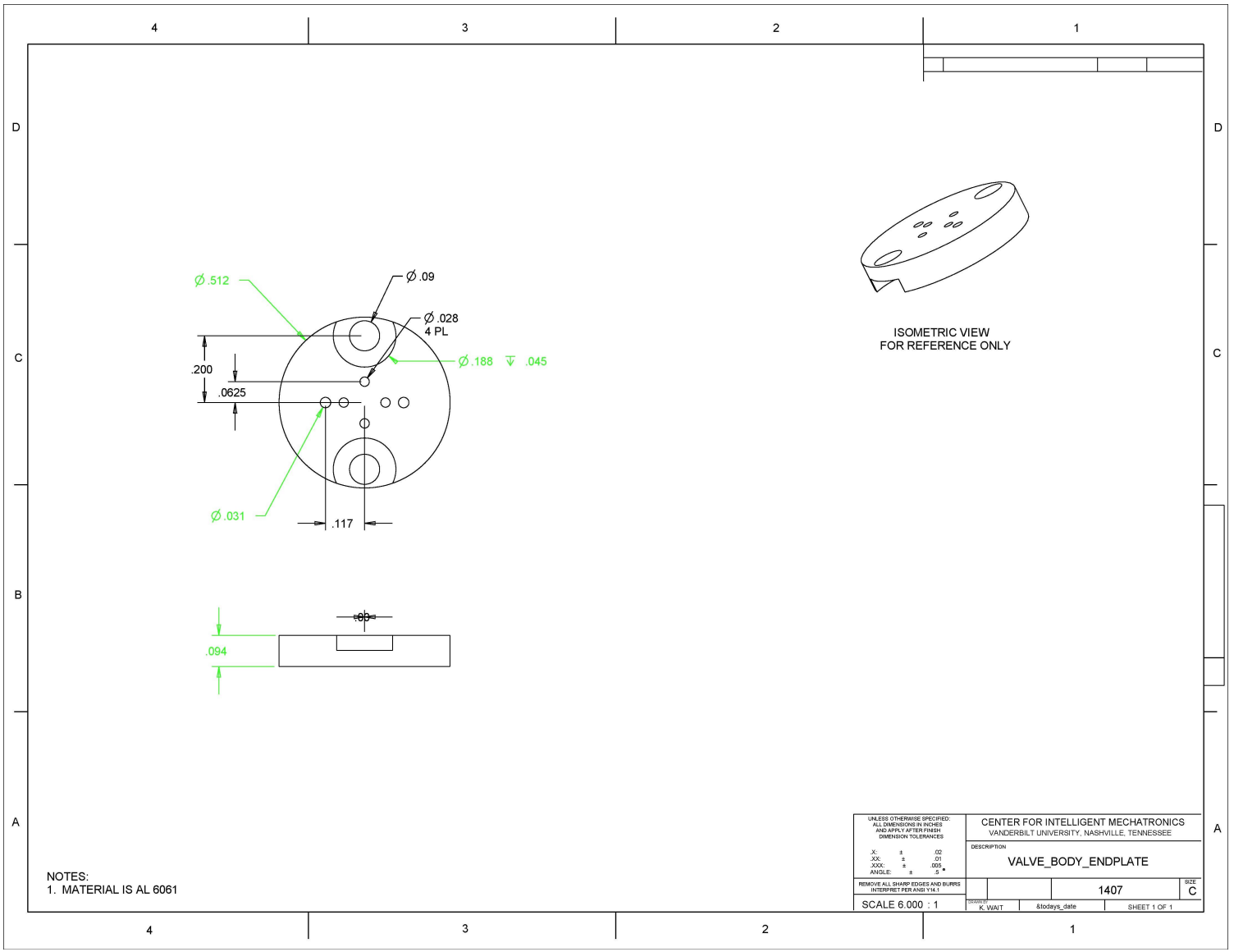
4
3
2
1
D
C
B
A
Ø .512
Ø .09
Ø .028
4 PL
Ø .188 ↧ .045
.200
.0625
Ø .031
.117
.094
ISOMETRIC VIEW
FOR REFERENCE ONLY
NOTES:
1. MATERIAL IS AL 6061
UNLESS OTHERWISE SPECIFIED:
ALL DIMENSIONS IN INCHES
AND APPLY AFTER FINISH
DIMENSION TOLERANCES
.X: ± .02
.XX: ± .01
.XXX: ± .005
ANGLE: ± .5 °
REMOVE ALL SHARP EDGES AND BURRS
INTERPRET PER ANSI Y14.1
SCALE 6.000 : 1
CENTER FOR INTELLIGENT MECHATRONICS
VANDERBILT UNIVERSITY, NASHVILLE, TENNESSEE
DESCRIPTION
VALVE_BODY_ENDPLATE
1407
SIZE
C
DRAWN BY
K. WAIT
&todays_date
SHEET 1 OF 1

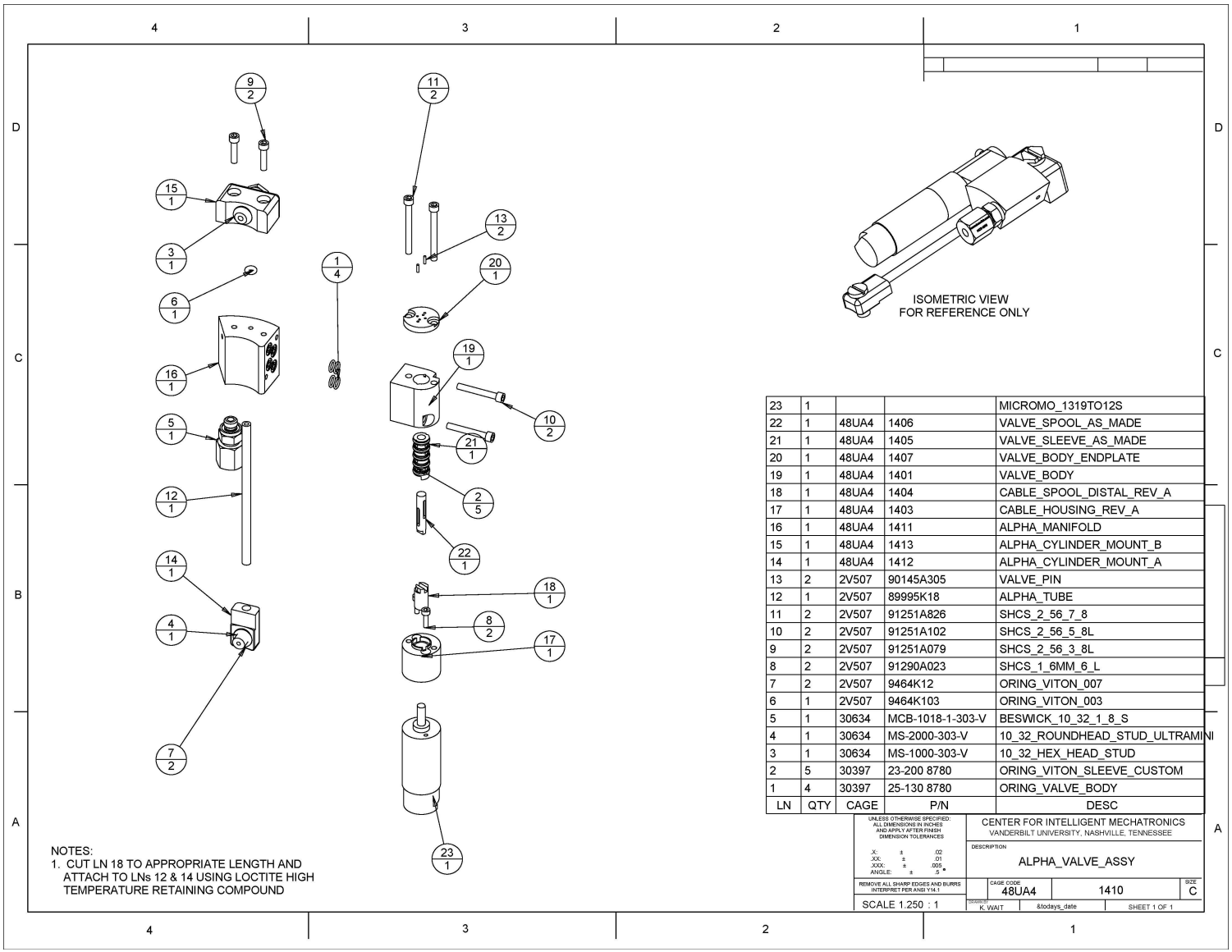

LN	QTY	CAGE	P/N	DESC
23	1			MICROMO_1319TO12S
22	1	48UA4	1406	VALVE_SPOOL_AS_MADE
21	1	48UA4	1405	VALVE_SLEEVE_AS_MADE
20	1	48UA4	1407	VALVE_BODY_ENDPLATE
19	1	48UA4	1401	VALVE_BODY
18	1	48UA4	1404	CABLE_SPOOL_DISTAL_REV_A
17	1	48UA4	1403	CABLE_HOUSING_REV_A
16	1	48UA4	1411	ALPHA_MANIFOLD
15	1	48UA4	1413	ALPHA_CYLINDER_MOUNT_B
14	1	48UA4	1412	ALPHA_CYLINDER_MOUNT_A
13	2	2V507	90145A305	VALVE_PIN
12	1	2V507	89995K18	ALPHA_TUBE
11	2	2V507	91251A826	SHCS_2_56_7_8
10	2	2V507	91251A102	SHCS_2_56_5_8L
9	2	2V507	91251A079	SHCS_2_56_3_8L
8	2	2V507	91290A023	SHCS_1_6MM_6_L
7	2	2V507	9464K12	ORING_VITON_007
6	1	2V507	9464K103	ORING_VITON_003
5	1	30634	MCB-1018-1-303-V	BESWICK_10_32_1_8_S
4	1	30634	MS-2000-303-V	10_32_ROUNDHEAD_STUD_ULTRAMINI
3	1	30634	MS-1000-303-V	10_32_HEX_HEAD_STUD
2	5	30397	23-200 8780	ORING_VITON_SLEEVE_CUSTOM
1	4	30397	25-130 8780	ORING_VALVE_BODY

NOTES:
1. CUT LN 18 TO APPROPRIATE LENGTH AND ATTACH TO LNs 12 & 14 USING LOCTITE HIGH TEMPERATURE RETAINING COMPOUND

UNLESS OTHERWISE SPECIFIED: ALL DIMENSIONS IN INCHES AND APPLY AFTER FINISH. DIMENSION TOLERANCES
.X: ± .02
.XX: ± .01
.XXX: ± .005
ANGLE: ± .5°

REMOVE ALL SHARP EDGES AND BURRS
INTERPRET PER ANSI Y14.1

SCALE 1.250 : 1

CENTER FOR INTELLIGENT MECHATRONICS
VANDERBILT UNIVERSITY, NASHVILLE, TENNESSEE

DESCRIPTION: ALPHA_VALVE_ASSY

CAGE CODE: 48UA4 | 1410 | SIZE C

DRAWN BY: K. WAIT | &todays_date | SHEET 1 OF 1

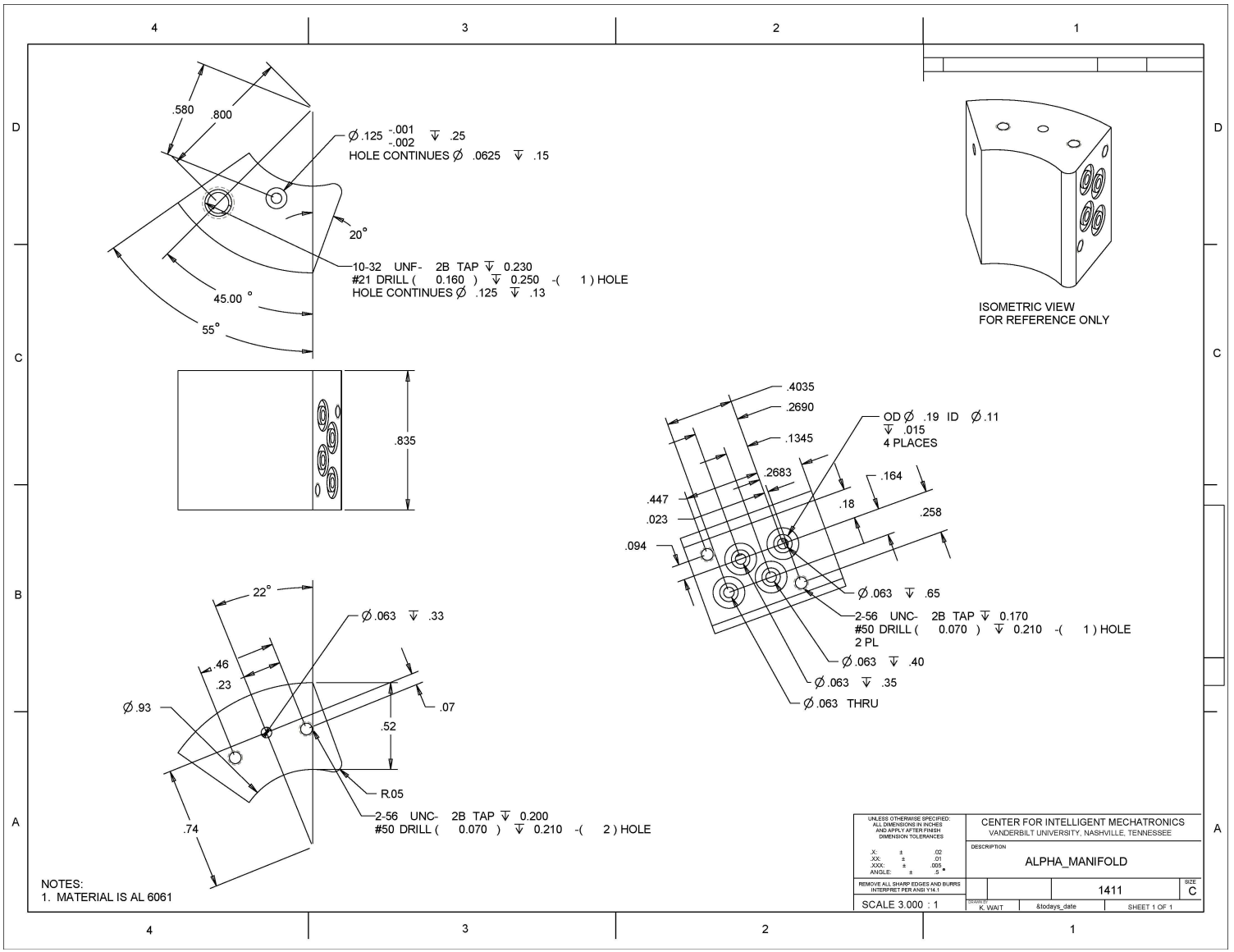
.580
.800
Ø .125 -.001 -.002 ↧ .25
HOLE CONTINUES Ø .0625 ↧ .15
20°
10-32 UNF- 2B TAP ↧ 0.230
#21 DRILL (0.160) ↧ 0.250 -(1) HOLE
HOLE CONTINUES Ø .125 ↧ .13
45.00 °
55°
.835
ISOMETRIC VIEW
FOR REFERENCE ONLY
.4035
.2690
.1345
.2683
.447
.023
.094
.164
.18
.258
OD Ø .19 ID Ø .11
↧ .015
4 PLACES
Ø .063 ↧ .65
2-56 UNC- 2B TAP ↧ 0.170
#50 DRILL (0.070) ↧ 0.210 -(1) HOLE
2 PL
Ø .063 ↧ .40
Ø .063 ↧ .35
Ø .063 THRU
22°
Ø .063 ↧ .33
.46
.23
Ø .93
.07
.52
R.05
.74
2-56 UNC- 2B TAP ↧ 0.200
#50 DRILL (0.070) ↧ 0.210 -(2) HOLE
NOTES:
1. MATERIAL IS AL 6061
UNLESS OTHERWISE SPECIFIED:
ALL DIMENSIONS IN INCHES
AND APPLY AFTER FINISH
DIMENSION TOLERANCES
.X ± .02
.XX ± .01
.XXX ± .005
ANGLE ± .5°
REMOVE ALL SHARP EDGES AND BURRS
INTERPRET PER ANSI Y14.1
SCALE 3.000 : 1
CENTER FOR INTELLIGENT MECHATRONICS
VANDERBILT UNIVERSITY, NASHVILLE, TENNESSEE
DESCRIPTION
ALPHA_MANIFOLD
1411
SIZE C
DRAWN BY K. WAIT
&todays_date
SHEET 1 OF 1

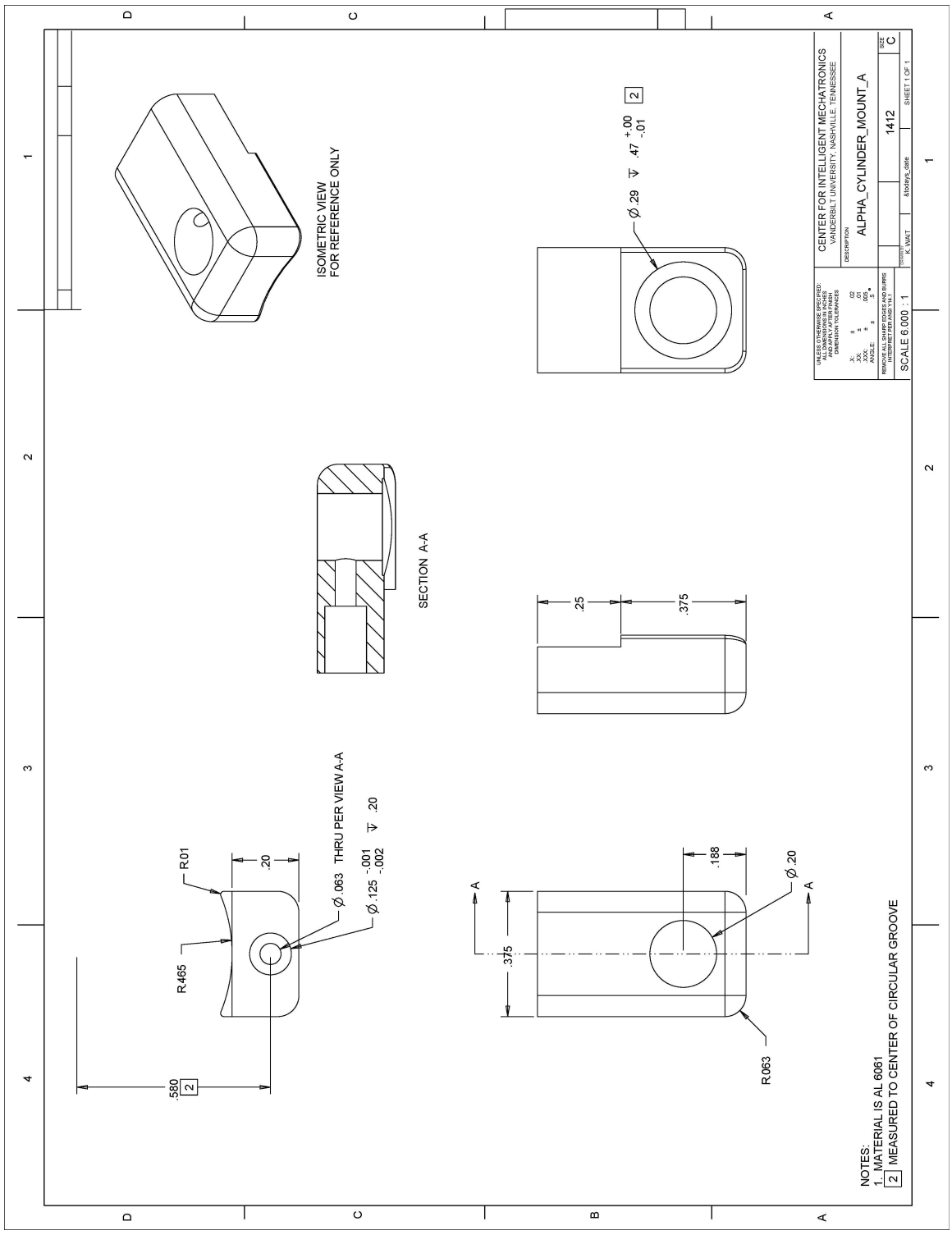
ISOMETRIC VIEW
FOR REFERENCE ONLY
SECTION A-A
Ø .29 ⌖ .47 +.00 -.01 2
.25
.375
R.01
.20
R.465
Ø .063 THRU PER VIEW A-A
Ø .125 +.001 -.002 ⌖ .20
.580 2
.375
.188
Ø .20
R.063
A
A
NOTES:
1. MATERIAL IS AL 6061
2 MEASURED TO CENTER OF CIRCULAR GROOVE
UNLESS OTHERWISE SPECIFIED:
ALL DIMENSIONS IN INCHES
AND APPLY AFTER FINISH
DIMENSION TOLERANCES
X: ± .02
XX: ± .01
XXX: ± .005
ANGLE: ± 5°
REMOVE ALL BURRS AND SHARP EDGES
FINISH: 125 RMS
SCALE 6.000 : 1
CENTER FOR INTELLIGENT MECHATRONICS
VANDERBILT UNIVERSITY, NASHVILLE, TENNESSEE
DESCRIPTION
ALPHA_CYLINDER_MOUNT_A
1412
SIZE C
DRAWN
K. WATT
&tookpts_date
SHEET 1 OF 1

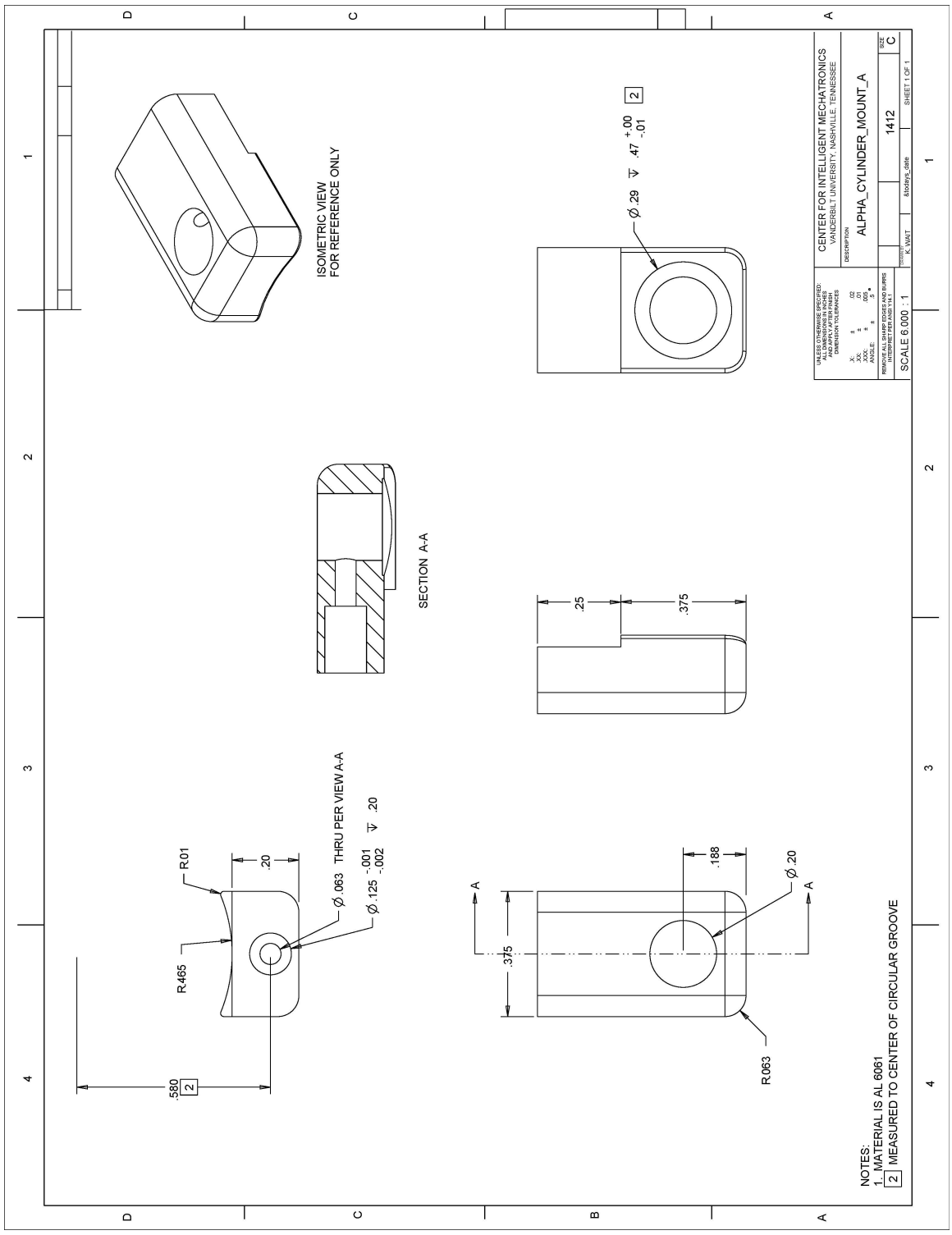
ISOMETRIC VIEW
FOR REFERENCE ONLY
SECTION A-A
Ø .29 ∀ .47 +.00 -.01 2
.25
.375
R.01
.20
R.465
Ø .063 THRU PER VIEW A-A
Ø .125 +.001 -.002 ∀ .20
.580 2
.375
.188
Ø .20
R.063
A
A
NOTES:
1. MATERIAL IS AL 6061
2 MEASURED TO CENTER OF CIRCULAR GROOVE
CENTER FOR INTELLIGENT MECHATRONICS
VANDERBILT UNIVERSITY, NASHVILLE, TENNESSEE
DESCRIPTION
ALPHA_CYLINDER_MOUNT_A
1412
SIZE C
SCALE 6.000 : 1
SHEET 1 OF 1
K_WATT
&tolerpts_date
UNLESS OTHERWISE SPECIFIED:
ALL DIMENSIONS IN INCHES
AND APPLY AFTER FINISH
DIMENSION TOLERANCES
REMOVE ALL SHARP EDGES AND BURRS
FINISH: 125 RMS

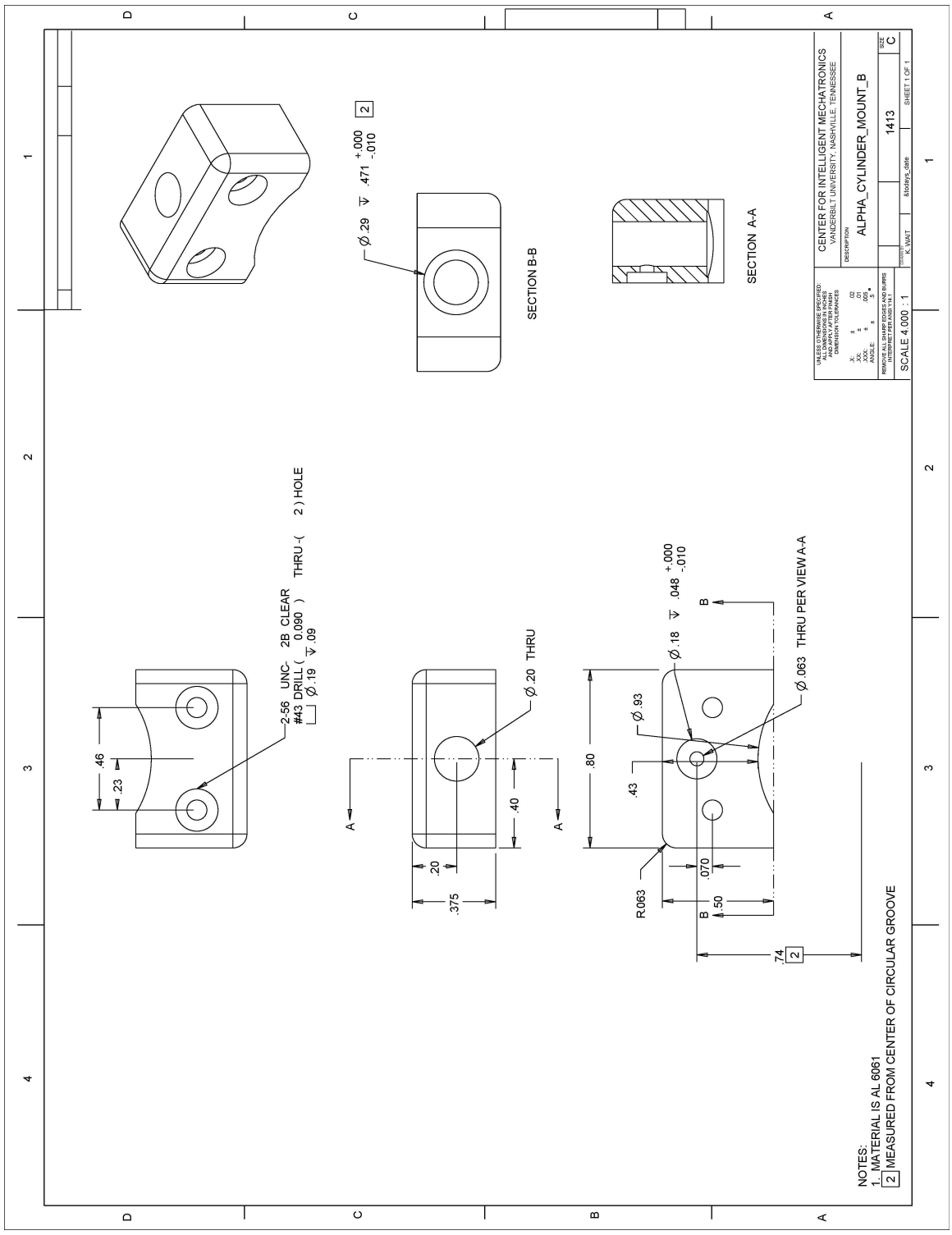
CENTER FOR INTELLIGENT MECHATRONICS
VANDERBILT UNIVERSITY, NASHVILLE, TENNESSEE
ALPHA_CYLINDER_MOUNT_B
1413
SIZE C
SCALE 4.000 : 1
SHEET 1 OF 1
K. WATT
&todays_date
UNLESS OTHERWISE SPECIFIED:
ALL DIMENSIONS ARE IN INCHES
AND APPLY AFTER FINISH
DIMENSION TOLERANCES
REMOVE ALL BURRS AND SHARP EDGES
FINISH: MILL FINISH
SECTION B-B
SECTION A-A
Ø .29 ⊽ .471 +.000 -.010 2
2-56 UNC 2B CLEAR THRU
#43 DRILL (0.090) THRU
Ø .19 ⊽ .09 2) HOLE
Ø .20 THRU
Ø .18 ⊽ .048 +.000 -.010
Ø .063 THRU PER VIEW A-A
R.063
NOTES:
1. MATERIAL IS AL 6061
2 MEASURED FROM CENTER OF CIRCULAR GROOVE

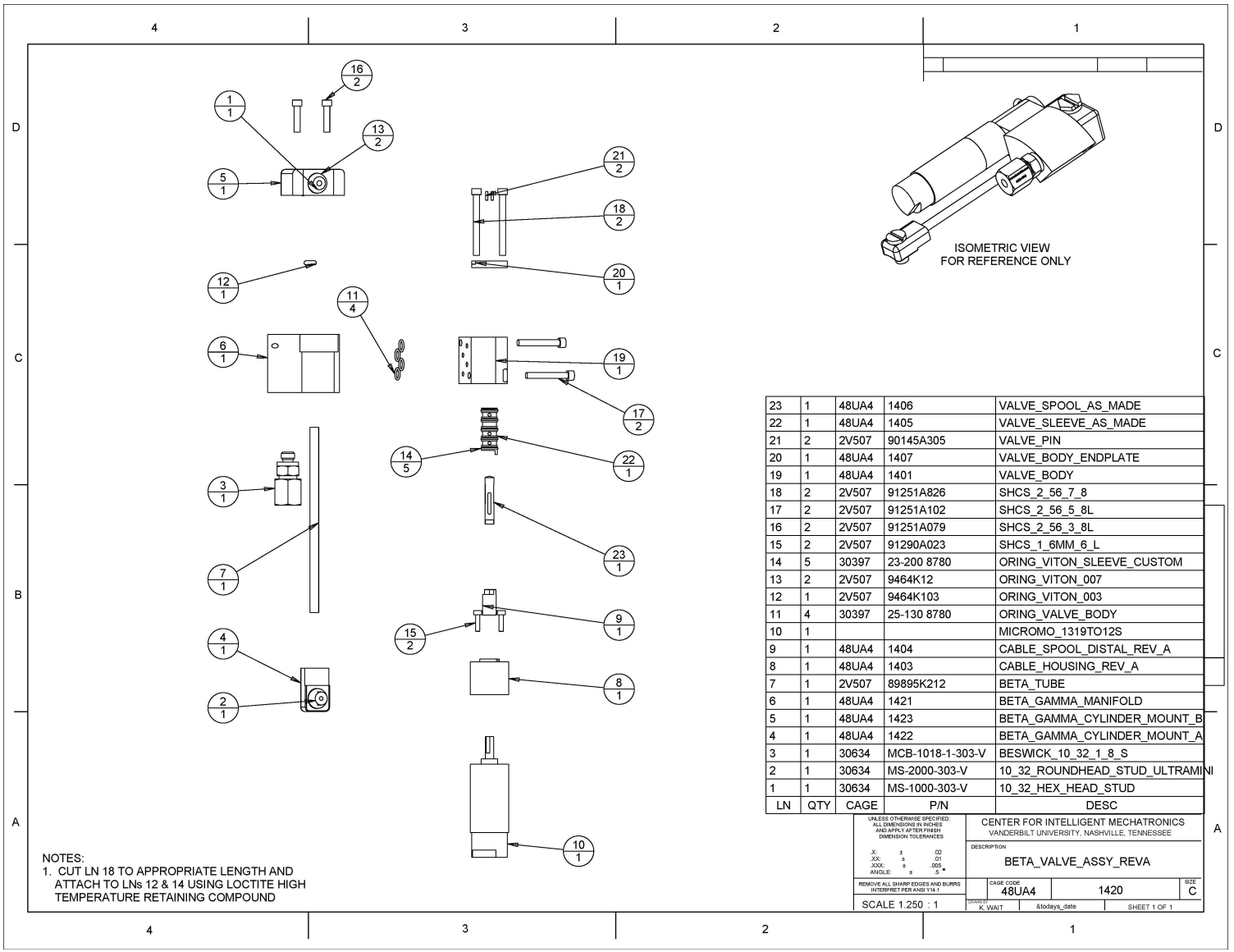

LN	QTY	CAGE	P/N	DESC
23	1	48UA4	1406	VALVE_SPOOL_AS_MADE
22	1	48UA4	1405	VALVE_SLEEVE_AS_MADE
21	2	2V507	90145A305	VALVE_PIN
20	1	48UA4	1407	VALVE_BODY_ENDPLATE
19	1	48UA4	1401	VALVE_BODY
18	2	2V507	91251A826	SHCS_2_56_7_8
17	2	2V507	91251A102	SHCS_2_56_5_8L
16	2	2V507	91251A079	SHCS_2_56_3_8L
15	2	2V507	91290A023	SHCS_1_6MM_6_L
14	5	30397	23-200 8780	ORING_VITON_SLEEVE_CUSTOM
13	2	2V507	9464K12	ORING_VITON_007
12	1	2V507	9464K103	ORING_VITON_003
11	4	30397	25-130 8780	ORING_VALVE_BODY
10	1			MICROMO_1319TO12S
9	1	48UA4	1404	CABLE_SPOOL_DISTAL_REV_A
8	1	48UA4	1403	CABLE_HOUSING_REV_A
7	1	2V507	89895K212	BETA_TUBE
6	1	48UA4	1421	BETA_GAMMA_MANIFOLD
5	1	48UA4	1423	BETA_GAMMA_CYLINDER_MOUNT_B
4	1	48UA4	1422	BETA_GAMMA_CYLINDER_MOUNT_A
3	1	30634	MCB-1018-1-303-V	BESWICK_10_32_1_8_S
2	1	30634	MS-2000-303-V	10_32_ROUNDHEAD_STUD_ULTRAMINI
1	1	30634	MS-1000-303-V	10_32_HEX_HEAD_STUD

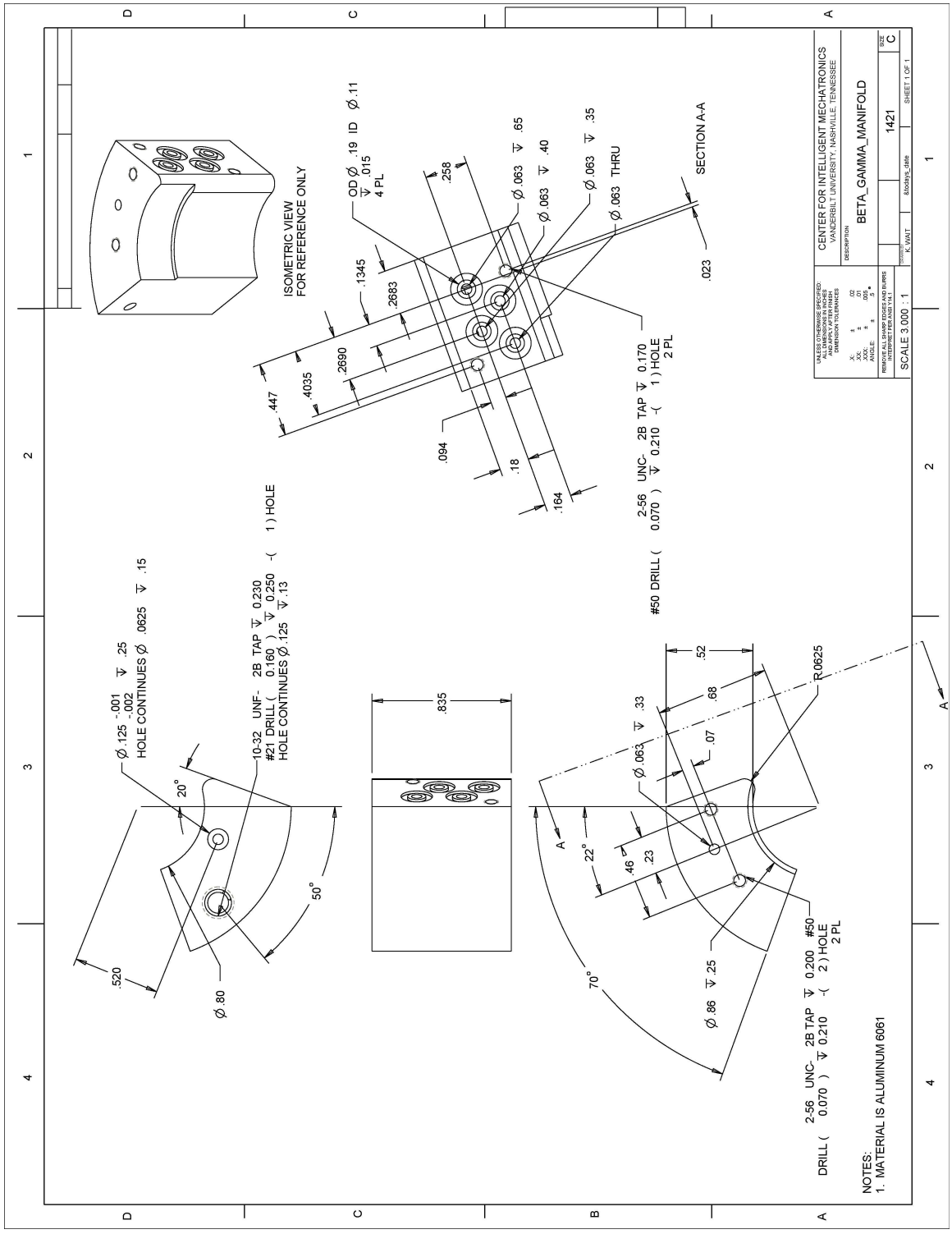
ISOMETRIC VIEW
FOR REFERENCE ONLY
SECTION A-A
CENTER FOR INTELLIGENT MECHATRONICS
VANDERBILT UNIVERSITY, NASHVILLE, TENNESSEE
BETA_GAMMA_MANIFOLD
1421
SCALE 3.000
SHEET 1 OF 1
K. WATT
NOTES:
1. MATERIAL IS ALUMINUM 6061

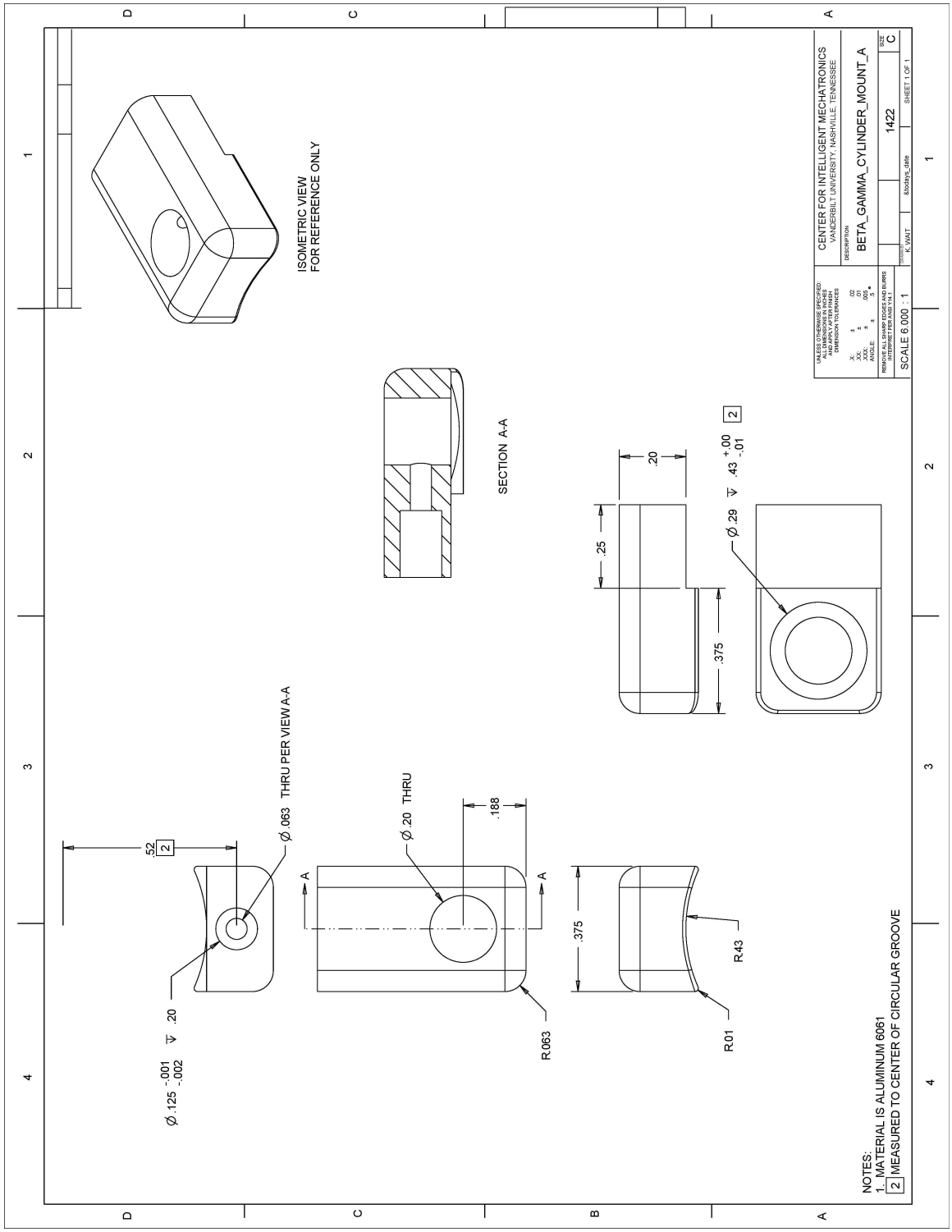
ISOMETRIC VIEW
FOR REFERENCE ONLY
SECTION A-A
Ø .063 THRU PER VIEW A-A
.52
2
Ø .20 THRU
.188
.20
.25
.375
Ø .29
.43 +.00 -.01
2
Ø .125 -.001 -.002
Ø .20
R.063
R.01
R.43
NOTES:
1. MATERIAL IS ALUMINUM 6061
2 MEASURED TO CENTER OF CIRCULAR GROOVE
CENTER FOR INTELLIGENT MECHATRONICS
VANDERBILT UNIVERSITY, NASHVILLE, TENNESSEE
BETA_GAMMA_CYLINDER_MOUNT_A
1422
SIZE C
SCALE 6.000
SHEET 1 OF 1
K. WATT

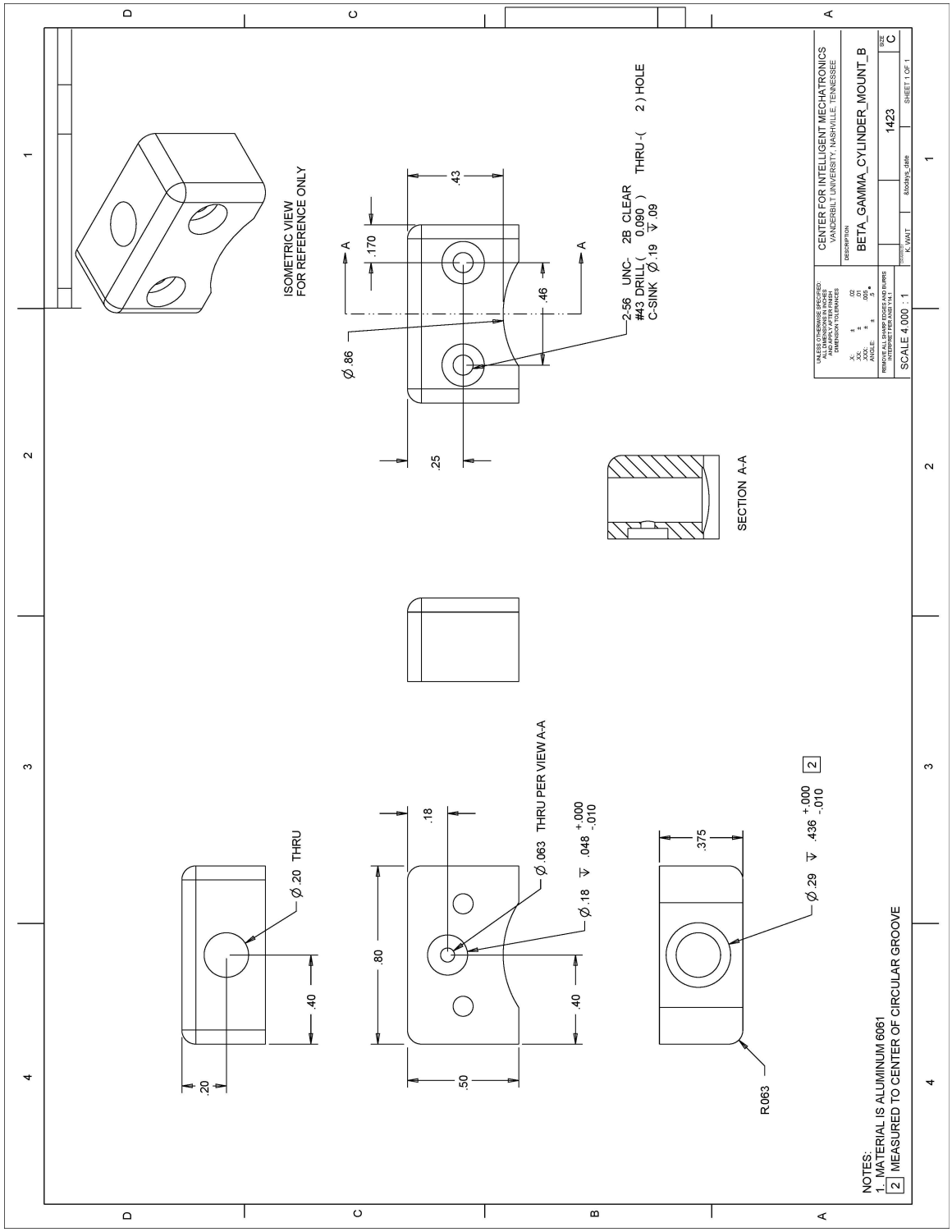
ISOMETRIC VIEW
FOR REFERENCE ONLY
Ø.86
.170
.43
.46
2.56 UNC- 2B CLEAR
#43 DRILL (0.090) THRU-(2) HOLE
C-SINK Ø.19 ↧.09
.25
SECTION A-A
Ø.20 THRU
.40
.20
.18
.80
Ø.063 THRU PER VIEW A-A
Ø.18 ↧ .048 +.000 -.010
.40
.50
.375
Ø.29 ↧ .436 +.000 -.010 2
R.063
NOTES:
1. MATERIAL IS ALUMINUM 6061
2 MEASURED TO CENTER OF CIRCULAR GROOVE
CENTER FOR INTELLIGENT MECHATRONICS
VANDERBILT UNIVERSITY, NASHVILLE, TENNESSEE
DESCRIPTION
BETA_GAMMA_CYLINDER_MOUNT_B
1423
SIZE C
K. WATT
SCALE 4.000 : 1
SHEET 1 OF 1

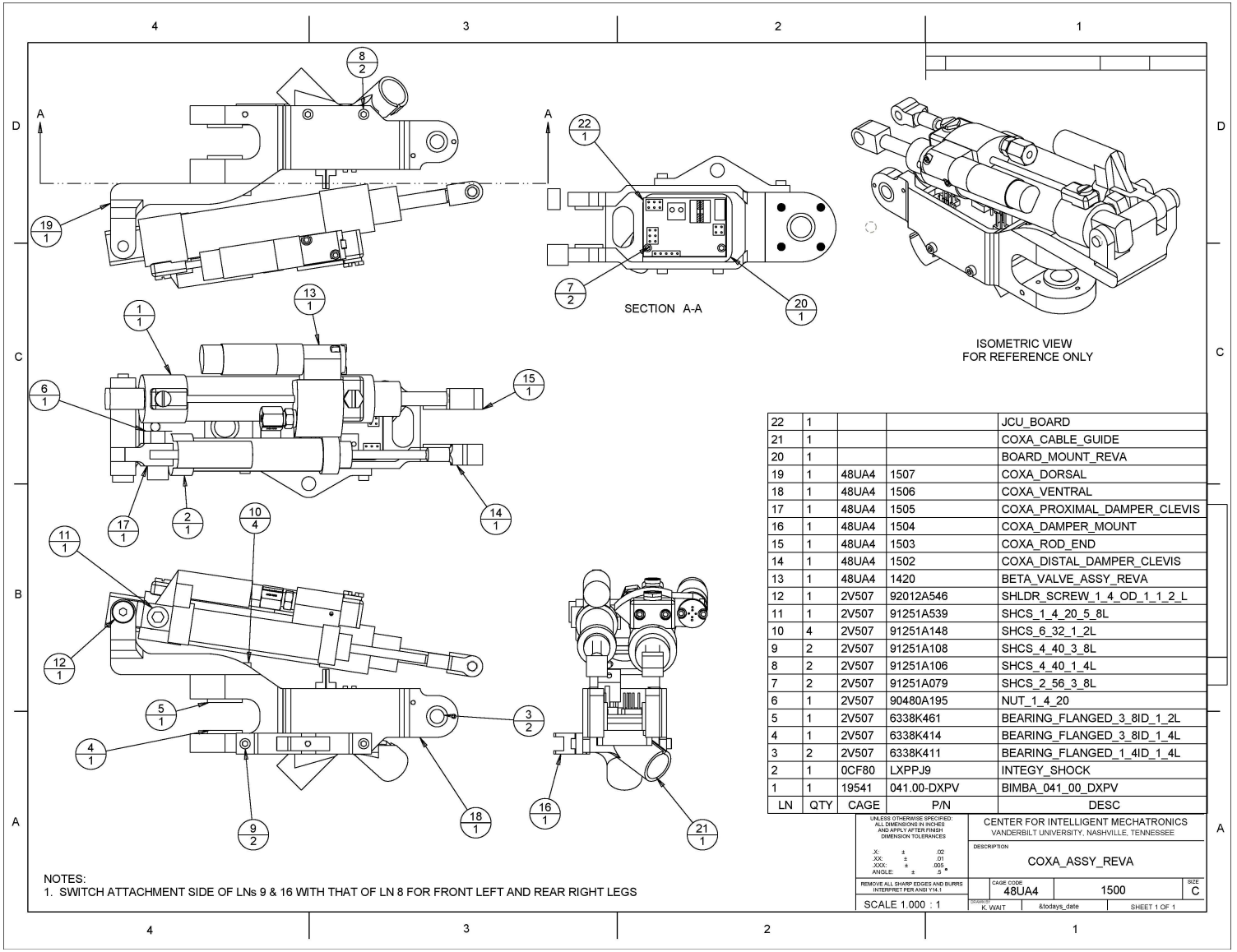

LN	QTY	CAGE	P/N	DESC
22	1			JCU_BOARD
21	1			COXA_CABLE_GUIDE
20	1			BOARD_MOUNT_REVA
19	1	48UA4	1507	COXA_DORSAL
18	1	48UA4	1506	COXA_VENTRAL
17	1	48UA4	1505	COXA_PROXIMAL_DAMPER_CLEVIS
16	1	48UA4	1504	COXA_DAMPER_MOUNT
15	1	48UA4	1503	COXA_ROD_END
14	1	48UA4	1502	COXA_DISTAL_DAMPER_CLEVIS
13	1	48UA4	1420	BETA_VALVE_ASSY_REVA
12	1	2V507	92012A546	SHLDR_SCREW_1_4_OD_1_1_2_L
11	1	2V507	91251A539	SHCS_1_4_20_5_8L
10	4	2V507	91251A148	SHCS_6_32_1_2L
9	2	2V507	91251A108	SHCS_4_40_3_8L
8	2	2V507	91251A106	SHCS_4_40_1_4L
7	2	2V507	91251A079	SHCS_2_56_3_8L
6	1	2V507	90480A195	NUT_1_4_20
5	1	2V507	6338K461	BEARING_FLANGED_3_8ID_1_2L
4	1	2V507	6338K414	BEARING_FLANGED_3_8ID_1_4L
3	2	2V507	6338K411	BEARING_FLANGED_1_4ID_1_4L
2	1	0CF80	LXPPJ9	INTEGY_SHOCK
1	1	19541	041.00-DXPV	BIMBA_041_00_DXPV

NOTES:
1. SWITCH ATTACHMENT SIDE OF LNs 9 & 16 WITH THAT OF LN 8 FOR FRONT LEFT AND REAR RIGHT LEGS

UNLESS OTHERWISE SPECIFIED:
ALL DIMENSIONS IN INCHES
AND APPLY AFTER FINISH
DIMENSION TOLERANCES
.X: ± .02
.XX: ± .01
.XXX: ± .005
ANGLE: ± .5°

REMOVE ALL SHARP EDGES AND BURRS
INTERPRET PER ANSI Y14.1

SCALE 1.000 : 1

CENTER FOR INTELLIGENT MECHATRONICS
VANDERBILT UNIVERSITY, NASHVILLE, TENNESSEE

DESCRIPTION
COXA_ASSY_REVA

CAGE CODE 48UA4 | 1500 | SIZE C

DRAWN BY K. WAIT | &todays_date | SHEET 1 OF 1

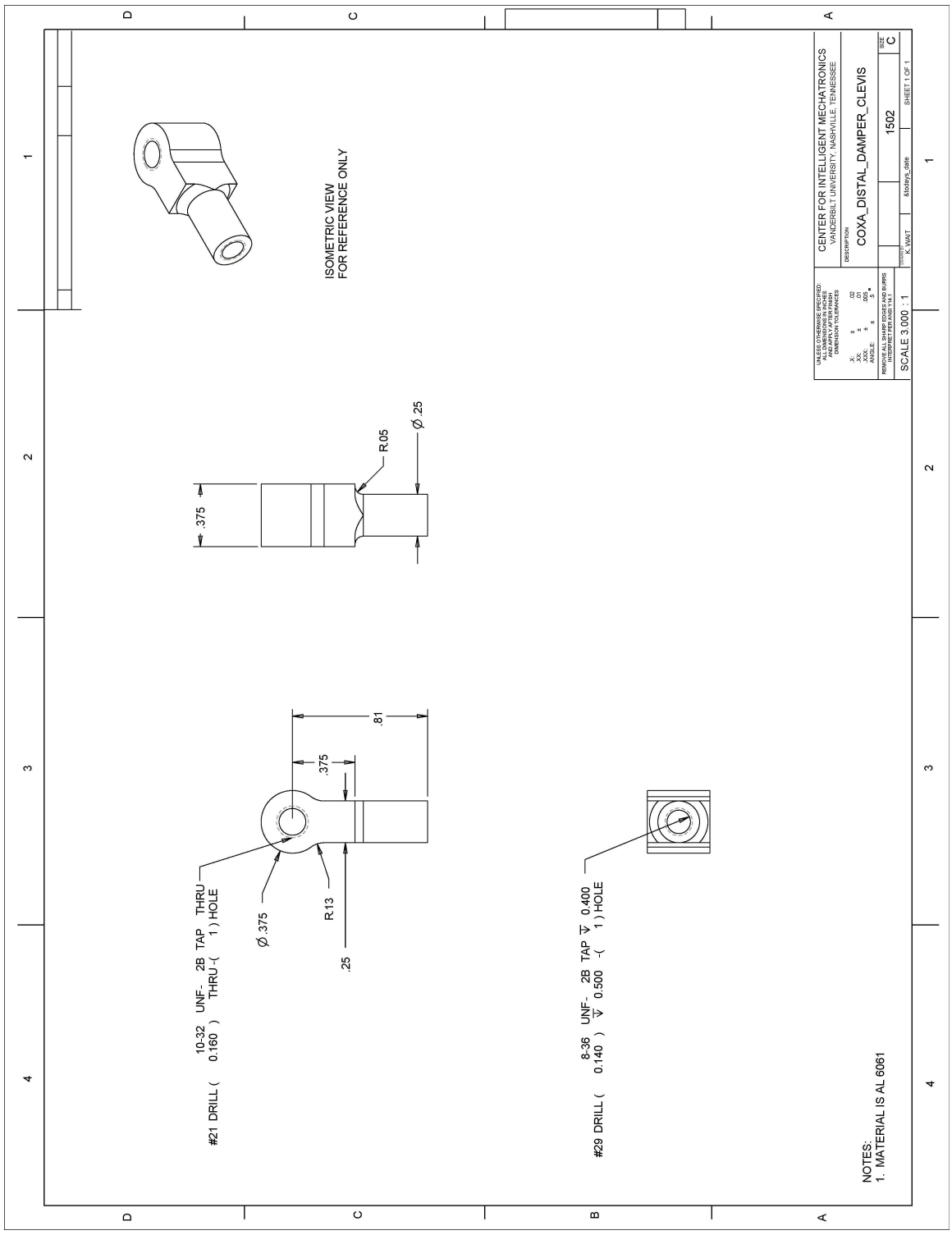
ISOMETRIC VIEW
FOR REFERENCE ONLY
.375
R.05
Ø.25
.81
.375
R13
.25
Ø.375
#21 DRILL (0.160) THRU -(1) HOLE
10-32 UNF- 2B TAP THRU
#29 DRILL (0.140) ↧ 0.500 -(1) HOLE
8-36 UNF- 2B TAP ↧ 0.400
NOTES:
1. MATERIAL IS AL 6061
CENTER FOR INTELLIGENT MECHATRONICS
VANDERBILT UNIVERSITY, NASHVILLE, TENNESSEE
DESCRIPTION
COXA_DISTAL_DAMPER_CLEVIS
1502
SIZE C
SCALE 3.000 : 1
SHEET 1 OF 1
K. WATT
&tookpts_date

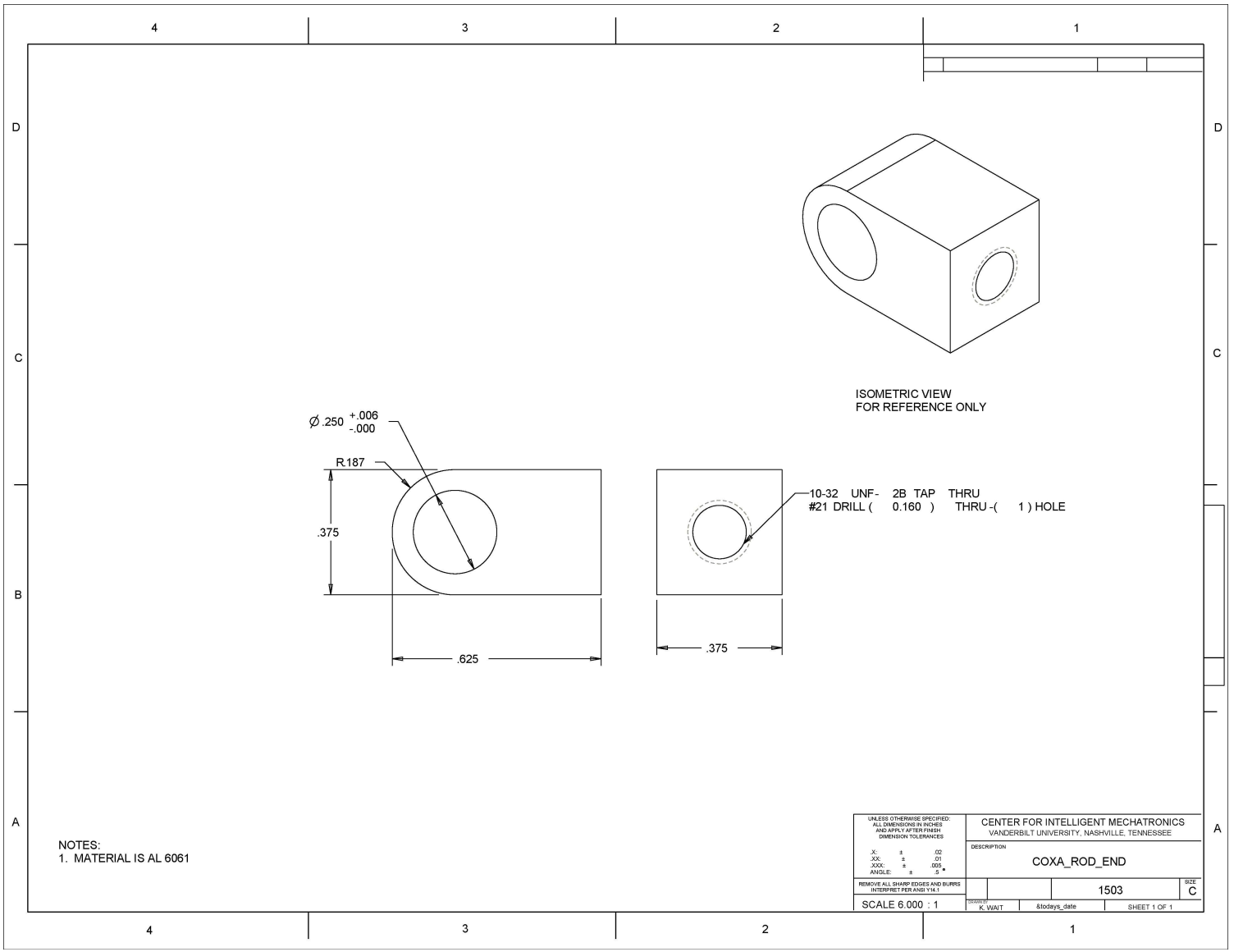
4
3
2
1
D
C
B
A
ISOMETRIC VIEW
FOR REFERENCE ONLY
Ø .250 +.006 -.000
R.187
.375
.625
.375
10-32 UNF- 2B TAP THRU
#21 DRILL (0.160) THRU -(1) HOLE
NOTES:
1. MATERIAL IS AL 6061
UNLESS OTHERWISE SPECIFIED:
ALL DIMENSIONS IN INCHES
AND APPLY AFTER FINISH
DIMENSION TOLERANCES
.X: ± .02
.XX: ± .01
.XXX: ± .005
ANGLE: ± .5°
REMOVE ALL SHARP EDGES AND BURRS
INTERPRET PER ANSI Y14.1
SCALE 6.000 : 1
CENTER FOR INTELLIGENT MECHATRONICS
VANDERBILT UNIVERSITY, NASHVILLE, TENNESSEE
DESCRIPTION
COXA_ROD_END
1503
SIZE
C
DRAWN BY
K. WAIT
&todays_date
SHEET 1 OF 1

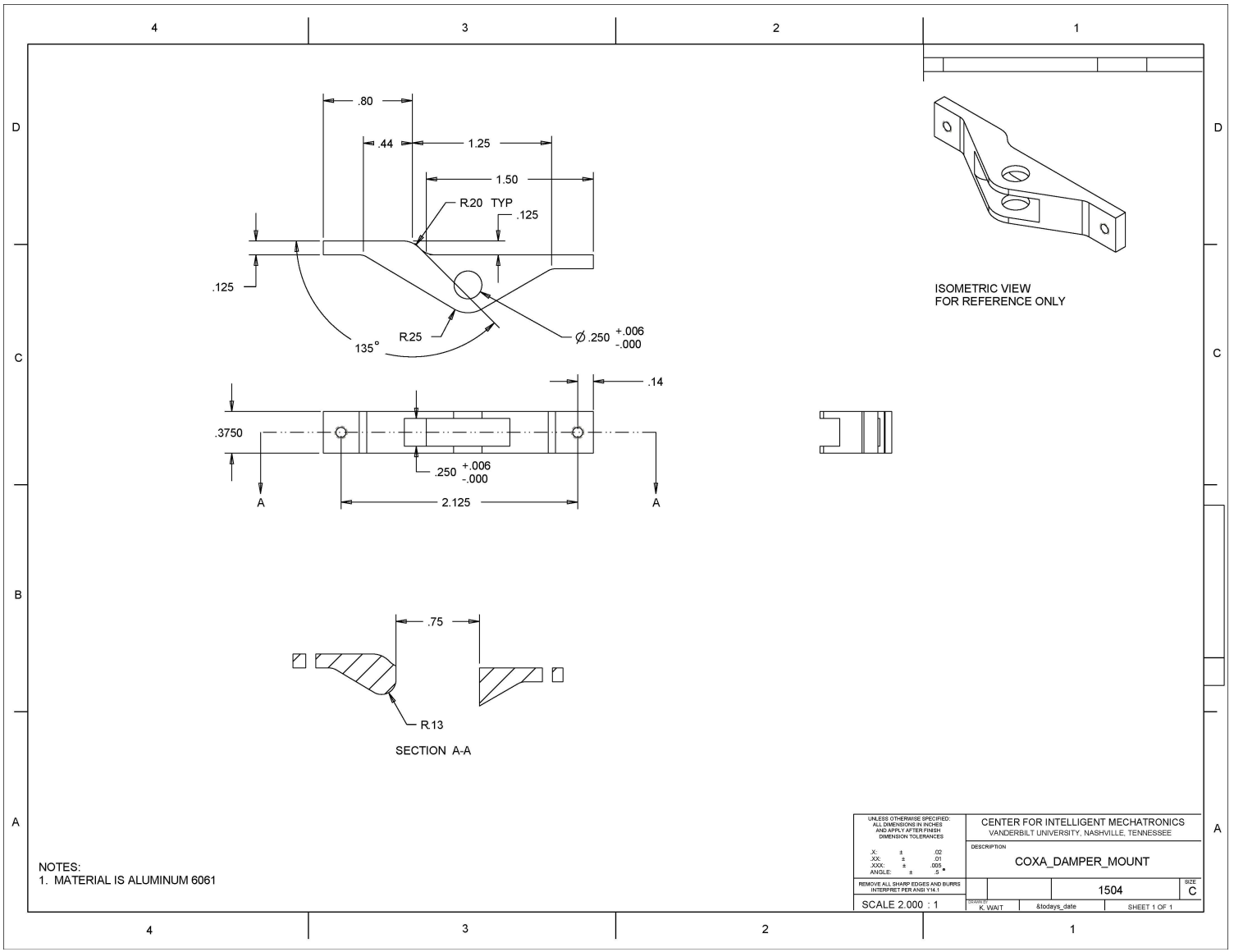
.80
.44
1.25
1.50
R.20 TYP
.125
.125
135°
R.25
Ø .250 +.006 -.000
.14
.3750
.250 +.006 -.000
A
A
2.125
.75
R.13
SECTION A-A
ISOMETRIC VIEW
FOR REFERENCE ONLY
NOTES:
1. MATERIAL IS ALUMINUM 6061
UNLESS OTHERWISE SPECIFIED: ALL DIMENSIONS IN INCHES AND APPLY AFTER FINISH
DIMENSION TOLERANCES
.X: ± .02
.XX: ± .01
.XXX: ± .005
ANGLE: ± .5°
REMOVE ALL SHARP EDGES AND BURRS
INTERPRET PER ANSI Y14.1
SCALE 2.000 : 1
CENTER FOR INTELLIGENT MECHATRONICS
VANDERBILT UNIVERSITY, NASHVILLE, TENNESSEE
DESCRIPTION
COXA_DAMPER_MOUNT
1504
SIZE C
DRAWN BY
K. WAIT
&todays_date
SHEET 1 OF 1

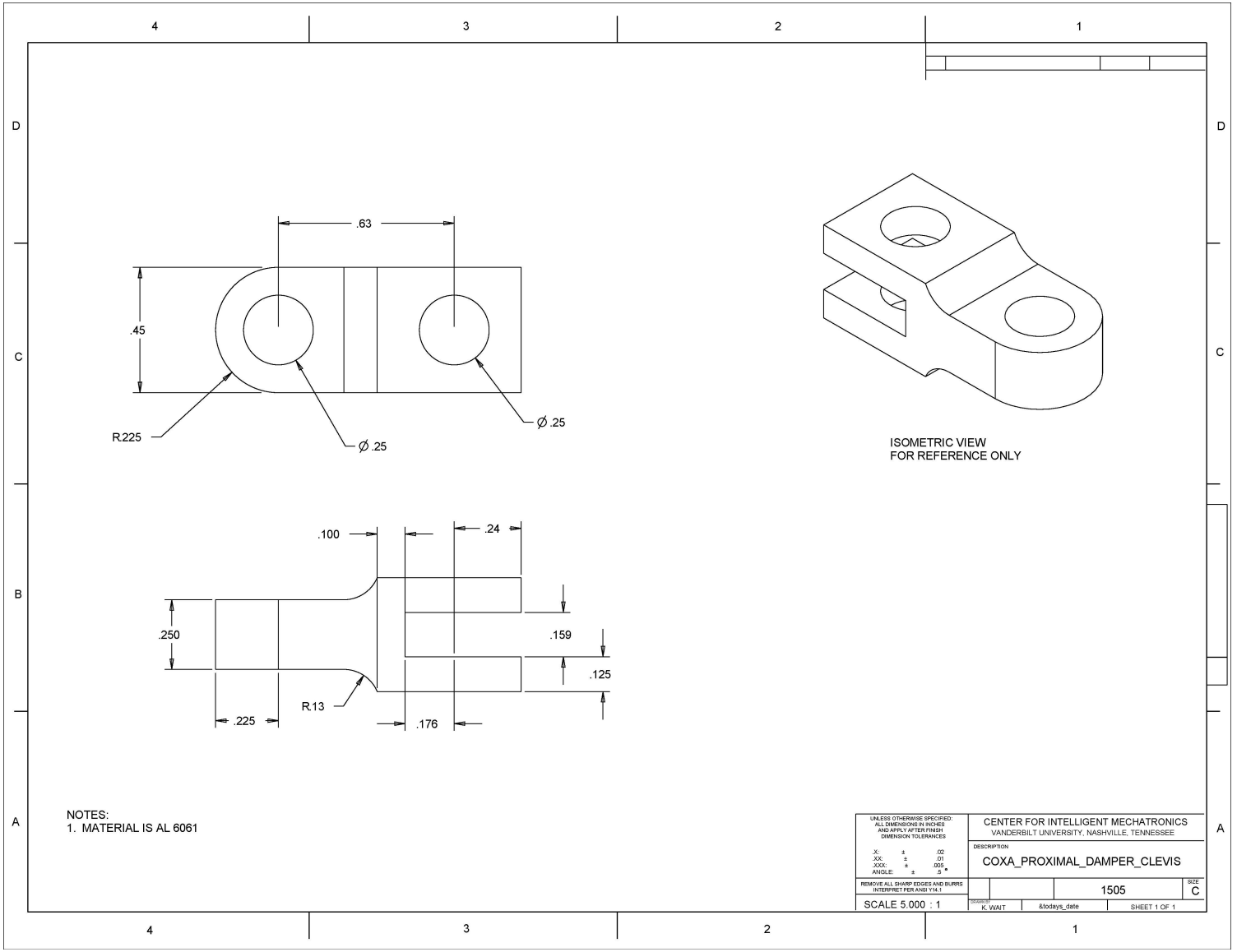
4
3
2
1
D
C
B
A
.63
.45
R.225
Ø .25
Ø .25
ISOMETRIC VIEW
FOR REFERENCE ONLY
.100
.24
.250
.159
.125
R.13
.225
.176
NOTES:
1. MATERIAL IS AL 6061
UNLESS OTHERWISE SPECIFIED:
ALL DIMENSIONS IN INCHES
AND APPLY AFTER FINISH
DIMENSION TOLERANCES
.X: ± .02
.XX: ± .01
.XXX: ± .005
ANGLE: ± .5°
REMOVE ALL SHARP EDGES AND BURRS
INTERPRET PER ANSI Y14.1
SCALE 5.000 : 1
CENTER FOR INTELLIGENT MECHATRONICS
VANDERBILT UNIVERSITY, NASHVILLE, TENNESSEE
DESCRIPTION
COXA_PROXIMAL_DAMPER_CLEVIS
1505
SIZE
C
DRAWN BY
K. WAIT
&todays_date
SHEET 1 OF 1

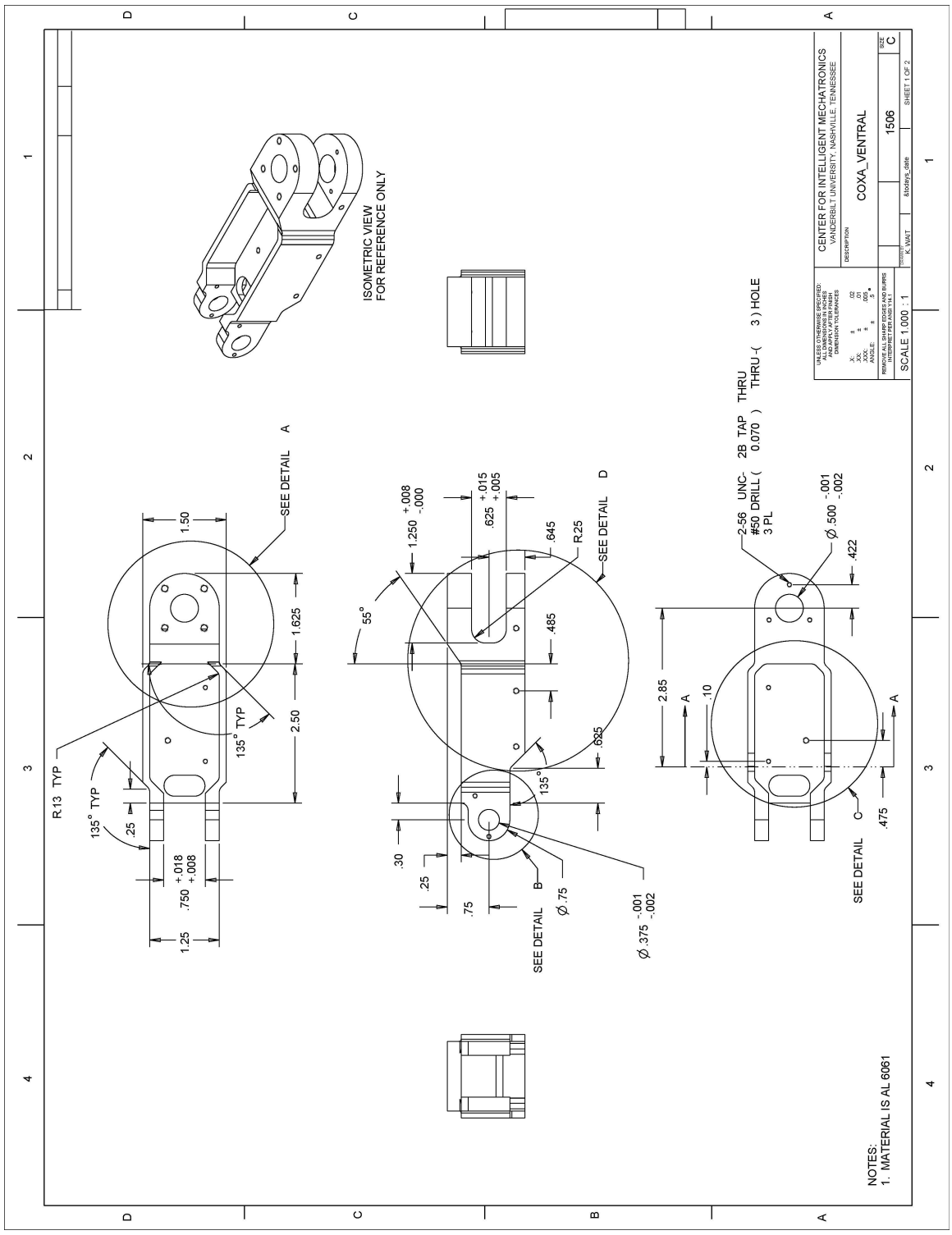
ISOMETRIC VIEW
FOR REFERENCE ONLY
SEE DETAIL A
SEE DETAIL B
SEE DETAIL C
SEE DETAIL D
R13 TYP
135° TYP
R.25
55°
2-56 UNC-2B TAP THRU
#50 DRILL (0.070) THRU -(3) HOLE
3 PL
NOTES:
1. MATERIAL IS AL 6061
CENTER FOR INTELLIGENT MECHATRONICS
VANDERBILT UNIVERSITY, NASHVILLE, TENNESSEE
DESCRIPTION
COXA_VENTRAL
1506
SIZE C
SCALE 1.000
SHEET 1 OF 2

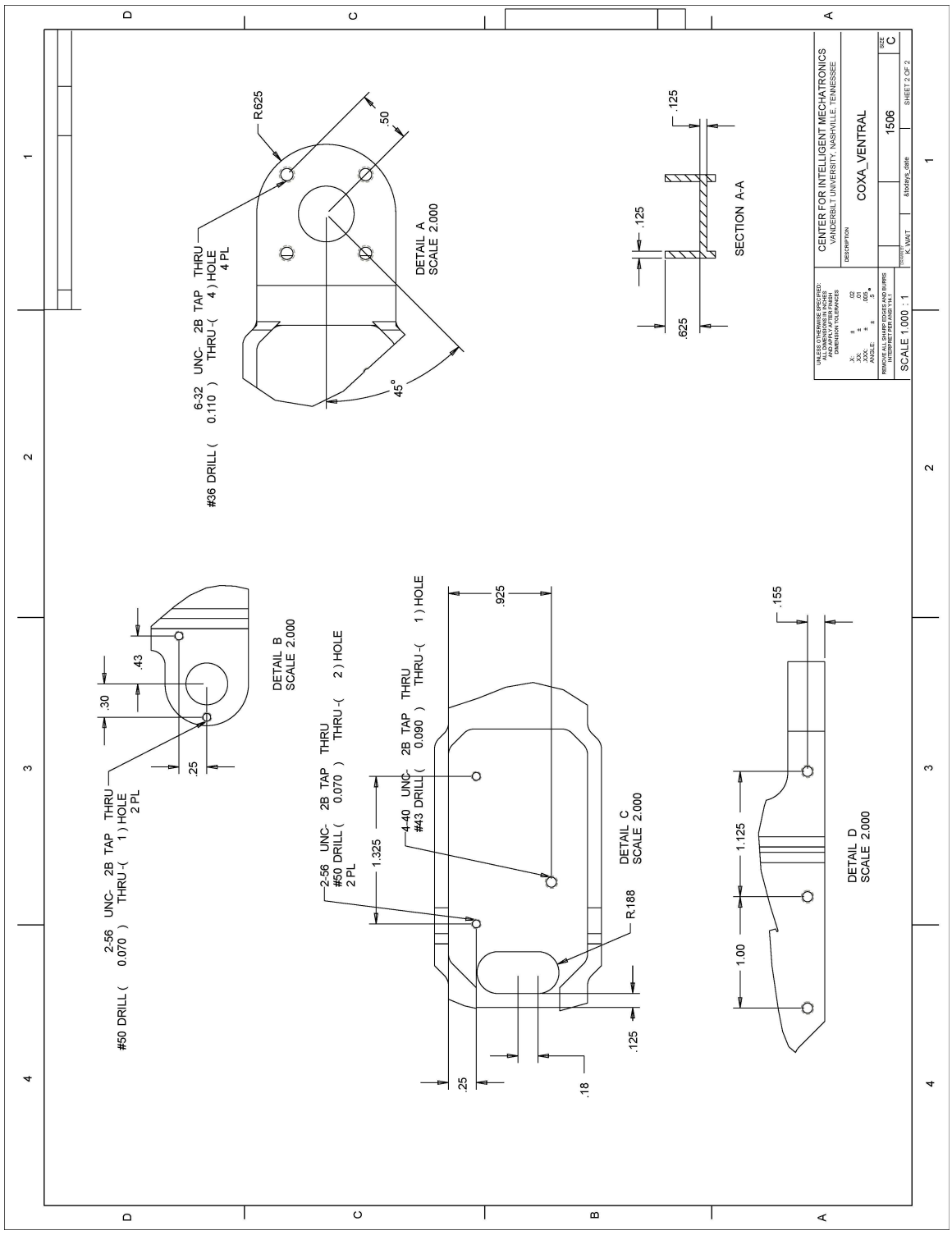
R.625
.50
#36 DRILL (0.110) 6-32 UNC- 2B TAP THRU
THRU -(4) HOLE
4 PL
DETAIL A
SCALE 2.000
.125
.125
.625
SECTION A-A
#50 DRILL (0.070) 2-56 UNC- 2B TAP THRU
THRU -(1) HOLE
2 PL
.43
.30
.25
DETAIL B
SCALE 2.000
#50 DRILL (0.070) 2-56 UNC- 2B TAP THRU
THRU -(2) HOLE
2 PL
1.325
#43 DRILL (0.090) 4-40 UNC- 2B TAP THRU
THRU -(1) HOLE
.925
R.188
.125
.25
.18
DETAIL C
SCALE 2.000
.155
1.125
1.00
DETAIL D
SCALE 2.000
UNLESS OTHERWISE SPECIFIED:
ALL DIMENSIONS IN INCHES
AND APPLY AFTER FINISH
DIMENSION TOLERANCES
X: ± .02
XX: ± .01
XXX: ± .005
ANGLE: ± 5°
REMOVE ALL SHARP EDGES AND BURRS
FINISH: PER ASSEMBLY
SCALE 1.000 : 1
CENTER FOR INTELLIGENT MECHATRONICS
VANDERBILT UNIVERSITY, NASHVILLE, TENNESSEE
DESCRIPTION
COXA_VENTRAL
1506
SIZE C
K. WATT
&todays_date
SHEET 2 OF 2

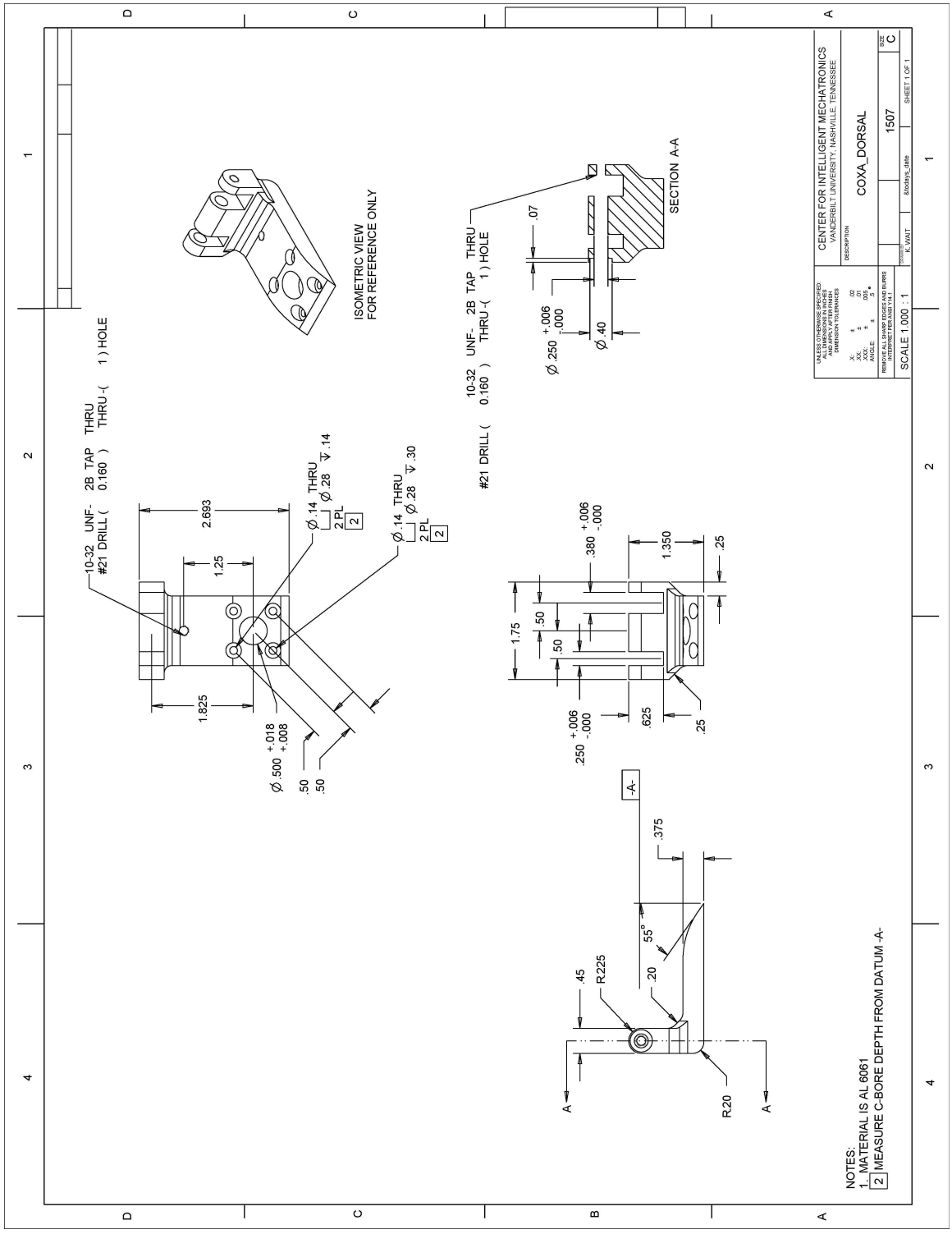
CENTER FOR INTELLIGENT MECHATRONICS
VANDERBILT UNIVERSITY, NASHVILLE, TENNESSEE
DESCRIPTION
COXA_DORSAL
1507
SIZE C
SCALE 1.000 : 1
SHEET 1 OF 1
K_WATT
&todays_date
ISOMETRIC VIEW
FOR REFERENCE ONLY
SECTION A-A
10-32 UNF- 2B TAP THRU
#21 DRILL (0.160) THRU -(1) HOLE
Ø .14 THRU
Ø .28 ⌴ .14
2 PL
2
Ø .14 THRU
Ø .28 ⌴ .30
2 PL
2
2.693
1.25
1.825
Ø .500 +.018 +.008
.50
.50
Ø .250 +.006 -.000
.07
Ø .40
.380 +.006 -.000
1.350
.25
1.75
.50
.50
.250 +.006 -.000
.625
.25
-A-
.375
55°
.45
R.225
.20
R20
A
A
NOTES:
1. MATERIAL IS AL 6061
2 MEASURE C-BORE DEPTH FROM DATUM -A-

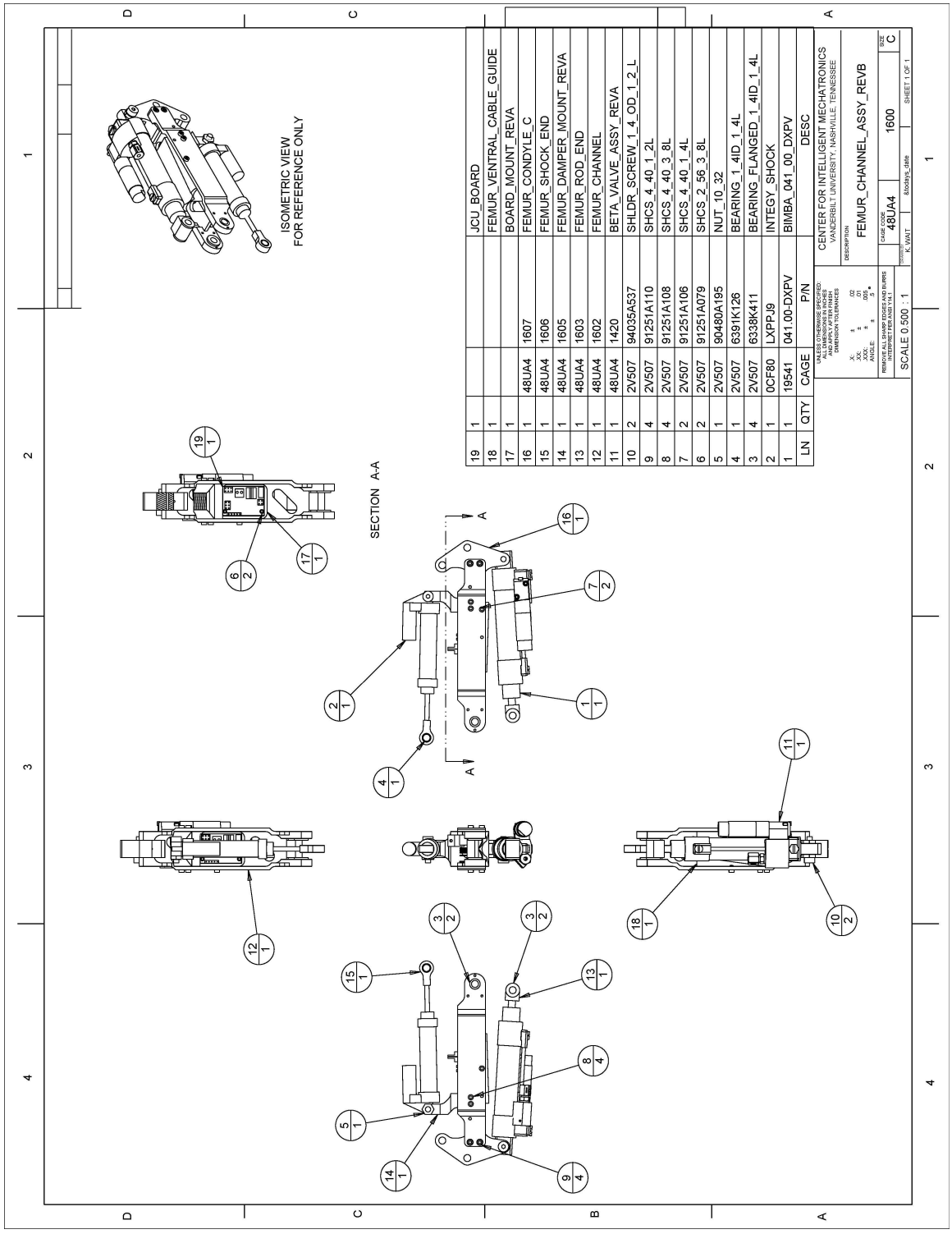

LN	QTY	CAGE	P/N	DESC
19	1			JCU_BOARD
18	1			FEMUR_VENTRAL_CABLE_GUIDE
17	1			BOARD_MOUNT_REVA
16	1	48UA4	1607	FEMUR_CONDYLE_C
15	1	48UA4	1606	FEMUR_SHOCK_END
14	1	48UA4	1605	FEMUR_DAMPER_MOUNT_REVA
13	1	48UA4	1603	FEMUR_ROD_END
12	1	48UA4	1602	FEMUR_CHANNEL
11	1	48UA4	1420	BETA_VALVE_ASSY_REVA
10	2	2V507	94035A537	SHLDR_SCREW_1_4_OD_1_2_L
9	4	2V507	91251A110	SHCS_4_40_1_2L
8	4	2V507	91251A108	SHCS_4_40_3_8L
7	2	2V507	91251A106	SHCS_4_40_1_4L
6	2	2V507	91251A079	SHCS_2_56_3_8L
5	1	2V507	90480A195	NUT_10_32
4	1	2V507	6391K126	BEARING_1_4ID_1_4L
3	4	2V507	6338K411	BEARING_FLANGED_1_4ID_1_4L
2	1	0CF80	LXPPJ9	INTEGY_SHOCK
1	1	19541	041.00-DXPV	BIMBA_041_00_DXPV

UNLESS OTHERWISE SPECIFIED:
ALL DIMENSIONS IN INCHES
AND APPLY AFTER FINISH
DIMENSION TOLERANCES

X: ± .02
XX: ± .01
XXX: ± .005
ANGLE: ± 5°

REMOVE ALL SHARP EDGES AND BURRS
FINISH: PER ASME Y14.1

SCALE 0.500 : 1

CENTER FOR INTELLIGENT MECHATRONICS
VANDERBILT UNIVERSITY, NASHVILLE, TENNESSEE

DESCRIPTION
FEMUR_CHANNEL_ASSY_REVB

CHAM_FORD
48UA4

1600

SIZE
C

DRAWN
K_WATT

stickerps_date

SHEET 1 OF 1

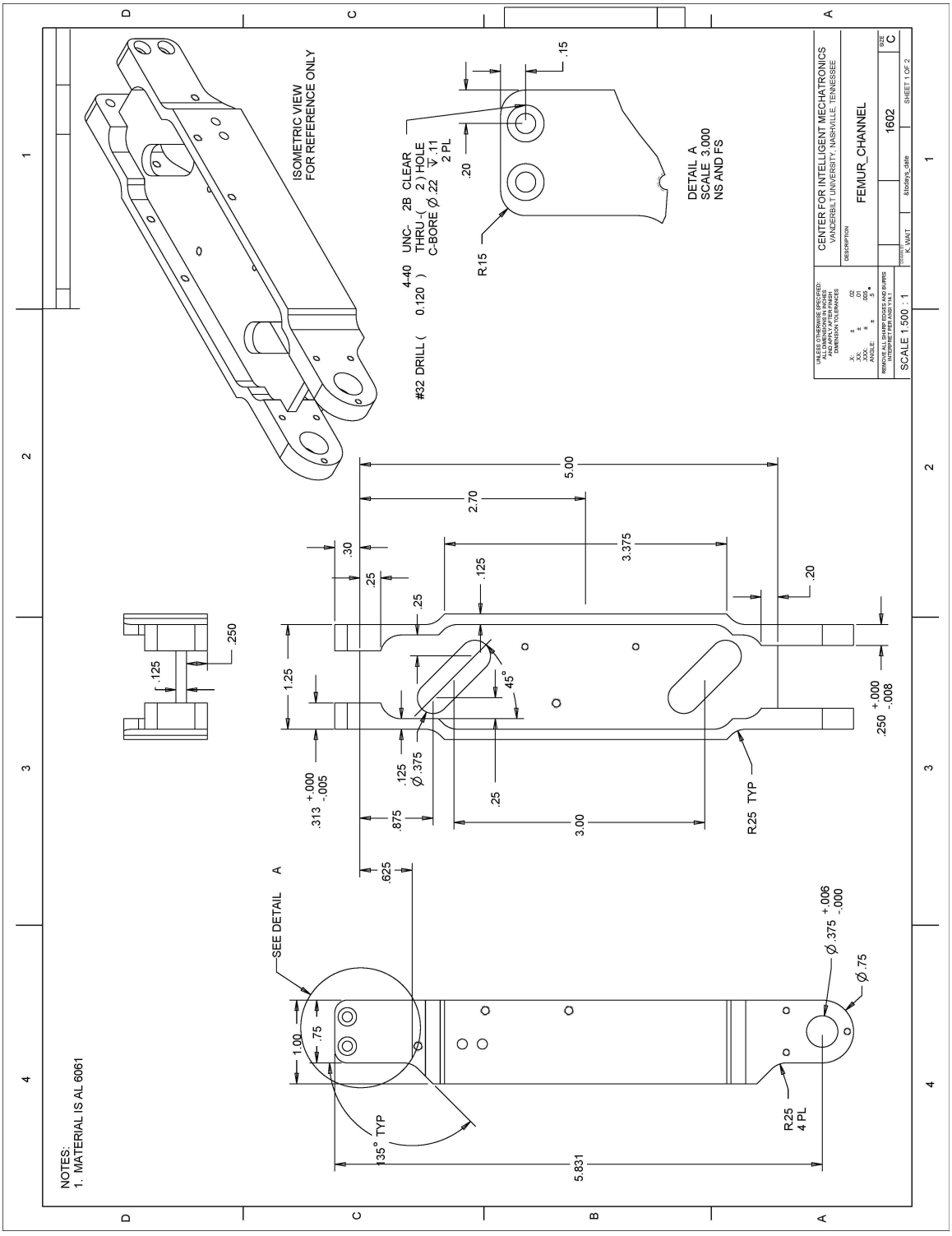
ISOMETRIC VIEW
FOR REFERENCE ONLY
#32 DRILL (0.120)
4-40 UNC- 2B CLEAR
THRU-(2) HOLE
C-BORE Ø .22 ↧ .11
2 PL
R.15
.15
.20
DETAIL A
SCALE 3.000
NS AND FS
CENTER FOR INTELLIGENT MECHATRONICS
VANDERBILT UNIVERSITY, NASHVILLE, TENNESSEE
FEMUR_CHANNEL
1602
SIZE C
SHEET 1 OF 2
K. WATT
SCALE 1.500
NOTES:
1. MATERIAL IS AL 6061
SEE DETAIL A
5.00
2.70
3.375
.30
.25
.125
.20
1.25
45°
.313 +.000 -.005
.875
Ø .375
3.00
R25 TYP
.250 +.000 -.008
.625
1.00
.75
135° TYP
5.831
R25
4 PL
Ø .375 +.006 -.000
Ø .75

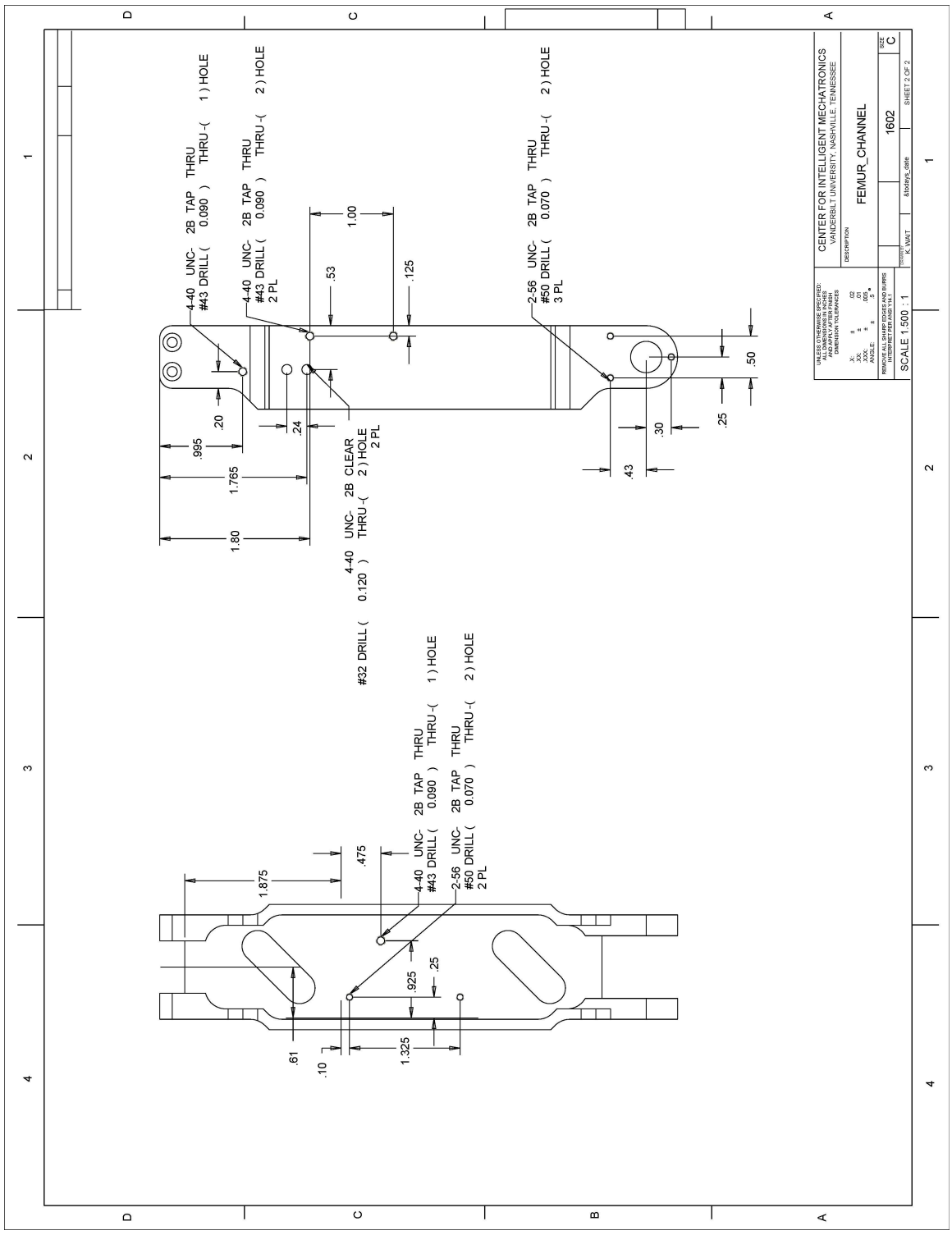
CENTER FOR INTELLIGENT MECHATRONICS
VANDERBILT UNIVERSITY, NASHVILLE, TENNESSEE
FEMUR_CHANNEL
1602
SIZE C
SHEET 2 OF 2
SCALE 1.500 : 1
K_WATT
4-40 UNC- 2B TAP THRU
#43 DRILL (0.090) THRU -(2) HOLE
2 PL
2-56 UNC- 2B TAP THRU
#50 DRILL (0.070) THRU -(2) HOLE
3 PL
#32 DRILL (0.120) 4-40 UNC- 2B CLEAR THRU -(2) HOLE 2 PL
1.00
.53
.125
.995
.20
1.765
.24
1.80
.43
.30
.25
.50
1.875
.475
.925
.25
.61
.10
1.325

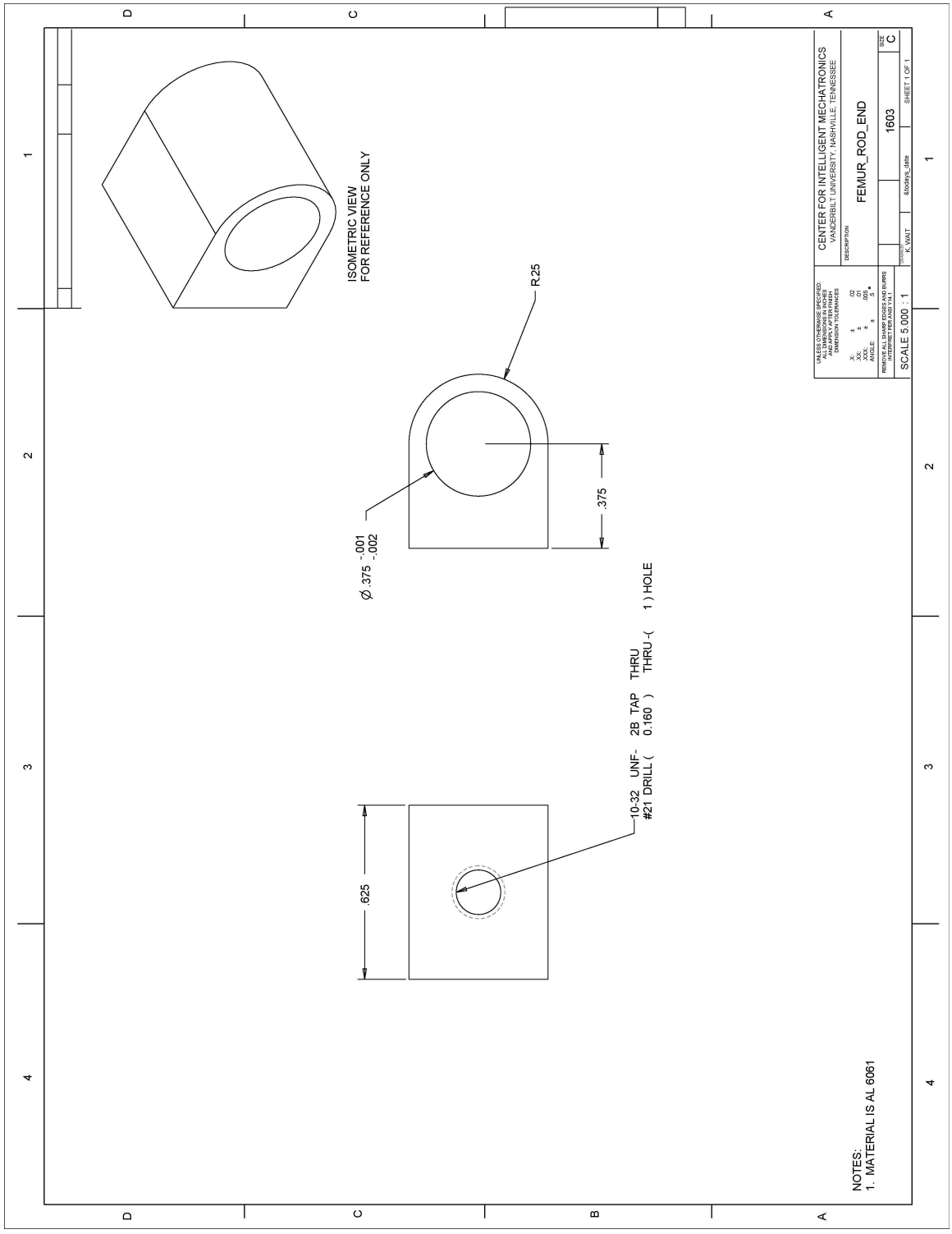
ISOMETRIC VIEW
FOR REFERENCE ONLY
R.25
Ø.375 -.001 -.002
.375
.625
10-32 UNF- 2B TAP THRU
#21 DRILL (0.160) THRU -(1) HOLE
NOTES:
1. MATERIAL IS AL 6061
CENTER FOR INTELLIGENT MECHATRONICS
VANDERBILT UNIVERSITY, NASHVILLE, TENNESSEE
DESCRIPTION
FEMUR_ROD_END
1603
SIZE C
SCALE 5.000 : 1
SHEET 1 OF 1
K. WATT
&todays_date
UNLESS OTHERWISE SPECIFIED:
REMOVE ALL BURRS AND SHARP EDGES
AND APPLY AFTER FINISH
DIMENSION TOLERANCES
REMOVE ALL SHARP EDGES AND FLARRE
FINISH: PER ANSI Y14.5

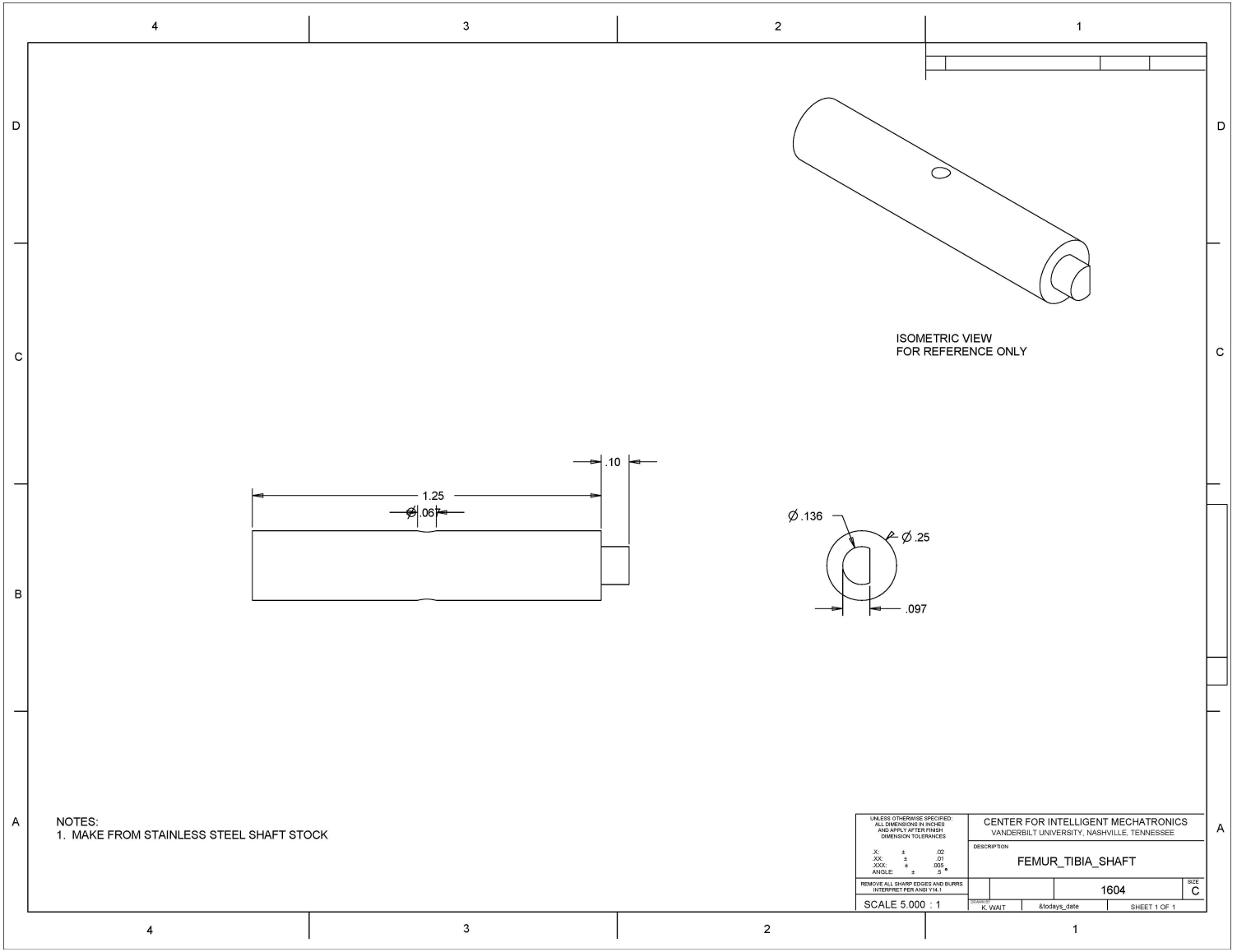
4
3
2
1
D
C
B
A
ISOMETRIC VIEW
FOR REFERENCE ONLY
.10
1.25
Ø.067
Ø.136
Ø.25
.097
NOTES:
1. MAKE FROM STAINLESS STEEL SHAFT STOCK
UNLESS OTHERWISE SPECIFIED:
ALL DIMENSIONS IN INCHES
AND APPLY AFTER FINISH
DIMENSION TOLERANCES
.X: ± .02
.XX: ± .01
.XXX: ± .005
ANGLE: ± .5 °
REMOVE ALL SHARP EDGES AND BURRS
INTERPRET PER ANSI Y14.1
SCALE 5.000 : 1
CENTER FOR INTELLIGENT MECHATRONICS
VANDERBILT UNIVERSITY, NASHVILLE, TENNESSEE
DESCRIPTION
FEMUR_TIBIA_SHAFT
1604
SIZE
C
DRAWN BY
K. WAIT
&todays_date
SHEET 1 OF 1

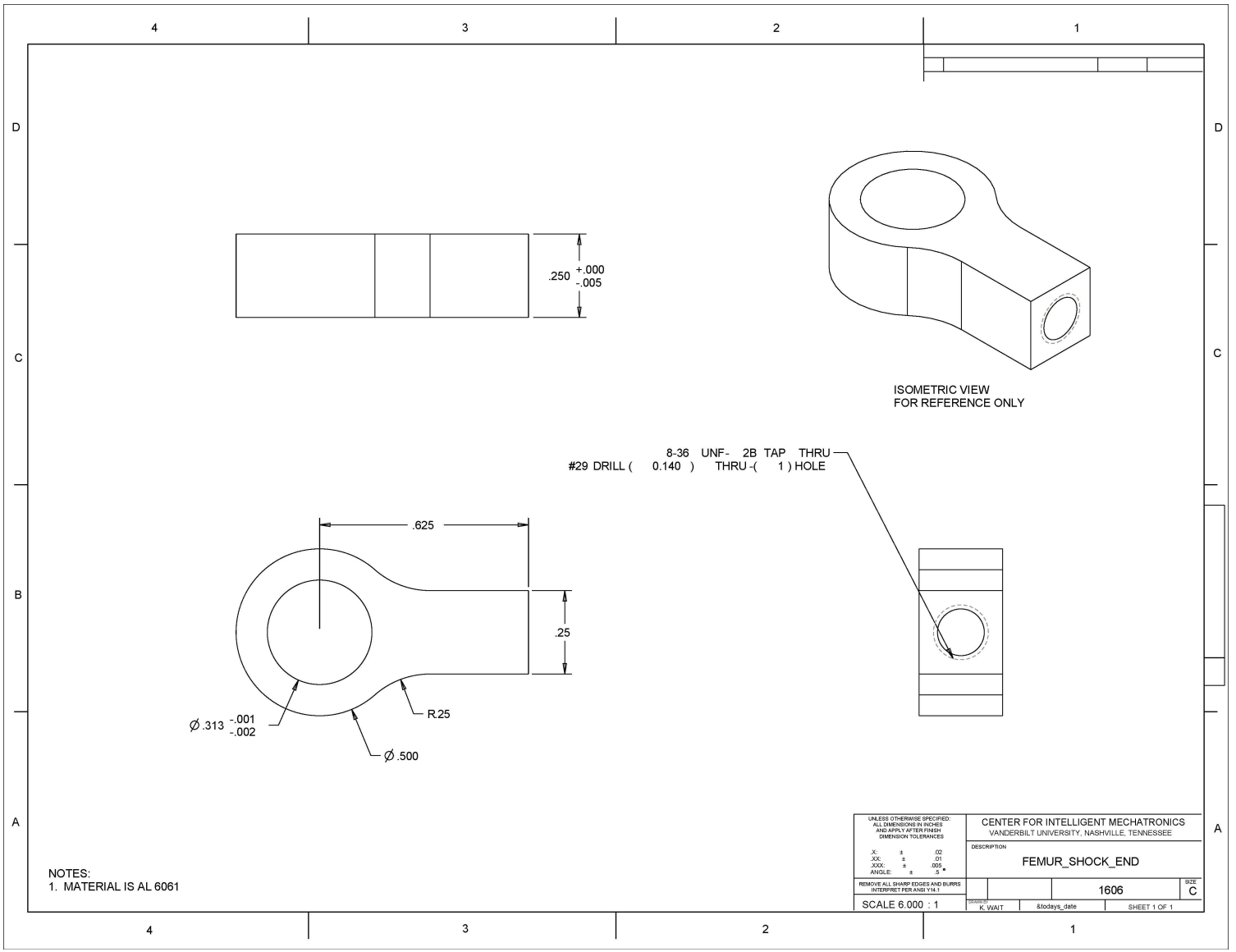
4
3
2
1
D
C
B
A
.250 +.000 -.005
ISOMETRIC VIEW
FOR REFERENCE ONLY
8-36 UNF- 2B TAP THRU
#29 DRILL (0.140) THRU -(1) HOLE
.625
.25
Ø .313 -.001 -.002
R.25
Ø .500
NOTES:
1. MATERIAL IS AL 6061
UNLESS OTHERWISE SPECIFIED:
ALL DIMENSIONS IN INCHES
AND APPLY AFTER FINISH
DIMENSION TOLERANCES
.X: ± .02
.XX: ± .01
.XXX: ± .005
ANGLE: ± .5 °
REMOVE ALL SHARP EDGES AND BURRS
INTERPRET PER ANSI Y14.1
SCALE 6.000 : 1
CENTER FOR INTELLIGENT MECHATRONICS
VANDERBILT UNIVERSITY, NASHVILLE, TENNESSEE
DESCRIPTION
FEMUR_SHOCK_END
SIZE
C
1606
DRAWN BY
K. WAIT
&todays_date
SHEET 1 OF 1

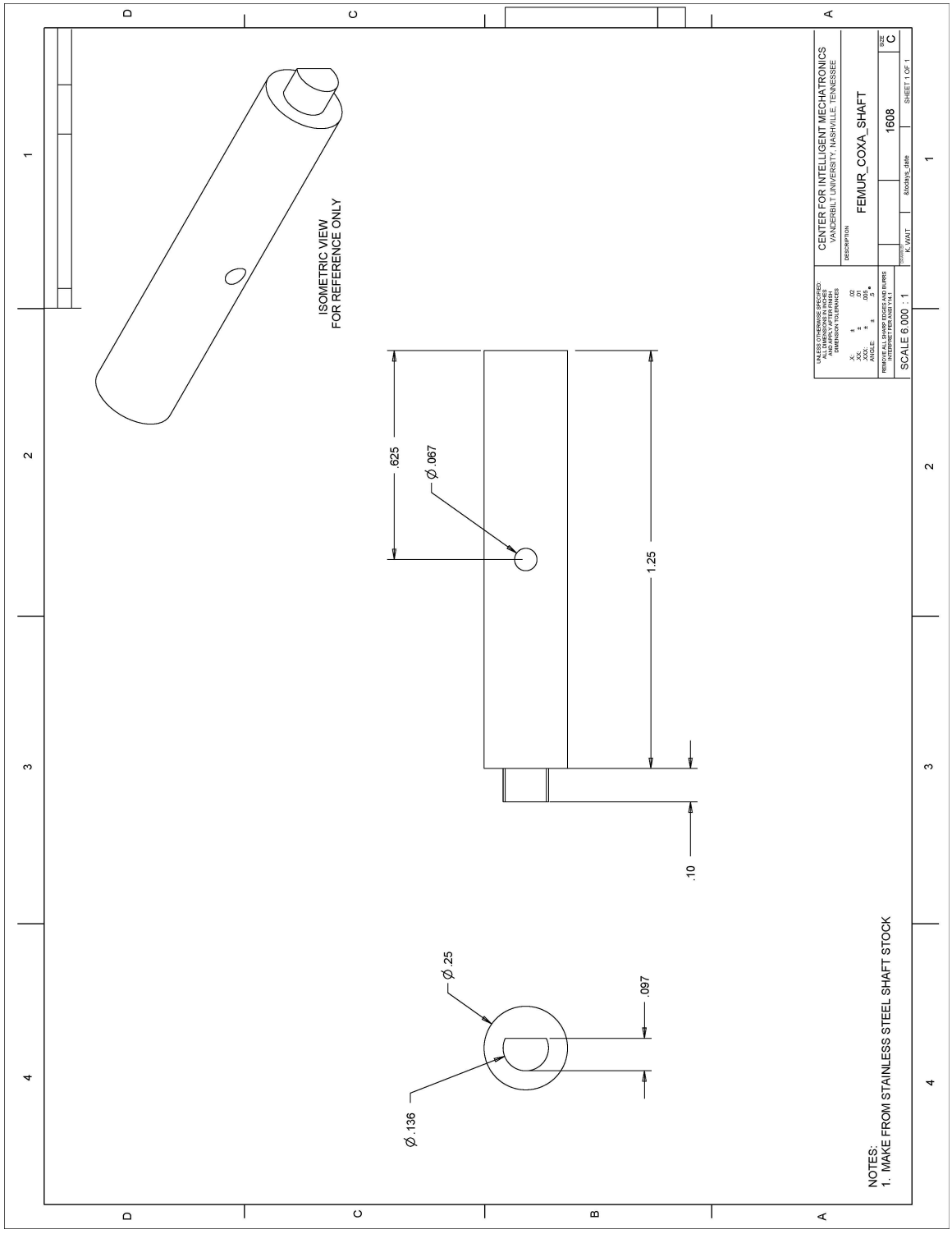
ISOMETRIC VIEW
FOR REFERENCE ONLY
.625
Ø .067
1.25
.10
Ø .25
.097
Ø .136
NOTES:
1. MAKE FROM STAINLESS STEEL SHAFT STOCK
CENTER FOR INTELLIGENT MECHATRONICS
VANDERBILT UNIVERSITY, NASHVILLE, TENNESSEE
DESCRIPTION
FEMUR_COXA_SHAFT
1608
SIZE C
SCALE 6.000 : 1
SHEET 1 OF 1
K. WATT
&tolerpts_date
UNLESS OTHERWISE SPECIFIED:
ALL DIMENSIONS IN INCHES
AND APPLY AFTER FINISH
DIMENSION TOLERANCES
REMOVE ALL SHARP EDGES AND BURRS
FINISH: AS MACHINED

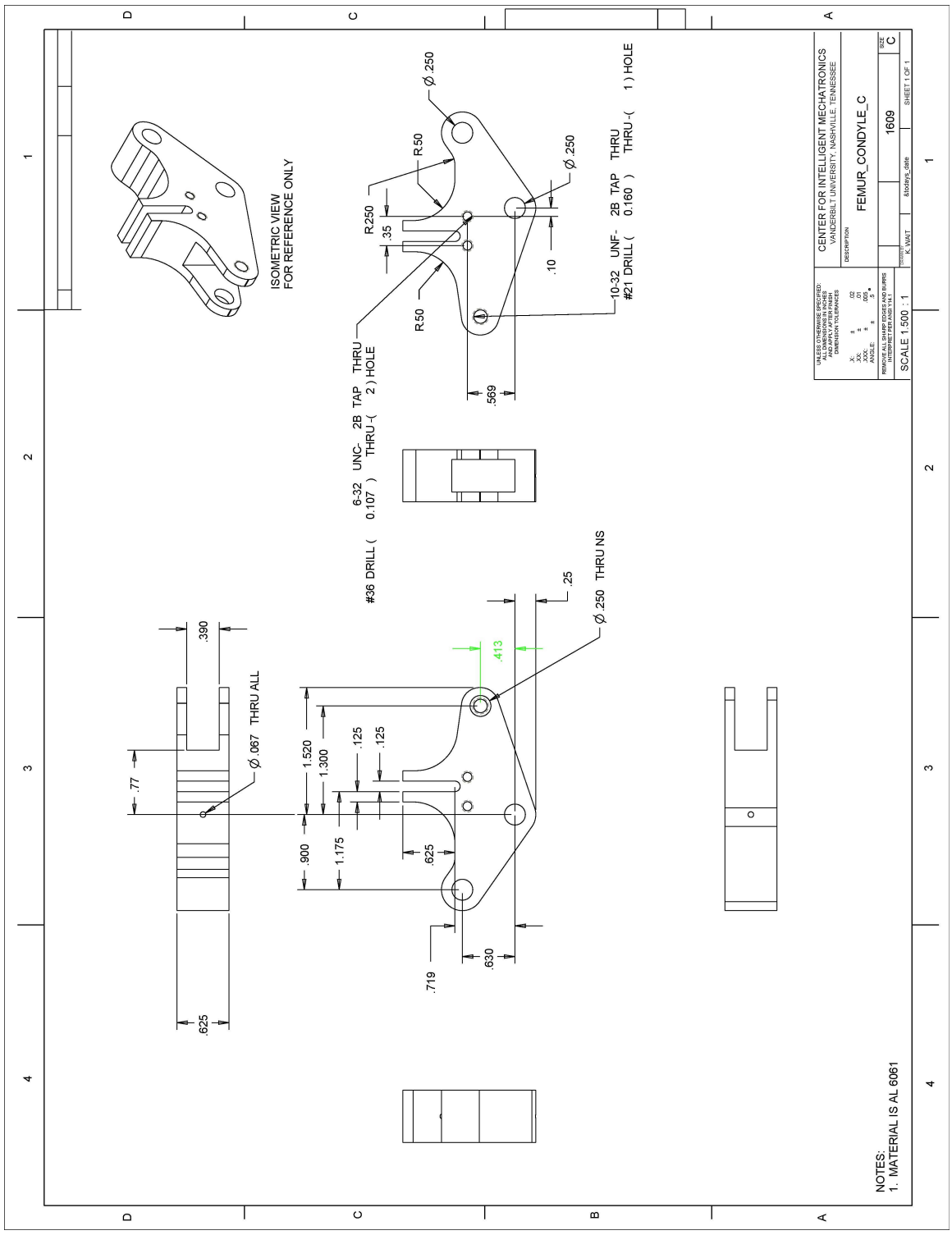
ISOMETRIC VIEW
FOR REFERENCE ONLY
Ø.250
R.50
R.250
.35
Ø.250
.10
R.50
10-32 UNF- 2B TAP THRU
#21 DRILL (0.160) THRU-(1) HOLE
6-32 UNC- 2B TAP THRU
#36 DRILL (0.107) THRU-(2) HOLE
.569
.25
Ø.250 THRU NS
.413
.390
Ø.067 THRU ALL
.77
1.520
1.300
.125
.125
.900
1.175
.625
.719
.630
.625
NOTES:
1. MATERIAL IS AL 6061
CENTER FOR INTELLIGENT MECHATRONICS
VANDERBILT UNIVERSITY, NASHVILLE, TENNESSEE
DESCRIPTION
FEMUR_CONDYLE_C
1609
SIZE C
K. WATT
SHEET 1 OF 1
SCALE 1.500 : 1

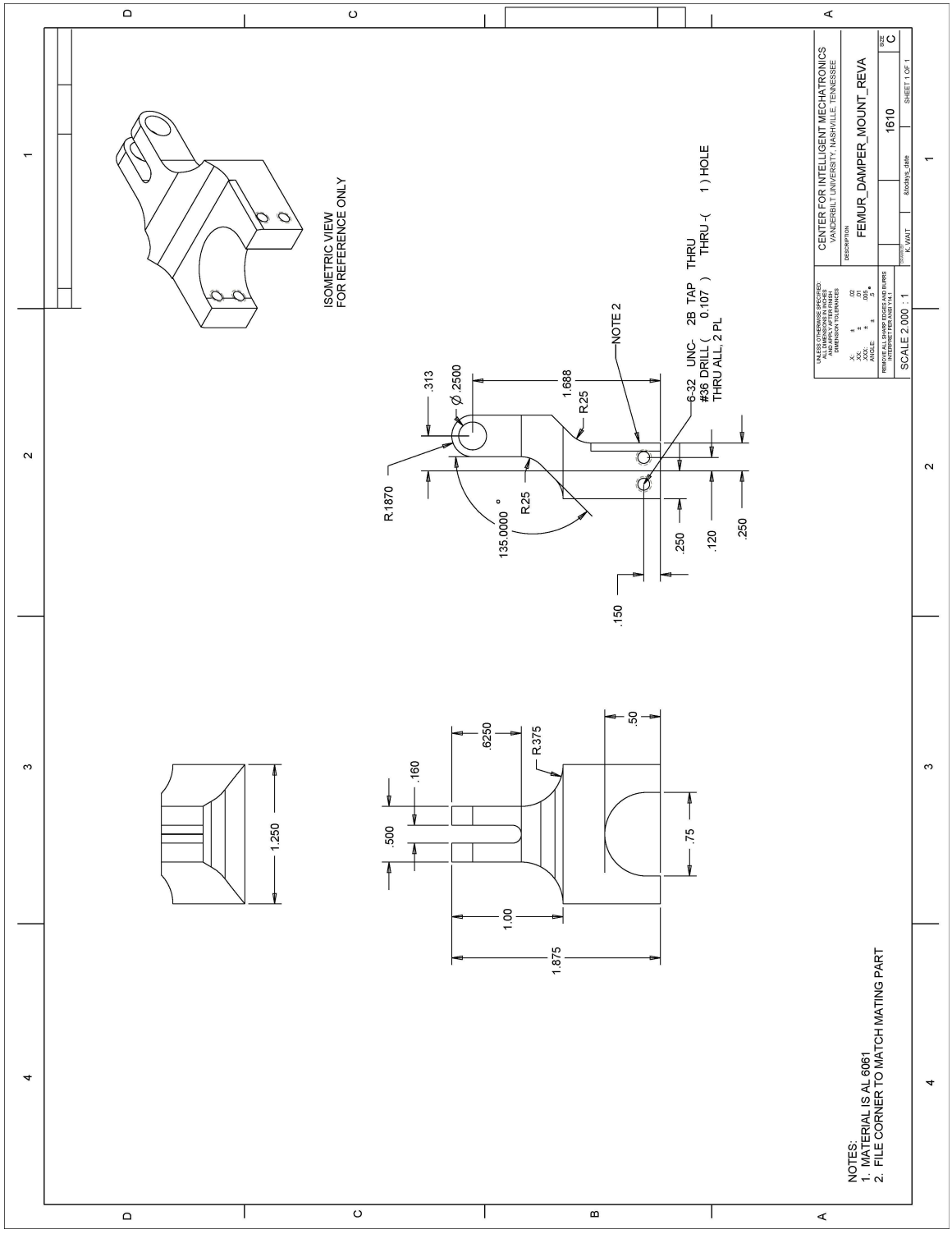
ISOMETRIC VIEW
FOR REFERENCE ONLY
NOTE 2
6-32 UNC- 2B TAP THRU
#36 DRILL (0.107) THRU -(1) HOLE
THRU ALL, 2 PL
.313
Ø .2500
1.688
R25
R.1870
R25
135.0000 °
.250
.120
.250
.150
.160
.500
.6250
R.375
.50
.75
1.00
1.875
1.250
NOTES:
1. MATERIAL IS AL 6061
2. FILE CORNER TO MATCH MATING PART
CENTER FOR INTELLIGENT MECHATRONICS
VANDERBILT UNIVERSITY, NASHVILLE, TENNESSEE
DESCRIPTION
FEMUR_DAMPER_MOUNT_REVA
1610
SIZE C
SCALE 2.000 : 1
SHEET 1 OF 1
K. WATT
&todwrg_date

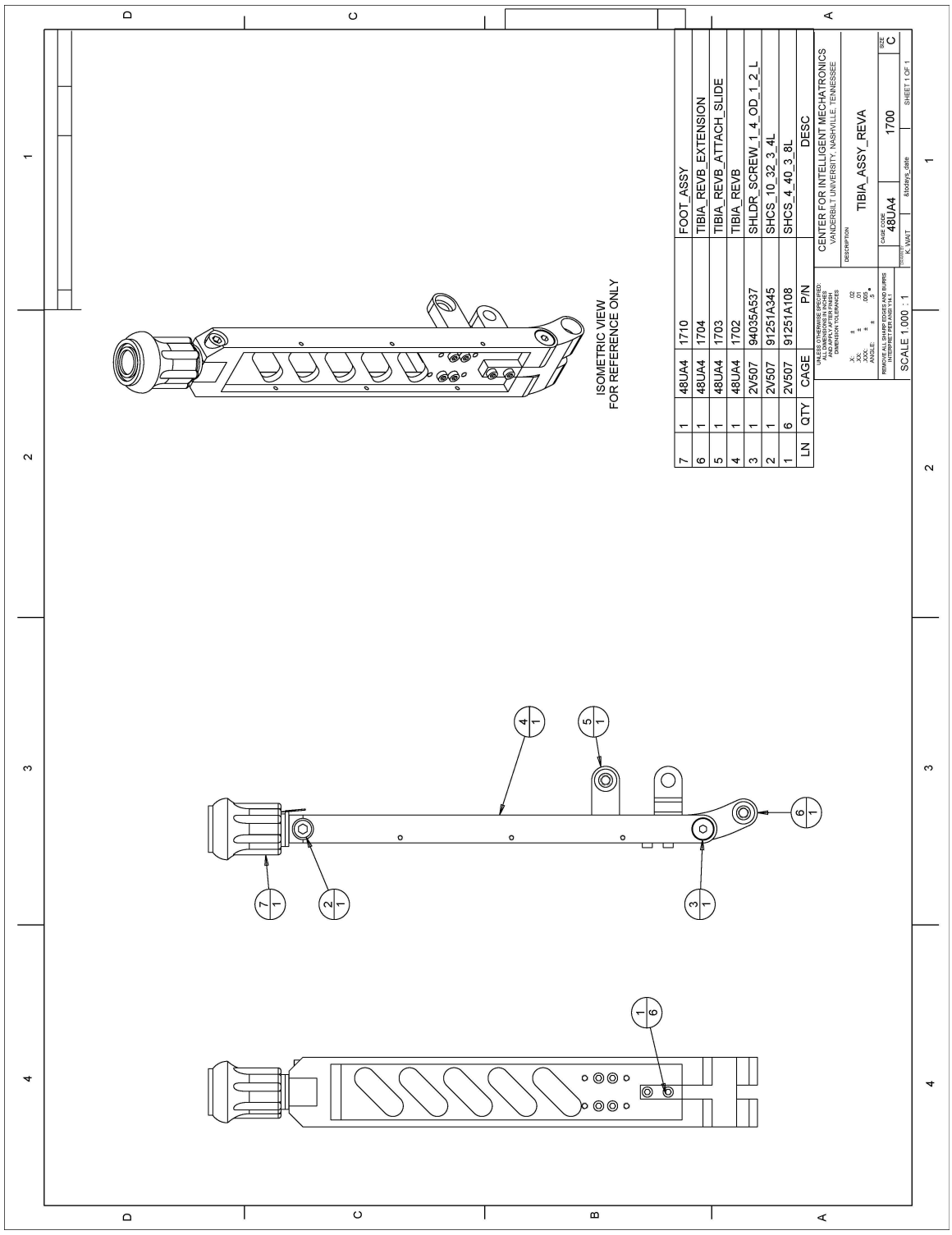
ISOMETRIC VIEW
FOR REFERENCE ONLY
7 1 48UA4 1710 FOOT_ASSY
6 1 48UA4 1704 TIBIA_REVB_EXTENSION
5 1 48UA4 1703 TIBIA_REVB_ATTACH_SLIDE
4 1 48UA4 1702 TIBIA_REVB
3 1 2V507 94035A537 SHLDR_SCREW_1_4_OD_1_2_L
2 1 2V507 91251A345 SHCS_10_32_3_4L
1 6 2V507 91251A108 SHCS_4_40_3_8L
LN QTY CAGE P/N DESC
CENTER FOR INTELLIGENT MECHATRONICS
VANDERBILT UNIVERSITY, NASHVILLE, TENNESSEE
TIBIA_ASSY_REVA
48UA4
1700
C
SCALE 1.000 1
SHEET 1 OF 1

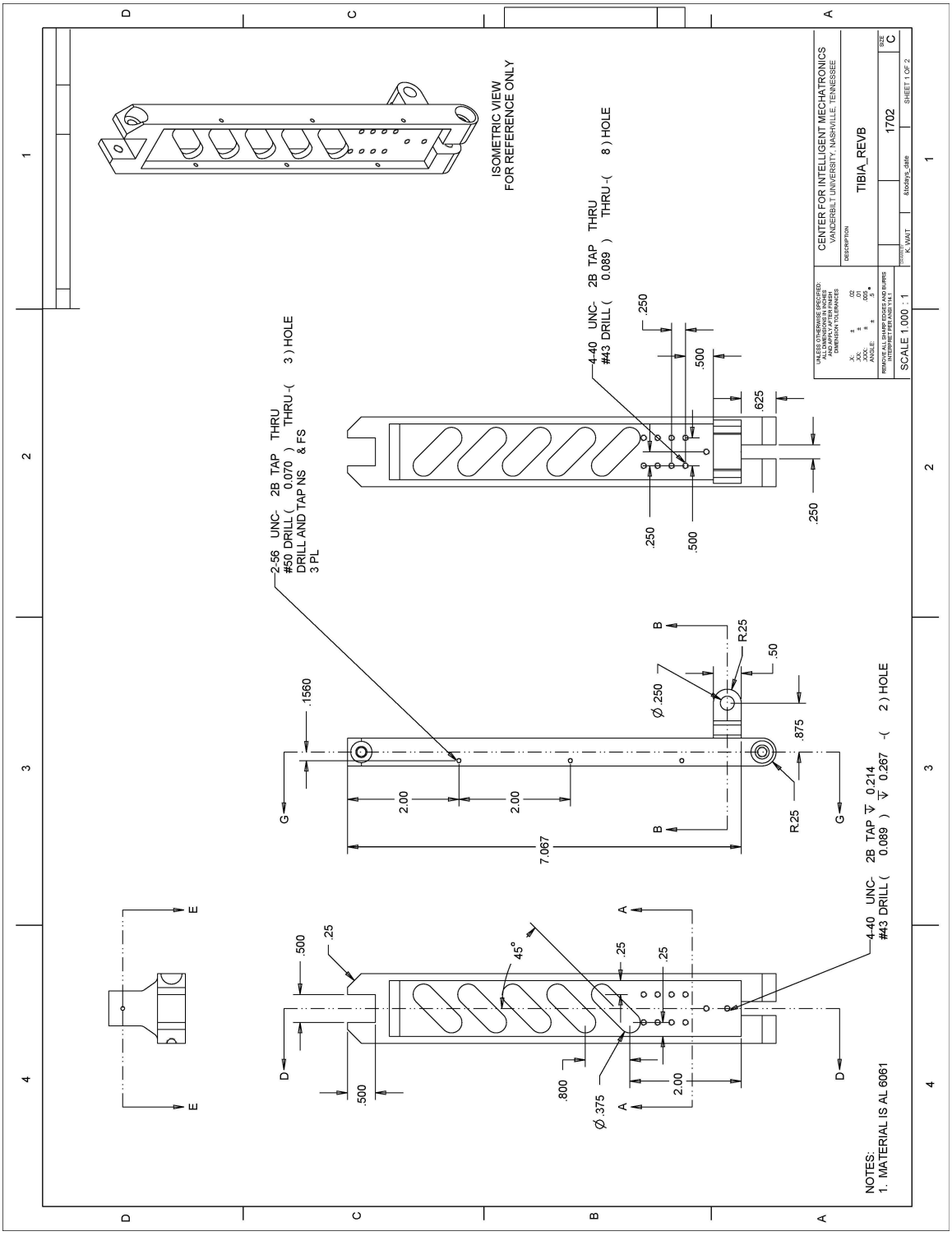
ISOMETRIC VIEW
FOR REFERENCE ONLY
4-40 UNC- 2B TAP THRU
#43 DRILL (0.089) THRU -(8) HOLE
2-56 UNC- 2B TAP THRU
#50 DRILL (0.070) THRU -(3) HOLE
DRILL AND TAP NS & FS
3 PL
4-40 UNC- 2B TAP ↧ 0.214
#43 DRILL (0.089) ↧ 0.267 -(2) HOLE
NOTES:
1. MATERIAL IS AL 6061
CENTER FOR INTELLIGENT MECHATRONICS
VANDERBILT UNIVERSITY, NASHVILLE, TENNESSEE
TIBIA_REVB
1702
SIZE C
SCALE 1.000
SHEET 1 OF 2
K. WATT

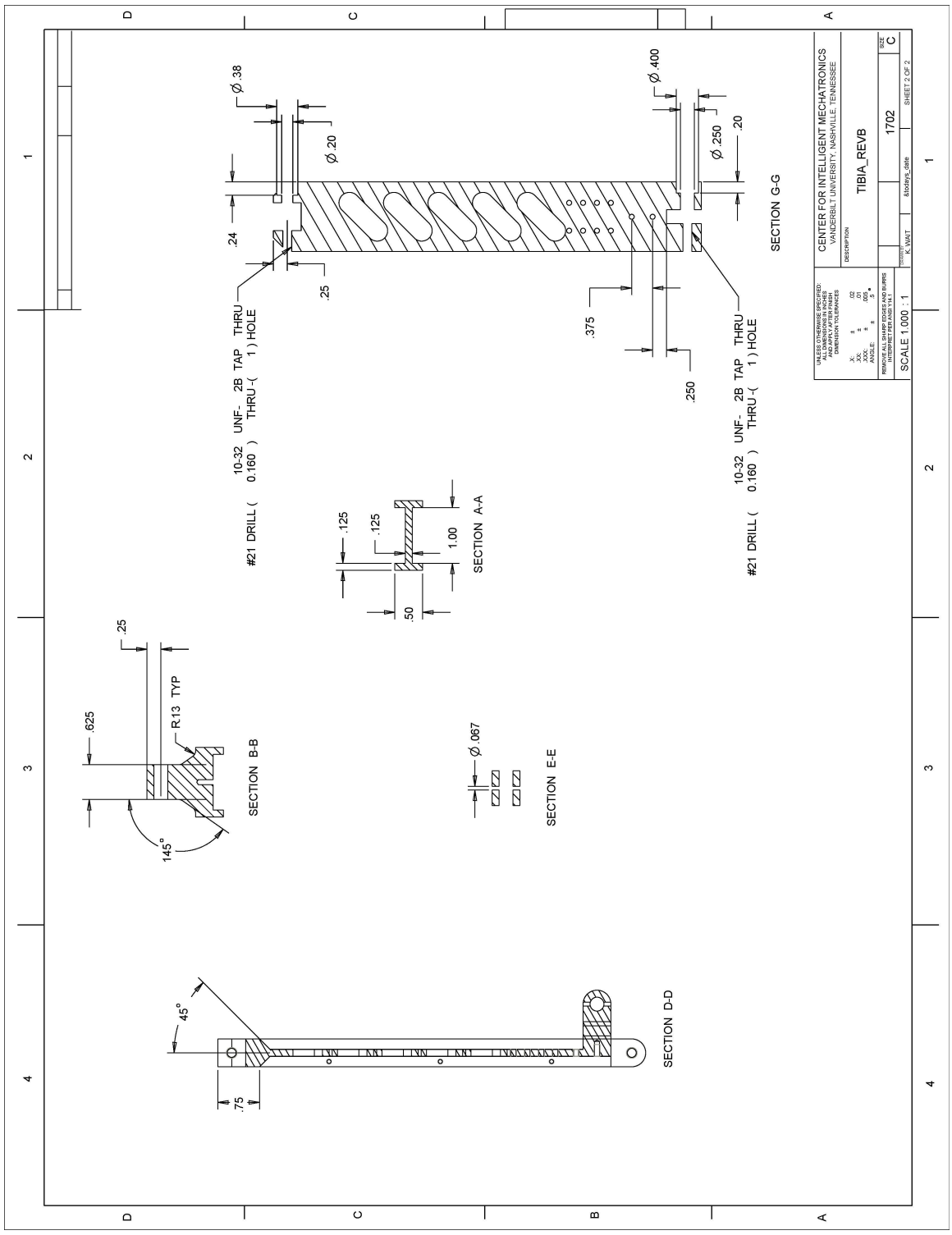
SECTION G-G
SECTION A-A
SECTION B-B
SECTION E-E
SECTION D-D
#21 DRILL (0.160) THRU
10-32 UNF- 2B TAP THRU
1) HOLE
THRU-(
Ø .38
Ø .20
Ø .400
Ø .250
.20
.24
.25
.375
.250
.125
.50
1.00
.625
R.13 TYP
145°
Ø .067
45°
.75
CENTER FOR INTELLIGENT MECHATRONICS
VANDERBILT UNIVERSITY, NASHVILLE, TENNESSEE
DESCRIPTION
TIBIA_REVB
1702
SIZE C
SHEET 2 OF 2
K. WATT
SCALE 1.000 : 1

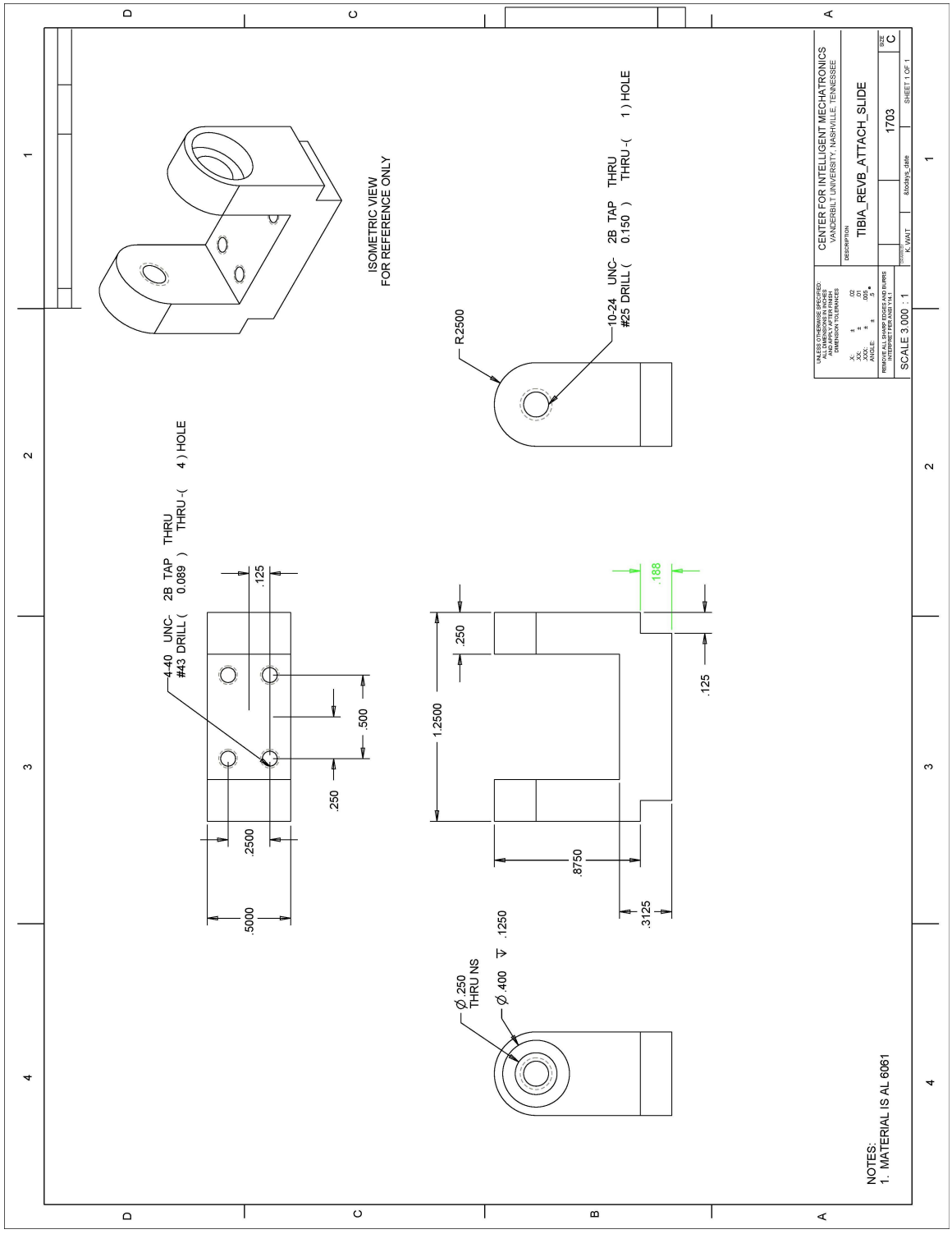
ISOMETRIC VIEW
FOR REFERENCE ONLY
R.2500
10-24 UNC- 2B TAP THRU
#25 DRILL (0.150) THRU -(1) HOLE
4-40 UNC- 2B TAP THRU
#43 DRILL (0.089) THRU -(4) HOLE
.125
.2500
.5000
.500
.250
1.2500
.250
.188
.125
.8750
.3125
Ø .250
THRU NS
Ø .400
.1250
NOTES:
1. MATERIAL IS AL 6061
CENTER FOR INTELLIGENT MECHATRONICS
VANDERBILT UNIVERSITY, NASHVILLE, TENNESSEE
DESCRIPTION
TIBIA_REVB_ATTACH_SLIDE
1703
SIZE C
K_WATT
SCALE 3.000 1:1
SHEET 1 OF 1

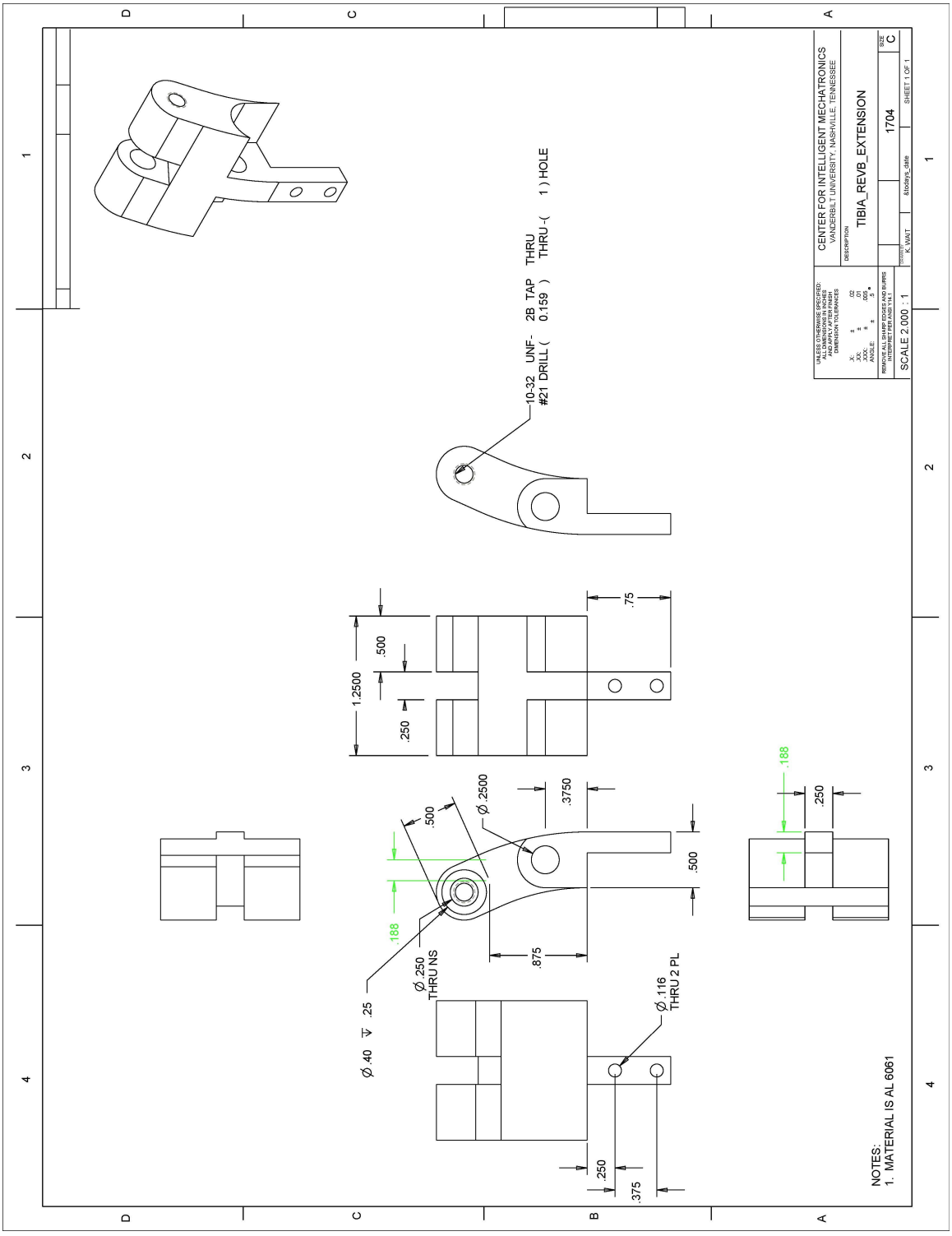
CENTER FOR INTELLIGENT MECHATRONICS
VANDERBILT UNIVERSITY, NASHVILLE, TENNESSEE
TIBIA_REVB_EXTENSION
1704
SIZE C
SCALE 2.000 : 1
SHEET 1 OF 1
K. WATT
10-32 UNF- 2B TAP THRU
#21 DRILL (0.159) THRU -(1) HOLE
1.2500
.500
.250
.75
.2500
.3750
.500
.875
.188
.250
THRU INS
.25
.40
.116
THRU 2 PL
.250
.375
NOTES:
1. MATERIAL IS AL 6061

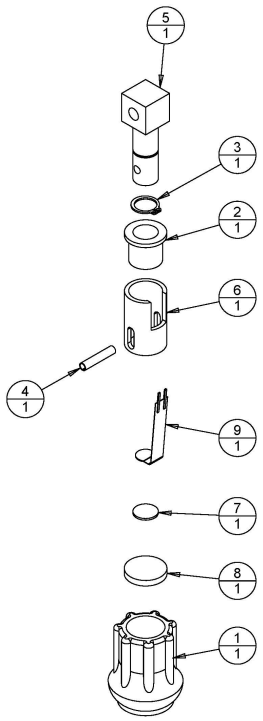

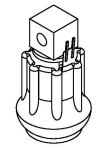

ISOMETRIC VIEW
FOR REFERENCE ONLY

LN	QTY	CAGE	P/N	DESC
9	1	5DSW2	S-20-1000-FS2	FSR
8	1	48UA4	1714	FSR_SLIDE_SURFACE
7	1	48UA4	1713	FSR_RUBBER_SPACER
6	1	48UA4	1712	FSR_BEARING_SLEEVE
5	1	48UA4	1711	TIBIA_END
4	1	2V507	98296A879	SPRING_PIN_1_8OD_5_8L
3	1	2V507	97633A170	SNAP_RING_3_8_ID
2	1	2V507	6338K461	BEARING_FLANGED_3_8ID_1_2L
1	1	2V507	2517T72	TARSUS

NOTES;
1. FEED CONNECTING END OF LN 9 THROUGH WIDE SLOT OF LN 6 BEFORE PRESSING LN 2 INTO LN 6
2. SLIDE ASSEMBLED LNs 2 & 6 ONTO LN 5 AND SECURE BY FORCING LN 3 ONTO GROOVE OF LN 5
3. PRESS LN 4 THROUGH GROOVE IN LN 6 AND INTO MATING HOLE IN LN 5 AFTER COMPLETING NOTES 1 & 2
4. ADHERE LN 7 ONTO LN 8 USING ARBITRARY ADHESIVE AND INSERT ASSEMBLY INTO LN 1

UNLESS OTHERWISE SPECIFIED:
ALL DIMENSIONS IN INCHES
AND APPLY AFTER FINISH
DIMENSION TOLERANCES
.X: ± .02
.XX: ± .01
.XXX: ± .005
ANGLE: ± .5°

REMOVE ALL SHARP EDGES AND BURRS
INTERPRET PER ANSI Y14.1

SCALE 1.000 : 1

CENTER FOR INTELLIGENT MECHATRONICS
VANDERBILT UNIVERSITY, NASHVILLE, TENNESSEE

DESCRIPTION
FOOT_ASSY

CAGE CODE		SIZE
48UA4	1710	C

DRAWN BY: K. WAIT | &todays_date | SHEET 1 OF 1

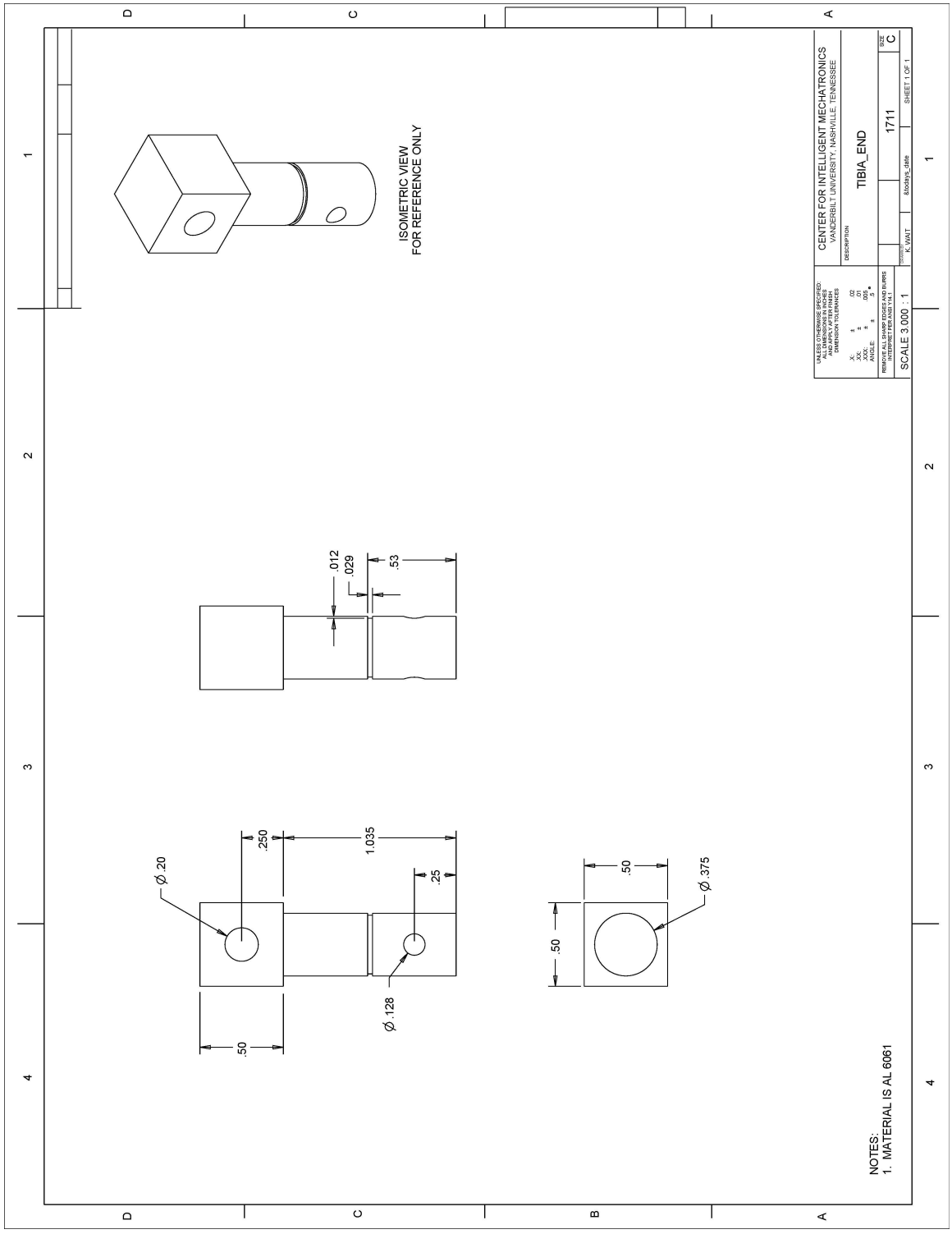
ISOMETRIC VIEW
FOR REFERENCE ONLY
.012
.029
.53
Ø .20
.250
1.035
.25
Ø .128
.50
.50
.50
Ø .375
NOTES:
1. MATERIAL IS AL 6061
CENTER FOR INTELLIGENT MECHATRONICS
VANDERBILT UNIVERSITY, NASHVILLE, TENNESSEE
TIBIA_END
1711
SIZE C
SHEET 1 OF 1
SCALE 3.000 : 1
K. WATT
&todrwg_date

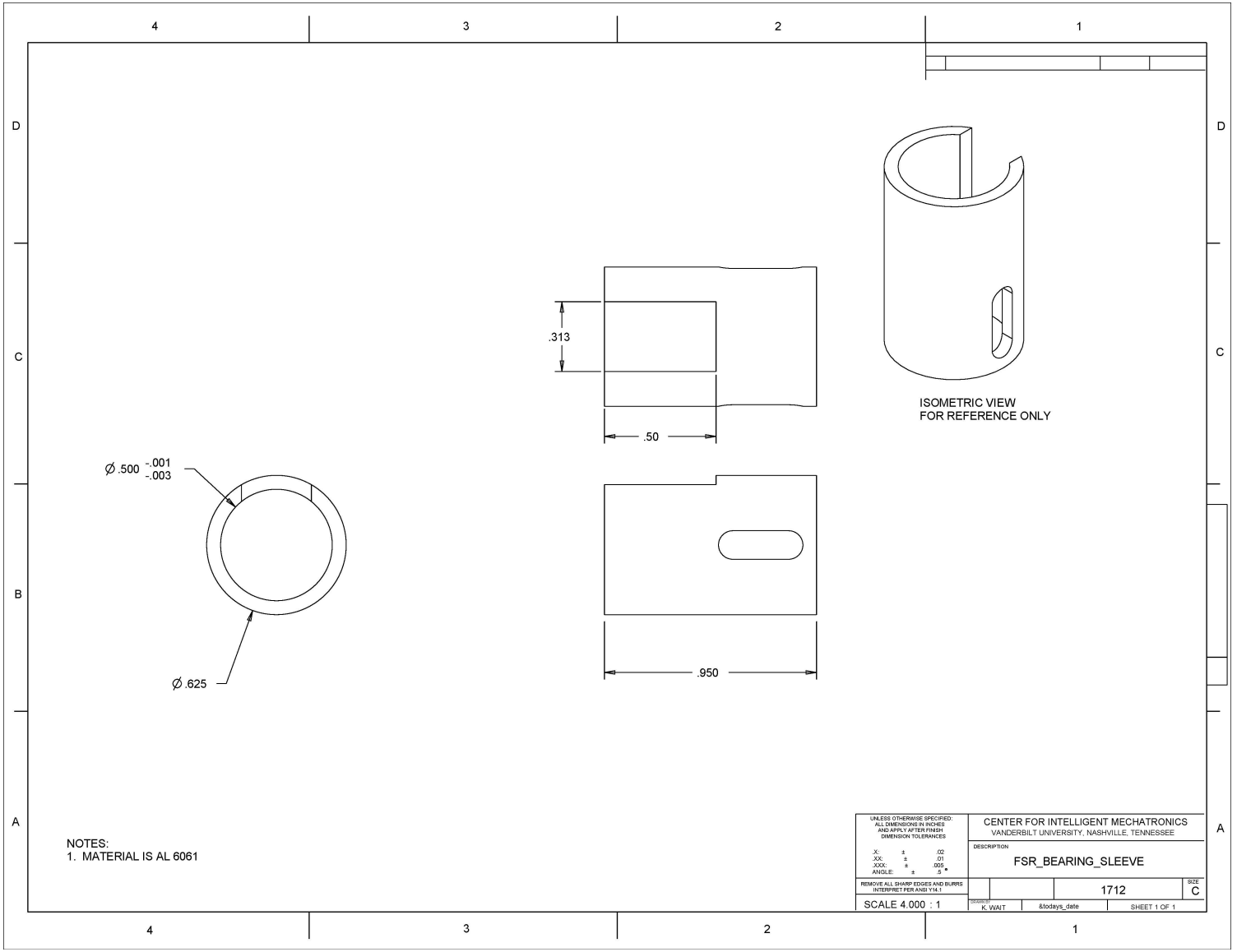
4
3
2
1
D
C
B
A
.313
.50
.950
Ø .500 -.001 -.003
Ø .625
ISOMETRIC VIEW
FOR REFERENCE ONLY
NOTES:
1. MATERIAL IS AL 6061
UNLESS OTHERWISE SPECIFIED:
ALL DIMENSIONS IN INCHES
AND APPLY AFTER FINISH
DIMENSION TOLERANCES
.X: ± .02
.XX: ± .01
.XXX: ± .005
ANGLE: ± .5°
REMOVE ALL SHARP EDGES AND BURRS
INTERPRET PER ANSI Y14.1
SCALE 4.000 : 1
CENTER FOR INTELLIGENT MECHATRONICS
VANDERBILT UNIVERSITY, NASHVILLE, TENNESSEE
DESCRIPTION
FSR_BEARING_SLEEVE
1712
SIZE
C
DRAWN BY
K. WAIT
&todays_date
SHEET 1 OF 1

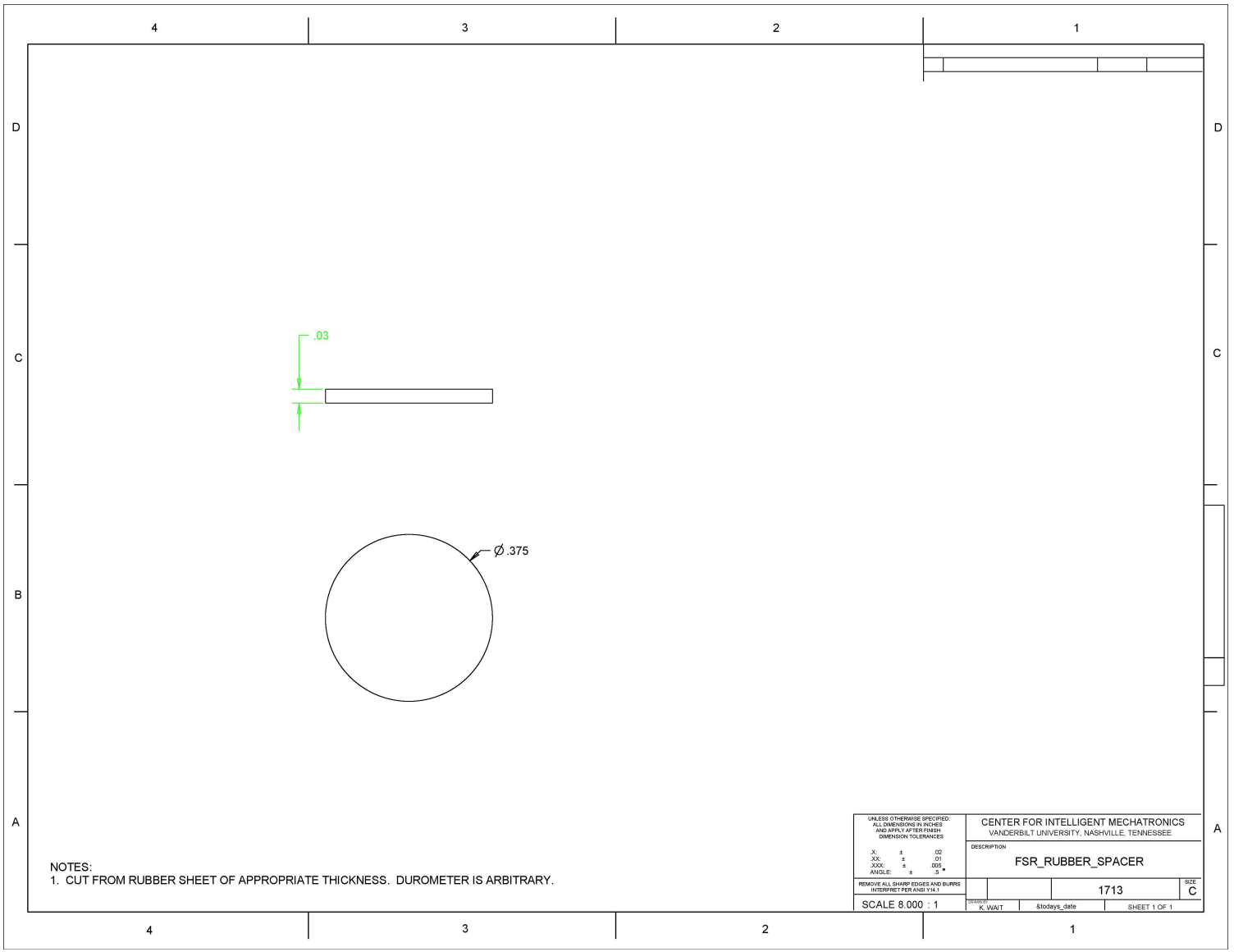
4
3
2
1
D
C
B
A
.03
Ø .375
NOTES:
1. CUT FROM RUBBER SHEET OF APPROPRIATE THICKNESS. DUROMETER IS ARBITRARY.
UNLESS OTHERWISE SPECIFIED:
ALL DIMENSIONS IN INCHES
AND APPLY AFTER FINISH
DIMENSION TOLERANCES
.X: ± .02
.XX: ± .01
.XXX: ± .005
ANGLE: ± .5 °
REMOVE ALL SHARP EDGES AND BURRS
INTERPRET PER ANSI Y14.1
SCALE 8.000 : 1
CENTER FOR INTELLIGENT MECHATRONICS
VANDERBILT UNIVERSITY, NASHVILLE, TENNESSEE
DESCRIPTION
FSR_RUBBER_SPACER
1713
SIZE
C
DRAWN BY
K. WAIT
&todays_date
SHEET 1 OF 1

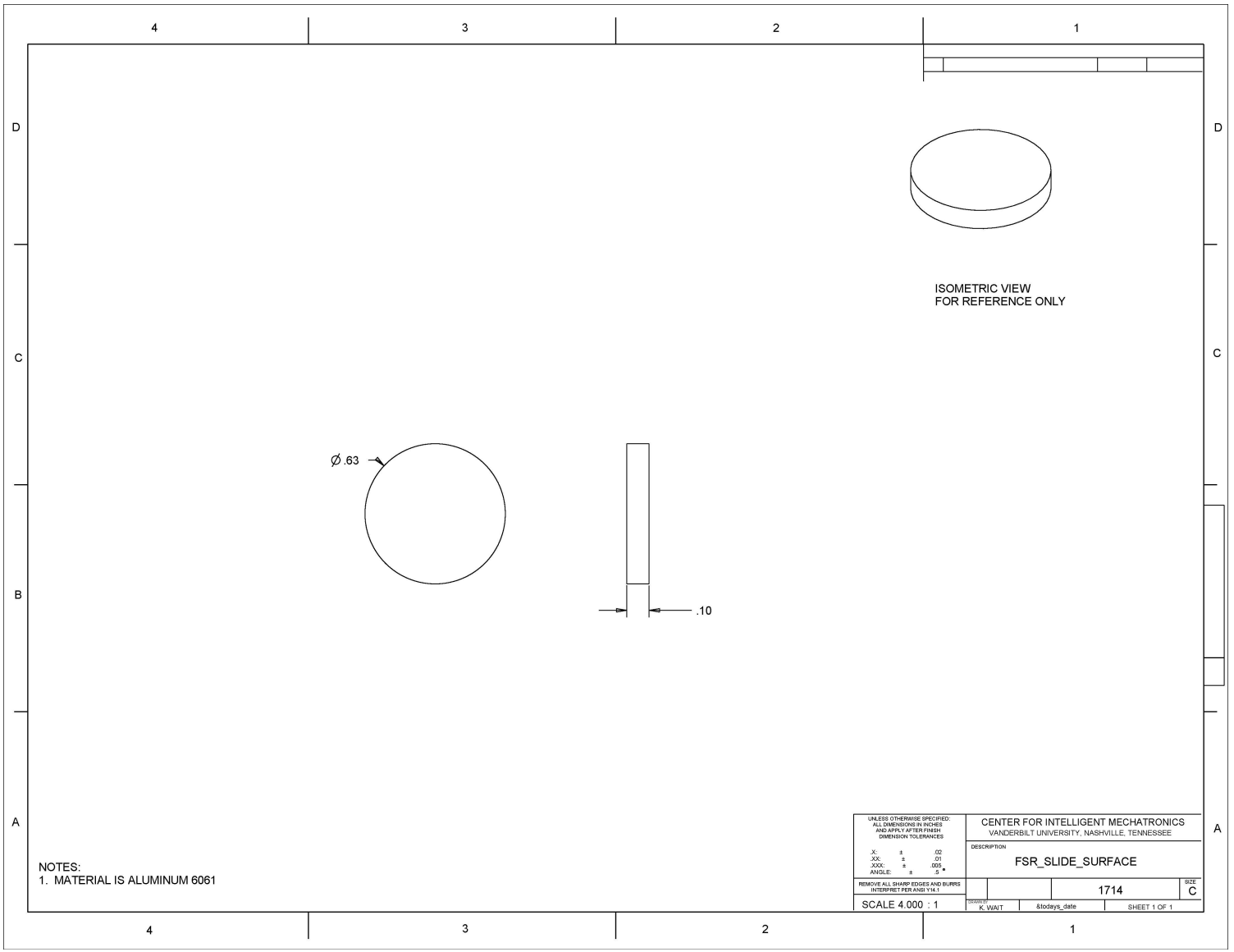
4
3
2
1
D
C
B
A
ISOMETRIC VIEW
FOR REFERENCE ONLY
Ø .63
.10
NOTES:
1. MATERIAL IS ALUMINUM 6061
UNLESS OTHERWISE SPECIFIED:
ALL DIMENSIONS IN INCHES
AND APPLY AFTER FINISH
DIMENSION TOLERANCES
.X: ± .02
.XX: ± .01
.XXX: ± .005
ANGLE: ± .5°
REMOVE ALL SHARP EDGES AND BURRS
INTERPRET PER ANSI Y14.1
SCALE 4.000 : 1
CENTER FOR INTELLIGENT MECHATRONICS
VANDERBILT UNIVERSITY, NASHVILLE, TENNESSEE
DESCRIPTION
FSR_SLIDE_SURFACE
1714
SIZE
C
DRAWN BY
K. WAIT
&todays_date
SHEET 1 OF 1

REFERENCES

[1] J.G. Cham, J.K. Karpick, and M.R. Cutkosky, "Stride Period Adaptation of a Biomimetic Running Hexapod," *The International Journal of Robotics Research*, vol. 23, Feb. 2004, pp. 141-153.

[2] M. Fujita, "AIBO: Toward the Era of Digital Creatures," *The International Journal of Robotics Research*, vol. 20, Oct. 2001, pp. 781-794.

[3] U. Saranli, M. Buehler, and D.E. Koditschek, "RHex: A Simple and Highly Mobile Hexapod Robot," *The International Journal of Robotics Research*, vol. 20, Jul. 2001, pp. 616-631.

[4] K.S. Espenschied, H.J. Chiel, R.D. Quinn, and R.D. Beer, "Leg Coordination Mechanisms in the Stick Insect Applied to Hexapod Robot Locomotion," *Adaptive Behavior*, vol. 1, Mar. 1993, pp. 455-468.

[5] S. Hirose, "A Study of Design and Control of a Quadruped Walking Vehicle," *The International Journal of Robotics Research*, vol. 3, Jun. 1984, pp. 113-133.

[6] M. Raibert, M. Chepponis, and H. Brown, "Running on four legs as though they were one," *Journal of Robotics and Automation*, vol. 2, 1986, pp. 70-82.

[7] R.A. Brooks, "A Robot that Walks; Emergent Behaviors from a Carefully Evolved Network," *Neural Computation*, vol. 1, Jun. 1989, pp. 253-262.

[8] C. Ferrell, "Robust agent control of an autonomous robot with many sensors and actuators," Thesis, MIT, 1993.

[9] B. Klaassen, R. Linnemann, D. Spenneberg, and F. Kirchner, "Biomimetic walking robot SCORPION: Control and modeling," *Robotics and Autonomous Systems*, vol. 41, Nov. 2002, pp. 69-76.

[10] D.C. Kar, "Design of Statically Stable Walking Robot: A Review," *Journal of Robotic Systems*, vol. 20, 2003, pp. 671-686.

[11] S. Kim, M. Spenko, S. Trujillo, B. Heyneman, D. Santos, and M. Cutkosky, "Smooth Vertical Surface Climbing With Directional Adhesion," *Transactions on Robotics*, vol. 24, 2008, pp. 65-74.

[12] M. Raibert, K. Blankespoor, G. Nelson, and R. Playter, "BigDog, the Rough-Terrain Quadruped Robot," *Proceedings of the 17th IFAC World Congress, 2008*, Seoul, Korea: 2008, pp. 10822-10825.

[13] I.E. Sutherland and M.K. Ullner, "Footprints in the Asphalt," *The International Journal of Robotics Research*, vol. 3, Jun. 1984, pp. 29-36.

[14] C.S. Tzafestas, N.K. M'Sirdi, and N. Manamani, "Adaptive Impedance Control Applied to a Pneumatic Legged Robot," *Journal of Intelligent and Robotic Systems*, vol. 20, 1997, pp. 105-129.

[15] D.R. Pugh, E.A. Ribble, T.E. Bihari, T.M. Walliser, M.R. Patterson, and K.J. Waldron, "Technical Description of the Adaptive Suspension Vehicle.," *International Journal of Robotics Research*, vol. 9, Apr. 1990, pp. 24-42.

[16] F. Kikuchi, Y. Ota, and S. Hirose, "Basic performance experiments for jumping quadruped," *Proceedings of the International Conference on Intelligent Robots and Systems*, 2003, pp. 3378-3383 vol.3.

[17] T. Tanaka and S. Hirose, "Development of leg-wheel hybrid quadruped "AirHopper" design of powerful light-weight leg with wheel," *Proceedings of the International Conference on Intelligent Robots and Systems*, 2008, pp. 3890-3895.

[18] G. Nelson and R. Quinn, "Posture control of a cockroach-like robot," *IEEE Control Systems Magazine*, vol. 19, 1999, pp. 9-14.

[19] G. Nelson, R. Quinn, R. Bachmann, W. Flannigan, R. Ritzmann, and J. Watson, "Design and simulation of a cockroach-like hexapod robot," *Proceedings of the International Conference on Robotics and Automation*, 1997, pp. 1106-1111 vol.2.

[20] B. Luk, A. Collie, and J. Billingsley, "Robug II: An intelligent wall climbing robot," *Proceedings of the International Conference on Robotics and Automation*, 1991, pp. 2342-2347 vol.3.

[21] B. Luk, A. Collie, V. Piefort, and G. Virk, "Robug III: a tele-operated climbing and walking robot," *Control, UKACC International Conference on*, 1996, pp. 347-352 vol.1.

[22] S. Galt, B. Luk, D. Cooke, and A. Collie, "A tele-operated semi-intelligent climbing robot for nuclear applications," *Mechatronics and Machine Vision in Practice, 1997. Proceedings., Fourth Annual Conference on*, 1997, pp. 118-123.

[23] M. Binnard, "Design of a small pneumatic walking robot," Thesis, MIT, 1995.

[24] K. Kuribayashi, "Criteria for the evaluation of new actuators as energy converters," *Advanced Robotics*, vol. 7, 1993, pp. 289-307.

[25] S. Kim, J.E. Clark, and M.R. Cutkosky, "iSprawl: Design and Tuning for High-speed Autonomous Open-loop Running ," *The International Journal of Robotics Research*, vol. 25, 2006, pp. 903-912.

[26] K. Aschenbeck, N. Kern, R. Bachmann, and R. Quinn, "Design of a Quadruped Robot Driven by Air Muscles," *Proceedings of the First IEEE/RAS-EMBS International Conference on Biomedical Robotics and Biomechatronics*, 2006, pp. 875-880.

[27] J.E. Bares and D.S. Wettergreen, "Dante II: Technical Description, Results, and Lessons Learned," *The International Journal of Robotics Research*, vol. 18, Jul. 1999, pp. 621-649.

[28] T. Doi, R. Hodoshima, S. Hirose, Y. Fukuda, T. Okamoto, and J. Mori, "Development of a quadruped walking robot to work on steep slopes, TITAN XI (walking motion with compensation for compliance)," *Intelligent Robots and Systems, Proceedings of the IEEE/RSJ International Conference on*, 2005, pp. 2067-2072.

[29] Y. Sakagami, R. Watanabe, C. Aoyama, S. Matsunaga, N. Higaki, and K. Fujimura, "The intelligent ASIMO: system overview and integration," *Intelligent Robots and Systems, Proceedings of the IEEE/RSJ International Conference on*, 2002, pp. 2478-2483 vol.3.

[30] J. Smith and I. Poulakakis, "Rotary gallop in the untethered quadrupedal robot scout II," *Intelligent Robots and Systems, Proceedings of the IEEE/RSJ International Conference on*, 2004, pp. 2556-2561 vol.3.

[31] J. Estremera and P. Gonzalez de Santos, "Free Gaits for Quadruped Robots over Irregular Terrain," *The International Journal of Robotics Research*, vol. 21, Feb. 2002, pp. 115-130.

[32] B. Gassmann, K. Scholl, and K. Berns, "Locomotion of LAURON III in rough terrain," *Advanced Intelligent Mechatronics, 2001. Proceedings. 2001 IEEE/ASME International Conference on*, 2001, pp. 959-964 vol.2.

[33] J. Chung, I. Park, and J. Oh, "On the Design and Development of a Quadruped Robot Platform," *Advanced Robotics*, vol. 24, 2010, pp. 277-298.

[34] M. Goldfarb, E.J. Barth, M.A. Gogola, and J.A. Wehrmeyer, "Design and energetic characterization of a liquid-propellant-powered actuator for self-powered robots," *Mechatronics, IEEE/ASME Transactions on*, vol. 8, 2003, pp. 254-262.

[35] K. Fite, T. Withrow, X. Shen, K. Wait, J. Mitchell, and M. Goldfarb, "A Gas-Actuated Anthropomorphic Prosthesis for Transhumeral Amputees," *Robotics, IEEE Transactions on*, vol. 24, 2008, pp. 159-169.

[36] K. Fite, T. Withrow, K. Wait, and M. Goldfarb, "Liquid-Fueled Actuation for an Anthropomorphic Upper Extremity Prosthesis," *Engineering in Medicine and Biology Society, Proceedings of the 28th Annual International Conference of the IEEE*, 2006, pp. 5638-5642.

[37] B. Shields, K. Fite, and M. Goldfarb, "Design, control, and energetic characterization of a solenoid-injected monopropellant-powered actuator," *Mechatronics, IEEE/ASME Transactions on*, vol. 11, 2006, pp. 477-487.

[38] J.A. Riofrio and E.J. Barth, "Design of a Free Piston Pneumatic Compressor as a Mobile Robot Power Supply," *Robotics and Automation, Proceedings of the IEEE International Conference on*, 2005, pp. 235-240.

[39] J.A. Riofrio and E.J. Barth, "A Free Piston Compressor as a Pneumatic Mobile Robot Power Supply: Design, Characterization and Experimental Operation," *International Journal of Fluid Power*, vol. 8, Mar. 2007, pp. 17-28.

[40] K.W. Wait and M. Goldfarb, "A Biologically Inspired Approach to the Coordination of Hexapedal Gait," *Robotics and Automation, Proceedings of the IEEE International Conference on*, 2007, pp. 275-280.

[41] K.W. Wait, S.A. Dalley, and M. Goldfarb, "Design and control of a biomimetic hexapedal walker," *Biomedical Robotics and Biomechatronics, Proceedings of the 2nd IEEE RAS & EMBS International Conference on*, 2008, pp. 270-275.

[42] K.W. Wait and M. Goldfarb, "Enhanced Performance and Stability in Pneumatic Servosystems With Supplemental Mechanical Damping," *Journal of Dynamic Systems, Measurement, and Control*, vol. 132, 2010, p. 041012.

[43] Bo-Hee Lee and In-Ku Lee, "The implementation of the gaits and body structure for hexapod robot," *Industrial Electronics, Proceedings of the IEEE International Symposium on*, 2001, pp. 1959-1964 vol.3.

[44] T. Zielinska, T. Goh, and Choong Kwong Chong, "Design of autonomous hexapod," *Robot Motion and Control, Proceedings of the First Workshop on*, 1999, pp. 65-69.

[45] J. Clark, J. Cham, S. Bailey, E. Froehlich, P. Nahata, R. Full, and M. Cutkosky, "Biomimetic design and fabrication of a hexapedal running robot," *Robotics and Automation, Proceedings of the IEEE International Conference on*, 2001, pp. 3643-3649 vol.4.

[46] Y. Tanaka and Y. Matoba, "Study of an intelligent hexapod walking robot," *Intelligent Robots and Systems, Proceedings of the IEEE/RSJ International Workshop on*, 1991, pp. 1535-1540 vol.3.

[47] U. Saranli, M. Buehler, and D. Koditschek, "Design, modeling and preliminary control of a compliant hexapod robot," *Robotics and Automation, Proceedings of the IEEE International Conference on*, 2000, pp. 2589-2596 vol.3.

[48] E. Klavins, H. Koms, R.J. Full, and D.E. Koditschek, "The Role of Reflexes Versus Central Pattern Generators in Dynamical Legged Locomotion," *Neurotechnology for Biomimetic Robots*, Cambridge, MA: MIT Press, 2002.

[49] H. Chiel, R. Beer, R. Quinn, and K. Espenschied, "Robustness of a distributed neural network controller for locomotion in a hexapod robot," *Robotics and Automation, IEEE Transactions on*, vol. 8, 1992, pp. 293-303.

[50] R.D. Quinn, G.M. Nelson, and R.E. Ritzmann, "Toward the Development of Agile and Mission Capable Legged Robots," *Neurotechnology for Biomimetic Robots*, Cambridge, MA: MIT Press, 2002.

[51] A. Calvitti and R.D. Beer, "Analysis of a distributed model of leg coordination," *Biological Cybernetics*, vol. 82, Feb. 2000, pp. 197-206.

[52] M. Svinin, K. Yamada, and K. Ueda, "Emergent synthesis of motion patterns for locomotion robots," *Artificial Intelligence in Engineering*, vol. 15, Oct. 2001, pp. 353-363.

[53] F. Pfeiffer, J. Eltze, and H. Weidemann, “Six-legged technical walking considering biological principles,” *Robotics and Autonomous Systems*, vol. 14, May. 1995, pp. 223-232.

[54] H. Cruse, J. Dean, V. Durr, T. Kindermann, J. Schmitz, and M. Schumm, “A decentralized, biologically based network for autonomous control of (hexapod) walking,” *Neurotechnology for Biomimetic Robots*, Cambridge, MA: MIT Press, 2002.

[55] H. Cruse, “What mechanisms coordinate leg movement in walking arthropods?,” *Trends in Neurosciences*, vol. 13, Jan. 1990, pp. 15-21.

[56] V. Durr, “Stereotypic leg searching movements in the stick insect: kinematic analysis, behavioural context and simulation,” *J Exp Biol*, vol. 204, May. 2001, pp. 1589-1604.

[57] K.B. Fite, J.E. Mitchell, E.J. Barth, and M. Goldfarb, “A Unified Force Controller for a Proportional-Injector Direct-Injection Monopropellant-Powered Actuator,” *Journal of Dynamic Systems, Measurement, and Control*, vol. 128, Mar. 2006, pp. 159-164.

[58] K.B. Fite and M. Goldfarb, “Design and energetic characterization of a proportional-injector monopropellant-powered actuator,” *Mechatronics, IEEE/ASME Transactions on*, vol. 11, 2006, pp. 196-204.

[59] K.S. Espenschied, R.D. Quinn, R.D. Beer, and H.J. Chiel, “Biologically based distributed control and local reflexes improve rough terrain locomotion in a hexapod robot ,” *Robotics and Autonomous Systems*, vol. 18, Jul. 1996, pp. 59-64.

[60] G.A. Pratt, “Low Impedance Walking Robots,” *Integr. Comp. Biol.*, vol. 42, Feb. 2002, pp. 174-181.

[61] N. Hogan, “An organizing principle for a class of voluntary movements,” *J. Neurosci.*, vol. 4, Nov. 1984, pp. 2745-2754.

[62] T. Flash and N. Hogan, “The coordination of arm movements: an experimentally confirmed mathematical model,” *J. Neurosci.*, vol. 5, Jul. 1985, pp. 1688-1703.

[63] K.B. Fite, J.E. Mitchell, E.J. Barth, and M. Goldfarb, “Design and Characterization of a Rotary Actuated Hot Gas Servovalve,” *ASME International Mechanical Engineering Congress and Exposition*, 2004, pp. 63-69.

[64] H. Cruse, “The function of the legs in the free walking stick insect, Carausius morosus,” *Journal of Comparative Physiology A: Neuroethology, Sensory, Neural, and Behavioral Physiology*, vol. 112, 1976, pp. 262, 235.

[65] H. Cruse and C. Bartling, “Movement of joint angles in the legs of a walking insect, Carausius morosus,” *Journal of Insect Physiology*, vol. 41, Sep. 1995, pp. 761-771.

[66] N. Hogan, “Adaptive control of mechanical impedance by coactivation of antagonist muscles,” *Automatic Control, IEEE Transactions on*, vol. 29, 1984, pp. 681-690.

[67] N. Hogan, “Impedance control - An approach to manipulation. I - Theory. II - Implementation. III - Applications,” *ASME Transactions Journal of Dynamic Systems and Measurement Control B,* vol. 107, 1985, pp. 24, 1.

[68] T. Roggendorf, “Comparing different controllers for the coordination of a six-legged walker,” *Biological Cybernetics*, vol. 92, Apr. 2005, pp. 261-274.

[69] F. Sup, A. Bohara, and M. Goldfarb, “Design and Control of a Powered Transfemoral Prosthesis,” *The International Journal of Robotics Research*, vol. 27, Feb. 2008, pp. 263-273.

[70] G. Bone and S. Ning, “Experimental Comparison of Position Tracking Control Algorithms for Pneumatic Cylinder Actuators,” *Mechatronics, IEEE/ASME Transactions on*, vol. 12, 2007, pp. 557-561.

[71] J. Bobrow and B. McDonell, “Modeling, identification, and control of a pneumatically actuated, force controllable robot,” *Robotics and Automation, IEEE Transactions on*, vol. 14, 1998, pp. 732-742.

[72] Z. Rao and G. Bone, “Nonlinear Modeling and Control of Servo Pneumatic Actuators,” *Control Systems Technology, IEEE Transactions on*, vol. 16, 2008, pp. 562-569.

[73] B.W. Surgenor and N.D. Vaughan, “Continuous Sliding Mode Control of a Pneumatic Actuator,” *Journal of Dynamic Systems, Measurement, and Control*, vol. 119, Sep. 1997, pp. 578-581.

[74] E. Richer and Y. Hurmuzlu, “A High Performance Pneumatic Force Actuator System: Part II—Nonlinear Controller Design,” *Journal of Dynamic Systems, Measurement, and Control*, vol. 122, Sep. 2000, pp. 426-434.

[75] K.A. Al-Dakkan, E.J. Barth, and M. Goldfarb, “Dynamic Constraint-Based Energy-Saving Control of Pneumatic Servo Systems,” *Journal of Dynamic Systems, Measurement, and Control*, vol. 128, Sep. 2006, pp. 655-662.

[76] X. Shen and M. Goldfarb, “Energy Saving in Pneumatic Servo Control Utilizing Interchamber Cross-Flow,” *Journal of Dynamic Systems, Measurement, and Control*, vol. 129, May. 2007, pp. 303-310.

[77] J. Wang, J. Pu, and P. Moore, “A practical control strategy for servo-pneumatic actuator systems,” *Control Engineering Practice*, vol. 7, Dec. 1999, pp. 1483-1488.

[78] T. Kimura, S. Hara, T. Fujita, and T. Kagawa, “Feedback linearization for pneumatic actuator systems with static friction,” *Control Engineering Practice*, vol. 5, Oct. 1997, pp. 1385-1394.

[79] J. Wang, D. Wang, P. Moore, and J. Pu, “Modelling study, analysis and robust servo control of pneumatic cylinder actuator systems,” *Control Theory and Applications, IEE Proceedings -*, vol. 148, 2001, pp. 35-42.

[80] J.L. Shearer, “Study of Pneumatic Processes in the Continuous Control of Motion With Compressed Air - I,II,” *Transactions of the ASME*, Feb. 1956, pp. 233-249.

[81] S. Liu and J. Bobrow, "An Analysis of a Pneumatic Servo System and Its Application to a Computer-Controlled Robot," *Journal of Dynamic Systems, Measurement, and Control*, vol. 110, Sep. 1988, pp. 228-235.

[82] J.J. Mannetje, "Pneumatic Servo Design Method Improves System Bandwidth Twenty-fold," *Control Engineering*, Jun. 1981, pp. 79-83.

[83] D.R. Vaughan, "Hot-Gas Actuators: Some Limits on the Response Speed," *ASME Journal of Basic Engineering*, Mar. 1965, pp. 113-119.

[84] J.F. Huff, "Precision Motion Control Device," U.S. Patent 3,176,801, April 6, 1965.

[85] M.J. Crosby, "Hydropneumatic drive apparatus," U.S. Patent 4,528,894, July 16, 1985.

[86] J.F. McCormick, "High speed pneumatic servo actuator with hydraulic damper," U.S. Patent 5,458,047, October 17, 1995.

[87] G. Klute, J. Czerniecki, and B. Hannaford, "McKibben artificial muscles: pneumatic actuators with biomechanical intelligence," *Advanced Intelligent Mechatronics, 1999. Proceedings. 1999 IEEE/ASME International Conference on*, 1999, pp. 221-226.

[88] M. Hildebrand, "The Quadrupedal Gaits of Vertebrates," *BioScience*, vol. 39, Dec. 1989, pp. 766-775.

[89] S. Grillner, "Neurobiological bases of rhythmic motor acts in vertebrates," *Science*, vol. 228, Apr. 1985, pp. 143-149.

[90] O. Kiehn and S.J.B. Butt, "Physiological, anatomical and genetic identification of CPG neurons in the developing mammalian spinal cord," *Progress in Neurobiology*, vol. 70, Jul. 2003, pp. 347-361.

[91] G. Goslow, H. Seeherman, C.R. Taylor, M. McCutchin, and N. Heglund, "Electrical activity and relative length changes of dog limb muscles as a function of speed and gait," *Journal of Experimental Biology*, vol. 94, 1981, pp. 15-42.

[92] V. Hugel and P. Blazevic, "Towards efficient implementation of quadruped gaits with duty factor of 0.75," *Proceedings of the International Conference on Robotics and Automation*, 1999, pp. 2360-2365 vol.3.

[93] D. Pongas, M. Mis, and S. Schaal, "A Robust Quadruped Walking Gait for Traversing Rough Terrain," *Proceedings of the International Conference on Robotics and Automation*, 2007, pp. 1474 - 1479.

[94] H. Weidemann, F. Pfeiffer, and J. Eltze, "The six-legged TUM walking robot," *Intelligent Robots and Systems. Proceedings of the IEEE/RSJ/GI International Conference on*, 1994, pp. 1026-1033 vol.2.

[95] A. Schneider, H. Cruse, and J. Schmitz, "Decentralized Control of Elastic Limbs in Closed Kinematic Chains," *The International Journal of Robotics Research*, vol. 25, Sep. 2006, pp. 913-930.

[96] H. Weidemann, F. Pfeiffer, and J. Eltze, “A design concept for legged robots derived from the walking stick insect,” *Intelligent Robots and Systems '93, IROS '93. Proceedings of the 1993 IEEE/RSJ International Conference on*, 1993, pp. 545-552 vol.1.

[97] R.B. McGhee and A.A. Frank, “On the stability properties of quadruped creeping gaits,” *Mathematical Biosciences*, vol. 3, Oct. 1968, pp. 331-351.

[98] H. Tsukagoshi, S. Hirose, and K. Yoneda, “Maneuvering operations of the quadruped walking robot on the slope,” *Intelligent Robots and Systems, Proceedings of the IEEE/RSJ International Conference on*, 1996, pp. 863-869 vol.2.

[99] M. Raibert, *Legged Robots That Balance*, MIT Press, 1986.

[100] J.Z. Kolter, Y. Kim, and A.Y. Ng, “Stereo vision and terrain modeling for quadruped robots,” *Proceedings of the International Conference on Robotics and Automation*, 2009, pp. 1557-1564.

[101] N. Ratliff, M. Zucker, J.A. Bagnell, and S. Srinivasa, “CHOMP: Gradient optimization techniques for efficient motion planning,” *Proceedings of the International Conference on Robotics and Automation*, 2009, pp. 489-494.

[102] J. Rebula, P. Neuhaus, B. Bonnlander, M. Johnson, and J. Pratt, “A Controller for the LittleDog Quadruped Walking on Rough Terrain,” *Proceedings of the International Conference on Robotics and Automation*, 2007, pp. 1467-1473.

[103] A. Shkolnik and R. Tedrake, “Inverse Kinematics for a Point-Foot Quadruped Robot with Dynamic Redundancy Resolution,” *Proceedings of the International Conference on Robotics and Automation*, 2007, pp. 4331-4336.

[104] J.J. Craig, *Introduction to Robotics: mechanics and control*, Reading, MA: Addison Wesley Longman, 1989.

[105] E. Muybridge, *Animals in Motion*, New York: Dover Publications, 1957.

[106] D.F. Hoyt and C.R. Taylor, “Gait and the energetics of locomotion in horses,” *Nature*, vol. 292, Jul. 1981, pp. 239-240.

[107] R.M. Alexander, “Walking and Running,” *The Mathematical Gazette*, vol. 80, Jul. 1996, pp. 262-266.